Contribution to the investigation of cell-to-module performance ratios in advanced heterojunction silicon photovoltaic technologies

Julien Eymard

N° d'ordre NNT : 2021LYSES014

THESE de DOCTORAT DE L'UNIVERSITE DE LYON

Opérée au sein du
Laboratoire Hubert Curien

Ecole Doctorale N° 488
Sciences Ingénierie Santé

Spécialité / discipline de doctorat:
Optique - Photonique - Hyperfréquences

Soutenue publiquement le 02/04/2021, par:
Julien Eymard

Contribution à l'analyse du ratio de performance cell-to-module dans les technologies photovoltaïques à hétérojonction de silicium

Contribution to the investigation of cell-to-module performance ratios in advanced heterojunction silicon photovoltaic technologies

Devant le jury composé de :

Anne KAMINSKI-CACHOPO	Professeure des Universités	INP de Grenoble	Présidente du jury
Beat RUHSTALLER	Professeur des Universités	Zurich University of Applied Sciences	Rapporteur
Christian SEASSAL	Professeur des Universités	Ecole Centrale de Lyon	Rapporteur
Eszter VOROSHAZI	Chargée de Recherche EPST	IMEC Leuven	Examinatrice
Matthieu DESPEISSE	Chargé de Recherche EPST	CSEM Switzerland	Examinateur
Raphael CLERC	Professeure des Universités	Saint Etienne – Université Jean Monnet	Directeur de thèse
Mathieu HEBERT	Maitre de conférence	Saint Etienne – Université Jean Monnet	Co-directeur de thèse
Benjamin COMMAULT	Ingénieur	CEA Grenoble	Co-encadrant de thèse

Abstract

Photovoltaic modules with higher efficiency can be envisaged by limiting the optical and electrical performance losses caused by cell integration. This thesis is mainly dedicated to the modelling of PV modules made up of silicon heterojunction solar cells (SHJ). There are already many tools for modelling the performance of a photovoltaic module, but it is necessary to adapt them to account for specificities of this technology, as well as latest developments in module design and interconnection. An optical and electrical model – mainly analytical – has been developed. A standardized classification of performance losses within the module was defined and enriched on the basis of previous work in the literature. Two loss items are analysed in more detail. The first is electrical: in order to reduce resistive losses, modules made up of cut cells have become the standard. The performance losses associated with cutting silicon heterojunction cells were missing data from the literature. An edge recombination current of 8 nA / cm has been measured before and after cutting, as well as a loss of photo-generated current. The impact on module performance has been modelled for different cutting geometries. The second is optical: new encapsulants material exhibit significant diffusive behaviour. A 4-flux model is developed to characterize its optical constants from spectrophotometric measurements in reflection and transmission, total and diffuse. A new item in performance losses is proposed, caused by backscattering of light. The impact on the photo-generated current of the module was analysed for two diffusive, UV opaque and transparent encapsulants.

Résumé

Des modules photovoltaïques de meilleurs rendements sont envisageables en limitant les pertes de performance optiques et électroniques engendrées par la mise en module des cellules. Cette thèse est principalement dédiée à la modélisation des modules PV constitués de cellules à hétérojonction de silicium. Les outils de modélisation de la performance d'un module photovoltaïque sont déjà nombreux, mais il est nécessaire de les adapter pour considérer certaines spécificités de cette technologie, ainsi que certaines évolutions des architectures de module. Un modèle optique et électrique, principalement analytique, a ainsi été développé. Une classification standardisée des pertes de performance au sein du module a été définie à partir de travaux précédents de la littérature, et enrichie. Deux postes de pertes sont analysés plus en détails. Le premier est électrique : afin de réduire les pertes résistives, les modules constitués de cellules découpées sont devenus la norme. Les pertes de performance liées à la découpe des cellules à hétérojonction de silicium étaient une donnée manquante de la littérature. Un courant de recombinaison de 8 nA/cm a été mesuré avant et après la découpe, ainsi qu'une perte de courant photo-généré. L'implication sur la performance module a été modélisée pour différentes géométries de découpe. Le second est optique : certains nouveaux encapsulants utilisés dans ces modules présentent un comportement diffusif non négligeable. Un modèle à 4-flux est développé pour en caractériser les constantes optiques à partir de mesures spectrophotométriques en réflexion et transmission, totale et diffuse. Un nouveau poste de perte de performance, par rétrodiffusion de la lumière dans les encapsulants, est proposé. L'impact sur le courant photo-généré du module a été analysé pour deux encapsulants diffusifs, opaque et transparent aux ultraviolets.

Remerciements

Raphaël Clerc et Mathieu Hébert, mes directeurs de thèse, vous avez rendu cette thèse passionnante sur le plan scientifique et enrichissante humainement. Merci pour votre expertise de grande qualité, pour la confiance et l'indépendance que vous m'avez accordée, de m'avoir bougé aux moments critiques, et merci de m'avoir si bien reçu à Saint-Etienne, amicalement ! Benjamin Commault, mon encadrant à l'INES, je te remercie pour la liberté accordée, et de m'avoir donné tous ces repères dans les dédales physiques, administratifs et techniques que j'ai pu rencontrer. J'ai aussi une pensée pour Maryline Joanny, ancienne cheffe du LMPV, qui a été à l'origine de la création de cette thèse. J'espère avoir rempli le « contrat » ! Enfin, un grand merci à Aude Derrier et Yannick Veschetti pour votre accompagnement et votre soutien moral aux bons moments.

Mention spéciale à la team des doctorants que j'ai pu fréquenter ! Stéphane, Nouha, Karim, Ichrak, Nicolas, Léo, Félix, Joël-Louis… Merci pour les discussions fort intéressantes. Je n'oublierai pas ces bureaux studieux… ou pas ! Désolé d'avoir pu être l'élément perturbateur, dès fois ☺. On se recroise vite, pour une soirée jeu, une sortie ski de rando ou une bière en terrasse (bientôt ?). Je vous envoie plein de bonnes ondes (avec l'arc du bureau !) pour la suite de vos aventures.

Ma thèse a été assez transversale, alors merci à vous tous des (anciens) laboratoires LMPO, LMPI et LMPV. Vincent, aka l'alpiniste un brin (?) taquin, tuteur officieux après la réorganisation : tu vas devoir encore me supporter un peu ;) Jean-François, le babos de l'équipe je viens te donner un coup de main dès que possible pour la construction. Merci Paul pour les nombreuses données et les drops à travers le bureau, à bientôt ! Merci Philipe pour les discussions sur l'orientation de la thèse et sur l'optique ! Petite pensée à mon bureau originel aussi : Stéphane, Camille, Amandine, Rémi et Paul ! C'était une belle intégration à l'INES. La team LabHJT (Félix, Léo, Wilfried, Samuel, Adrien, Delfina, Jean-François...), merci pour toutes les données, les modèles, les infos sur ce monde des cellules qui paraissait hostile ☺

Pour affronter ce parcours du combattant, mieux vaut aussi être bien entouré et se changer les idées! Merci Dr. DreyDrey d'avoir été mon ainée d'un an et de m'avoir fait éviter quelques pièges. J'arrive bientôt à vélo à Neuchâtel ! Satureja, toujours présente même si expatriée (j'arrive aussi !). Dans une autre vie j'aurais choisi ton parcours, on te recrute quand tu veux sur Jaya ! Eloïse, une très belle rencontre pour une année haute en couleur, tu vas me voir souvent à Toulouse. Merci à la team été 2020 (Toto, Lalou, Evan, Lulu, Flo…) pour cette troisième année de thèse qui nécessitait de… décompresser comme il faut!

Hip-hip-hip-Houra pour les amis spéciaux avec qui j'ai vécu: Vico et sa rigueur inspirante, merci de m'avoir fait découvrir l'escalade, plie moi cette thèse, et RDV en Savoie! Blaisou, le référent irréductible des sports extrêmes, profite bien du nouveau boulot, et à bientôt sur nos deux roues suspendues ! Et bien sûr Mr. Anderson, fils des Andes : l'ouverture d'esprit et le partage incarné, heureux de continuer l'aventure Aquarium 2.0 avec toi (et Lucie) ! Bob, immense merci pour les relectures, et go pour la belle aventure Jaya ! La team Phelma : Pinol, Diana, Carole, Valou… à très bientôt aussi !

Et évidemment, merci à la famille d'être toujours présent, d'avoir tout fait pour que je réussisse, de l'école jusqu'à cette fin de thèse, c'est en grande partie grâce à vous que j'en suis là. Une pensée particulière en ce moment pour papi Pierre.

Contents

General Introduction

This work is a contribution to the modelling and analysis of the main performance losses and gains caused by the integration of heterojunction silicon photovoltaic cells in modules.

Chapter I provides a context of the work carried out during this thesis and a presentation of the scientific basis necessary to approach it. Part I.A is a general and rather personal foreword on the different dimensions of the current ecological crisis, regarding the place that photovoltaic energy occupies in it. We will therefore talk about the systemic dimension of the crisis and the role of energy will be presented. We will see why climate change is forcing us to move away from fossil fuels and how low-carbon energies, including photovoltaics, are part of the solution.

Readers who are already aware can skip directly to Part I.B, which presents the technical basics of photovoltaics. We will briefly present the functioning of a solar cell and a module in terms of optics and electronics, emphasizing the specificities of the main technology developed at INES: heterojunction mono-crystalline silicon solar cells (HJT). Finally, we will show the importance of numerical and experimental analysis of optical and electrical losses for improving the performance of a module.

Chapter II couples the state of the art of PV module modelling with the presentation of the simplified CTMod model developed during this thesis. Part II.A presents the complete operation of the CTMod model. The methods for characterizing the model input parameters are presented, and compared to the state of the art. We will also explain all the calculations performed to obtain the performance of the module. Finally, we will propose a standardized classification of the absolute power losses in a module, based on the fusion of existing works. This classification allows cell-to-module analysis, but also comparison of module's performance at different stages of manufacturing. It also allows a comparison of different module architectures.

Part II.B presents the main software and tools for modelling PV module performance and losses. Some limitations of these models with regard to performance losses in silicon heterojunction modules will be discussed: cell resistive effects, losses due to solar cell cutting, diffusive encapsulants. It will be the opportunity to compare the optical results of CTMod with the Sunsolve ray tracing simulation reference.

Chapter III assessed the two main impacts of the integration of cut-out HJT cells on the performance of a module. Part III.A is therefore dedicated to the analysis of the limitation of resistive losses in cell interconnections caused by a lowered photo-generated current. This effect is documented in the literature and used in industry. This will be the opportunity to test the good electrical behaviour of the CTMod model, to identify the impact on the CTM ratio and on the performance of the module. We will also analyse the impact of the cutting as a

function of the incident irradiance, as well as the number of cell interconnection ribbons and the distance between cells in an integrated module.

However, laser cell cutting also involves losses through the creation of new recombinant edges and through the degradation of the active layers of the cell. The importance of cutting losses in silicon HJT cells has been little studied until now. The second Part III.B is therefore an analysis of these losses, by taking them into account in a two-diode model equivalent circuit. We will then study the coupled impact of the expected resistive gains in module as explained in Part III.A, associated with the cell performance losses occurring when cutting. Finally, we will try to predict the performance of a large module made up of half-cells.

Chapter IV is dedicated to improving the understanding of optical loss mechanisms in new diffusing encapsulants used for heterojunction modules. Current performance models take into account the absorption and surface reflection of these materials, but diffusive behaviour implies a new loss item: backscattering. The first Part IV.A of chapter 4 will present in detail the experimental method used for the determination of the optical constants of the encapsulants: measurements are done on spectrophotometers with integrating sphere.

The second Part IV.B will present the theoretical corpus describing absorption, reflection and scattering in a thick, flat, parallel-sided layer. We will use a 4-flow optical model: two collimated flows of opposite direction, as well as two anisotropic diffuse flows.

Finally, in the third Part IV.C, we will try to prove the necessity of using such a model to correctly extract the optical constants from the encapsulant. We will then apply this model to two highly diffusing thermoplastic polyolefin encapsulants, UV-transmissive and UV-absorbing type.

Thus, within the framework of this thesis, we proposed a simplified model for calculating the initial performance of a heterojunction silicon module, allowing the analysis of the loss stations and the comparison of various module architecture. We have combined state-of-the-art approaches and enriched them with specificities of HJT technology. Electrically, we proposed the generic consideration of losses during the cutting of HJT cells. Optically, we proposed a new power loss item in a module, linked to the backscattering of diffusive encapsulants.

Introduction générale

Ce travail est une contribution à la modélisation et à l'analyse des principales pertes et gains de performance engendrés par l'intégration de cellules photovoltaïques en silicium à hétérojonction dans des modules.

Le chapitre I fournit le contexte du travail réalisé au cours de cette thèse et une présentation des bases scientifiques nécessaires pour l'aborder. La partie I.A est un avant-propos général et personnel sur les différentes dimensions de la crise écologique actuelle, concernant la place qu'y occupe l'énergie photovoltaïque. Nous parlerons donc de la dimension systémique de la crise et le rôle de l'énergie sera présenté. Nous verrons pourquoi le changement climatique nous oblige à nous détourner des énergies fossiles et comment les énergies à faible émission de carbone, dont le photovoltaïque, font partie de la solution.

Les lecteurs déjà sensibilisés peuvent passer directement à la partie I.B, qui présente les bases techniques du photovoltaïque. Nous présenterons brièvement le fonctionnement d'une cellule solaire et d'un module en termes d'optique et d'électronique, en insistant sur les spécificités de la principale technologie développée à l'INES : les cellules solaires en silicium monocristallin à hétérojonction (HJT). Enfin, nous montrerons l'importance de l'analyse numérique et expérimentale des pertes optiques et électriques pour améliorer les performances d'un module.

Le chapitre II couple l'état de l'art de la modélisation des modules PV avec la présentation du modèle simplifié CTMod développé au cours de cette thèse. La partie II.A présente le fonctionnement complet du modèle CTMod. Les méthodes de caractérisation des paramètres d'entrée du modèle sont présentées, et comparées à l'état de l'art. Nous expliquerons également tous les calculs effectués pour obtenir les performances du module. Enfin, nous proposerons une classification standardisée des pertes de puissance absolue dans un module, basée sur la fusion des travaux existants. Cette classification permet une analyse cellule à module (CTM), mais aussi une comparaison des performances des modules à différents stades de fabrication. Elle permet également de comparer les différentes architectures de modules.

La partie II.B présente les principaux logiciels et outils de modélisation des performances et des pertes des modules PV. Certaines limites de ces modèles concernant les pertes de performance des modules à hétérojonction de silicium seront discutées : effets résistifs des cellules, pertes dues à la découpe des cellules solaires, encapsulants diffusifs. Ce sera l'occasion de comparer les résultats optiques de CTMod avec la référence de simulation par lancer de rayons pour le photovoltaïque: Sunsolve.

Le chapitre III évalue les deux principaux impacts de l'intégration de cellules HJT découpée sur les performances d'un module. La partie III.A est donc consacrée à l'analyse de la limitation des pertes résistives dans les interconnexions des cellules causées par une diminution du courant photo-généré. Cet effet est documenté dans la littérature et utilisé dans

l'industrie. Ce sera l'occasion de tester le bon comportement électrique du modèle CTMod, d'identifier l'impact sur le ratio CTM et sur les performances du module. Nous analyserons également l'impact de la découpe en fonction de l'irradiance incidente, ainsi que du nombre de rubans d'interconnexion des cellules et de la distance entre les cellules dans un module.

Cependant, la découpe laser des cellules implique également des pertes par la création de nouvelles arêtes recombinantes et par la dégradation des couches actives de la cellule. L'importance des pertes par découpe dans les cellules HJT en silicium a été peu étudiée jusqu'à présent. La deuxième partie III.B est donc une analyse de ces pertes, en les prenant en compte dans un modèle de circuit équivalent à deux diodes. Nous étudierons ensuite l'impact couplé des gains résistifs attendus dans le module tels qu'expliqués dans la partie III.A, associés aux pertes de performance des cellules survenant lors de la découpe. Enfin, nous tenterons de prédire les performances d'un grand module composé de demi-cellules.

Le chapitre IV est consacré à l'amélioration de la compréhension des mécanismes de perte optique dans les nouveaux encapsulants diffusants utilisés notamment dans les modules à hétérojonction. Les modèles de performance actuels prennent en compte l'absorption et la réflexion de surface de ces matériaux, mais le comportement diffusant implique un nouveau poste de perte par rétrodiffusion. La première partie IV.A du chapitre 4 présentera en détail la méthode expérimentale utilisée pour la détermination des constantes optiques des encapsulants : les mesures sont effectuées sur des spectrophotomètres avec sphère d'intégration.

La deuxième partie IV.B présentera le corpus théorique décrivant l'absorption, la réflexion et la diffusion dans une couche épaisse, plane et à faces parallèles. Nous utiliserons un modèle optique à 4 flux : deux flux collimatés de direction opposée, ainsi que deux flux diffus anisotropes. Enfin, dans la troisième partie IV.C, nous tenterons de prouver la nécessité d'utiliser un tel modèle pour extraire correctement les constantes optiques de l'encapsulant. Nous appliquerons ensuite ce modèle à deux encapsulants thermoplastiques polyoléfines hautement diffusants, de type UV-transmissif et UV-absorbant.

Ainsi, dans le cadre de cette thèse, nous avons proposé un modèle simplifié de calcul des performances initiales d'un module silicium à hétérojonction, permettant l'analyse des postes de pertes et la comparaison de différentes architectures de modules. Nous avons combiné des approches de l'état de l'art et les avons enrichies des spécificités de la technologie HJT. Sur le plan électrique, nous avons proposé la prise en compte générique des pertes lors de la découpe des cellules HJT. Optiquement, nous avons proposé un nouveau poste de perte de puissance dans un module, lié à la rétrodiffusion des encapsulants diffusifs.

Chapter I

Photovoltaic energy in the scope of the life global crisis

This context-setting chapter presents the place of photovoltaics in the world in current ecological and climatic cries. It also presents the scientific basis of this technology and why numerical studies are an asset for improving its performance.

Ce chapitre de mise en contexte présente la place du photovoltaïque dans le monde dans les cris écologiques et climatiques actuels. Il présente également les bases scientifiques de cette technologie et pourquoi les études numériques sont un atout pour améliorer ses performances.

Part I.A Tackle life crisis and climate change: the need for sobriety and cleaner energy

Life on Earth is undergoing a major crisis, unique since its appearance more than 3.5 billion years ago.

I.A.1 General context: the current multi-faceted life crisis

Diversity within species, between species and in ecosystems, as well as many fundamental contributions from nature are being rapidly degraded [1]. If massive extinctions have already taken place, they all had a geological origin. The current Holocene extinction is the first one whose origin is attributable to a species: Homo-Sapiens. Even more terrible, humanity is now fully aware of it. Thus, the formula of the astrophysicist and philosopher Aurélien Barrau takes all its meaning: "We are in the first deliberate extermination of life on Earth". His reflectance have largely inspired this introduction.

Western societies have been gradually aware of the instability of their developments for at least a century (the following list of events is of course not exhaustive). In the 19th century, the discovery of the greenhouse effect by Fourier [2], its origin by Tyndall [3] and the impact on terrestrial temperature by Arrhenius [4] highlights that humanity can have a significant global impact on the entire planet. The great financial crash of 1929, the protests of 1968, the oil shocks of 1973 and 1979, the subprime crisis of 2008 and most recently the Covid-19 crisis, are some examples of financial and social crises that have helped to impress upon people's consciences the need for more sustainable development. Major industrial and ecological disasters have also left their mark: the nuclear accidents of Chernobyl and Fukushima, major oil spills (Deepwater Horizon, Exxon Valdez, Erika, etc...), and other industrial disasters (Seveso, etc...).

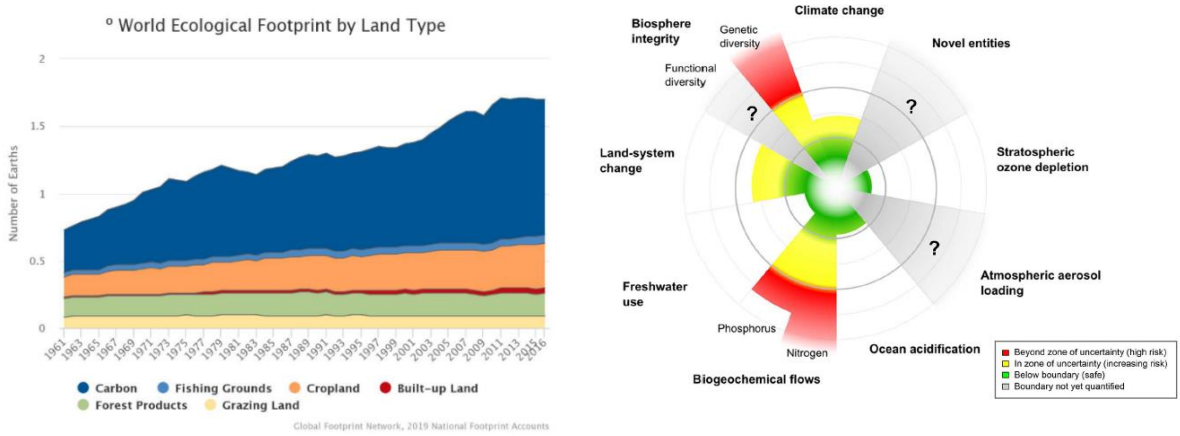

Figure 1. Left: The number of Earths needed to support humanity.(Global Footprint Network datas). Right: nine planetary boundaries have been identified, eleven if sub-categories are included (from Steffen et al., 2015).

"The day of the overshoot", an indicator of human impact in relation to the Earth's bio capacity, continues to decline [5]. Published by the NGO "Global Footprint Network", it corresponded to a use of 0.73 Earth in 1961, and 1.69 Earth in 2019, as shown in Figure 1 (left): our ecological debts is growing since 1970. Steffen *et al.* and the 2015 update defined nine global limits in 2009 and show that three have already been exceeded: the limit on eroding genetic diversity, the limit on the phosphorus cycle, and the limit on the nitrogen cycle (Figure 1-right) [6], [7]. But even for the limits that have not been exceeded, the trends are worrying.

Thus, climate change is far from being the only problem created by humanity. Global warming, which occupies most of the media space when it comes to the current crisis, is not at this stage the reason for the erosion of life. It is the whole of our ways of life that is to be questioned: our way of eating, consuming and producing, communicating and entertaining ourselves. Our way of eating, because the consumption of meat, the use of pesticides, deforestation, have well-known deleterious consequences on biodiversity. Our way of entertaining ourselves, because mass tourism implies an increased displacement of populations, soil artificialisation of virgin spaces. The explosion of digital content has undermined the digital promise of an impossible dematerialized economy, without impact: the need for raw materials is unavoidable, and they are obtained in gigantic extraction mines where the use of toxic products is the norm.

The origins and consequences of the crisis are manifold, as are our levers for action. But each of the following points are not sufficient.

The crisis has a component of individual ethics. For a whole system to change, it is irreversibly necessary to change individual behaviours. The actions that we can choose to take will have a major impact: change our diet for local bio and, reduce waste and consumption, use our cars less, learn to travel again, and question the value of our profession. In a world that must decline, and as Westerners, maintaining our lifestyles will be to the detriment of the world's poorest people. Obviously, everyone must act within their means. But some behaviours that are positively connoted today should become shameful in people's minds. Displaying one's outrageous wealth via one's huge car and/or house should not be a symbol of success.

The current crisis also has a demographic component. Of course the world would be better off if there were fewer of us, but the current situation is what it is: there are 7.5 billion of us. Drastically reducing the population is possible, but with generally disastrous social consequences. For example, China's one-child policy will stabilize the population several generations after the measures are implemented, but has already led to child abandonment and infanticide, forced abortions and sterilization, gender imbalance... Even more dramatic are the processes of unwanted reduction of the population: diseases, famines or wars. The ethically acceptable solutions to stabilize the population in developing countries are known: education of women, health insurance, unemployment insurance, ageing insurance and reduction of the individual's ecological footprint. In addition, the United Nations population projections envisage a stabilization of the world population at around 12 billion in 2100. The systemic modelling done in the report "Limits to Growth" shows a decrease in population at these time horizons.

Certain currents of thought identify the main origin of the crisis as political: neo-liberalism, or capitalism. This is certainly partly true, because of the tendency towards accumulation, less regulation of the markets, short-termism, and the deepening of

inequalities that these systems have generated. That is not a sufficient explanation either: extractivism may well take place in a socialist or communist regime. Part of the solution must be political, because individual ethics are not enough: certain personal wishes and collective necessities will always remain opposed. Major systemic transformations are by definition political. However, politicians often argue that they have not been elected to implement measures of the magnitude needed to resolve the crisis. Promising economic decline, and that everyone will become less rich is far from being a good electoral argument. Since the 1950s, many summits have been held: Earth Summits of Rio and Johannesburg, conference of Parties (COP) every year, conference on Biodiversity… Many reports have been addressed to politicians (Meadow report "Limits to Growth" from the Club of Rome [8], six IPCC assessments on climate change [9], Brundtland assessment on sustainable development [10]…). Many associations and NGOs have been created: World Wide Fund in 1961, Friends of Earth in 1969, Greenpeace in 1971, etc. Number of international agreements (Kyoto protocol), and many world demonstrations and strikes for the climate. Some marginal changes have been initiated at different scales (Plan climat-air-énergie territorial in France, etc.). Despite all this, the trajectory is more than ever exponential (Figure 2 – right) [6] and remains both ethically catastrophic and suicidal for humanity.

The economic causes of the crisis are obvious. The convention that economic growth is the alpha and omega of a society is a problem. The very definition of growth, which focuses only on wealth creation in the sense of GDP, neglects a host of other more fundamental indicators of a happy society. Negative externalities are difficult to quantify, which invites us to question our notion of value. The best-known criticism of the pursuit of economic growth is the Meadows Report commissioned by the Club of Rome and published in 1972 "Limits To Growth" [8]. This Systems Dynamics Report, and its subsequent updates, noted that any pursuit of economic growth ends in collapse, in the sense of GDP per capita and population. Different updates all mentioned we are closely following the scenario "business as usual", where world population start to decline in 2030 (Figure 2 - left), after industrial production and food per capita in 2020 [11]. Contrary to what may be heard from politics, it is no longer the time for sustainable development or green growth in their historical assertions. Decoupling ecological impacts from economic growth from GDP, while possible in relative terms, is impossible in absolute terms [12]. Thus, no matter how effective our technologies are, since our ecological footprint must be greatly reduced to ensure a viable future, reduction in the current economic sense is necessary. The failure to put a book value on the resources - as such - that we exploit, coupled with the lack of interest in the commons, already explained by Hardin in 1968 in "The Tragedy of the Commons.

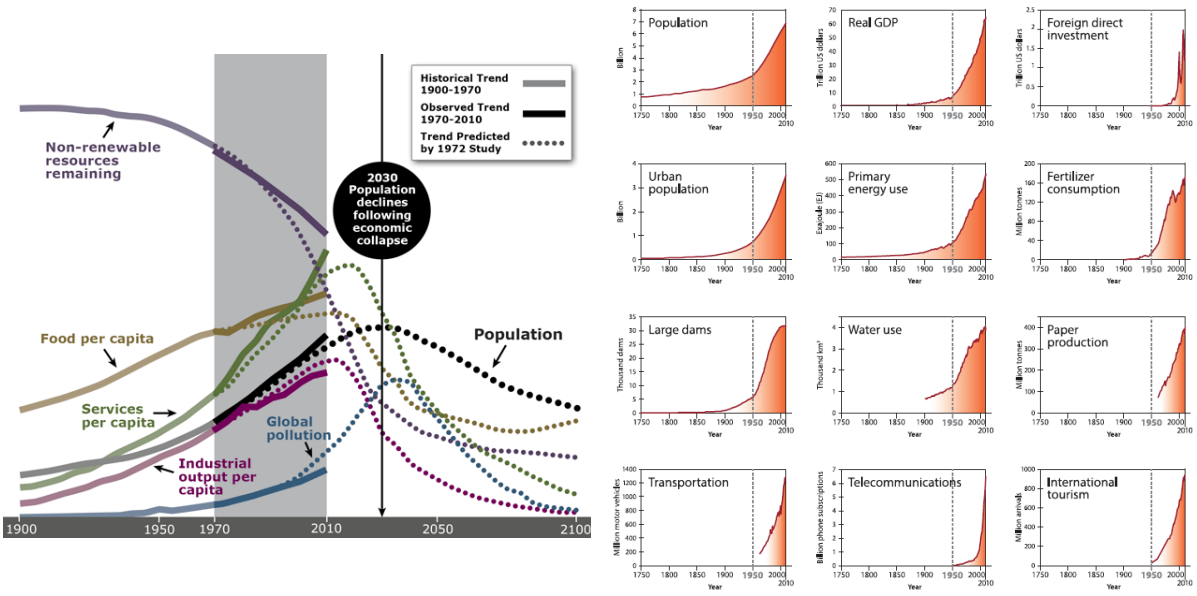

Figure 2: The 40 years update of the Meadows report "Limits to Growth", made by G. Turner in 2014 [11](Left). Trends from 1750 to 2010 in globally aggregated indicators for socio-economic development, from Steffen et al., 2015 (Right).

The technical dimension of the crisis is often also presented as its number one remedy. Obviously, technological advances in energy efficiency, treatment of diseases, combating inequalities, etc. are necessary. However, a solution in itself must really be one, and it must not take the problem elsewhere. Technology must remain a means - and not an end in itself - even though it is now more than ever a sacrality, as Jacques Ellul has already analysed [13] or Serge Latouche [14]. Above all, we must not forget that technique can have perverse effects, even on the things it claims to solve. The best known is undoubtedly the Jevons paradox: Technological improvements can increase the efficiency with which a resource is used, but the total consumption of that resource may increase rather than decrease. Its more general form is the "rebound effect". For example, the digital revolution promised to dematerialize our economy so that it would become less energy and material consuming. Unfortunately, usage has increased considerably and digital technology now accounts for 3.7% of global greenhouse gas emissions, and the supply of certain rare metals is becoming critical [15]. The automotive and aviation industries are sectors that are suffering from the rebound effect. Only political and economic control can prevent it. Another limitation of the technique in its present form is the dispersive use and the impossibility of complete recycling of the raw materials. This has led to the need to move from "high-tech" to "low-tech", as studied by Phillipe Bihouix [16].

Finally, the current crisis has an energy dimension. Energy is central to the current crisis, since its control is what allows us to transform our environment. It is intimately linked to all of the above: it has a demographic, political, economic and technical dimension. It is also intimately linked to climate change. Our dependence on fossil fuels is catastrophic, not only because of their effects on global warming, but also because they are limited. Their production will necessarily go through a maximum before declining. Once again, the energy issue should not be isolated from the rest: an industrial intensive livestock farm using renewable energy, made from local materials, still retains its deadly dimension.

Thus, the energy and technical aspect is only a component of a more global crisis. But we are no longer at a time of choice: all the components must be dealt with, and the energy issue therefore deserves to be addressed. That's what we'll see in the next part.

I.A.2 Climate change and energy: less and cleaner consumption

What is energy? One of the best definition is given by Richard Feynman in "The Feynman Lectures on Physics" [17]:

"*There is a fact, or if you wish, a law, governing all natural phenomena that are known to date. There is no known exception to this law – it is exact so far as we know. The law is called the conservation of energy. It states that there is a certain quantity, which we call energy that does not change in manifold changes which nature undergoes. That is a most abstract idea, because it is a mathematical principle; it says that there is a numerical quantity which does not change when something happens.* "

So energy is the hallmark of change: in any transformation, energy is at stake. It can be in kinetic or potential form. Energy is subject to the law of conservation: the total energy of a closed system is conserved. During a transformation, energy simply changes its nature. For example, it can change from a potential form to a kinetic form when a body falls or from a chemical form to a thermal form during combustion. More fundamentally, energy conservation, as Noether's theorem shows, is the mathematical consequence of the fact that physical laws are invariable by time translation. This is almost the definition of a physical law. If it ceases to be valid from one moment to the next, or changes form, then it no longer has the value of a law.

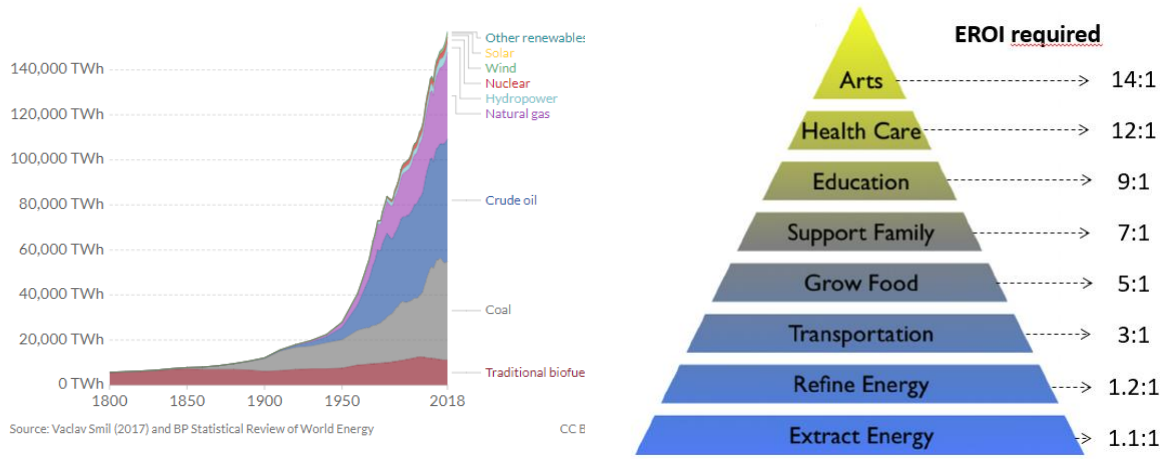

Figure 3: Evolution of primary energy production in TWh from 1800 to 2017. Graph from the International Energy Agency. In 1990, humanity consumed about 8 700 Mtoe per year of primary energy, for more than 14 000 in 2017 (Left). Pyramid of a society's energy needs, according to Lambert et al., 2014. The higher the energy return rate (EROI), the more different functions a society can perform, from basic activities to cultural activities (Right).

The first of the energies used by humanity is that stored in chemical form in food, and mainly transformed into mechanical energy (movement) by our body. Then, humans have used the mechanical energy of animals to achieve more "transformations" of the environment. Renewable energies were the first to be used historically - living beings aside: the wind to navigate or to turn mills, the movement of water transformed into rotational movement by paddle wheels, the sun as energy to dry crops... It was the democratization of the steam engine in the 17th - 18th century, then the combustion engine, that made it possible to use much more concentrated energies: coal, then oil and gas. More recently, the mastery of nuclear energy and the development of modern renewable energies have completed the mix. It is striking to note that all the energies mentioned have always been added to the pre-existing ones. There is, at present, no replacement of one energy by another, as shown by the Figure 3-left. The share of each energy source has remained relatively constant. Total consumption has almost doubled. We can see the gradual emergence of new renewable energies: wind, solar, geothermal ... which together represent 1.8% of the 2017 mix (257 Mtoe of the 14 000 total).

One of the main characteristics of energy is its energy return rate or ERoEI (Energy Return on Energy Invested, sometimes called also EROI).The idea behind this ratio is simple. In order to recover resources whose initial energy is converted into a more practical energy for a given use, well, energy is needed. For example, to extract oil, you have to use energy to build the well, to run the pumps and so on. This is true for any energy. An EROI less than one means that more than one unit of energy is used to recover one unit of energy. So there is no point in collecting this energy. It is therefore necessary to favour energies with a high EROI, which means that more of the extracted energy is usable in the end for society. This factor therefore has major societal consequences. Indeed, not all the activities of our companies can be maintained with any global EROI. Indeed, the available energy will first be allocated to vital functions of the economy such as energy collection, power supply. Then to intermediate functions such as education and health, and only at the end, if there is energy left over, it will be allocated to culture. Each stratum of civilization therefore needs a minimum level of REOI to be maintained [18]. This is called the “Pyramid of society’s energetic needs” by Lambert *et al.*, and is drawn on the Figure 3-right for a society fuelled by conventional oil. The EROI is to be handled with care. Figures and conclusions may vary according to the boundaries of the system under study. This indicator can be misleading when comparing energies, especially if the end use is not the same (e.g. electricity production versus heat engine for transport).

The increasing use of fossil fuels (coal, oil, gas) is what has made possible the exponential growth previously explained. Because they have a high EROI, we have been able to achieve many more transformations of our environment, and raise our standard of living (unevenly across classes, of course). This is illustrated by the number of energy slave at our disposal. An energy slave is the imaginary equivalent in human labour of what machines do to guarantee our standard of living. In France, we each have an average of 400 energy slaves per person, with large disparities according to wealth.

But these energies have two major drawbacks. They are fossil, and therefore non-renewable, since a deposit is formed in several million years. Their production will therefore inevitably reach a peak before decreasing, until it disappears. The peak for conventional oil was passed in 2008, and the peak for all oil combined will probably be passed in 2020. Coupled with the inevitable decline in their production, fossil fuels are also subject to the law of diminishing EROI. The simplest deposits are exploited first, so newly discovered fields

inevitably have lower EROI. More importantly, these energies are high emitters of carbon dioxide, a greenhouse gas, whose atmospheric concentration and the radiative forcing it induces is a major cause of current global warming. This should push us to get out of fossil fuels faster than simply waiting for them to run out. In fact, in order to envisage limiting global warming to 2°C, we have an unbeatable budget of 1000 GtCO2 until 2100. This implies leaving a large part of the fossil energies already discovered in the ground: new explorations therefore make no sense. It also implies that we will be allowed to emit in the next 30 years only half of the emissions already made in the past (with a population that will continue to grow) [9].

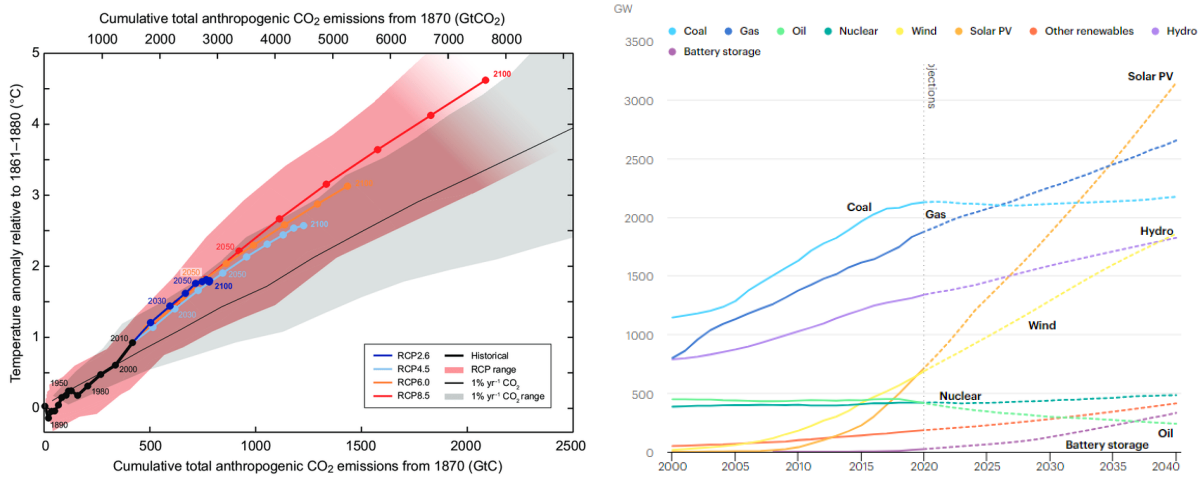

Figure 4: Temperature anomaly relative to cumulative total anthropogenic CO2 emission from 1870. Respecting the Paris agreements, and limiting global warming to two degrees, means emitting only 3000 GtCO2 by 2100, bearing in mind that we have already emitted 2000 GtCO2. The current commitments of the countries lead us for the moment on a trajectory of +3.5°C (Left). Installed power generation capacity by source in the Stated Policies Scenario of the World Energy Outlook 2019 published by IEA [19]. Historical trends until 2020, projections from 2019 to 2040. Solar PV becomes the largest component of global installed capacity (Right).

The conclusions of the 5th IPCC report on climate change are unambiguous [9]. In the synthesis for decision-makers, the following four aspects are addressed: Observed Changes and their Causes – future climate changes, risks and impacts – futures pathways for adaptation, mitigation and sustainable development – adaptation and mitigation.

- "Human influence on the climate system is clear, and recent anthropogenic emissions of greenhouse gases are the highest in history. Recent climate changes have had widespread impacts on human and natural systems »
- "Continued emission of greenhouse gases will cause further warming and long-lasting changes in all components of the climate system, increasing the likelihood of severe, pervasive and irreversible impacts for people and ecosystems. Limiting climate change would require substantial and sustained reductions in greenhouse gas emissions which, together with adaptation, can limit climate change risks"
- Adaptation and mitigation are complementary strategies for reducing and managing the risks of climate change. Substantial emissions reductions over the next few decades can reduce climate risks in the 21st century and beyond, increase prospects

for effective adaptation, reduce the costs and challenges of mitigation in the longer term and contribute to climate-resilient pathways for sustainable development

Many adaptation and mitigation options can help address climate change, but no single option is sufficient by itself. Effective implementation depends on policies and cooperation at all scales and can be enhanced through integrated responses that link adaptation and mitigation with other societal objectives.

As opposed to fossil fuels, renewable energy transforms into final energy an energy that will not run out at the time scales we are interested in. Hydropower, via mass or run-of-river dams, is the most widely used renewable energy in the world. Biomass and bio-fuels are renewable resources because plants grow back and can therefore store carbon from the atmosphere in the form of organic matter. The exploitation of the earth's heat, via geothermal energy, remains marginal on a global scale. In recent decades, two energies have developed exponentially: wind power and solar energy. Renewable energy does not mean perfect energy. As these energies are generally much diluted, large areas are needed to collect it, so many places whose virgin aspect can be affected. Collectors (solar panels, wind turbines...) therefore require many resources. Their scarcity, and the impact of their extraction should not be neglected. The limitation of rare materials or and recycling must be anticipated. Finally, renewable energies are often intermittent. This can pose problems on the stability of electricity networks, requires means of compensating for production troughs and/or means of storage deployed on a large scale.

A transition towards a more energy-efficient, and therefore diminishing, society is therefore necessary for biodiversity issues, but also for climate change. Residual energy will have to be de-carbonised, with the least possible impact on living organisms and with limited consumption of resources. In this sense, photovoltaics has its rightful place.

I.A.3 Photovoltaic: from a theoretical quirk to a fast growing industry

The photovoltaic effect is a photoelectric effect, i.e. an electron emission under the influence of light, which appears only from a wavelength threshold. Alexandre Becquerel first discovered the photovoltaic effect in 1839 by studying electrochemical cell. In 1887, Heinrich Hertz studied the effect of UV radiation on charged bodies. From 1888 to 1891, Aleksandr Stoletov studied the photoelectric effect and deduced the proportionality between the intensity of the incident light and the photo-generated current. J. J. Thompson in 1899 studied the effect of UV light in Crookes tubes, and was the first to speak of a corpuscle to describe the photoelectric effect. Following in the footsteps of Hertz, Wilhehlm Hallwachs and Phillip Lenard studied the photoelectric effect in detail between 1886 and 1902, showing in particular the positive electrical charging of zinc surfaces when lighted by UV light. Lenard shows that this can generate an electric current, which stops as soon as the UV radiation is stopped. Max Planck, in 1900, studies the radiation of the black body and suggests that things happen as if light were organized in packages. It was Albert Einstein, in 1905, who published his proposal to quantify light to explain the photoelectric effect, which would open the field to quantum mechanics. He was awarded the Nobel Prize for this discovery in 1921.

The research then becomes more applied to device design. In 1941, Vadim Lashkaryov discovered the pn junction in CuO2 and Ag2S cells. In 1946, Russell Ohl semiconductor (SC) researcher patented the concept of modern version of the solar cell: "Light sensitive device".

It was only in 1954 that three researchers of the Bell Laboratories designed the first functional solar cell (Fuller, Chapin and Pearson). This first solar cell was not passivated. It was in 1957 that engineer Mohamed Atalla developed the passivation process, which made it possible to improve performance. The cells are now functional devices and powerful enough to consider power generation applications. It was in 1958 that this energy was used on the Vanguard 1 satellite, to supplement the operation of the main battery.

At that time, the race for performance and the lack of better technologies in terms of power per kilogram launch in space made these devices expensive. Based on silicon, solar cells have gradually benefited from lower prices made possible by the scaling up of the semiconductor industry. Working groups were set up in the 1970s to democratise photovoltaic energy. These initiatives came from governments and major technology and oil companies (Exxon, Shell... whose activity appeared fragile following the two oil crises). Reducing costs by improving performance, reducing material quantities, optimizing processes, the delocalization of production to China, and scaling up - enabled exponential growth in installed capacity. This is shown in the learning curve of photovoltaic industry (Figure 5), also known as Swanson's law: The solar module prices fall 23.5% for every doubling of industry capacity. The solar module prices is only a small part of the total cost of electricity resulting from PV power plant construction and exploitation. When including all the building, maintenance and financial cost, and compared with the amount of electricity generated over the life of the plant, we obtain the levelized cost of electricity (LCOE). This indicator is also declining considerably over time. It has been divided by more than four between 2010 and 2018, from 370$/MWh in 2010 to 90$/MWh in 2018. In 2020, some projects in highly sunny region approach 15$/MWh.

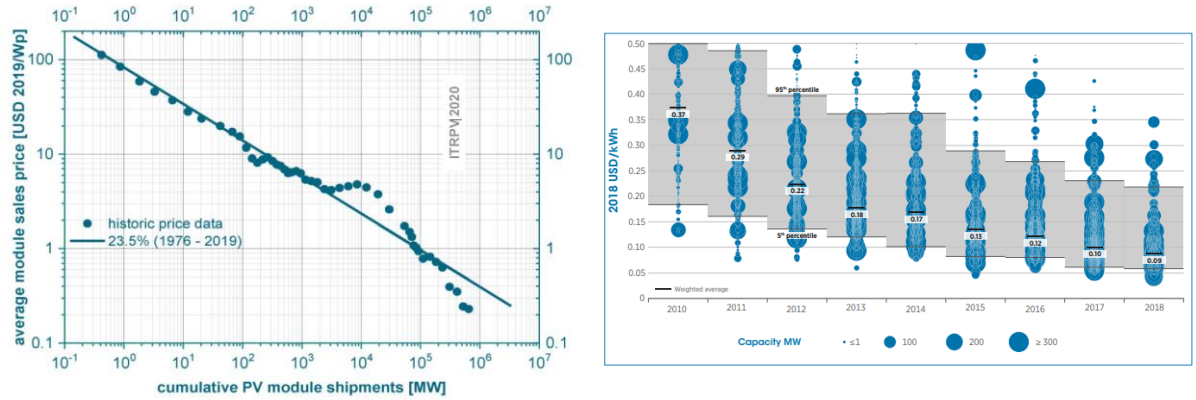

Figure 5: Learning curve of PV module industry by ITRPV [20]. The solar module prices fall from 100$2019 by Watt peak (1976) to 0.2$ / Wp in 2019. It correspond to a fall of 23.5% for every doubling of industry capacity. Since 2004 and after a few years of stagnation, the fall in prices has accelerated (Left). Drop in levelized cost of electricity (LCOE) for mainstream photovoltaics project from 2010 to 2028 (IRENA [21]). The average LCOE in 2018 is 90 $/MWh without storage (Right).

As prices have fallen, the use of photovoltaics has diversified. The application mainly in terms of installed power is obviously the large photovoltaic power plants on the ground: this is "mainstream" photovoltaics. But other uses are emerging. As said before, space has been the first user of this technology. Photovoltaic energy is also a means of powering public and private buildings (BIPV: building integrated PV), and to move towards the French

objectives of positive energy buildings (BEPOS) included in the thermal regulation 2020 (RT 2020, postponed to January 1st, 2021). These buildings must consume less energy than they produce. The integration of PV in vehicles (VIPV: Vehicle integrated PV) allows to power electronics, or even to significantly increase their autonomy in the case of hybrids or electric vehicles. These vehicles, most of them experimental, can be cars, trucks, boats and even airplanes. PV is useful for powering sites isolated from the electrical grid. The development of floating PV, first on sterile water bodies (old mines...) and then on the sea is a reality. Photovoltaic energy is also integrated into street furniture, such as street lamps, and into roads as a means of powering signage. Indoor applications, where the energy collected is low and diffuse, are beginning to emerge as a potential energy source for the development of connected objects. Photovoltaics, as an electrolyser power source, may also have its place in the production of decarbonized hydrogen.

Part I.B Technical prerequisites of photovoltaic technology

A photovoltaic system is a system that allows the conversion of the energy of light into electricity, for operating times compatible with the various applications previously mentioned. It consists of several technological stages with very specific roles.

The first element is the photovoltaic cell, which is the element allowing the conversion of photons into electron, from the properties of semiconductor materials. The second element is the module, which electrically connects several cells, protecting them from environmental aggressions (mechanical, chemical...). The third level is the complete system, several modules are connected, and power electronics (inverter in particular) allows to adapt the form of electrical energy for a given use.

I.B.1 Conversion of light energy into electricity: the cell, the basic component of a photovoltaic system

A solar cell can therefore transform light into electricity. This can be summarized in 4 main steps: (i) the generation of an electron from a photon, (ii) the collection of this electron to generate a current, (iii) the application of a voltage across the cell, (iv) the use of the power by dissipation in resistances or in the connected load.

A photon is able to bring energy to an electron strongly bound to the atoms of the cell material (in the Valence band for the inorganic semi-conductor or HOMO in the organic semi-conductor. If the energy is higher than a threshold value called "bandgap", the electron goes into an excited state which allows it to conduct current (the conduction band in inorganic SC or LUMO in organic one). It leaves behind a hole in the electronic structure: this is generally referred to as the generation of an electron-hole pair rather than an electron. This is possible because the materials used in a photovoltaic cell are capable of absorbing incident radiation above the band gap. The absorption coefficient of semiconductor materials define how deep into a material light can penetrate before it is absorbed. It is generally high for short wavelengths (ultraviolet-UV) and decreases progressively with the wavelength: it is much lower in infrared (IR). This causes a pattern of electron-pair generation that reaches its maximum on the front side of the cell and gradually decreases towards the back side of the cell.

This electron-hole pair is in a meta-stable state: electrically neutral, the electron and the hole can recombine (the electron returns to a less energetic state by releasing its energy). Thus, it is necessary to collect this electron-hole pair to produce an electric current. This role is fulfilled by the pn junction: by contacting two semiconductor materials with different energy levels (valence bands and conduction bands), an electric field is obtained which is able to separate the electrons from the holes. The doping of a material - the controlled addition of specific impurities to the base material - makes it possible to change the energy levels. The use of different materials together also allows different energy levels to be obtained. The electron-hole pairs can reach the pn junction thanks to the phenomenon of diffusion and thermal agitation. The charge carriers are created inhomogeneously in the thickness of the cell: their concentration will homogenize, assisted by the random thermal agitation and the concentration gradient.

The pn junction is the heart of a solar cell. It is the site of two opposing phenomena (Figure 6). The side of the junction where the dopants are electron donors (n-side) has an excess of electrons (electrons are the majority carriers). The side of the junction where the dopants are electron receptors (or hole donor, p-side) has an excess of hole (holes are the majority carriers). When the two materials are brought into contact, the excess electrons from the n-side diffuse to the p-side and vice versa. This has the effect of leaving the fixed atoms of the lattice with an excess of positive charge (n-side) and an excess of negative charge (p-side): a potential difference sets up (called build-in voltage V_{bi}), accompanied by an electric field. This region where an electric field exists is called the depletion zone (or space charge region): only very few electrons and holes can be found there, because they are quickly dragged by the force of the electric field to the n-side for electrons and to the p-side for holes. The electric field thus has an opposite effect to the diffusion phenomenon of the majority carriers: it forces the holes to remain on the p-side and the electrons to remain on the n-side. An equilibrium is established where the diffusion and drift currents (due to the electric field) compensate each other for both holes and electrons. If an external voltage V is applied to the junction (called "bias"), the electric-field decreases (forward bias) or increases (reverse bias). It causes a new equilibrium to be reach, where the drift or the diffusion mechanisms are dominant: a net current flow can exist.

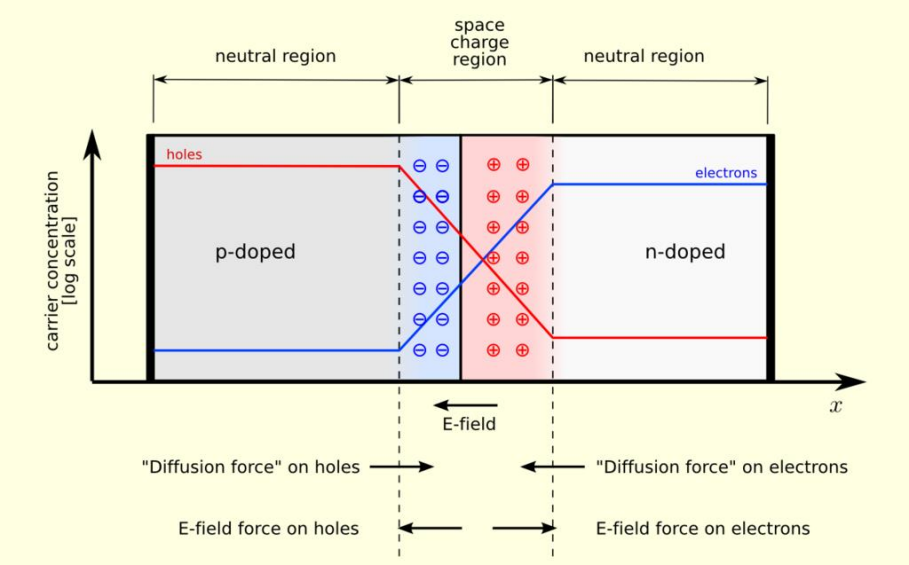

Figure 6: Schematic diagram of a pn junction at thermodynamic equilibrium, taken from [22].

Thus, if an electron-hole pair is able to reach the pn junction before recombining. The negatively charged electrons are directed to one side of the cell, while the positively charged holes are directed to the other side: an electric current can be set up. An electron-hole pair can recombine in several ways. The first one is radiative: the electron and the hole recombine by emitting a photon of energy equal to that of the bandgap, so the energy is lost in the form of emitted light. This phenomenon is not very present in semiconductors with indirect bandgap like silicon. The second way is recombination due to defects in the semiconductor, it is called Shockley-Read-Hall (SRH) recombination [23], [24]. The energy is lost as heat transmitted to the crystal lattices. These defects can be of several kinds: misalignment of the

crystal lattice, replacement of some atoms by others (impurities, wanted as in the case of doping, or unwanted in the case of contamination). These defects are localized either in the cell volume or on the cell interfaces between the different materials. The third type of recombination, called Auger recombination, involves three particles or pseudo-particles: the electron-hole pair recombines, but the energy is neither emitted as light nor transformed into heat by a defect. It is transmitted to an electron of the same atom in the conduction band, which is then thermalized [25], [26]. This type of recombination is present in semiconductors where the number of charge carriers is high (high injection level). Other mechanisms of recombination exist, more exotic, involving multiple level of defects for example [27].

Each of these mechanisms is associated with a probability of recombination. The higher this probability, the lower the lifetime of the electron-hole pair. If this lifetime is too low, the electron-hole pair does not have the time to diffuse to the pn junction to be separated. The probability that the electron-hole pair is collected is thus stronger near the pn junction, and weaker when we move away from it: this is the effect of volume and surface recombination (Figure 7).

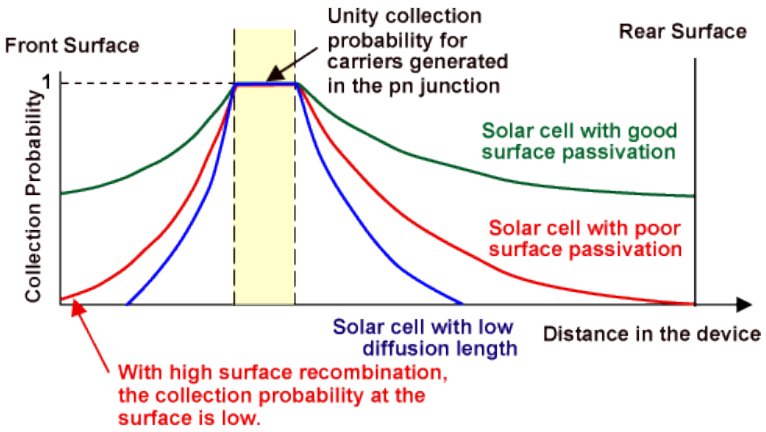

Figure 7: Collection probability in the thickness of a solar device. Taken from PVEducation website [28].

The quantum efficiency (QE) is a notion that summarize the ability of the cell to generate electron from photon, and to collect them. It is the ratio of the number of carriers (electron) collected by the cell to the number of photons incident. It is a spectral value. The quantum efficiency of photons with wavelength above the bandgap is reduced near zero. In the UV wavelength, photons are absorbed mainly on the front side of the cell. If the QE is reduced in this region, it can be explained by a high surface recombination rate. In the infrared region, if the QE is reduce, it can be caused to a high rear surface recombination rate. The reduction of the overall QE can be caused by a low diffusion length in the semiconductor volume. Those main effects are plotted in the Figure 8. Photons with higher energy than the bandgap can be absorbed, but the excess energy is lost as heat in a process called thermalization. At low wavelength, the photons have large energy: the ratio of photons to power is reduced.

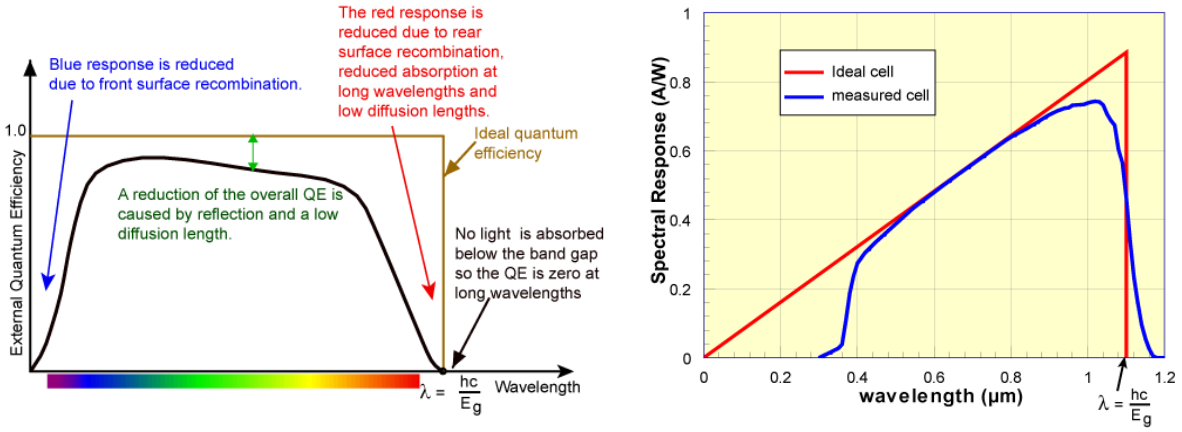

Figure 8: Example of quantum efficiency of a silicon solar cell and the main reasons of non ideality (Left). Example of ideal and measure spectral response Taken from PVEducation website [29].

The collection of electron-hole pairs therefore generates a current, but without voltage, no power can be produced. Thus, in a short circuit situation, where the positive and negative terminals of the cell are connected, the charge carriers freely loop the circuit and no voltage appears. But in an open circuit situation, the plus charges (holes) and negative charges (electrons) accumulate on both sides of the cell: this creates a potential difference and thus an electric field. This electric field opposes the electric field in the pn junction: another equilibrium point is reached, where the photo-generated current is exactly compensated by the diffusion current in the junction. At this point no current flows, despite the existence of a voltage: no power is produced. Between the two points (short-circuit and open-circuit), there is both a photo-generated current and a voltage: the cell produces electrical power.

The pn junction acts like a Schokley's diode, whose equation is:

$$I(V) = I_0\left(\exp\left(\frac{V}{V_{th}}\right) - 1\right) \qquad \text{I.1}$$

In this equation, I_0 is called the dark saturation current – the leakage of the diode without photo-generation. The thermal voltage, V_{th} is equal to k_BT/q, where k_B is the Boltzmann's constant, T is the temperature and q is the absolute value of electron charge. An external voltage V is applied to the diode. If V = 0, the diode is at equilibrium and no current can flow because of current diffusion equalling the drift current. If a reverse bias V < 0 is applied, it increases the build-in voltage of the junction and the electric field: very small diffusion of majority carrier is possible, because there is not enough charge carrier with a kinetic energy enough to out pass the voltage barrier. Thus, the current across the pn junction is dominated by the current of the minority carrier (electron) that have diffused to the pn junction from the p-side and drained by the electric field to the n-side. This is exactly $-I_0$, and this is why I_0 is sometimes referred as the diffusion current [30]. If a forward bias is applied, the diffusion a majority carrier increases exponentially. The electron of the n-side diffuse to the p-side where they diffuse approximately to one diffusion length and recombine.

By combining the equation of the Shockley's diode to the photo current generator I_{ph}, we have the most simple equation for the current-voltage characteristic of a solar cell.

$$I(V) = I_{ph} - I_0\left(\exp\left(\frac{V}{V_{th}}\right) - 1\right) \qquad \text{I.2}$$

This equation needs to be completed with different terms to better represent a solar cell. First, it is possible to add a series resistance to model the voltage loss due to the resistive elements of the cell. As we will see in Chapter 2, this series resistance is a one-dimensional approximation of a 3-dimensional resistive grid.

In parallel to the diode, it may be necessary to add a resistance, called a shunt resistance, which reflects a possibility for the photo-generated current to short-circuit the pn junction via defects in the volume or at the edges of the cell.

Finally, a second diode (recombination diode) is usually added to diode 1 (diffusion diode). This second diode models recombination phenomena of a different nature: SRH recombination in the depletion zone, on the edges of the cell... More details are given in chapter 2 and chapter 3. The most commonly used equation to describe the current-voltage characteristic (IV) of a photovoltaic cell, or two-diode model, is the following:

$$I(V) = I_{ph} - I_{01}\left(\exp\left(\frac{V + IR_s}{n_1 V_{th}}\right) - 1\right) - I_{02}\left(\exp\left(\frac{V + IR_s}{n_2 V_{th}}\right) - 1\right) - \frac{V + IR_s}{R_{sh}} \qquad \text{I.3}$$

Where I_{01} and I_{02} are the saturation current of the first diode (diffusion diode) and second diode (recombination diode), R_s is the lumped series resistance, R_{sh} is the shunt resistance. The factor n_1 and n_2 are called ideality factor. The commonly used values are n_1 = 1 and n_2 = 2, but actual values can differ depending on the cell technology and potential exotic recombination mechanism occurring. The equivalent circuit corresponding to this model is given on the Figure 9.

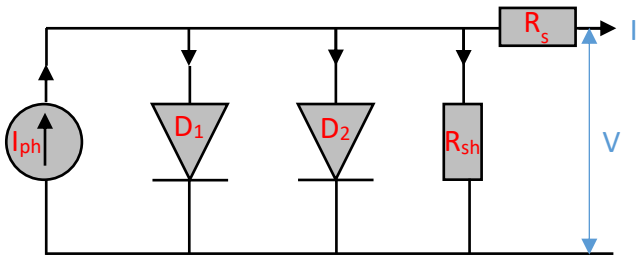

Figure 9: Equivalent electrical circuit of a solar cell: two-diode model.

This model of cell in equivalent circuit is therefore generally sufficient to reproduce the current-voltage characteristic of a standard technology photovoltaic cell. An example of curve IV, and its associated power-voltage curve, is given in Figure 10. The IV curve of a cell can be measured using a solar simulator, or flash-tester. This device reproduces most faithfully the spectrum of the sun under standard conditions (STC). A variable load is connected to the terminals of the cell. During the illumination time, the external load is varied, to change the voltage at the cell terminals. The generated current I is measured. As already seen, at V = 0,

the measured current correspond to the short-circuit current I_{sc}. When increasing the voltage, the diodes become more and more conductive, and the total current of the cell decreases. When it reaches zero, it is called the open circuit voltage V_{oc}. These two points correspond to zero power. Between these two points, the power increases and goes through a maximum. The voltage at the maximum power point (MPP) is called V_{mpp}. The current at V_{mpp} is called I_{mpp}. These are the four main IV parameters of the solar cell, from which we can derive other IV parameters. The fill factor FF = (I_{mpp} V_{mpp}) / (I_{sc} V_{oc}). The larger the FF, the more rectangular the IV curve of the cell. The smaller the FF, the flatter the curve. High recombination rate in the cell, high series resistance, or low shunt resistance are all factors that reduce the FF of the cell. The maximum power of the cell is thus $P_{mpp} = I_{mpp} V_{mpp}$. The efficiency of the cell is defined as the ratio of the generated power on the incident power $\eta = P_{mpp} / P_{in}$. In the case of the standard test conditions (T=25°C), the spectrum is called AM1.5g. It has an integrated power over all wavelength of 1000 W/m².

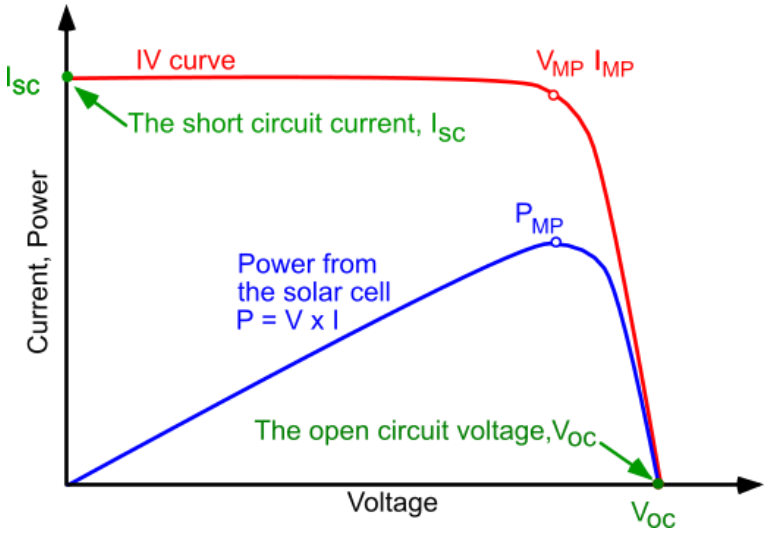

Figure 10: Example of a current-voltage (IV) characteristic of a solar cell (red), and the corresponding power-voltage characteristic (blue).

Different solar cell technologies are available. A graph of the evolution of the performance of the best laboratory cells for each technology is shown in Figure 11. The most common technology in earth energy production are crystalline silicon-based cells. A distinction is made between cells made of multi-crystals (multicrystalline) and cells made of a single crystal (monocrystalline). It is also possible to use heterojunctions, which use different bandgap semiconductors. These cells are usually several tens of micrometres thick. The performance record for this category is held by Kaneka with a heterojunction cell that contacts a crystalline silicon with a hydrogenated amorphous silicon (a-Si:H/c-Si): 26.7%. Some technologies use semiconductor-based thin films such as CIGS (Copper Indium Gallium and Selenium...), CdTe (Cadmium Telluride) or thin films of hydrogenated amorphous silicon (a-Si:H). In this category, the record is currently held by SolarFrontier with a CIGS cell without concentrator at 23.35%.

In order to increase the efficiency of the cells, it is possible to use several pn junctions, using semiconductors with different bandgap. This makes it possible to capture a larger part

of the solar spectrum. It is these types of cells that hold the world record for solar cell efficiency: NREL has created a 6-junction cell with an efficiency of 47.1% (143 x concentration). At the same time, technologies, which NREL calls "Emerging PV", bring together organic, perovskite, dye-sensitized and more. The record is currently held by Oxford PV with a 29.5% efficiency silicon/perovskite tandem cell.

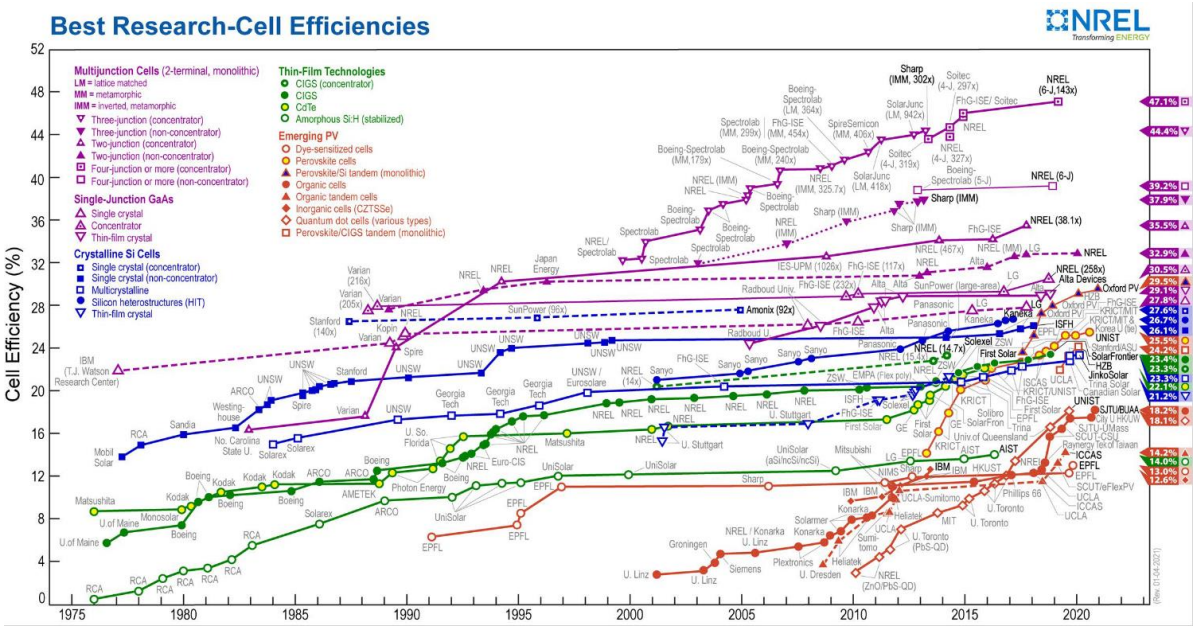

Figure 11: Evolution of best research-cell efficiencies for different cell technology. Graph made by the National Renewable Energy Laboratory (NREL) of United States [31].

At the National Institute of Solar Energy, where this thesis was carried out, the main technology is a heterojunction cell based on a bulk of n-doped single-crystalline silicon (n c-Si). Two nanometric layers of hydrogenated amorphous silicon (a-Si:H) passively cover the front and back surface of the c-Si to ensure a low level of defects and thus recombination (intrinsic, non-doped layers). On the front side, an n-doped hydrogenated amorphous silicon nanometric thickness layer is added, and a p-doped layer on the back side to form the junction (back side emitter). Two layers of transparent conductive oxides (TCO) are added on the front and back side to transport the current laterally to the screen-printed silver paste metallization fingers. A photo and a schematic view of the cell are given in Figure 12.

The cell is bifacial, i.e. it can produce energy from the front and from the back. The current record on the CEA INES pilot line is 25.0% on a cell of M2 format limited to 213 cm² (the edges, recombinant, are masked). On unmasked M2 cells, the efficiency record at CEA INES is 24.63% [32]. The objective is to reach 24% average efficiency in production line in 2021.

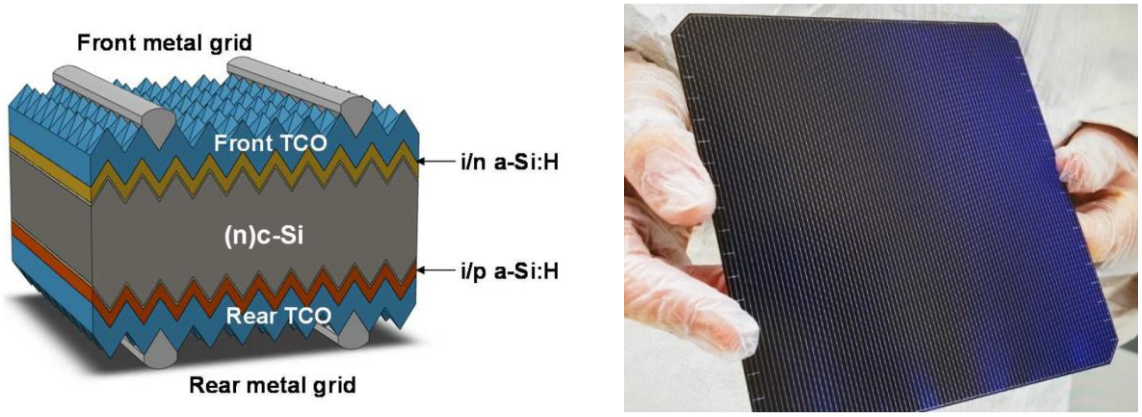

Figure 12: Schematic view of the different layer of the a-Si:H / c-Si heterojunction solar cell of CEA INES laboratory (left). Picture of the corresponding 244.33 cm² solar cell

The cell is therefore the heart of a photovoltaic system: it converts light into electricity. But it cannot be used alone: it is a fragile device.

I.B.2 Photovoltaic modules: a compromise between protecting cells and maintaining their performance

A photovoltaic module is an assembly of photovoltaic cells, electrically connected and protected from mechanical, chemical and electrical damage to ensure reliability and durability. The process of module creation (module manufacturing) must also ensure that the user or installer is protected from electrical shock. However, the materials used to fulfil these functions must allow the cell's initial optical and electrical performance to be preserved as much as possible. Thus, a balance must be found between protective functions to ensure good performance over the long term, while maintaining correct initial performance of the module.

A schematic view of the different layer of a module is presented in the Figure 13, associated with a picture of module mounted on support at INES facilities.

The first step in creating a module is the interconnection of the individual cells. The purpose of this step is to obtain a specific voltage and current for a given application, by playing on the parallel series arrangement of the cells. The cells are usually interconnected by copper ribbons and/or electro-conductive adhesive, connecting the front side of a cell to the rear side of the next one. The resulting structure is called layout. These cell interconnection can have two main impacts on cell performance: (i) an electrical impact through the addition of a series resistance contribution R_s that increases Joules losses. (ii) an optical impact, since the electrical interconnection may shade part of the cell and decrease its photo-generated current I_{ph}. This step is carried out by machines called "stringer"

The next step is to encapsulate the module in different layers to ensure the mechanical and chemical protection of the cells. Two main types of materials are used. A transparent polymer encapsulant is used on the front and back side of the cell layout. A glass is placed on the front side, and a backsheet (rigid polymer layer) is placed on the back side. In the case of

bifacial modules, a glass or a transparent backsheet is preferred on the back side. This stack is passed through a laminator: a machine that applies a time profile of pressure and temperature, to make the encapsulant ductile and adhere to the cells and glasses and / or backsheet. The encapsulant can absorb mechanical shocks and protects the cells. The glass and/or backsheet ensures the mechanical rigidity of the assembly. These two layers chemically protect the cells from external aggressions (water, oxygen...). They also provide electrical insulation. However, they are not perfectly transparent: a certain part of the incident light can be reflected or absorbed before reaching the cell.

An aluminium frame can be placed around the module to increase its rigidity. Finally, a junction box with cables is added, to simplify the connection of the modules to each other in a complete system.

In addition to the optical and electrical losses due to the protective layers and interconnection elements, two other examples of performance losses due to module assembly can be cited.

Firstly, the sum of the surface area of all cells is generally smaller than the surface area of the module. Spacing is necessary between cells to pass interconnection ribbons or to avoid short circuits. Gaps are also needed between the cells and the edges of the module to ensure electrical isolation. These spaces do not produce power: they therefore contribute to decrease the total efficiency of the module.

Second, it is possible that not all cells used are the same and therefore do not produce the same current. This is problematic if they are interconnected in series (which is most of the time the case): indeed the current flowing in all the cells in series must be the same. This will force the cells to change their operating voltage to work at a point of operation where the currents are equal. This phenomenon is the cause of losses, compared to a case where all the cells are identical. This is one of the reasons why the cells are usually sorted according to their IV parameters before being integrated into the modules.

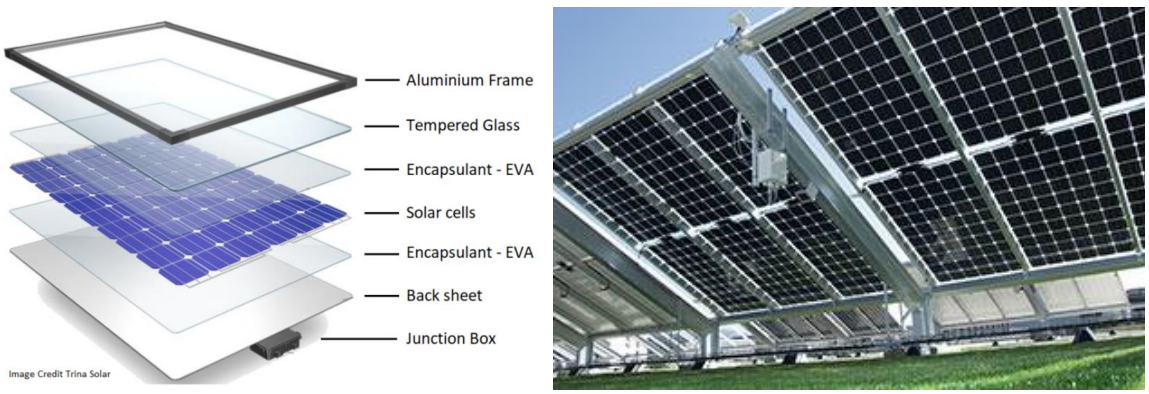

Figure 13: Schematic view of the different part of a mainstream monofacial module (left). Example of bifacial module (no backsheet at rear side) mounted as a system (right).

The losses observed during the module setup are generally analysed in relation to the cell performance, and are grouped under the term cell-to-module ratio (CTM): it is defined as

the ratio between the module performance and the performance of the cells that compose it. It is most often defined in terms of electrical power, as the MPP power of the module over the sum of the powers of the individual cells:

$$CTM_{P_{mpp}} = \frac{P_{mpp_{module}}}{\sum P_{mpp_{cellule}}} \qquad \text{I.4}$$

But it can also be defined for all the other IV parameters previously mentioned: CTM_{Isc}, CTM_{Voc}, CTM_{Impp}, CTM_{Vmpp}, CTM_{FF} and CTM_{η}. This is a key parameters for the quality of the module manufacturing steps, in particular to compare the impact of a fixed module architecture for several types of integrated cells. It is therefore a tool for improving the performance of a module. Aiming at increasing this ratio (and thus reducing the performance losses induced by the module implementation) is a necessary but not sufficient objective. The International Technological Roadmap for Photovoltaic (ITRPV) publishes in its 2020 report the expected increase of the CTM_{Pmpp} for the coming years (Figure 14).

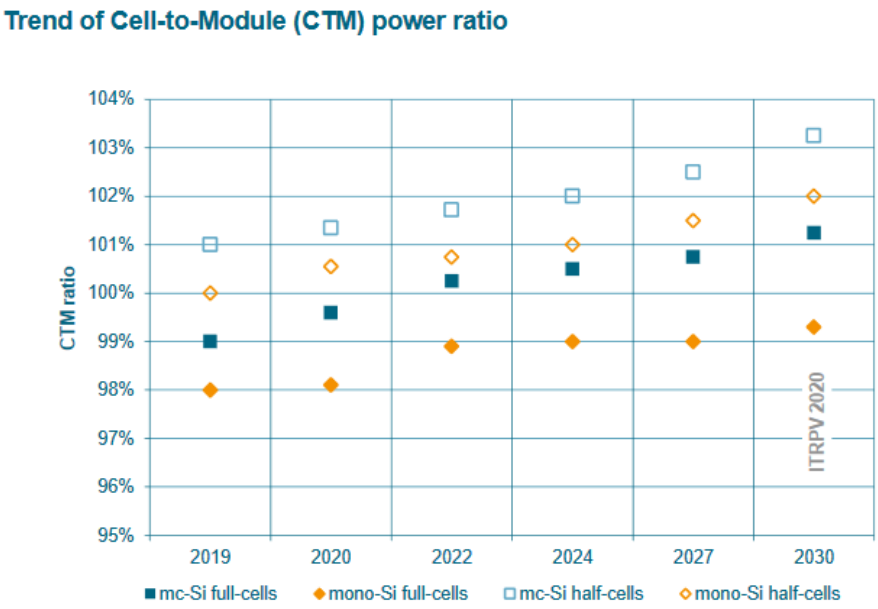

Figure 14: Trend of cell-to-module (CTM) power ratio for the next ten years as forecasted by the ITRPV 2020.

We can see that for the industrial modules we are interested in (mono Si full-cell and half-cell), the average CTM was 98% (full-cell) and 100.5% (half-cell) in 2020. ITRPV anticipates that these ratios will increase to 99.3% (full-cell) and 102% (half-cell) in 2030, an increase of about 1.5% of the power of a module with constant cell performance. The full-cell and half-cell architectures consist respectively in integrating whole and cells cut in two equal part in a module. The reasons for the difference between these two architectures are explained in Chapter II and Chapter III.

Chapter II

State of the art in module performance modelling and CTMod simplified model description

This chapter is devoted to the description of the simplified CTMod model for forecasting the performance of a module and the associated losses. In the first part, we will present the optical and electronic phenomena involved in a module, together with a detailed description of the models used. We will first introduce what the necessary input parameters are, how they can be measured, or taken from the literature. We will then see the details of the optical, semiconductor and resistive calculations to obtain the full IV characteristic of the module. Then, we will detail the calculation of the absolute power losses in a module according to standardized categories, which allow to perform a "Cell-To-Module" (CTM) analysis, and to compare different module architectures. In the second part, we will see what module performance modelling software already exists. One of them, Sunsolve, was selected for a detailed benchmarking of our optical model, on a realistic module configuration.

Ce chapitre est consacré à la description du modèle simplifié CTMod pour la prévision des performances d'un module et des pertes associées. Dans une première partie, nous présenterons les phénomènes optiques et électroniques mis en jeu dans un module, ainsi qu'une description détaillée des modèles utilisés. Nous présenterons d'abord quels sont les paramètres d'entrée nécessaires, comment ils peuvent être mesurés, ou récupérés dans la littérature. Nous verrons ensuite le détail des calculs optiques, semi-conducteurs et résistifs pour obtenir la caractéristique IV complète du module. Puis, nous détaillerons le calcul des pertes de puissance absolues dans un module selon des catégories standardisées, qui permettent de réaliser une analyse "Cell-To-Module" (CTM), et de comparer différentes architectures de modules. Dans la deuxième partie, nous verrons quels logiciels de modélisation de la performance des modules existent déjà. L'un d'entre eux, Sunsolve, a été sélectionné pour un benchmarking détaillé de notre modèle optique, sur une configuration de module réaliste.

Part II.A Description of the main optical and electronic effects in a module through the presentation of CTMod simplified model

Recreating a complete module model better than the existing state of the art is a difficult challenge. Each of the loss items in a module has been the subject of several publications and theses. However, creating a simplified model, valid under standard test conditions (STC: AM1.5g, 25 °C, normal incidence), or similar test conditions (BIFI 10 ...) is more accessible. The motivation of developing a module model are:

1. The main models available, efficient and proven by experience in recent years, do not have their source code accessible, although they are well documented. It is a problem from our point of view for a thesis work. It can be difficult to understand in hindsight what exactly happened in those black boxes. They are more dedicated to industry for R&D work.

2. The photovoltaic modules laboratory in which this thesis took place wanted to pool the scattered simulation skills already available to create a complete model. This thesis is a first approach in this direction.

3. Heterojunction modules have certain peculiarities which, at the beginning of this thesis, were only partially integrable by existing models. This is the case, for example, for the lateral transport of current in SHJ cells (Chapter 2), the use of electrically conductive glue for bonding the cell interconnection ribbons, the losses during the cutting of heterojunction cells (Chapter 3), or the use of encapsulants which may exhibit a diffusing optical behaviour (Chapter 4).

Throughout the description of the model used, we will present the case of a reference module. This module will be used for the description of input parameters, loss calculations, and comparison with the literature. The main characteristics of this bifacial module is a glass / glass architecture, without anti-reflection coating, with a high-cut off EVA type encapsulation. The 21.7% full-cell interconnection is made by 6 textured ribbons.

The proposed model is as follows: the input parameters feed a simple analytical optical model and a model of the series resistance. They serve as inputs to an equivalent circuit model which allows to calculate the IV parameters of the module. From the optical, resistive and equivalent circuit model, we can model all the losses in the module. The schematic diagram is shown on the Figure 15.

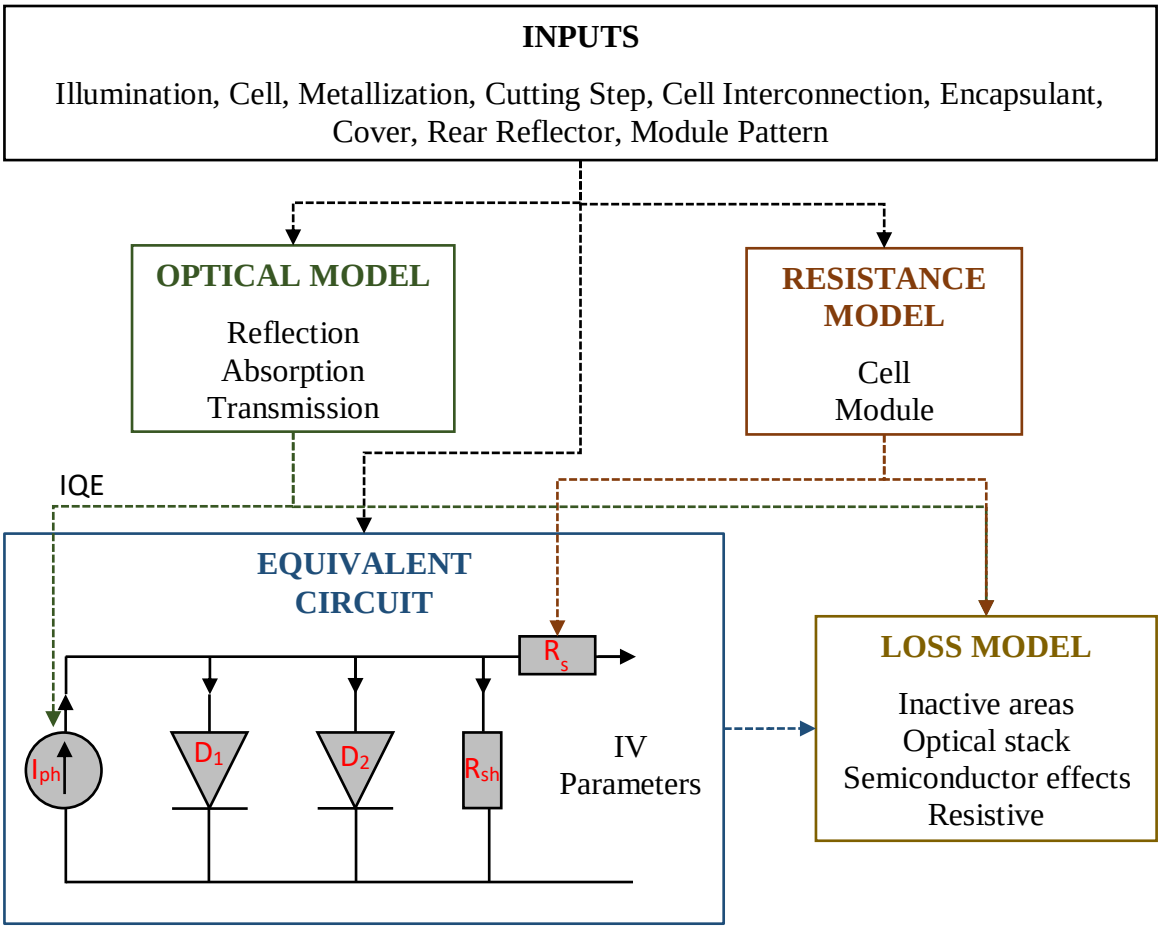

Figure 15: Schematic diagram of the main coupled blocks of the model developed in the thesis.

II.A.1 Main input parameters useful for modelling a module: definition, characterization and state of the art

In this section, the main parameters used by the calculation of the module performed are introduced, and methods for measuring them are also briefly reviewed.

Definition of external conditions

The incident light on the panel is modelled by a spectral irradiance S_{irr}, in W/m²/m. It can correspond to the AM 1.5 g spectrum or to any other spectrum desired for the study. The wavelength range goes from 300 to 2450 nm for all the spectral input parameters which will be studied. This range was chosen because it covers most of the optical phenomena that impact a module. Going below 300 nm can be useful for studies of resistance of a module to UVs, but is not relevant for the performance of a module in STCs. The integrated power of the AM1.5g spectrum is 1000 W / m², the part between 0 and 300 nm represents 0.002 W/m² (< 2.10^{-4} %), and the part between 2450 nm and infinity represents 8.5 W/m² (0.85 %) – computed with SMARTS [33] . When it is used, the AM1.5g spectrum is therefore multiplied by a normalization factor of 1.0085 to represent 1000 W / m² even between 300 and 2450 nm.

A number of sun n_{sun} is also defined, which is a simple multiplication factor of the base irradiance S_{irr}. Finally, two other multiplication factors are used: one for the front (m_f) and one for the rear (m_r). The spectral irradiance on the front face is therefore $S_{irr,f} = m_f \ n_{sun} \ S_{irr}$ and the irradiance on the rear face is $S_{irr,r} = m_r \ n_{sun} \ S_{irr}$.

The temperature of the environment, which is assumed to be equal to the module temperature, is also introduced. At the moment, the model does not account for any radiative transfer within the module, nor thermal exchanges with the environment. But, as we will see hereafter, it allows IV parameters correction thanks to the temperature coefficients of the cell.

In our reference case study, we use an irradiance corresponding to the AM1.5g spectrum, in a BIFI 10 situation: $n_{sun} = 1$, $m_f = 1$ and $m_r = 0.1$ (Figure 16).

Definition of module pattern

The pattern of the module must be entered: inter-cell distance, inter-string distance, module margins as well as the number of strings and the number of cells per string of the module. The reference case is a model of 6 strings spaced 3 mm apart and 12 cells per string spaced also 3 mm apart. The margins are 1.5 cm wide for left and right, and 2.5 cm for top and bottom to avoid shading by the junction box and to ensure a distance of 1.5 cm between inter-string ribbons and the module edges.

II.A.1.a *Non-metallized cell parameters: Optics, quantum efficiency, resistance and 2-diodes model of equivalent circuit*

The aim of the model is to take into account the smallest number parameters of the cell, while remaining general enough to perform Cell-to-Module (CTM) calculations. The model only allows to process solar cells with a-Si: H / c-Si heterojunctions.

The first spectral data of the cell is its external quantum efficiency (EQE). This value must be measured at the air-cell interface, $EQE_{c,air}$. The cell must not be metallized. It is necessary to avoid the use of an infrared reflective chuck on the back side of the cell, or that the EQE benefits from the reflection of the infrared rays on the back metallization of the cell. The EQE is ideally measured on the front and back side of the cell, but if the back side cannot be measured, a simple multiplication factor is applied to the front side, corresponding to the intrinsic bifaciality factor of the cell. In practice this factor is due to the asymmetry of the cell (position of the p-i-n junction, thickness of each of the amorphous layers, TCO, etc.). It is fixed to 96.3 % for the reference case. This value as been obtained at INES by I_{sc} measurement of SHJ cells with symmetrical metallization print in front side and rear sides.

Then, the total reflectance $R_{c,air}$ and total transmittance $T_{c,air}$ of the cell must be measured on a completely non-metallized cell also in air-cell interface. Due to the textured surface, the measurements should be made on a UV-Vis-NIR spectrophotometer with an integrating sphere and a light trap to avoid parasitic reflections. The details of the optical measurements are described in chapter 3 (which discuss mostly encapsulant measurements, but the method is still valid for cells). These reflectance and transmittance values will be used for the calculation of the internal quantum efficiency (IQE). They must therefore be performed on a cell of the same type as the one used for the measurement of the EQE. The measurement must be carried out on the front and back of the cell (four measurements in total). In our case

study, the spectrum, EQE and reflectance / transmittance values on the front side of the cell are given in Figure 16.

The choice was made to model the optics by ray tracing, and we want to avoid modelling the cell layers in our model. However, it is necessary to know how the reflectance and transmittance of the cell evolves from an air-cell interface to an encapsulant-cell interface. For that, we made simulations with the software of PVLighthouse "Wafer Ray Tracer" [34]. The goal is to calculate the reflectance and transmittance of a cell at the air-cell interface and at the encapsulant-cell interface.

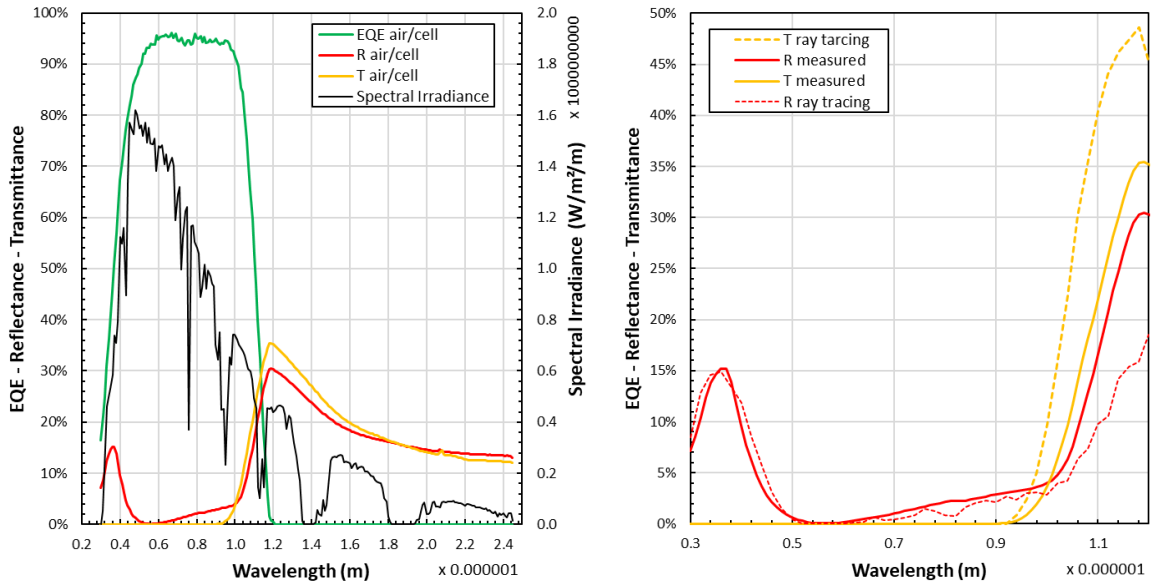

Figure 16: EQE, total reflectance and total transmittance of the front side of the reference cell measured in air-cell interface. Spectral irradiance of the AM1.5g spectrum (left). Comparison of simulated (wafer ray tracer) and measures total reflectance and transmittance (right).

The mean size of the random upright pyramids of INES SHJ cells is 2 µm (base). It is automatically measured by the singular brilliance of the vertices by optical microscopy. This average varies from 1.5 to 2.5 µm from run to run but remains globally fixed depending on the types of additives and the implementation in the texturing baths. SEM measurements show that for sizes of average 2 µm the distribution is 1 to 5 µm with a large majority in the 1.5 / 3 µm range. No flat area is generally observed. The angle of the pyramids to the base is theoretically 54.74°, but experimental studies have shown that it can be as low as 50-52 ° for random upright pyramids [35].

The thickness of the thin films used are: 71.4 nm for the front and rear side ITO, 11.9 nm for the front side n-type amorphous layer, 9.4 nm for the front side intrinsic amorphous layer, 13.4 nm for the intrinsic rear side amorphous layer and 6.3 nm for the rear side p-type amorphous silicon layer. The c-Si n-type bulk is 150 µm thick. The value of refractive index n and extinction coefficient k for each layer have been measured and extracted in previous work at INES with spectrophotometer UV-Vis-NIR.

The comparison of the measured and simulated total reflectance and transmittance of the front side of the reference cell is given on the Figure 16 (right). The agreement is good, except over 1000 nm. Indeed, as the pyramid have a typical size in the order of the wavelength, beyond 1000 nm, wave diffraction should be included. It is not the case in a ray tracing model, which only include geometrical optic effects and interferences in the thin films optical stack. It is known that in this condition, ray-tracing overestimates the transmittance and underestimates the reflectance, unless a Phong scattering model with an exponent of 25 is used [36].

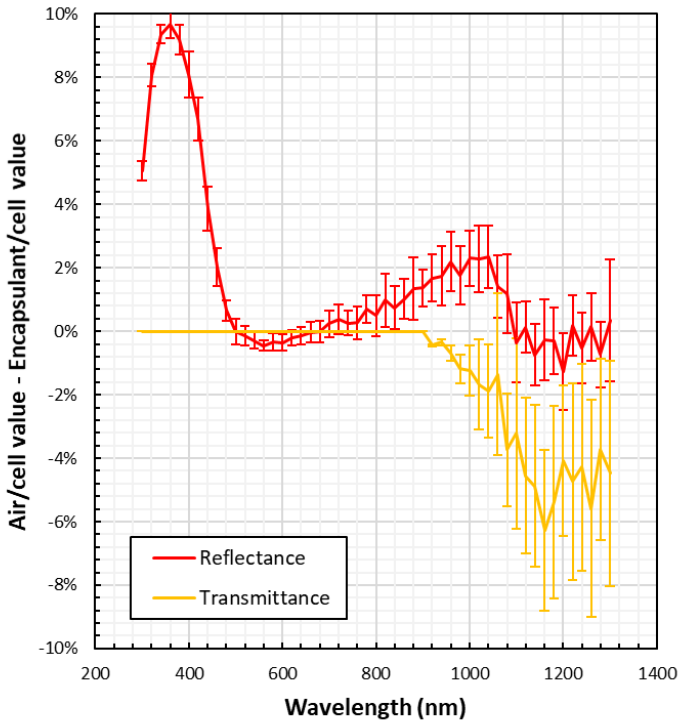

Figure 17: Difference of reflectance and transmittance between the values computed with ray-tracing in air/cell geometry and encapsulant/cell geometry. The uncertainties mentioned come from random behaviour of ray-tracing study.

We define two quantities called Q_R (respectively Q_T), the difference between reflectance (respectively transmittance) in air/cell and in encapsulant/cell configuration: $Q_R = R_{c,air} - R_{c,enc}$ and $Q_T = T_{c,air} - T_{c,enc}$. These two quantities allow us to re-compute a value of transmittance and reflectance of the cell in an encapsulant-cell interface from measurement of R & T in an air-cell interface. Why not simply use the simulated value of $R_{c,enc}$ and $T_{c,enc}$ obtained by ray tracing simulation ? As mentioned before, there is a gap between experimental values of R &T and simulated one over 1000 nm, but we make the assumption that the relative variation (in the form of Q_R and Q_T) is still correct, even with the phenomenon of diffraction on the back side. The value of Q_R and Q_T are plotted on the Figure 17. We note that the reflectance of the cell in air/cell geometry is always higher than in encapsulant, especially around 300 nm (+9.5 %) and around 1000 nm (+2 %). Between 450 and 700 nm, there is no obvious difference, as between 1050 and 1300 nm.

For transmittance, the air / cell interface value is always lower than that of the encapsulant / cell, with a minimum of -6% around 1200 nm. The difference is zero from 300 to 900 nm since the two corresponding values are zero (silicon absorbs everything).

The uncertainties mentioned in Figure 17 are related to the random aspect of ray tracing simulation, and not to uncertainty on input parameters, which are much lower. To obtain these standard deviations, 10 simulations of 50,000 rays each were carried out. The wavelength step was set at 20 nm, therefore with an average of 45 rays per wavelength.

As an example, the average Q_R value over the wavelength range 300 to 1300 nm and weighted by the EQE and the AM1.5g spectrum is 1.14 %. The same value for Q_T gives -0.23 %. In total, the gain in I_{sc} during the passage of a cell in air interface and encapsulating interface is 0.9%, a value consistent with what is expected for cells with a random upright pyramid quality texturing. The alkaline etching is known to have better performance on I_{sc} of the cell, but the gain in module is reduced, even if the I_{sc} in module remain higher [37]–[39].

Two diodes model of the cell

The cell is described by a two-diode model, with ideality factors fixed at $n_1 = 1$ and $n_2 = 2$. It is possible to describe the cell with ideality factors other than these values if no consideration of cell cutting is subsequently carried out (see chapter 3 for more details). The series resistance of the cell is completely recalculated from sub-parameters, and is therefore not an input parameter of the simulation. All the data relating to the series resistance of the SHJ cell (experimental models and characterization) come from a thesis carried out at INES by Leo Basset [40]. Extracting the parameters therefore boils down to the values of J_{01}, J_{02} and r_{shunt}. As the shunt losses of a SHJ cell are generally low, the value of r_{shunt} is generally taken to be infinite (see chapter 3). The values of J_{01} and J_{02} are obtained by the fit of an I_{sc}-V_{oc} curve to overcome the effect of series resistance. I_{sc}-V_{oc} curves are obtained by plotting the variation of I_{sc} as a function of the V_{oc} for different illumination level. The V_{oc} is not impacted by series resistance. The I_{sc} is not impacted for standard value of series resistance (R_s < 10 Ohm.cm²) [41]. An IV curve is thus obtained without series resistive effects. They can also be obtained by fitting a Light IV curve in STCs where the effect of series resistance is corrected from voltage dependence. In the reference case, the following values are used: J_{01} = 11.14 fA/cm² and J_{02} = 6.871 nA/cm²: they correspond to an efficiency of 21.7 % when a series resistance of 0.7 Ohm.cm² and a J_{ph} of 37.65 mA/cm² are added in the 2-diodes model.

All the characteristic values of the cell are surface related, but it is necessary to set the size of the wafer used: its surface, its length in the X and Y direction. The thickness of the wafer, doping, and the injection level at the maximum power point MPP can be entered and used to calculate the resistivity of crystalline silicon.

The resistance values of the amorphous interfaces of the cell can be entered. For our current case study, a resistance of 90 mOhm.cm² for the front amorphous interface and of 250 mOhm.cm² for the rear amorphous interface is used. The sheet resistance of the ITO on the front face must also be provided. The values for the study case are 250 Ohm/sq on the front face and 150 Ohm/sq on the rear face. These values correspond to a cell of 21.7 % of efficiency, with a FF of 79.0 %.

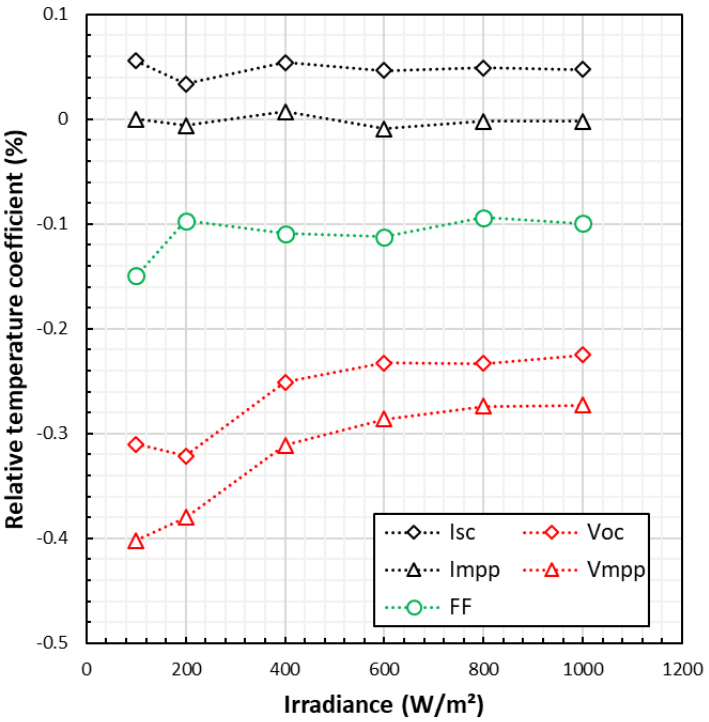

Figure 18: Temperature coefficient of IV parameters determined as a function of irradiance used as input parameters of the model.

Finally, the temperature coefficients of the cell for I_{sc}, V_{oc}, I_{mpp} and V_{mpp} are entered. Their values are tabulated according to the irradiance. These values were not obtained during this thesis, but at INES for reference SHJ modules within the framework of the European project AMPERE. The results are shown in Figure 18. The temperature coefficient of I_{sc} and I_{mpp} are relatively stable with irradiance at respectively +0.05 %/°C and 0.00 %/°C. The temperature coefficient for V_{oc} and V_{mpp} increase with irradiance: from -0.32 %/°C at 200 W/m² to -0.22 %/°C at 1000 W/m² for the V_{oc}, and from -0.38 %/°C to -0.27 %/°C for the V_{mpp}. This variation are known for silicon and explained by the logarithmic dependence of V_{oc} with Irradiance [42], [43].

Information on a possible cutting step of the cell can also be provided. Indeed, the use of cut-out cell, for example half of a cell, has an interest for the reduction of resistive losses in the interconnections of cells. This is the subject of chapter 3, on gains and losses on cutting for heterojunction cells and modules. The necessary input parameters are the losses of photo-generated current, the additional recombination current of diode two per unit of length cut (J02, edge), and the number of cuts made (half-cell, third-cell ... sixth cell for shingle interconnection).

II.A.1.b *Solar cell metallization and interconnection: electrical resistance and optical shading*

Definition of inputs parameters for the metallization

The metallization defined in the model requires the contact resistance values between the ITO and the low-temperature metallization paste. In our reference case, a contact resistance of 20 mOhm.cm² is used, determined by Basset *et al.* [40].

First, the physical width of the fingers must be determined. To this aim, a KEYENCE™ optical microscope was used. An example of picture and profile taken from the instrument are presented in the Figure 19. The mean physical width of the base of the finger is determined to be 61 µm. The shape of the finger section is a bell curve closer to the Gaussian. The finger height according to the transverse profile is 17 µm, but as the longitudinal profile shows, it is very variable: an average value of 18 ± 4 µm, with a maximum of 27 µm and a minimum of 10 µm. It is indeed the total width of the deposited paste that has to be quantified, since it is this entire surface which will be able to reflect the irradiance differently in comparison with the cell.

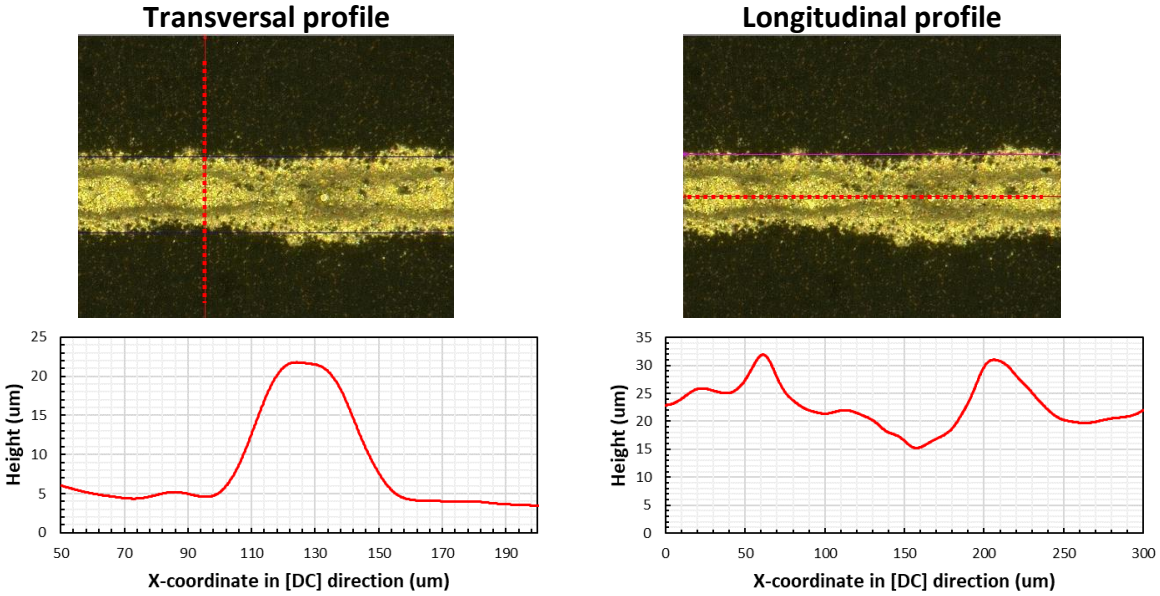

Figure 19: Picture taken from KAYENCE microscope measurement of single print finger for BB6 configuration. Associated profile in transversal and longitudinal directions.

Light incident on a finger can be absorbed or reflected. Depending on the profile of the finger, it can be reflected towards the cell and participate in the photo-generation. A finger therefore has an optical width $w_{f,opt}$ smaller than its physical width $w_{f,phy}$. These two widths are linked by the effective width $w_{f,eff} = w_{f,opt} / w_{f,phy}$, smaller than 1. This effective width is different depending on whether the cell is measured in air or encapsulated in a module. It also differs according to the profile of the finger and therefore according to the metallization method used. It depends on the more or less diffusing nature of the finger surface. Finally, it

depends on the incident angle of the light and on the wavelength. All these dependencies have been explored by the previous works.

An illustration is given in Figure 20. In the case of a cell in air, light (specular or diffuse) that is not reflected directly to the cell is lost. In the case of an encapsulated cell, this same light is not totally lost because it can be reflected (totally or partially, depending on the angle) at the glass / air interface. The effective width of an encapsulated finger is therefore smaller than the width in air.

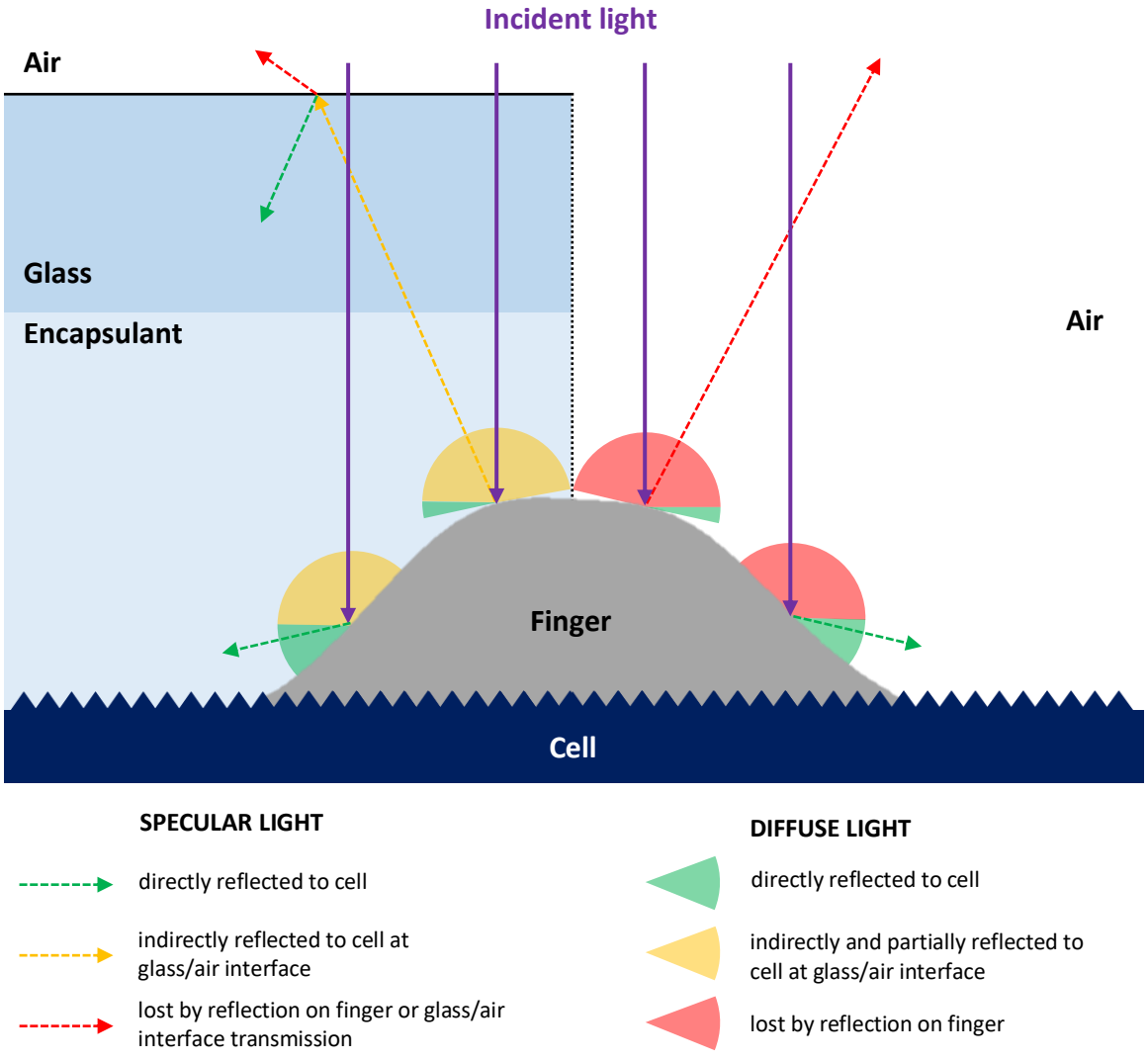

Figure 20: Explanatory diagram of the phenomenon of effective optical width for a finger of an encapsulated cell (left) and of a non-encapsulated cell (right). The scales are not respected.

In 1992, Blakers *et al*. studied the effective width of silver finger deposited by electro-plating for space applications [44]. Their cross-section is close to half a disc. The authors studied the dependence of the effective width on the azimuth and elevation angle, for an encapsulated cell. At normal incidence, they obtain an effective width of 70 % in air, and 35% when the cell is encapsulated. Their analytical model considers only specular light. In 1999, Stuckings *et al*. studied the same type of finger, and found experimental values of effective

width in encapsulated cell between 30 and 40 % [45]. The experimental method consists in measuring the reflectance of a metallized and non-metallized cell, encapsulated or not. The dependence of this value on the optical index of the encapsulant was found negligible. The fingers are 97 % reflective and 3 % is absorbed.

In 2008, Glunz *et al.* compared the experimental effective optical width of fingers deposited by screen-printing or by aerosol jet-printing [46]. They used experimental method proposed by Stuckings *et al*., adding spectral dependency of the reflectance. For Aerosol-printed cell with wide line distance, they found an effective width of 95 % in air and 35 % in module. For screen printed cell, they found an effective width of 90 % in air and 45 % in module. They found minor dependency in the range 600-1000 nm, because of the quasi constant complex refractive index of silver, encapsulants and glass in this spectral range. The measure is based only on reflectance measurement and thus does not contain a weighting by the EQE of the cell.

In 2014, Levrat *et al*. measured the effective optical width of screen-printed silver fingers and cross-section interconnecting wires [47]. They used an experimental method based on the EQE and a special metallization mask, consisting in moving an EQE spot of 20x20 mm² over an increasingly metallized area. For the fingers, they find an effective width gain of 43 % by going from a measurement in air to a measurement in module with encapsulant + glass. Assuming an effective finger width in air of 90 %, this represents an effective encapsulated width of 51 %. It is also in 2014 that Voltan *et al.* measured optical width of single and double screen-printed finger with micro LBIC at 826 nm [48]. They obtained an effective optical width of 85 % in air and 50 % in module for single print, 71 % in air and 38 % in module for double print.

In 2015, Rodriguez *et al*. measured the effective optical width of silver finger obtained by single screen-printing, double screen-printing and dispensing [49]. They used a spectrally resolved LBIC for 6 wavelengths: 405, 532, 658, 780, 940 and 1064 nm. For single screen-printed fingers, they obtain an effective width of 95 % in air and 72 % in module. For the double print, they get 87 % in air and 60 % in module. Finally, for dispensing, they obtain a value of 72 % in air and 46 % in module.

In 2016, Witteck *et al*. measured the effective width of single screen-printed fingerprints in air by a reflectance method [50] [51]. They get an average value of 89 %. They simulated by ray tracing the effective width in module, and found an average value of 45 %. The impact of the part of Lambertian scattering in the total reflected light has little influence in the probable range of this parameter (between 60 % and 90 % of diffuse reflectance).

All the effective optical width values in air and in module for screen-printed fingers are summarized in Table 1. The values range from 85 to 95 % for the value in air and from 45 to 72 % for the value in module. The effective optical width of the fingers is a necessary parameter of our model.

	Effective optical width (air)	Effective optical width (module)	Module / Air	EQE weighting
Glunz *et al. (2008)*	90 %	45 %	50 %	No
Levrat *et al. (2014)*	/	/	57 %	Yes
Voltan *et al. (2014)*	85 % (71)	50 % (38)	59 % (54)	No
Rodriguez *et al. (2015)*	95 % (87)	72 % (60)	76 % (69)	Yes
Witteck *et al. (2016)*	89 %	45 % (ray-tracing)	51 %	Yes (air) No (module)

Table 1: Summary of the different value of effective optical width for screen-printed finger, as obtained by the literature. The value in brackets corresponds to double-print.

To measure the optical width value in air of the screen-printed finger of our reference case, several batches of cells were produced with variable pitches on the rear face (0.2, 0.4, 0.6, 0.9, 1.3, 1.8 and 2.1 mm) for a pitch on the front face of 2.1 mm. In each batch, the short circuit current I_{sc} of the back side of the 20 cells was measured. Since the print screens are different, it results in lines of different width. The width of the fingers corresponding to each pitch was measured and integrated into the model. It can be seen that the 95 % effective optical width value of Rodriguez *et al*. causes a systematic underestimation of the I_{sc} (Figure 21). The error is logically all the greater as the pitch on the rear face is low, since the metallized part of the cartridge is greater. An error of 0.5 A is reached on an I_{sc} of 6.5 A for a pitch of 0.2 mm (i.e. an error of 7.7 %). The value of Voltan *et al.* (85 %) – produce an overestimation of 0.2 A for a rear side pitch of 0.2mm. By modifying the value of effective optical width W_{eff} to 88 %, the fit of the experimental data is much better, with an error contained within 0.05 A, corresponding to the experimental uncertainty. This value of 88 % lies in the range of the values obtain by literature (Table 1).

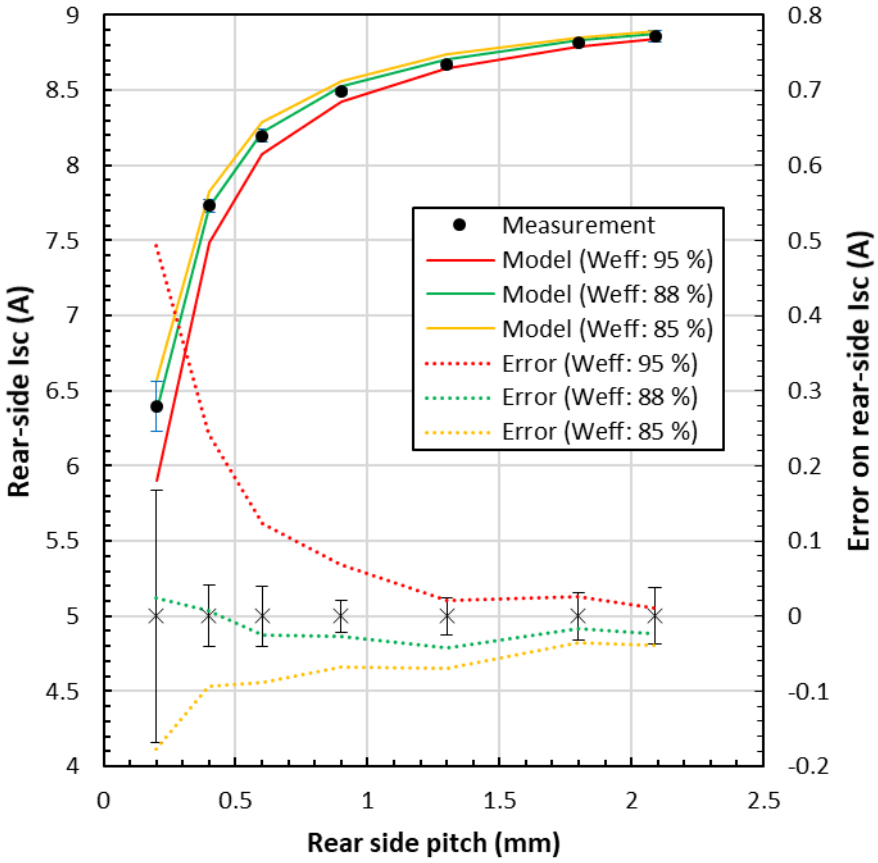

Figure 21: Evolution of the rear-side I_{sc} as a function of the rear side pitch. Model with effective optical width of 95 %, 88 % and 85 % are compared. The value of I_{sc} are shown on the left axis, the corresponding error made is plotted on the right axis.

The optical impact of the fingers is described as follows: the optical width of the fingers is equal to the effective optical width multiplied by the physical width: $w_{f,opt} = w_{f,eff} \cdot w_{f,phy}$. The effective optical width for our reference case is 88 % in air. In module, the results obtained were not repeatable. We will therefore use the values of Witteck *et al.*, 45 %. They correspond best to the value obtained for an air measurement (89 % vs 88 %) and are also the most recent. They are also consistent with the values of Voltan *et al.*

We are now interested in the resistive and mass parameters of the fingers. The fingers are described by an electrical aspect ratio AR_f which gives the mean height h of the finger according to its physical width $w_{f,phy}$: $h = AR_f \cdot w_{f,phy}$. This allow to calculate the section of the finger as $S_f = AR_f \cdot w_{f,phy}^2$. This should not be confused with a value often mentioned in the characterization work of the fingers "the optical aspect ratio", which gives the maximum height of the finger as a function of its width [49], [52]. The section of the finger is linked to the line resistance of the finger, given a certain paste resistivity. The section of the finger is also linked to the total finger mass of paste deposit on each side, given a certain paste density. In practice, it is the reverse that is done: the measurements of line resistance of the fingers and of the deposited mass are used to determine an aspect ratio AR_f and an effective resistivity, according to the following protocol:

1. Determine the AR_f for front and rears side, given the mass of paste deposited. The total mass M_f is given in function of the total length of fingers on cell L_f, the section of the finger S_f and the density d_f of the paste after curing:

$$M_f = L_f \, AR_f \, w_{f,phy}^2 \, d_f$$

The length of finger can be easily measured on the cell, the density of the paste is given by the manufacturer, the physical width has been previously determined and the total mass deposited is obtained by weighing the cell before deposition and after curing.

2. Determine the effective resistivity $\rho_{f,eff}$ of the finger, for front side and rear side, given the line resistance:

$$R_{f,L} = \frac{\rho_{f,eff}}{AR_f \, w_{f,phy}^2}$$

The effective resistivity is higher than the resistivity of the paste, because it takes into account inhomogeneities in the section of the finger and its porous nature [53]. This comes from the intensive propriety of the $R_{f,L}$, unlike the mass which is extensive.

The values used for the reference case are summarized in Table 2.

Model inputs parameters	**Front side**	**Rear side**
Contact resistance (mOhm.cm²)	20	20
Pitch (mm)	2.1	0.7
Physical width (µm)	55	55
Optical effective width in air	88 %	88 %
Optical effective width in module	45 %	45 %
Electrical aspect ratio	22.5 %	17.3 %
Effective resistivity (µOhm.cm)	6.81	5.21
Density (g/cm³)	9.4	9.4
Preliminary measurements		
Line Resistance (Ohm/cm)	1	1
Finger mass (M2 wafer) (mg)	45	92

Table 2: List of the parameters used in modelling of the reference case for front side and rear side metallization.

The busbar of the metallization can be of three kind:

- 'Busbar less', if multi-wire technology is used for cell-interconnection: no additional parameters are needed.
- 'One line', described by the width and the height of the busbar line, but also a fill factor if the line is dotted.

- ‘Two lines’, described by the width and the height of the two lines, but also the distance between the two lines.

In our reference case, the ‘one line’ design is chosen, with a width of 60 µm, a fill factor of unity (the line is continuous) and a height computed with the aspect ratio of the finger.

Definition of inputs parameters for the cell interconnection

There are two mains types of cell interconnection: ribbon-based interconnection (rectangular section or circular section) or shingle-type interconnection (Figure 22).

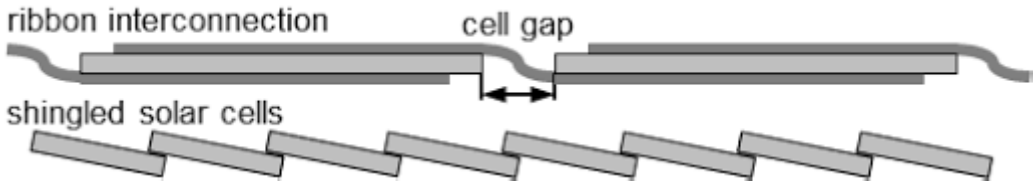

Figure 22: Ribbon-based interconnection (top) and shingle-based interconnection (bottom). Taken from Mittag et al. [54].

C*ase of ribbon-based interconnection*

If the interconnection corresponds to the 'ribbon' case, the front face and rear face can be different. In a conventional architecture, they are however identical, since the front face of a cell is connected with the rear face of the following cell. But in an architecture of the "monolithic" type (one in two cells is turned over, its rear face being on the front side of the module), it is theoretically possible to use different interconnections on the front face and on the rear face.

The first parameter to be entered is the number of ribbons used for interconnection, or the spacing between these bands. It is then necessary to specify the type of section (circular or rectangular) of the ribbons. In the circular case, the diameter of the core (usually made of copper) should be indicated. In the case of a rectangular section, the width and height of the ribbon must be entered. For both cases, the thickness of the coating on the core of the ribbon is also to be mentioned. For each of the materials (core of the ribbon and coating), resistivity and density must be provided. All these values are generally provided with accuracy by the supplier. Standard coating types have very little impact on resistive losses [53], but adding this impact to the model can be easily done to study the resistive behaviour of exotic coatings.

The last parameter for interconnect ribbons is its effective optical width. In the same way as for the fingers, some of the light which arrives on the ribbons can be reflected on the cell, directly or by multiple reflection on the air / glass interface. We also use a scalar parameter. The effective optical width values for "flat" rectangular ribbons are commonly taken at 90 %. For textured ribbons, the literature shows rather values of 30 % in nominal incidence with an AM1.5g spectrum. For ribbons with a circular cross-section, the values of the literature range from 60 to 40 %. A diagram of the reflection on the ribbons is presented in Figure 23 for the most common particular cases: ribbon with circular section, and ribbon with rectangular section and textured in V-groove. These values can be determined by measuring EQE, as presented below.

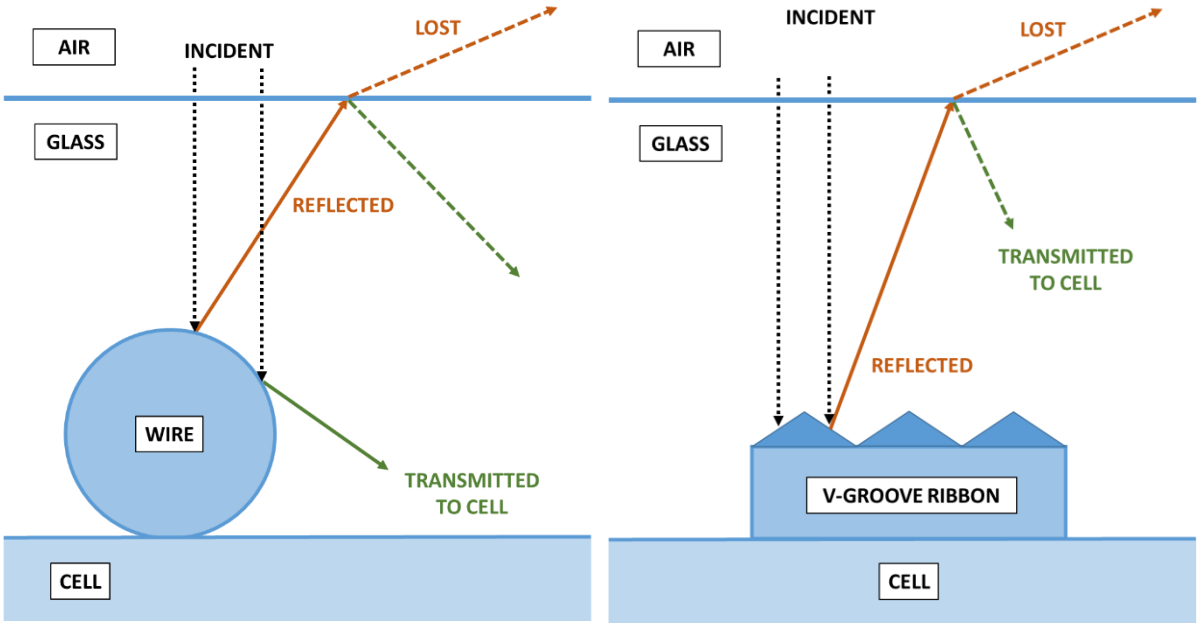

Figure 23: Diagram of the reflections at the origin of the effective optical width of the cell interconnect ribbons (wires on the left, textured V-grooves ribbons on the right).

Textured V-groove ribbons are used in our reference case. These ribbons include V-grooves, whose inclination has been calculated to trap the incident beam after reflection on the ribbon by total reflection at the glass/air interface.

A first series of EQE measurement is carried out on the cell between two fingers, in several positions of the cell (see Figure 24). The beam size is estimated to be 3 x 1 mm. We thus obtain the EQE of the bare cell, without interconnection ribbon (photo on the left). A second series of measurements is carried out with the EQE spot on the textured ribbons (photo on the right): we can see the secondary reflection spots.

The results of the EQE measurement in the cases described above are shown in Figure 25. The EQE of the cell encapsulated in the module reaches a maximum of 90 %, in the case of a textured V-groove ribbon, it is 70 % at most, and only 13 % in the case of a non-textured rectangular section ribbon. To extract the value of the effective width of the ribbons, the photo-generated current is calculated for each case with an AM1.5g spectrum. The ratio of the photo-generated current calculated for the EQE spot on the ribbon, and the current calculated for the EQE spot on the cell gives the effective value of the optical width of the ribbon (see the right table of Figure 25). Measurement on wires were not possible with our EQE because of the size of the spot, wider than the diameter of the wire.

Local EQE on cell (in module) **Local EQE on textured ribbon (in module)**

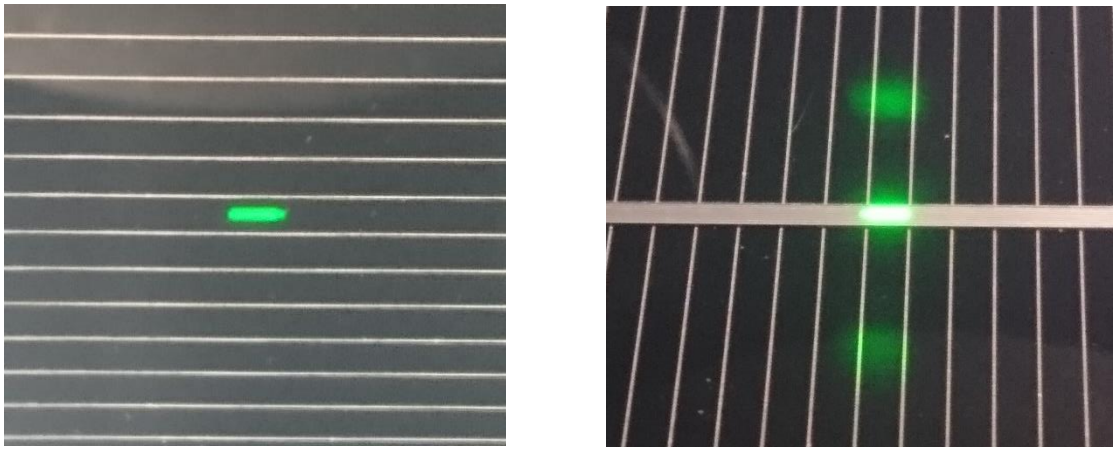

Figure 24: Localisation of the spot of EQE at 550 nm for the determination of effective optical width of ribbons. First serie of measurement on the cell encapsulated in module (left). Second serie of measurements on the V-groove textured ribbons (right).

The effective optical width of the textured ribbon is not 0 %, and that of the un-textured ribbon is not 100 % for several reasons: (i) the coating of the ribbon (here pure silver) has not a reflectance equal to 100 % and feature some surface roughness, (ii) glass does not have perfect surface roughness and can scatter some light, (iii) cell has lower EQE for rays with non-normal incidence. In our reference case, we are using 6 textured V-groove ribbons, with a width of 800 µm and an average thickness of 200 µm, with a copper core of resistivity 1.68 µOhm.cm and a coating of pure silver of 5 µm, resistivity of 1.59 µOhm.cm. The optical width of these ribbons is therefore taken at 27.1 %, as determined previously.

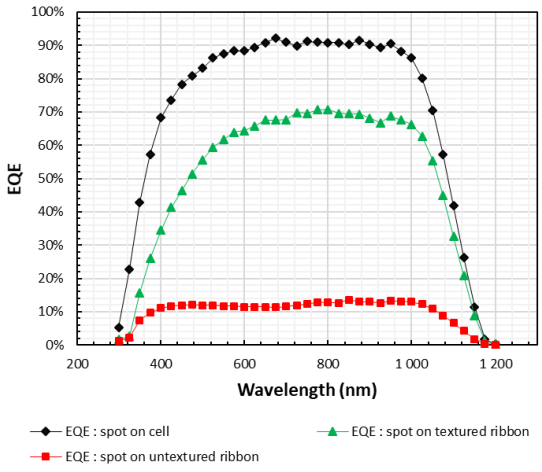

	Cell	Flat ribbon	V-groove ribbon
J_{ph} *(mA/cm²)*	37.0	5.20	27.0
Effective optical width	/	86.0 %	27.1 %

Figure 25: Measure of EQE of the encapsulated cell (no metallization), and EQE of ribbons (textured and flat) on the left. Corresponding photo generated current and deduce effective width of V-groove textured and flat ribbon.

In 2010, Glaeser *et al.* measured an increase of 1.3 % in Jsc with structured ribbons compared to flat ones. Ribbons cause a shading of 4 % of the solar cell [55]. The texturing profile was far from optimal. In 2013, Schneider *et al.* measured a 2.5 % gain in Jsc with structured ribbons, but the total coverage of the cell is unknown [56]. In 2016, Holst *et al.* have studied the increasing of light harvesting by such structured cell interconnection ribbons, experimentally and with ray-tracing [57]. For a mini-module of M1 wafer with 3 ribbons of 1.5 mm width, they get an extra 1.7 % gain in simulated J_{sc} for the textured ribbon compared to the flat ribbons The experimental value lies between +1.35 % and + 2.25 %, for a total shading of the cell of 2.88 %. Muehleisen *et al.* in 2016 have measured in similar gain of 1.8 % using structured ribbons instead of flat ones, for a shading of 2.3 % [58]. Using our values of optical effective width in Figure 25, we obtain a total optical effective width of 3 x 1.5 x 0.86 = 3.87mm for flat ribbons (2.48 % of shading), and 3 x 1.5 x 0.27 = 1.21mm (0.78 % of shading). The difference between flat and textured ribbon is thus 1.7 $\%_{abs}$, in very good agreement with Holst *et al.* and Muheleisen *et al.* values at normal incidence.

In the case of circular wires, no measurement have been realized, because of the size of the EQE spot, wider that the circular wires. Because we don't know exactly the size of the spot, it is not possible to obtain the effective optical width. In 2012 Braun *et al.* made a first theoretical calculation where they found that wire have an effective optical width of 70 % in air and 36 % in a module [59]. In 2013, Söderstrom *et al.* found an experimental value of effective optical width in module of 75 %, far from the theoretical one predicted. [60]. They obtain this value with linear regression on the I_{sc} of module made with different number of wire. The coating of the wire was made at 50 % of Indium. In 2014, Levrat *et al.* found a value 60-70 % with the same method used to determine effective optical width of finger [47]. It is unclear in their work if the value applies for cell in air or encapsulated. They used coating made of InSn. In 2016, McIntosh *et al.* perform optical ray tracing on multi-wire module and found an optical effective width of 35 % in module if the reflectance of the coating at normal incidence is 100 % [61]. If the reflectance is only 70 %, as it is the case for tin, the effective width is increased to 55 %. More recently in 2019, Witteck *et al.* measured value of optical width of wire in module of 67 % from the mean of 6 wavelength laser measurements [62]. The type of wire coating used is not specified.

The result seems to be highly dependent on the reflectance of the coating used on top of the wire. For example, at 550 nm and normal incidence, tin has a reflectance of 83 % and only 74 % at an angle of incidence of 80° and non-polarized light. Tin is used in alloy such as SnPb, or lead-free alloy: SnBiAg. At the same wavelength, silver (Ag) has a reflectance of 98 %, almost constant up to 80°. Lead has a reflectance of 92 % at normal incidence and 89 % at 80°. Bismuth (Bi) has a reflectance of 95 % at 0° and 94 % at 80°.

In the case of modules made of heterojunction cells, due to the sensitivity of the cells to temperature, it is not clear yet if soldering of the ribbons to the busbars is possible without damaging the cell. Recent studies seem to show that this is possible [63]. It is therefore necessary to use an electrically conductive adhesive or a low-temperature melting alloy. The curing temperature of these pastes, around 200 degrees Celsius depending on the type of paste, does not damage the amorphous layers of the cell. They induce an additional series resistance, which is taken into account by indicating the following parameters: width of the

deposited ECA, thickness, resistivity of the ECA (37 mOhm.cm, given by the supplier). The same interconnection is used on the front face and on the rear face.

The interconnection ribbons between the strings of the module have a rectangular section, whatever the cell interconnection method used (ribbon or shingle). The necessary parameters are, as for the cell interconnection ribbons of rectangular section: the width, the thickness and the resistivity of the core and of the coating of the ribbons. In our case study, we use ribbons 5mm wide and 300 µm thick, with a copper core and a coating of 20 µm in tin-bismuth-silver alloy with a resistivity of 13 µOhm.cm.

Case of shingle type interconnection

In the case of a shingle interconnection, no ribbons is used. The front and rear faces of the cells are interconnected by an electrically conductive adhesive of the same type as the one used for bonding the ribbon to the busbar. The parameters necessary for modelling are therefore reduced to: the width, the thickness and the resistivity of the ECA, as well as the distance of overlap of one cell by the other.

II.A.1.c *Optical layers and module pattern: glass, encapsulant and backsheet impact on module performance*

Transparent materials: glass and encapsulants

The different optical layers are mainly: glass, encapsulants and backsheets. On the front of the module (and on the rear side in the case of bifacial module), the glasses and the encapsulants participate to the same general role: to protect the cells chemically and mechanically. They must also have good durability. But first, it must ensure good quality optical transmittance. The phenomena that limit optical transmittance are: reflectance at the interfaces of two different materials, absorption of light within the volume of materials, and possibly certain light scattering phenomena.

Whatever the type of optical simulation used (ray tracing, transmittance matrix method, analytical method), optical constant of these materials are required. The refractive index n makes it possible to quantify the reflectance at the interfaces of materials. The extinction coefficient k, or the absorption coefficient alpha (m-1) provides information on the absorption in a thickness e of the material. Depending on the types of materials used, a light scattering coefficient s (m^{-1}) may also be useful.

New encapsulants, used in particular for heterojunction modules, significantly scatter light. This phenomenon poses a challenge for the characterization of the input parameters of optical constant. It is also legitimate to wonder about the impact it causes on the performance of a module. This is the whole object of chapter 4: to develop a model allowing to characterize precisely and simultaneously the indices n, k and s, and to model the impact they have on the performance of a module.

Reflective materials: backsheet and white encapsulant:

The rear optical layers of a monofacial module have a different optical role. As shown in Figure 16, the incident spectrum on the inter-cell spaces is diffused by the backsheet, in a more or less Lambertian way. Part of this irradiance has an angle sufficient to be in total reflection at the glass / air interface, and the rays can be redirected towards the cell. A part,

with a lower incidence angle is in partial reflection, and therefore another part is lost by transmittance of the interface. Part of the infrared light can pass through the cell and be reflected by the backsheet or white encapsulant and increase photo generation.

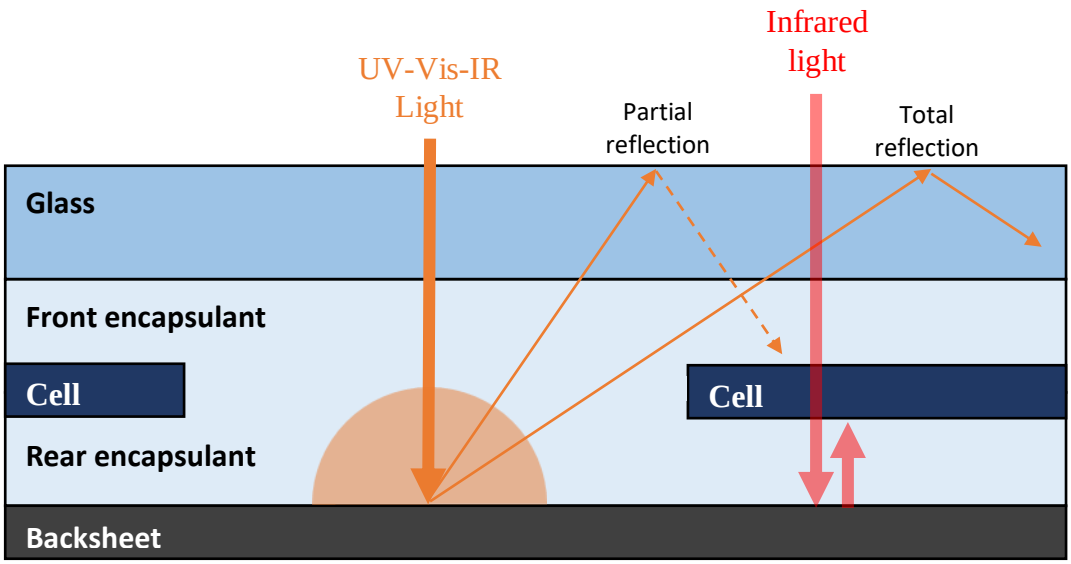

Figure 26: Schematic diagram of the coupling gains by light reflection on a diffusing backsheet in the inter-cell space. Part of the light is redirected towards the cell by total or partial reflection at the glass / air interface.

The phenomenon of optical coupling for the light incident on the inter-cell spaces is all the more important as the distance between the cells is great. It can be taken into account analytically according to the procedure used by Haedrich *et al.* [64]. This method consists in measuring the evolution of the photo-generated current of a mini-module by using masks of increasing size to control the inter-cell space. It is thus possible to obtain a gain curve of the I_{sc} in function of the inter-cell distance. Obviously, this experimental method is specific to the parameters of the module used: type of backsheet or white EVA, absorption in the front optical layers of the module, presence or not of an anti-reflection on the glass, type of texturing of the cell. This behaviour is highly dependent on the angular reflectance of the backsheet [65], [66]. It implies that the cell located at the border of the module with backsheet or white encapsulant will benefit more from current boost, thanks to the module border around 15 mm [67].

The type of curve obtained is shown in Figure 27. The two examples correspond to different optical stack configurations. Uncertainties were calculated from measurements of 4 similar modules per configuration. The first configuration corresponds to the use of a glass without anti-reflection on the front face, of a transparent encapsulant based on polyolefin on the front and rear face, and of a backsheet. The maximum gain obtained at an inter-cell distance of 10 mm is 4 %. A better configuration is the use of an anti-reflective glass on the front face, with a transparent EVA on the front face, a white EVA diffusing on the back face and a backsheet. The gain is 5 % at 10mm.

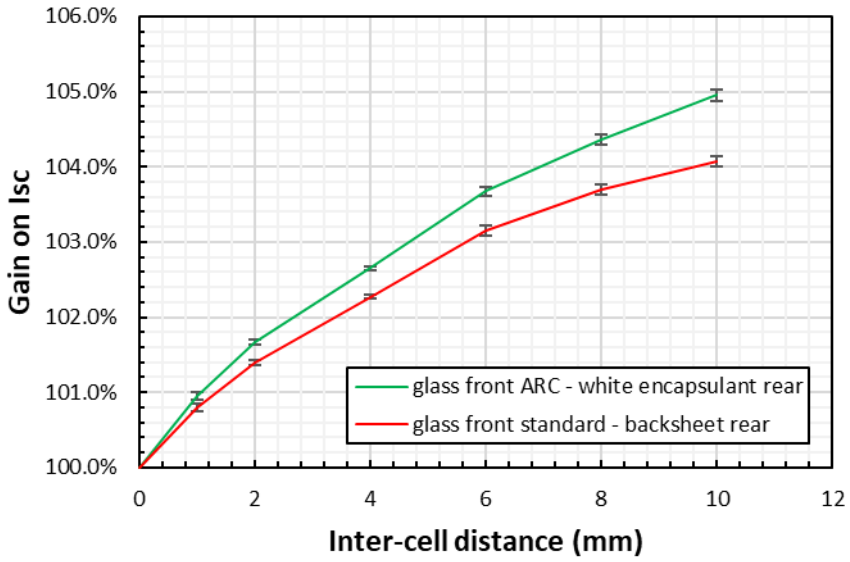

Figure 27: Gain on the I_{sc} as a function of the inter-cell distance for two optical stack configurations.

The experimental curves are then fitted by an exponential model, whose two main parameters - the maximum gain at an infinite distance and the characteristic distance where we obtain 68 % of the gain - are entered into the model.

$$\frac{\Delta I_{sc}}{I_{sc}}(d_{cell}) = G_{max}\left(1 - \exp\left(\frac{d_{cell}}{d_{carac}}\right)\right) \qquad \text{II.1}$$

To take into account the reflection of the light which passes through the cell - and which can therefore also be redirected towards the rear face of the cell - a reflectance value of the backsheet at normal incidence must also be entered.

In our reference case, we will not use a glass / backsheet module, but a glass / glass module. The previously mentioned entries will therefore not be used. On the other hand, this will be the case in chapter 3 on the effects of the integration of cut-cells in a module. Indeed, the inter-cell spaces increases with the number of cells.

II.A.2 Detailed calculation steps of the CTMod model to obtain the performance of the module

All the cells constituting the module are considered to be identical. The model is therefore based on the calculation of the performance of an equivalent cell.

II.A.2.a *Cell, metallization and interconnection: optical and resistive computations*

First, the surface parameters of the equivalent circuit model (J_{01}, J_{02}, r_{sh}) are transformed into absolute parameters (I_{01}, I_{02}, R_{sh}) by multiplying or dividing by the area of the wafer A_{wafer}: $I_{01} = J_{01}\, A_{wafer}$, $I_{02} = J_{02}\, A_{wafer}$ and $R_{sh} = r_{sh} / A_{wafer}$.

Modification of the inputs parameters due to a cutting step

The input parameters mentioned in the previous part are given for a cell of precise size. To simulate the effect of integrating cells cut into a module, two choices are possible. (i) Enter all the parameters of this cell and deactivate the modelling of the cutting step or (ii) enter the parameters of the uncut cell and activate the modelling of the cutting step.

If the second choice is made, the modelling of the cutting step involves several changes of the parameters of the initial cell. The number of sub-cells $N_{subcell}$ generated by cutting is calculated as the function of the number of cutting step in x ($N_{cut,x}$) and y direction ($N_{cut,y}$):

$$N_{subcell} = (N_{cut,x} + 1)(N_{cut,y} + 1) \quad \text{II.2}$$

The total length $L_{edge,tot}$ of cut edge is then calculated as a function of the length of the wafer in x ($L_{wafer,x}$) and y direction ($L_{wafer,y}$):

$$L_{edge,tot} = 2(N_{cut,x}\, L_{wafer,x} + N_{cut,y}\, L_{wafer,y}) \quad \text{II.3}$$

The factor two comes from the fact that one considers that one edge is open for the two sub-cells which were obtained by a cut. The additional recombination current $I_{02,edge}$ generated by the cutting step is calculated as a function of the linear losses $I_{02,edge,L}$ and the total length of cut edge:

$$I_{02,edge} = I_{02,edge,L} * L_{edge,tot} \quad \text{II.4}$$

The percentage loss on the photo-generated $dI_{ph,edge}$ current caused by the cutting step is calculated as a function of its linear value $dI_{ph,edge,L}$ and the length of the edge:

$$dI_{ph,edge} = dI_{ph,edge,L} * L_{edge,tot} \quad \text{II.5}$$

The absolute values of the parameters of the equivalent circuit are then corrected to correspond to those of a sub-cell:

$$I_{01,new} = I_{01,old}/N_{subcell} \quad \text{II.6}$$
$$I_{02,new} = (I_{02,old} + I_{02,edge})/N_{subcell} \quad \text{II.7}$$
$$R_{sh,new} = R_{sh,old} * N_{subcell} \quad \text{II.8}$$

The geometrical parameters of the wafer are modified accordingly to:

$$A_{wafer,new} = A_{wafer,old}/N_{subcell} \quad \text{II.9}$$
$$L_{wafer,x,new} = L_{wafer,x,old}/(N_{cut,y} + 1) \quad \text{II.10}$$
$$L_{wafer,y,new} = L_{wafer,y,old}/(N_{cut,x} + 1) \quad \text{II.11}$$

The number of cell by string $N_{cell,string}$ and the number of string N_{string} are also modified, to obtain a module where all sub-cells are connected in series, like a standard architecture:

$$N_{cell,string,new} = N_{cell,string,old}\,(N_{cut,x} + 1) \quad \text{II.12}$$

$$N_{string,new} = N_{string,old}(N_{cut,y} + 1) \quad \text{II.13}$$

In the case of a shingle architecture modelling, a difference exist in the orientation of the finger compared to the string:

$$N_{cell,string,new} = N_{cell,string,old}\ (N_{cut,y} + 1) \quad \text{II.14}$$

$$N_{string,new} = N_{string,old}(N_{cut,x} + 1) \quad \text{II.15}$$

Finally the number of cell in the module is computed:

$$N_{cell} = N_{string} * N_{cell,string} \quad \text{II.16}$$

Computing series resistance contribution of silicon bulk, amorphous layers and ITO

The resistance calculations of the internal layers of the cell: bulk in silicon, interfaces of amorphous layers and ITO were developed during Leo Basset's thesis: "Contact Electrodes for Heterojunction Silicon Solar Cells: Evaluation and Optimization of the Electron Contact" [68]. All the details of the calculations are available in the manuscript.

The resistivity of the n-doped silicon bulk is expressed as function of doping N_D, injection at MPP Δp_{mpp}, hole and electron mobility (μ_p and μ_n) and elementary charge q:

$$\rho_{cSi} = \frac{1}{q(N_D + \Delta p_{MPP})\mu_n + \Delta p_{MPP}\ \mu_p} \quad \text{II.17}$$

The contribution to the series resistance is thus computed from resistivity, thickness and area of the wafer:

$$R_{s,cSi} = \rho_{cSi} *\ h_{wafer}/A_{wafer} \quad \text{II.18}$$

The sheet resistance of the silicon is also defined, as:

$$R_{sh,wafer} = \rho_{cSi}/h_{wafer} \quad \text{II.19}$$

The series resistance contribution of the amorphous front and rear layers are computed:

$$R_{s,aSi,front} = r_{s,aSi,front}/A_{wafer} \quad \text{II.20}$$

$$R_{s,aSi,rear} = r_{s,aSi,rear}/A_{wafer} \quad \text{II.21}$$

The contribution of front ITO to the series resistance is obtained by computing the equivalent sheet resistance of the ITO on top of the silicon bulk:

$$\mathrm{R_{sh,eqITO,front}} = \frac{\mathrm{R_{sh,wafer}} * \mathrm{R_{sh,ITO,front}}}{\left(\mathrm{R_{sh,wafer}} + \mathrm{R_{sh,ITO,front}}\right)} \quad \text{II.22}$$

This equivalent sheet resistance comes from the lateral transport of charge carriers, possible in ITO but also in bulk silicon. The series resistance of front ITO is computed from the ITO equivalent sheet resistance, the front pitch of the finger p_{front} and wafer area:

$$R_{s,ITO,front} = \left(\frac{1}{12}\right) R_{sh,eqITO,front} * \frac{p_{front}^2}{A_{wafer}} \quad \text{II.23}$$

Parallel transport between ITO and silicon bulk is not possible on the rear side, due to the presence of the pn-junction. Consequently, the contribution of the ITO on the rear face to the series resistance is simply:

$$R_{s,ITO,rear} = \left(\frac{1}{12}\right) R_{sh,ITO,rear} * \frac{p_{rear}^2}{A_{wafer}} \quad \text{II.24}$$

Calculation for metallization: geometry, contact and line resistance, cell shading

The calculations are similar for the front face and for the rear face. The number of finger n_f is computed with the length of the wafer in Y dimension and the pitch p:

$$n_f = \text{round}\left(\frac{L_{wafer,y}}{p}\right) - 1 \quad \text{II.25}$$

The grid edge g_e – the distance between the finger and the edge of the cell – is given by the difference between the grid size and the wafer size:

$$g_e = \frac{\left(L_{wafer,y} - (n_f - 1)p\right)}{2} \quad \text{II.26}$$

The lengths of the metallization grid in the x and y direction ($L_{grid,x}$ and $L_{grid,y}$) are therefore:

$$L_{grid,x} = L_{wafer,x} - 2\,g_e \quad \text{II.27}$$
$$L_{grid,y} = L_{wafer,y} - 2\,g_e \quad \text{II.28}$$

The length of the fingers needs to be determined next. For the case of an H-pattern interconnection, where the cell interconnection ribbons are perpendicular to the finger, the length of a finger L_f will be called half the distance between two ribbons. This is the resistive useful length. We start by determining the distance between the ribbons d_{ir}, which is expressed as a function of the size of $L_{wafer,x}$ and the number of cell interconnection ribbon used, n_r:

$$d_{ir} = \frac{L_{wafer,x}}{n_r} \quad \text{II.29}$$

The length of finger L_f is reduced by the width of the busbar w_{bb}:

$$L_f = \frac{d_{ir} - w_{bb}}{2} \quad \text{II.30}$$

In the case where the cell interconnection is of the shingle type, the length of the fingers is simply expressed in function of the shingle overlap $d_{shingle}$:

$$L_f = L_{grid,x} - d_{shingle} \quad \text{II.31}$$

To calculate the contact resistance of the fingers, we first need the transfer length $L_{f,t}$. This length is expressed as a function of the metal / ITO contact resistance $r_{s,c}$ and the ITO sheet resistance:

$$L_{f,t} = \sqrt{r_{s,c}/R_{sh,ITO}} \quad \text{II.32}$$

The series resistance is expressed with the transfer length, the finger pitch p, the physical width of a finger $w_{f,phy}$ and the area of the wafer:

$$R_{s,c} = r_{s,c} \frac{p * \coth\left(\frac{w_{f,phy}}{2L_{f,t}}\right)}{2\, L_{f,t}\, A_{wafer}} \quad \text{II.33}$$

The contribution of the fingers to the series resistance can then be determined. We start by calculating the section of the fingers S_f from their physical width and their aspect ratio AR_f:

$$S_f = AR_f * w_{f,phy}^2 \quad \text{II.34}$$

The line resistance $R_{s,f,L}$ can be computed next:

$$R_{s,f,L} = \rho_f / S_f \quad \text{II.35}$$

From the line resistance, the length of a finger, the number of finger and the number of ribbon number, we compute the contribution of the finger to the series resistances:

$$R_{s,f} = \frac{1}{3} R_{s,f,L} * \frac{L_f}{2n_f * n_r} \quad \text{II.36}$$

The factor $2n_fn_r$ represents the number of elementary finger length put in parallel connection which participates in the conduction of the current. In the case of shingle architecture, we use a value of n_r=1/2.

The next step is to determine the shading of the cell caused by the fingers. First, the optical width of a $w_{f,opt}$ finger is defined as its physical width multiplied by its effective optical width:

$$w_{f,opt} = w_{f,eff} * w_{f,phy} \quad \text{II.37}$$

The total length of finger $L_{f,tot}$ present on the cell is then calculated, according to the length of a finger L_f and the number of elementary lengths on the cell:

$$L_{f,tot} = L_f * 2n_f * n_r \quad \text{II.38}$$

And the effective shading Sha_f of the fingers on the cell:

$$Sha_f = w_{f,opt} * L_{f,tot} / A_{wafer} \quad \text{II.39}$$

The share of metallized cell $M_{part,f}$ is also determined:

$$M_{part,f} = w_{f,phy} * L_{f,tot} / A_{wafer} \quad \text{II.40}$$

Finally, the total volume $V_{f,tot}$, and total mass $M_{f,tot}$ of metallisation paste is computed from the density of the finger paste d_f:

$$V_{f,tot} = S_f * L_{f,tot} \quad \text{II.41}$$
$$M_{f,tot} = V_{f,tot} * m_f \quad \text{II.42}$$

To conclude with the modelling of the impact of the metallization, we calculate the total volume and the total mass of the busbars, if there are any. The total mass of metallization paste M_p is obtained by the sum of the mass of the fingers and the busbars:

$$M_p = M_{f,tot} + M_{bb,tot} \quad \text{II.43}$$

All of these calculations are done for the front and back sides. The total mass of paste deposited is then calculated.

Calculation of the geometry, resistance and shading of cell interconnection

Two main cases are to be considered in this part. A shingle type interconnection, or an interconnection with ribbons.

In the case of a shingle interconnection, the cells are connected by an electrically conductive paste (ECA). The length of ECA $L_{ECA,shingle}$ is given by the length of the size of the metallization grid and the factor of filling for ECA $Fill_{Eca,shingle}$:

$$L_{ECA,shingle} = L_{grid,y} * Fill_{ECA,shingle} \quad \text{II.44}$$

From the input parameters of the width of the deposited ECA $W_{ECA,shingle}$, we compute the total area of ECA deposited on cell $A_{ECA,shingle}$:

$$A_{ECA,shingle} = L_{ECA,shingle} * W_{ECA,shingle} \quad \text{II.45}$$

The ECA contribution to the series resistance is given then by the ECA thickness $h_{ECA,shingle}$:

$$R_{s,ECA,shingle} = \rho_{ECA,shingle} * h_{ECA,shingle} / A_{ECA,shingle} \quad \text{II.46}$$

We can then determine the volume $V_{ECA,shingle}$ and mass of ECA $M_{ECA,shingle}$ for shingle architecture from the density of the ECA $d_{ECA,shingle}$:

$$V_{ECA,shingle} = A_{ECA,shingle} * h_{ECA,shingle} \quad \text{II.47}$$

$$M_{ECA,shingle} = V_{ECA,shingle} * d_{ECA,shingle} \quad \text{II.48}$$

Finally, the shading of the cell overlapping is needed for module performance computation. Even if in shingle case, a cell is shaded by another cell, it is a loss from a power point of view, because all the active area cannot take part in the photo-generation. The shingle shading $Sha_{shingle}$ is defined as a function of shingle overlap $W_{shingle}$, number of cell by string, the length of the wafer in y direction and the area of the wafer.

$$Sha_{shingle} = \frac{(N_{cell,string} - 1)W_{shingle} * L_{wafer,y}}{N_{cell,string} * A_{wafer}} \quad \text{II.49}$$

In the case of ribbon interconnection, more calculations are needed. They will be given for the example of the front panel, but are equally valid for the rear panel of the module. The first step is to compute the total section of the ribbons. It is the sum of the section of the copper core and of the coating. For the copper core, if it is a circular shaped ribbon of diameter D_r and coating of thickness $h_{coating}$:

$$S_{r,core} = \pi \left(\frac{D_r}{2}\right)^2 \quad \text{II.50}$$

$$S_{r,coating} = \pi \left(\frac{D_r + 2h_{coating}}{2}\right)^2 - S_{r,core} \quad \text{II.51}$$

If it is a rectangular shaped ribbon with a width W_r and thickness h_r:

$$S_{r,core} = W_r * h_r \quad \text{II.52}$$

$$S_{r,coating} = (W_r + 2h_{coating})(h_r + 2h_{coating}) - S_{r,core} \quad \text{II.53}$$

The optical width of the ribbons is obtained by the projection of the ribbon to the cell, multiplied by their effective optical width $W_{r,eff}$. In the case of circular ribbon and in the case of rectangular ribbon:

$$W_{r,opt} = W_{r,eff} \left(D_r + 2h_{coating}\right) \quad \text{II.54}$$

$$W_{r,opt} = W_{r,eff} \left(W_r + 2h_{coating}\right) \quad \text{II.55}$$

If the busbar under the ribbon is wider than the ribbon itself, it participates in the shading of the cell. The optical width of the ribbon is then corrected by the excess of busbar. The width of the busbar is W_{bb} and if it is discontinued or padded, a fill factor $Fill_{bb}$ is applied:

$$W_{r,opt,new} = W_{r,opt} + \max\left(0, W_{bb} - \left(W_r + 2h_{coating}\right)\right) Fill_{bb} \quad \text{II.56}$$

The cell interconnection ribbons can be soldered on the metallization, or glued with electro-conductive adhesive (ECA). In the case of soldering, we neglect the contact resistance

between metals. In the case of gluing, the ECA geometry and resistance has to be determined. The ECA length is computed, as a function of the length of the busbar L_{bb} and the fill factor of the ECA $Fill_{ECA}$ if the deposit is discontinuous:

$$L_{ECA} = L_{bb} * Fill_{ECA} \quad \text{II.57}$$

The area of ECA A_{ECA} is determined from the width of ECA deposited W_{ECA}:

$$A_{ECA} = W_{ECA} * L_{ECA} \quad \text{II.58}$$

The contribution of ECA to series resistance is also added, using its thickness h_{ECA}:

$$R_{s,ECA} = \rho_{ECA} * \ h_{ECA}/A_{ECA} \quad \text{II.59}$$

The total volume V_{ECA} and total mass M_{ECA} of the ECA used is then computed from thickness, total area and density d_{ECA}:

$$V_{ECA} = A_{ECA} * h_{ECA} \quad \text{II.60}$$
$$M_{ECA} = V_{ECA} * d_{ECA} \quad \text{II.61}$$

The current flowing in cell-interconnections ribbons is not constant: it is zero from one edge of the cell and all the currents coming from fingers adds to reach a maximum on the other edge of the cell. This discrete behaviour is taken into account by summing the resistive effect of each additional current contribution from fingers. A correcting factor k_r is thus computed from the number of finger n_f:

$$k_r = \frac{n_f(2n_f - 1)}{6(n_f - 1)^2} \quad \text{II.62}$$

In the case of an infinite number of finger, this correcting factor is equal to 1/3, which is the correcting factor for a linear current increase in a conductor. At the other extremum, if there are only two fingers (one at the beginning of the ribbons, the other at the end), this correcting factor is unity: this is the case of a constant current in the ribbon.

The line resistance of the ribbons $R_{s,r,L}$ is computed from the parallel line resistance of the coating and the core of the ribbon, the resistivity of the ribbon's core $\rho_{r,core}$ and of the ribbon's coating $\rho_{r,coating}$:

$$R_{s,r,L} = \frac{\rho_{r,core} * \rho_{r,coat}}{S_{r,coating} * \rho_{r,core} + \ S_{r,core} * \ \rho_{r,coat}} \quad \text{II.63}$$

The length of a ribbon onto the cell is considered to be the same as the one of the metallization grid in y direction plus the grid edge:

$$L_r = \ \mathrm{L_{grid,y}} + g_e \quad \text{II.64}$$

There is two contributions on series resistance coming from cell-interconnection ribbons. The contribution of the ribbons on the cell $R_{s,r,c}$, where the current increase by step for each finger, as a function of ribbon length, line resistance and correcting factor:

$$R_{s,r,c} = k_r * R_{s,f,L} * L_r \quad \text{II.65}$$

And a second contribution from the part of the ribbon in the inter-cell area, where the current is constant and at its maximum value, as a function of the inter-cell distance d_{ic}, corrected by the fact that there is a number of inter-cell space in a string equal to the number of cell plus one (we consider the distance between the cell and the inter-string ribbons as equal). Because all the value mentioned here are computed for front and rear side, and to avoid counting it twice, it is also divided by two:

$$R_{s,r,ic} = R_{s,f,L} * d_{ic}\ (N_{cell,string} + 1)/(2N_{cell,string}) \quad \text{II.66}$$

The total contribution of cell interconnection ribbons to series resistance $R_{s,r}$ is the sum:

$$R_{s,r} = R_{s,r,c} + R_{s,r,ic} \quad \text{II.67}$$

The optical area of the ribbons $A_{r,opt}$ and the shading ratio Sha_r shading area of the ribbon is computed from the total optic width $W_{r,opt}$ and the length L_r of the ribbons:

$$A_{r,opt} = W_{r,opt} * L_r \quad \text{II.68}$$
$$Sha_r = A_{r,opt}\ /A_{wafer} \quad \text{II.69}$$

Finally, as every elements of the metallization / interconnection, we compute the volume and the mass of the core and coating, from the total length of ribbons $L_{r,tot}$, and the density of the ribbon's core $d_{r,core}$ and coating $d_{r,coating}$:

$$L_{r,tot} = L_r + d_{ic}\ (N_{cell,string} + 1)/(2N_{cell,string}) \quad \text{II.70}$$
$$V_{r,core} = L_{r,tot} * S_{r,core} \quad \text{II.71}$$
$$V_{r,coating} = L_{r,tot} * S_{r,coating} \quad \text{II.72}$$
$$M_{r,core} = V_{r,core} * d_{r,core} \quad \text{II.73}$$
$$M_{r,coating} = V_{r,coating} * d_{r,coating} \quad \text{II.74}$$

Calculation of the geometry and resistance of string interconnection

The string interconnection ribbons have a rectangular cross-section. They are also made of two parts: a core (often in copper) and a coating. The computation done are very similar with the cell interconnection ribbon. We start computing the section of the core $S_{rIS,core}$ and of the coating $S_{rIS,coating}$, from the width W_{rIS} and thickness h_{rIS} of the core and thickness of the coating $h_{rIS,coating}$:

$$S_{rIS,core} = W_{rIS} * h_{rIS} \quad \text{II.75}$$
$$S_{rIS,coating} = \left(W_{rIS} + 2h_{rIS,coating}\right)\left(h_{rIS} + 2h_{rIS,coating}\right) - S_{rIS,core} \quad \text{II.76}$$

In the case of a cell interconnection with ribbon, the current flowing in string-interconnections ribbons follow the same behaviour as the one in the cell-interconnections ribbons, with the difference that the role of the fingers is replaced by that of the cell interconnection ribbons. There is also a correcting factor k_{rIS} for the series resistance:

$$k_{rIS} = \frac{n_r(2n_r - 1)}{6(n_r - 1)^2} \quad \text{II.77}$$

The length of the ribbons L_{rIS} is linked to the length of the grid in the x-direction, from which we subtracted the distance between a cell interconnection ribbon and the edge of the cell:

$$L_{rIS} = \mathrm{L_{grid,x}} \left(1 - \frac{1}{2n_r}\right) \quad \text{II.78}$$

In the case of a shingle interconnection, the value of the correcting factor depends on the number of finger on the cell:

$$k_{rIS} = \frac{n_f(2n_f - 1)}{6(n_f - 1)^2} \quad \text{II.79}$$

The length of the ribbons in shingle architecture is the total length of the grid:

$$L_{rIS} = L_{grid,x} \quad \text{II.80}$$

The line resistance of the ribbons $R_{s,rIS,L}$ is computed from the parallel line resistance of the coating and the core of the ribbon, the resistivity of the ribbon's core $\rho_{rIS,core}$ and of the ribbon's coating $\rho_{rIS,coating}$:

$$R_{s,rIS,L} = \frac{\rho_{rIS,core} * \rho_{rIS,coat}}{S_{rIS,coating} * \rho_{rIS,core} + S_{rIS,core} * \rho_{ISr,coat}} \quad \text{II.81}$$

There are two contributions on series resistance coming from string-interconnection ribbons. The contribution of the ribbons linked to the width of the cell $R_{s,rIS,c}$ is weighted by the number of string on the number of cell, to compute the contribution for a single equivalent cell:

$$R_{s,rIS,c} = k_{rIS} * R_{s,rIS,L} * L_{rIS} * 2N_{string}/N_{cell} \quad \text{II.82}$$

And a second contribution $R_{s,rIS,s}$ from the part of the ribbon in the inter-string area, computed as a function of the distance between string d_{is}:

$$R_{s,rIS,s} = R_{s,rIS,L} * d_{is} \left(N_{string} - 1\right)/N_{cell} \quad \text{II.83}$$

It is possible to account for the additional contribution of the output ribbons, which connects the cell strings to the junction boxes. It is computed as a function of the length of the output ribbons L_{rO}:

$$R_{s,rIS,O} = R_{s,rIS,L} * L_{rO} \quad \text{II.84}$$

The total volume and the total mass of the inter-string ribbons for the core and the coating is computed from the total length of the ribbons $L_{rIS,tot}$, from the density of the core $d_{rIS,core}$ and the coating $d_{rIS,coating}$:

$$L_{rIS,tot} = \frac{2L_{rIS} * N_{string} + d_{is}(N_{string} - 1) + L_{rO}}{N_{cell}} \quad \text{II.85}$$

$$V_{rIS,core} = L_{rIS,tot} * S_{rIS,core} \quad \text{II.86}$$

$$V_{rIS,coating} = L_{rIS,tot} * S_{rIS,coating} \quad \text{II.87}$$

$$M_{rIS,core} = V_{rIS,core} * d_{rIS,core} \quad \text{II.88}$$

$$M_{rIS,coating} = V_{rIS,coating} * d_{rIS,coating} \quad \text{II.89}$$

II.A.2.b *Calculation of the impact of the optical stack on the photo-generated current of the module*

The method is mainly based on the work of Haedrich *et al.* and Hanifi *et al*. [64], [69] The front and rear irradiance $S_{irr,f}$ and $S_{irr,r}$ are computed from the number of of sun n_{sun}, the front and rear multiplier m_f and m_r and the base irradiance S_{irr}:

$$S_{irr,f} = m_f * n_{sun} * S_{irr} \quad \text{II.90}$$

$$S_{irr,r} = m_r * n_{sun} * S_{irr} \quad \text{II.91}$$

We present the computation for the front side only. All the values presented here are dependent upon the wavelength. We omit this dependency for sack of simplicity.

The reflectance of the front cover $R_{cov,f}$ is computed from the effective refractive index of the layer $n_{cov,f}$ (taken into account a possible anti-reflecting coating). The volume transmittance of the layer $T_{cov,f}$ is computed from absorption coefficient $\alpha_{cov,f}$ and thickness of the layer $h_{cov,f}$:

$$R_{cov,f} = \left(\frac{n_{cov,f} - 1}{n_{cov,f} + 1}\right)^2 \quad \text{II.92}$$

$$T_{cov,f} = \exp(-\alpha_{cov,f} * h_{cov,f}) \quad \text{II.93}$$

The reflectance at the interface between glass and encapsulants in neglected. The internal transmittance of the encapsulants $T_{encap,f}$ and the backscattering $B_{encap,f}$ in the case of diffusive encapsulants are computed with a model fully detailed in the chapter IV. This two values are computed from the absorption coefficient $\alpha_{cov,f}$, the scattering coefficient $s_{cov,f}$, the asymmetry factor $g_{cov,f}$ and the encapsulants thickness $h_{cov,f}$.

If a foil is present in the module, the internal transmittance $T_{foil,f}$ is computed from the absorption coefficient $\alpha_{foil,f}$ and the thickness of the foil $h_{foil,f}$:

$$T_{foil,f} = \exp\left(-\alpha_{foil,f} * h_{foil,f}\right) \quad \text{II.94}$$

Next, the shading of the cell by fingers and cell-interconnection is applied, as pre-computed in the previous part.

The non-metallized cell reflectance $R_{cell,nometal}$ and transmission $T_{cell,nometal}$ are input of the model, precomputed by the Sunsolve ray-tracer as described in the inputs parameters of the model (Part II.A). But the transmission of the cell in module as to be corrected for two reasons.

First, the metallization at the rear side behaves as a reflector because the interface of ITO/ silver of the finger is reflective at 95 %, almost constant with wavelength. The transmission is thus corrected from 95 % of the metallization part of the rear side):

$$T_{cell,metal} = T_{cell,nometal}(1 - 0.95\ M_{part,r}) \quad \text{II.95}$$

Second, if there is a good reflector on the rear side of the module (for example, a backsheet or a white encapsulant) with reflectance $R_{cov,r}$, the rear optical stack can reflect a part of the transmitted irradiance back to the cell. The cell transmittance T_{cell} is thus computed from the transmittance of the metallized cell in module $T_{cell,metal}$, from the rear foil transmittance (if any), the non-metallized cell reflectance and the shading of the finger and of the ribbons at the rear side

$$T_{cell} = T_{cell,metal}(1 - T_{foil,r}^2 R_{cov,r}\left(1 - R_{cell,nometal}\right)\left(1 - Sha_{f,r} - Sha_{r,r}\right) \quad \text{II.96}$$

The absorption A_{cell} of the cell is by definition:

$$A_{cell} = 1 - R_{cell} - T_{cell} \quad \text{II.97}$$

The irradiance absorbed S_{cell} by the cell is thus computed from the previous factors:

$$S_{cell} = S_{irr}\left(1 - R_{cov,f}\right)T_{cov,f} * T_{encap,f} * T_{foil,f}\left(1 - Sha_{f,f} - Sha_{r,f}\right)A_{cell} \quad \text{II.98}$$

Hanifi *et al.* applied a factor that take into account the part of the irradiance below the bandgap that cannot take part in the photo-generation. We do not use this factor because it is included in the cell transmission factor as computed in equation II.97.

The part of the absorbed irradiance with a photon energy higher than the one of the bandgap will be thermalized. The equivalent irradiance after thermalization S_{therm} is expressed as a function of the wavelength of the gap λ_{gap}:

$$S_{therm} = S_{cell} * \frac{\lambda}{\lambda_{gap}} \quad \text{II.99}$$

For an electron-hole pair generated, only the fraction corresponding to the internal quantum efficiency contributes to the the photo-generated current I_{ph}. The irradiance after the collection efficiency S_{coll}:

$$S_{coll} = S_{therm} * IQE \quad \text{II.100}$$

The photo-generated current from the front irradiance $I_{ph,f}$ is then computed by numerical integration of the irradiance on the whole spectral range as a function of the area of the wafer and the *q/hc* factor:

$$I_{ph,f} = A_{wafer} * \frac{q}{h\,c} \int_{\lambda_{min}}^{\lambda_{max}} S_{coll}\ \lambda\ d\lambda \quad \text{II.101}$$

where λ_{min} = 300 nm and λ_{max} = 2450 nm. The numerical integration is performed with a trapezoidal method. The same approach is used to compute the current generated by the rear irradiance $I_{ph,r}$.

Once the photo-generated currents have been calculated, we apply to them empirical gains and losses coming from two sources: (i) the gains by reflections on the inter-cell spaces if there is a backsheet type reflector or white encapsulants, (ii) losses generated by a possible cutting step.

The gain from the inter-cell space is recalled, as a function of the inter-cell space d_{ic} the characteristic distance d_{carac} (input parameter) and the maximum relative gain in I_{sc}, G_{max}:

$$\frac{\Delta I_{sc}}{I_{sc}}(d) = G_{max}\left(1 - \exp\left(\frac{d}{d_{carac}}\right)\right) \quad \text{II.102}$$

But this equation is valid only for a certain cell geometry. For example, using the same module architecture (backsheet, glass, inter-cell…) but with half-cell instead of full-cell give greater value of relative I_{sc} gains. This is due to a greater ratio of perimeter over area in half cell than if full cell. The equation need to be corrected to take into account the perimeter over area ratio $p_{A,ref}$ of the cell used for extraction of d_{carac} and G_{max}

$$G_{Isc}(d) = \frac{\Delta I_{sc}}{I_{sc}}(d) = G_{max}\left(1 - \exp\left(\frac{d}{d_{carac}}\right)\right)\frac{p_A}{p_{A,ref}} \quad \text{II.103}$$

Where p_A is the perimeter to area ratio of the current cell under study.

The amount of light reflected back to the cell by the backsheet is thus higher when d increase. This distance d is different on each side of the cell. For a central cell of the module, the length d is the inter-cell distance for top and bottom edge. It is the inter-string distance for left and right edges. If the cell has an edge near the margin of the module, it has also to be taken onto account.

Considering the inter-cell I_{sc} gain, the distance d_{ic} is used in the exponential term. The perimeter to area ratio is expressed as a function of the length of the wafer in x direction and

the area of the wafer. The number of cell by string is used to compute the number of relevant edges (for a one cell equivalent):

$$G_{Isc}(ic) = G_{max}\left(1 - \exp\left(\frac{d_{ic}}{d_{carac}}\right)\right)\frac{L_{wafer,x}/A_{wafer}}{p_{A,ref}}\frac{2\left(N_{cell,string} - 1\right)}{N_{cell,string}} \quad \text{II.104}$$

Considering the inter-string I_{sc} gain, the distance d_{is} is used in the exponential term. The perimeter to area ratio is expressed as a function of the length of the wafer in y direction and the area of the wafer. The number of string is used to compute the number of relevant edges (for a one cell equivalent):

$$G_{Isc}(is) = G_{max}\left(1 - \exp\left(\frac{d_{is}}{d_{carac}}\right)\right)\frac{L_{wafer,y}/A_{wafer}}{p_{A,ref}}\frac{2\left(N_{string} - 1\right)}{N_{string}} \quad \text{II.105}$$

Considering the margin I_{sc} gain, the length of each margin is used in the exponential term: top margin $d_{m,top}$, bottom $d_{m,bott}$, left margin $d_{m,left}$ and right margin $d_{m,right}$:

$$G_{Isc}(m_{top}) = G_{max}\left(1 - \exp\left(\frac{d_{m,top}}{d_{carac}}\right)\right)\frac{L_{wafer,x}/A_{wafer}}{p_{A,ref}}\frac{1}{N_{cell,string}} \quad \text{II.106}$$

$$G_{Isc}(m_{bott}) = G_{max}\left(1 - \exp\left(\frac{d_{m,bott}}{d_{carac}}\right)\right)\frac{L_{wafer,x}/A_{wafer}}{p_{A,ref}}\frac{1}{N_{cell,string}} \quad \text{II.107}$$

$$G_{Isc}(m_{left}) = G_{max}\left(1 - \exp\left(\frac{d_{m,left}}{d_{carac}}\right)\right)\frac{L_{wafer,y}/A_{wafer}}{p_{A,ref}}\frac{1}{N_{string}} \quad \text{II.108}$$

$$G_{Isc}(m_{right}) = G_{max}\left(1 - \exp\left(\frac{d_{m,right}}{d_{carac}}\right)\right)\frac{L_{wafer,y}/A_{wafer}}{p_{A,ref}}\frac{1}{N_{string}} \quad \text{II.109}$$

In the case of a shingle architecture, the inter-cell I_{sc} gain is zero, but other remains. The photo-generated current is then corrected by the aforementioned gains: $I_{ph,f}$

$$I_{ph,f} = I_{ph,f}\left(1 + G_{Isc}(is) + G_{Isc}(ic) + G_{Isc}(m_{top}) + G_{Isc}(m_{bott}) + G_{Isc}(m_{left}) + G_{Isc}(m_{right})\right) \quad \text{II.110}$$

Finally, the last correction on the photo-generated current correspond to the losses caused by a potential cutting step. It is computed from the percentage of I_{ph} loss as computed at the begin of the part II.A.2.

$$I_{ph,f} = I_{ph,f}\left(1 + dI_{ph,edge}\right) \quad \text{II.111}$$

The total photo-generated current Iph is the sum of the front and the rear contribution:

$$I_{ph} = I_{ph,f} + I_{ph,r} \quad \text{II.112}$$

II.A.2.c *Solve Equivalent circuit for cell and module*

All the terms of the 2-diodes model are now computed: I_{ph}, I_{01}, n_1, I_{02}, n_2, R_s and R_{sh}

$$I(V) = I_{ph} - I_{01}\left(\exp\left(\frac{V + IR_s}{n_1 V_{th}}\right) - 1\right) - I_{02}\left(\exp\left(\frac{V + IR_s}{n_2 V_{th}}\right) - 1\right) - \frac{V + IR_s}{R_{sh}} \quad \text{II.113}$$

This equation is not analytically solvable for any value of voltage V. Numerical methods are needed. It is necessary to put the equation in the form of F(I) = 0:

$$F(I,V) = 0 = I_{ph} - I_{01}\left(\exp\left(\frac{V + IR_s}{n_1 V_{th}}\right) - 1\right) - I_{02}\left(\exp\left(\frac{V + IR_s}{n_2 V_{th}}\right) - 1\right) - \frac{V + IR_s}{R_{sh}} - I \quad \text{II.114}$$

In this form, numerical method to solve non-linear equation can be used. In our case, we use "fzero" function of Matlab©. All the IV curve can be computed by varying the value of voltage V. We start at V=0 V – at the short-circuit current – where a good first estimate of the current I(V=0) is $I_0 = I_{ph}$. The voltage V in then increased by a dV value, and the corresponding value of I(V+dV) is computed with initial estimate I_0 equal to the value of I(V). In this way, the current value of I is used as first estimate for the next value of I, using the propriety of continuity of the function F(I).

The four main IV parameter I_{sc}, V_{oc}, I_{mpp}, V_{mpp} can be computed without computing the complete IV curve. Special cases of equation II.114 are used. Considering I_{sc}, the value of V is fixed to 0, we obtain:

$$F(I_{sc}) = 0 = I_{ph} - I_{01}\left(\exp\left(\frac{I_{sc}R_s}{n_1 V_{th}}\right) - 1\right) - I_{02}\left(\exp\left(\frac{I_{sc}R_s}{n_2 V_{th}}\right) - 1\right) - \frac{V + I_{sc}R_s}{R_{sh}} - I_{sc} \quad \text{II.115}$$

Considering V_{oc}, the current I is by definition 0:

$$F(V_{oc}) = 0 = I_{ph} - I_{01}\left(\exp\left(\frac{V_{oc}}{n_1 V_{th}}\right) - 1\right) - I_{02}\left(\exp\left(\frac{V_{oc}}{n_2 V_{th}}\right) - 1\right) - \frac{V_{oc}}{R_{sh}} \quad \text{II.116}$$

Considering the I_{mpp} and V_{mpp}, the equation is the same as the number: II.113

But a second equation is needed to compute both unknowns. The definition of the maximum power point is used: it is the point where the derivative of the power is zero.

$$\frac{dP}{dV} = \frac{d(IV)}{dV} = V\frac{dI}{dV} + I = 0 \quad \text{II.117}$$

$$\frac{dI}{dV} = \frac{G(I,V)}{1 + G(I,V)R_s} \quad \text{II.118}$$

with

$$G(I,V) = \frac{I_{01}}{n_1 V_{th}} \exp\left(\frac{V + IR_s}{n_1\, V_{th}}\right) + \frac{I_{02}}{n_2 V_{th}} \exp\left(\frac{V + IR_s}{n_2\, V_{th}}\right) + \frac{1}{R_{sh}} \quad \text{II.119}$$

From the previous equations, we can compute the value of the IV parameters I_{mpp} and V_{mpp} , from the system with two equations and two unknowns:

$$\begin{cases} F(I_{mpp}, V_{mpp}) = 0 \\ V_{mpp}\, \dfrac{G(I_{mpp}, V_{mpp})}{1 + G(I_{mpp}, V_{mpp}) R_s} + I_{mpp} = 0 \end{cases} \quad \text{II.120}$$

All this four IV parameters I_{sc}, V_{oc}, I_{mpp}, V_{mpp} are computed for a one-cell equivalent module, as mentioned previously. Some changes are required to have the values for the complete module. The module is considered to have N_{serie} cells in series and $N_{parallel}$ cells in parallel, where the product of both value must equal the total number of cells:

$$N_{serie} * N_{parallel} = N_{cell} = N_{cell,string} * N_{string} \quad \text{II.121}$$

We define the four IV parameters of the total module:

$$I_{sc,module} = N_{parallel} *\ I_{sc} \quad \text{II.122}$$
$$V_{oc,module} = N_{serie} *\ V_{oc} \quad \text{II.123}$$
$$I_{mpp,module} = N_{parallel} * I_{mpp} \quad \text{II.124}$$
$$V_{mpp,module} = N_{serie} * V_{mpp} \quad \text{II.125}$$

From the IV parameters I_{sc}, V_{oc}, I_{mpp}, V_{mpp}, we compute the maximum power P_{mpp} and the fill factor FF:

$$P_{mpp,module} =\ I_{mpp,module} * V_{mpp,module} \quad \text{II.126}$$
$$FF_{module} =\ P_{mpp,module}\ /(\ I_{sc,module}\ V_{oc,module}) \quad \text{II.127}$$

The length of the module is x-direction is expressed as a function of the length of the wafer, the number of string, the inter-string distance and the left and right margins:

$$L_{x,module} = L_{wafer,x}\ * N_{string} + d_{is}(N_{string} - 1) + d_{m,left} + d_{m,right} \quad \text{II.128}$$

The length of the module is y-direction is expressed as a function of the length of the wafer, the number of cell by string, the inter-cell distance and the top and bottom margins:

$$L_{y,module} = L_{wafer,y} * N_{cell,string} + d_{ic}(N_{cell,string} - 1) + d_{m,top} + d_{m,bott} \quad \text{II.129}$$

In the case of shingle architecture, the inter-cell distance is replaced by the shingle overlap:

$$L_{y,module} = L_{wafer,y} *\ N_{cell,string} - W_{shingle}(N_{cell,string} - 1) + d_{m,top} + d_{m,bott} \quad \text{II.130}$$

The area of the module A_{module} is thus:

$$A_{module} = L_{x,module} * L_{y,module} \quad \text{II.131}$$

From the total area of the module, the front and rear irradiance $S_{irr,f}$ and $S_{irr,r}$ we compute the efficiency of the module:

$$\eta_{module} = \frac{P_{mpp,module}}{(S_{irr,f} + S_{irr,r})A_{module}} \quad \text{II.132}$$

This marks the end of the module performance calculation. The next step is to compute all the losses occurring in the energy conversion.

II.A.3 Calculation of a standardized classification of the absolute module losses

All the power contained in the incident energy is the light cannot be converted into electrical power. A large part is lost by heating or by reflection of the irradiance out of the module. These absolute losses are computed from all the values previously computed for module performance. This approach of "absolute losses" allow to easily compare different module architecture, eventually at different manufacturing steps.

II.A.3.a *Calculation of all losses for a given architecture: analysis and consistency of results*

The total incident power $P_{incident}$ is computed from the front and rear spectral irradiance:

$$P_{incident} = P_{incident,f} + P_{incident,r} = A_{module} \int_{\lambda_{min}}^{\lambda_{max}} (S_{irr,f} + S_{irr,r}) d\lambda \quad \text{II.133}$$

Losses by inactive areas of the module

The inactive areas of the module are divided into nine zones: the top, bottom, left and right margin, the corner of the modules (intersection of margins), the inter-cell area, the inter-string area, the inter cell/string (intersection of inter-cell area and inter-string area), and the pseudo square areas if the cell is not squared. The calculations are the same for front and rear irradiance, only the front side is reported. We note the power density of incident light:

$$p_{irr,f} = \int_{\lambda_{min}}^{\lambda_{max}} S_{irr,f}\, d\lambda \quad \text{II.134}$$

The power losses from the top, bottom, left and right margins $P_{m,top}$, $P_{m,bott}$, $P_{m,left}$, $P_{m,right}$ are computed as:

$$P_{m,top} = d_{m,top}\, (L_{x,module} - d_{m,left} - d_{m,right})\, p_{irr,f} \quad \text{II.135}$$

$$P_{m,bott} = d_{m,bott}\,(L_{x,module} - d_{m,left} - d_{m,right})\,p_{irr,f} \quad \text{II.136}$$
$$P_{m,right} = d_{m,right}\,(L_{y,module} - d_{m,top} - d_{m,bott})\,p_{irr,f} \quad \text{II.137}$$
$$P_{m,left} = d_{m,left}\,(L_{y,module} - d_{m,top} - d_{m,bott})\,p_{irr,f} \quad \text{II.138}$$

The power losses from the corner of the module $P_{m,corner}$ are expressed as:

$$P_{m,corner} = \left(d_{m,top}(d_{m,right} + d_{m,left}) + d_{m,bott}(d_{m,right} + d_{m,left})\right) p_{irr,f} \quad \text{II.139}$$

The power losses from the inter-cell P_{ic} and inter-string P_{is} areas are computed by:

$$P_{ic} = d_{ic} * L_{wafer,x} * N_{string}\,(N_{cell,string} - 1)\,p_{irr,f} \quad \text{II.140}$$
$$P_{is} = d_{is} * L_{wafer,y} * N_{cell,string}\,(N_{string} - 1)\,p_{irr,f} \quad \text{II.141}$$

And the power losses from the intersection of the inter-cell and inter-string areas $P_{ic,is}$ are computed as:

$$P_{ic,is} = d_{ic} * d_{is}\,(N_{string} - 1)\,(N_{cell,string} - 1)\,p_{irr,f} \quad \text{II.142}$$

Finally, the power losses caused by the pseudo square areas P_{PSQ} are given by:

$$P_{PSQ} = \left(L_{wafer,x} * L_{wafer,y} - A_{wafer}\right) N_{cell} * p_{irr,f} \quad \text{II.143}$$

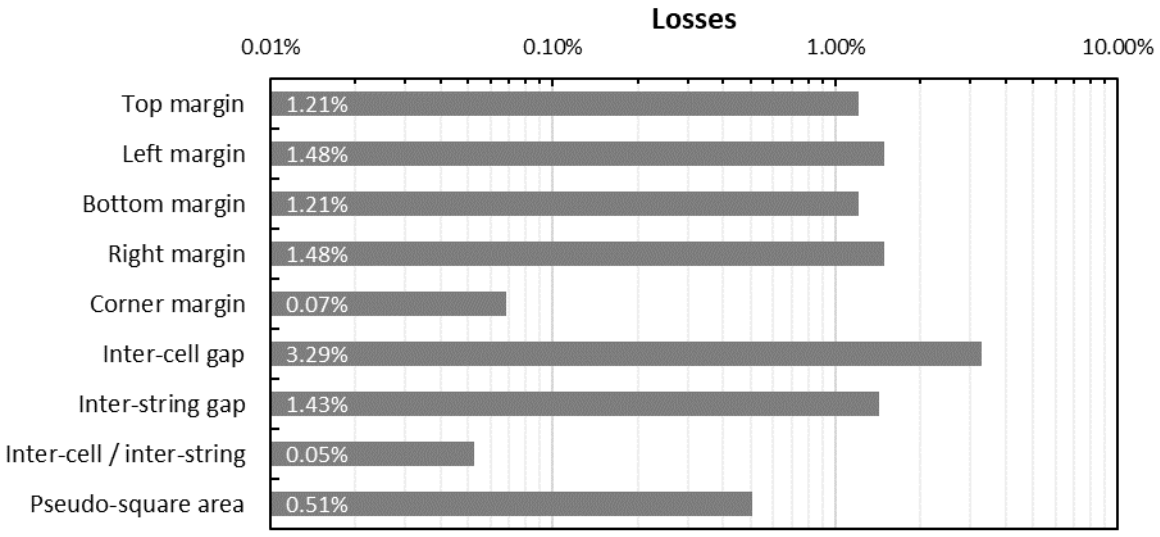

Figure 28: Summary of the power lost by inactive areas of the module for the reference. The main losses are, in order of importance: inter-cell gap, left and right margins, inter-string gap, top and bottom margins and PSQ areas.

All the losses due to inactive area are corrected from the gain in I_{sc} from these areas due to reflective back cover (backsheet or white encapsulants). The power lost by inactive areas is thus corrected with the power corresponding to the gain in I_{sc} of this part k of the module (k

can be margins, inter-cell areas…). The voltage of the energy gap is used to perform the correction: $hc/q\lambda_{gap}$.

$$P_{k,new} = P_{k,old} - N_{cell} * I_{ph,f} * G_{Isc}(k) \frac{hc}{q\lambda_{gap}} \quad \text{II.144}$$

An example of the losses caused by inactive areas for the reference is given in the Figure 28. Together, these losses represent 10.7 % of the incident power.

Losses by optical stack of the module

The power losses due to optical stack can be of three different kinds: reflection by the module, transmission by the module, absorption by the layers. The choice is made to consider that incident light is lost by the optical stack only for the part of light hitting the active areas. If not, it is counted in the aforementioned losses by inactive areas. As a consequence, what we call "glass absorption" is not the total power absorbed by the glass, but only the part above active areas. We consider more relevant to have a direct value of losses caused by inactive areas: this allow comparison of different module architecture in a more practical way. However, this choice has also drawbacks: the value of power absorbed cannot be used as volume heat source for example.

The power lost by the reflectance of the front cover of the module is the integral of the incident spectral irradiance multiplied by the spectral reflectance of the air/cover interface, and multiplied by the total active area of the module:

$$P_{R,cov,f} = N_{cell}\, A_{wafer} \int_{\lambda_{min}}^{\lambda_{max}} S_{irr,f} R_{cov,f}\, d\lambda \quad \text{II.145}$$

The power lost by the front cover absorption is the integral of the incident spectral irradiance multiplied by the spectral transmittance of the air/cover interface and the spectral volume absorbance of the cover:

$$P_{A,cov,f} = N_{cell}\, A_{wafer} \int_{\lambda_{min}}^{\lambda_{max}} S_{irr,f}\left(1 - R_{cov,f}\right)\left(1 - T_{cov,f}\right) d\lambda \quad \text{II.146}$$

The power lost by backscattering in the encapsulant is the integral of the part of the incident spectral irradiance that has been transmitted by the air/cover interface and by the cover volume, multiplied by the spectral backscattering of the encapsulant:

$$P_{B,encap,f} = N_{cell}\, A_{wafer} \int_{\lambda_{min}}^{\lambda_{max}} S_{irr,f}\left(1 - R_{cov,f}\right) T_{cov,f}\, B_{encap,f}\, d\lambda \quad \text{II.147}$$

The power lost by encapsulant absorption is the integral of the part of incident spectral irradiance that has been transmitted by the air/cover interface and by the cover volume, multiplied by the amount of light that has not been backscattered nor transmitted by the encapsulant volume:

$$P_{A,encap,f} = N_{cell}\, A_{wafer} \int_{\lambda_{min}}^{\lambda_{max}} S_{irr,f}\left(1 - R_{cov,f}\right) T_{cov,f}\, \left(1 - B_{encap,f} - T_{encap,f}\right) d\lambda \quad \text{II.148}$$

The power lost by the foil absorption (if any) is the integral of the part of incident spectral irradiance that has been transmitted by the air/cover interface, by the cover volume and by the encapsulant volume, multiplied by the amount of light not transmitted (absorbed) by the foil:

$$P_{A,foil,f} = N_{cell}\, A_{wafer} \int_{\lambda_{min}}^{\lambda_{max}} S_{irr,f}\left(1 - R_{cov,f}\right) T_{cov,f} T_{encap,f} (1 - T_{foil,f}) d\lambda \quad \text{II.149}$$

The power lost by the finger shading is expressed as a function of the light transmitted to the finger, i.e. transmitted by the air/cover interface, by the cover volume, by the encapsulant volume and by the foil volume. It is multiplied by the total finger optical area of the module and thus include the “effective shading”:

$$P_{Sha,f,f} = N_{cell}\, A_{f,opt} \int_{\lambda_{min}}^{\lambda_{max}} S_{irr,f}\left(1 - R_{cov,f}\right) T_{cov,f} T_{encap,f} T_{foil,f}\, d\lambda \quad \text{II.150}$$

The power lost by the ribbons shading is expressed as a function of the light transmitted to the finger, i.e. transmitted by the air/cover interface, by the cover volume, by the encapsulant volume and by the foil volume. It is multiplied by the total ribbons optical area of the module and thus include the “effective shading”:

$$P_{Sha,r,f} = N_{cell}\, A_{r,opt} \int_{\lambda_{min}}^{\lambda_{max}} S_{irr,f}\left(1 - R_{cov,f}\right) T_{cov,f} T_{encap,f} T_{foil,f}\, d\lambda \quad \text{II.151}$$

The power lost by the cell reflectance expressed as a function of the light transmitted to the cell, i.e. transmitted by the air/cover interface, by the cover volume, by the encapsulant volume and by the foil volume, and then multiplied by the spectral reflectance of the cell. It is multiplied by the total active area which has been removed from ribbons and finger optical area of the module:

$$P_{R,cell,f} = N_{cell}\, \left(A_{wafer} - A_{r,opt}\right) \int_{\lambda_{min}}^{\lambda_{max}} S_{irr,f}\, \left(1 - R_{cov,f}\right) T_{cov,f}\, T_{encap,f}\, T_{foil,f}\, R_{cell,f}\, d\lambda \quad \text{II.152}$$

And the power lost by cell transmission is:

$$P_{T,cell,f} = N_{cell}\left(A_{wafer} - A_{r,opt}\right)\int_{\lambda_{min}}^{\lambda_{max}} S_{irr,f}(1 - R_{cov,f})T_{cov,f}T_{encap,f}T_{foil,f}\,T_{cell,f}\,d\lambda \quad \text{II.153}$$

Finally, the part of the spectrum absorbed by the cell is:

$$S_{A,cell,f} = S_{irr,f}(1 - R_{cov,f})T_{cov,f}T_{encap,f}T_{foil,f}\left(1 - R_{cell,f} - T_{cell,f}\right) \quad \text{II.154}$$

An example of the losses caused by optical stack for the reference case is given in the Figure 29. The losses in order of importance are: cell reflection, cell transmission, cover reflection (no anti-reflective coating is used), encapsulant absorption, cell reflection, finger effective shading, cover absorption and ribbon effective shading. As mentioned previously, the cell reflection losses are overestimated because of the secondary reflection of the diffuse flux at the glass-air interface, not taken into account in our model. No foil nor backscattering encapsulant is used here. Together, these losses represent 17.1 % of the incident power.

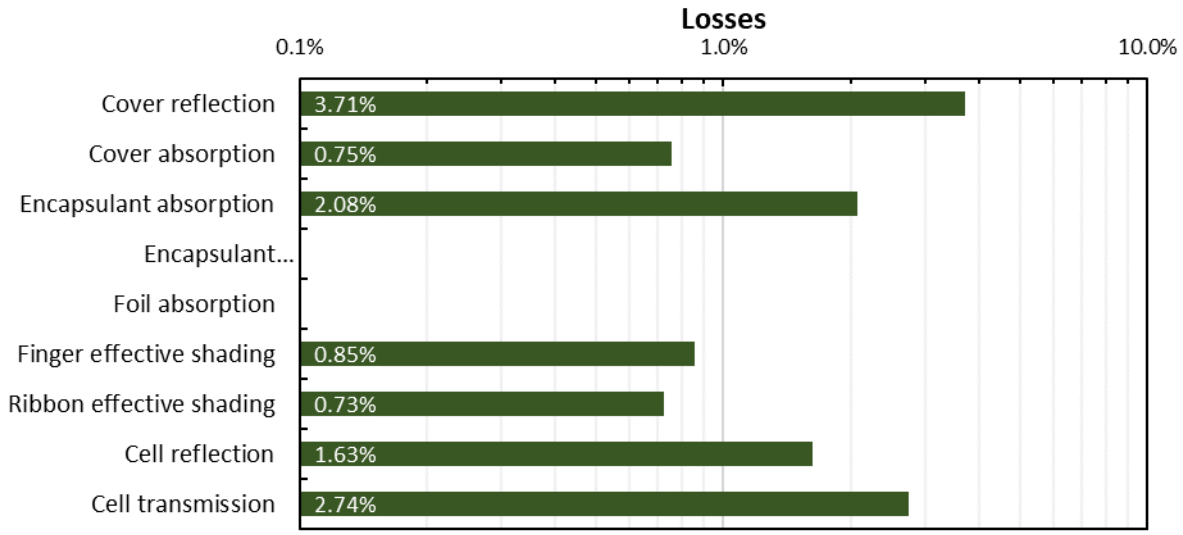

Figure 29: Summary of the power lost by optical stack of the module for the reference case described in II.A.1.

Semiconductor losses

The main losses in a photovoltaic module are located within the cell and are referred as "semiconductor losses". An approach similar to Hanifi *et al.* is used [70], their approach is presented in details in part II.B.1. Power losses from semiconductor physics effects are: the losses from below band gap photons, losses by thermalization of electron-hole pairs with higher energy than the band gap, the losses by not optimal collection efficiency, the losses by thermodynamic effects (angle mismatch, Carnot losses).

The first loss is caused by photons with energy lower than the effective band gap. The band gap of the crystalline silicon is 1.14 eV at 298.15K, corresponding to a wavelength gap

λ_{gap} of 1088 nm [71]. In principle, for wavelength greater than λ_{gap}, c-Si does not absorb photons. But non-zero IQE can be observed even for wavelength greater than λ_{gap} [72], as the absorption coefficient of c-Si is non zero even for $\lambda > \lambda_{gap}$ [73]. Silicon has indeed a non-zero density of states for energy higher than band gap and it is thus possible to have a non-negligible IQE, in particular for thick wafer. Silicon has an indirect band-gap, and electron-hole pair generation can be phonon-assisted with thermal budget of 25 meV. High doping level can also decrease the band gap energy in a process called band-gap narrowing [74]. For all these reasons, silicon band-gap is not well-defined and the IQE of the cell can be non-zero for $\lambda > \lambda_{gap}$. We use a numerical rather than a physical definition for the band gap, i.e. the wavelength at which the WQI of the cell is less than 0.01 %.

The loss caused by below band gap photons are expressed as the integral of the part of incident irradiance that has been absorbed by the cell:

$$P_{belowBG} = N_{cell}\left(A_{wafer} - A_{r,opt}\right)\int_{\lambda_{gap}}^{\lambda_{max}} S_{irr,f}\left(1-R_{cov,f}\right)T_{cov,f}T_{encap,f}T_{foil,f}\left(1 - R_{cell,f} - T_{cell,f}\right)d\lambda \quad \text{II.155}$$

The second loss is caused by thermalization of the electron hole pair. All the energy higher than the band gap energy is lost by thermalization with a ratio of λ / λ_{gap}:

$$P_{therma} = N_{cell}\left(A_{wafer} - A_{r,opt}\right)\int_{\lambda_{min}}^{\lambda_{gap}} S_{irr,f}\left(1-R_{cov,f}\right)T_{cov,f}T_{encap,f}T_{foil,f}\left(1 - R_{cell,f} - T_{cell,f}\right)(1-\lambda/\lambda_{gap})\,d\lambda \quad \text{II.156}$$

The losses from the not optimal collection efficiency (1-IQE) is:

$$P_{IQE} = N_{cell}\left(A_{wafer} - A_{r,opt}\right)\int_{\lambda_{min}}^{\lambda_{gap}} S_{irr,f}\left(1-R_{cov,f}\right)T_{cov,f}T_{encap,f}T_{foil,f}\left(1 - R_{cell,f} - T_{cell,f}\right)\frac{\lambda}{\lambda_{gap}}(1-IQE)\;d\lambda \quad \text{II.157}$$

We call thermodynamic losses the difference of the power collected by the cell and the power generated by the I_{ph} current generator at the maximum power point MPP point. It include a fraction of the common thermodynamic losses called “Radiative recombination”, “Angle mismatch” and “Carnot losses” [75], [76]. It is computed as:

$$P_{thermo} = I_{ph}(V_{gap} - (V_{mpp} + I_{mpp}R_s)) \quad \text{II.158}$$

The power lost by the diminishing value of I_{ph} due to a cutting step is:

$$P_{Iph,cut} = N_{cell}\, I_{ph,f}\, dI_{ph,edge}\left(V_{mpp} + I_{mpp}R_s\right) \quad \text{II.159}$$

We add the power dissipated by each elements of the two-diode equivalent model, excepting the resistive components. The power dissipated by the first diode at the maximum power point (MPP) is:

$$P_{D1} = N_{cell}\, I_{01} \left(\exp\left(\frac{V_{mpp} + I_{mpp} R_s}{n_1\, V_{th}} \right) - 1 \right) \left(V_{mpp} + I_{mpp} R_s \right) \qquad \text{II.160}$$

The power dissipated by the second diode at MPP is divided in two components: the one from the base value of I02, the other from the additional I02 edge coming from a possible cutting step.

$$P_{D2,base} = N_{cell} \left(I_{02} - I_{02,edge} \right) \left(\exp\left(\frac{V_{mpp} + I_{mpp} R_s}{n_2\, V_{th}} \right) - 1 \right) \left(V_{mpp} + I_{mpp} R_s \right) \qquad \text{II.161}$$

$$P_{D2,cut} = N_{cell}\, I_{02,edge} \left(\exp\left(\frac{V_{mpp} + I_{mpp} R_s}{n_2\, V_{th}} \right) - 1 \right) \left(V_{mpp} + I_{mpp} R_s \right) \qquad \text{II.162}$$

The power lost by the shunt of the cells is given by:

$$P_{Sh} = N_{cell} \left(V_{mpp} + I_{mpp} R_s \right)^2 / R_{sh} \qquad \text{II.163}$$

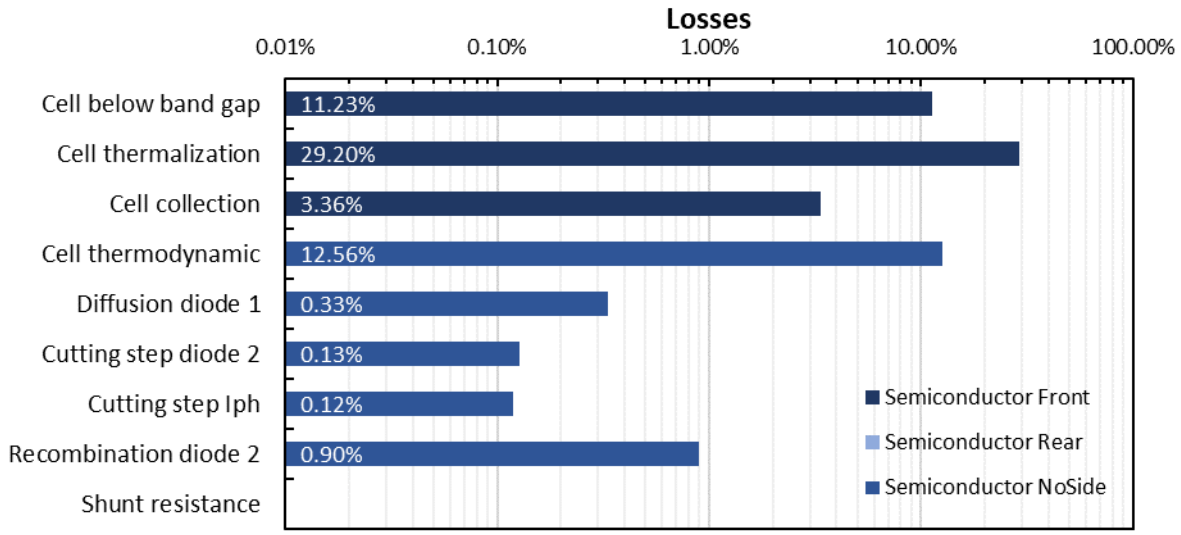

Figure 30: Summary of the power lost by "semiconductor effects"

An example of the losses caused by optical stack for the reference case is given in the Figure 30. The main loss item is thermalization, followed by thermodynamic losses in the cell, then losses due to photons with an energy smaller than the bandgap, and non-optimal collection efficiency. The main loss item is thermalization, followed by thermodynamic losses in the cell, then losses due to photons with an energy smaller than the bandgap, and non-optimal collection efficiency. Then come the recombination losses produced by diode 2, then

diode 1 and finally the cutting losses. Together, these losses represent 52.9 % of the incident power.

Joule losses

All the Joule resistive losses are then computed from the values of individual series resistance contribution of each elements, multiplied by the square of the I_{mpp}:

$$P_{R_s} = N_{cell}\, R_s\, I_{mpp}^2 \qquad \text{II.164}$$

An example of the losses caused by optical stack for the reference case is given in the Figure 31. The five most important losses are in order: the resistance of the amorphous layers, the resistance of the ITO, the resistance of the fingers, the inter-cell ribbons, and the contact resistance of the fingers on the ITO. Summing all resistive losses, we arrive at 0.92 % of the total incident power.

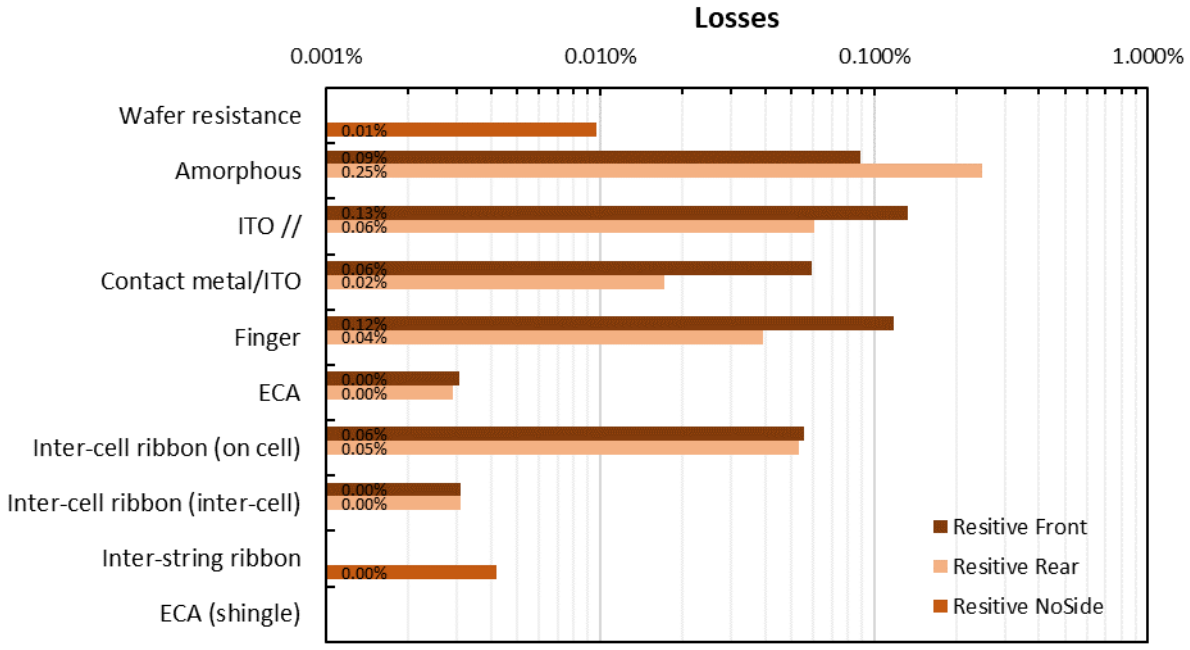

Figure 31: Summary of the power lost Joule resistive effect

At the end of the loss computation, a verification step is added: the incident power subtracted from the sum of all the power losses mentioned in this part must equal the module power computed in the module performance part.

We recall here that the losses calculated in this part are the absolute losses, i.e. the power lost taking into account the whole incident spectrum. Thus, the spectral behaviour of optical layers beyond the wavelength of the silicon energy gap has an influence on the losses generated by these layers. For example, the absorption in the encapsulant for wavelengths above 1200 nm influences the losses generated by this optical component, even if it will not make any difference on the photo-generated current.

As a summary, we propose Figure 32 which summarizes the main loss items in the reference module, expressed this time in terms of absolute power. At the end, we obtain an electrical power supplied by the module of 358 W, i.e. a module efficiency of 18.27 %.

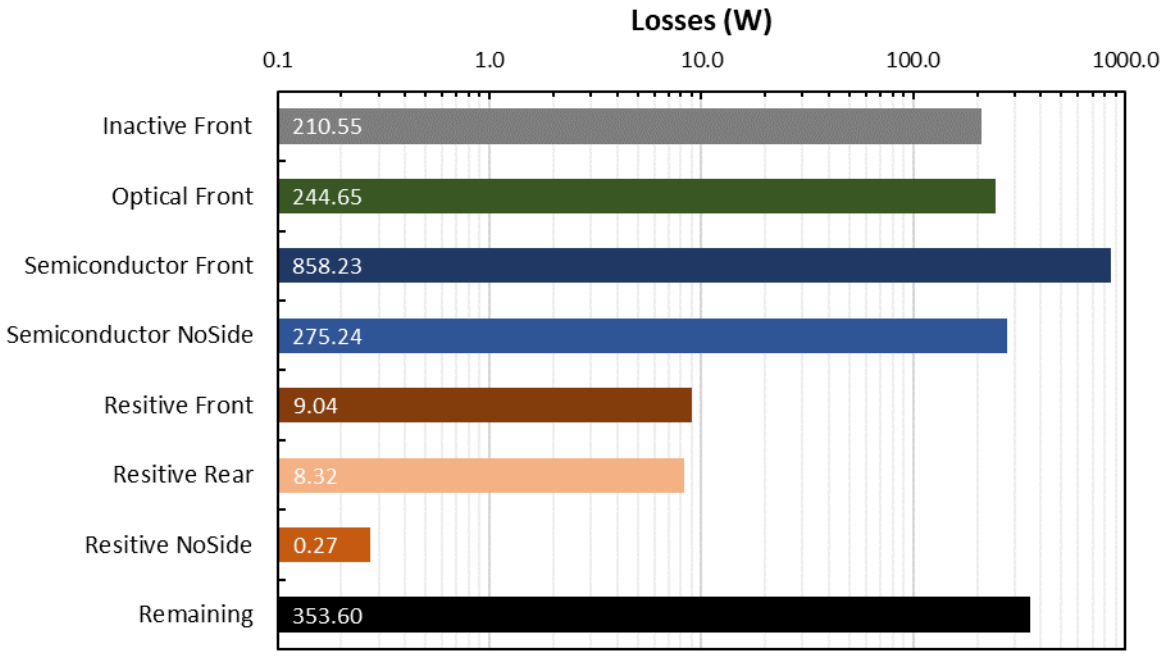

Figure 32: Summary of the power losses by main items, and the remaining power, i.e. the maximum electrical power available

II.A.3.b *Generalization of the CTM ratio for the analysis of a module and the comparison of various architecture*

From the work described in the previous section, we thus have at our disposal all the power losses, absolute and relative to the incident power, which take place in the device under study. This study was done above for one module. It is possible to do the same study for the cell alone, not encapsulated and without interconnection. By making the difference of the losses for each of the mentioned stations, we can thus analyse in details the influence of the module realization. We consider that the cell is in an IV measurement geometry where the current and voltage probes are positioned on the busbars.

We will perform the difference of the relative losses between case 1 (Module) and case 2 (cell). The difference in relative losses is preferable to the difference in absolute losses because the incident power on a 2 m² module is obviously not the same as the incident power on a 244.33 cm² cell.

The Figure 33 presents the differences of relative losses due to inactive areas between module and cell. In the case of cell, no inactive areas are considered. The difference is thus positive for every items, and equal the value of losses as measured in the module case. A

positive difference between module and cell means that it represents a loss for module compared to cell.

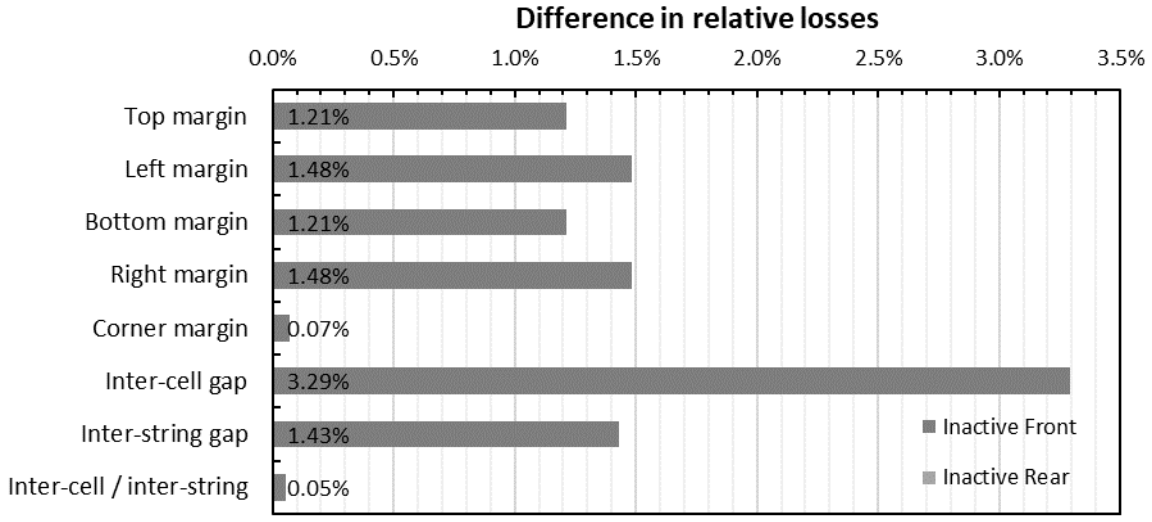

Figure 33: Summary of the difference in relative power losses between module and cell for the inactive areas items.

The Figure 34 presents the differences of relative losses due to optical stack between module and cell. The cover reflection, cover absorption, encapsulant absorption and ribbon shading are positive value: it is a loss from cell to module architecture. Conversely, the finger effective shading loss is 0.85 % in module and 2.15 % in cell: this represents a gain from cell to module of 1.3 %. Similarly, the refractive index of encapsulant being higher than the one of air, the difference in cell reflectance caused a gain of 1.4 % between cell and module. The losses by cell transmission are almost not affected by module production: 2.7 % in both case.

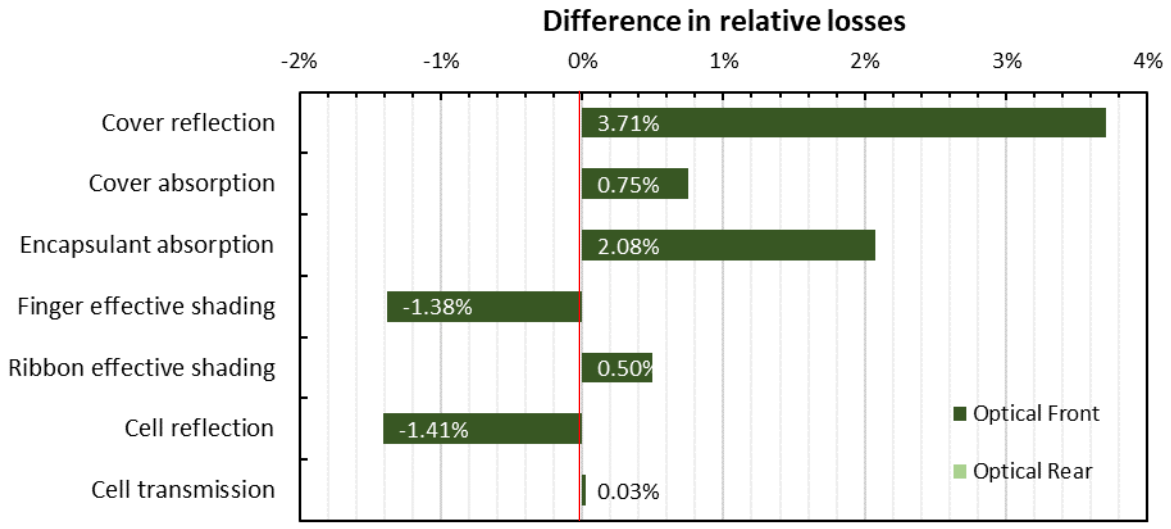

Figure 34: Summary of the difference in relative power losses between module and cell for the optical stack items.

The Figure 35 presents the differences of relative losses due to “semiconductor effects” between module and cell. In the case of the cell, a larger part of the incident power is lost by semiconductor effects, especially the below band gap, thermalization, cell collection efficiency and cell thermodynamic effects. Indeed, a part of the light that has not been absorbed nor reflected in module stack components can be lost during these steps. This results in a current at MPP of 8.12 A in module and 8.51 A in cell. Some other losses are due to the 2-diodes model components: diode 1, diode 2. Positive differences are caused by the cutting steps performed on the full cell to obtain half-cell in the reference module.

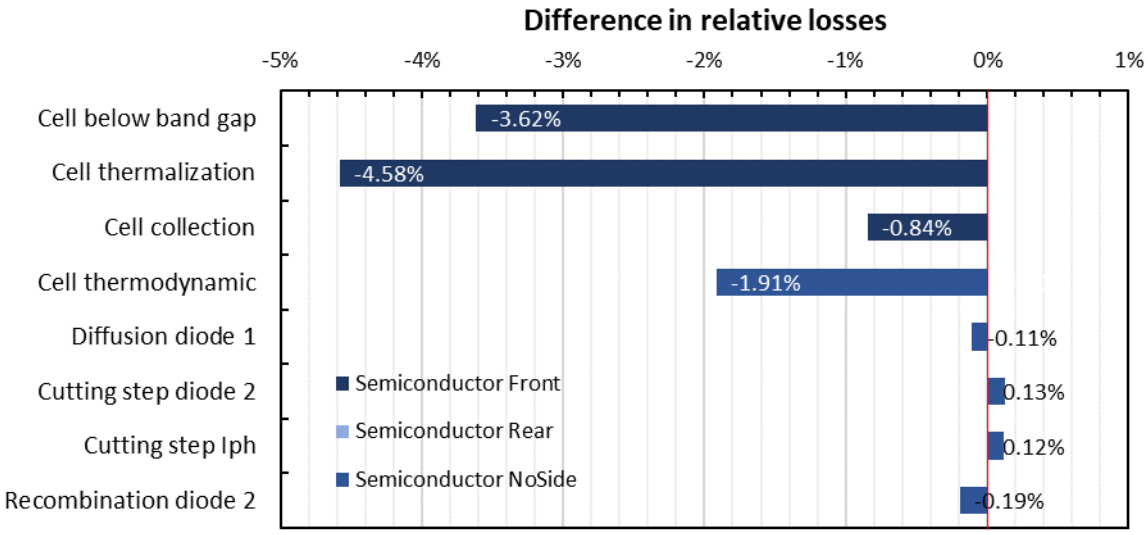

Figure 35: Summary of the difference in relative power losses between module and cell for the semiconductor items.

The Figure 36 presents the differences of relative losses due to Joule resistive effects between module and cell. The electro-conductive adhesive ECA, inter-cell and inter-string ribbons are components present in the module and not in the cell: the corresponding difference in relative losses is necessarily positive. The resistive parts of the cell are present both in module and cell case study. The difference is negative: it means it is a gain when going from cell to module. This is explained by the higher photo-generated current in cell. If the optical module stack cause losses on the I_{sc}, Joule effects in cell are reduced.

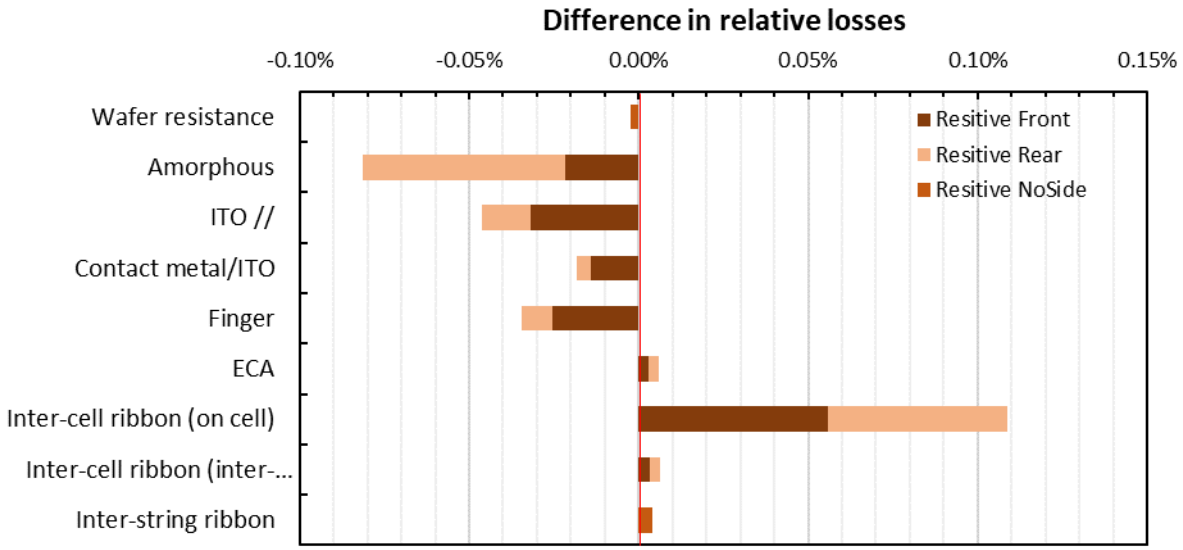

Figure 36: Summary of the difference in relative power losses between module and cell for Joule resistive items

As a conclusion, the Figure 37, represents the difference of relative losses between module and cell categorized by principal losses items, and the difference in remaining power. The inactive areas represent a difference of 10.18 % in relative losses to the advantage of the cell configuration, as do the 4.28 % difference from optical stack. The "semiconductor effects" cause a difference of 11.01 % to the advantage of the module configuration. The effect of Joule resistive losses in cell and in module compensates each other. The remaining available relative power difference is -3.40 % meaning the cell as an efficiency 3.4 % greater than the module. Of course, it corresponds perfectly to the computed value of module efficiency (18.04 %) and cell efficiency (21.44 %).

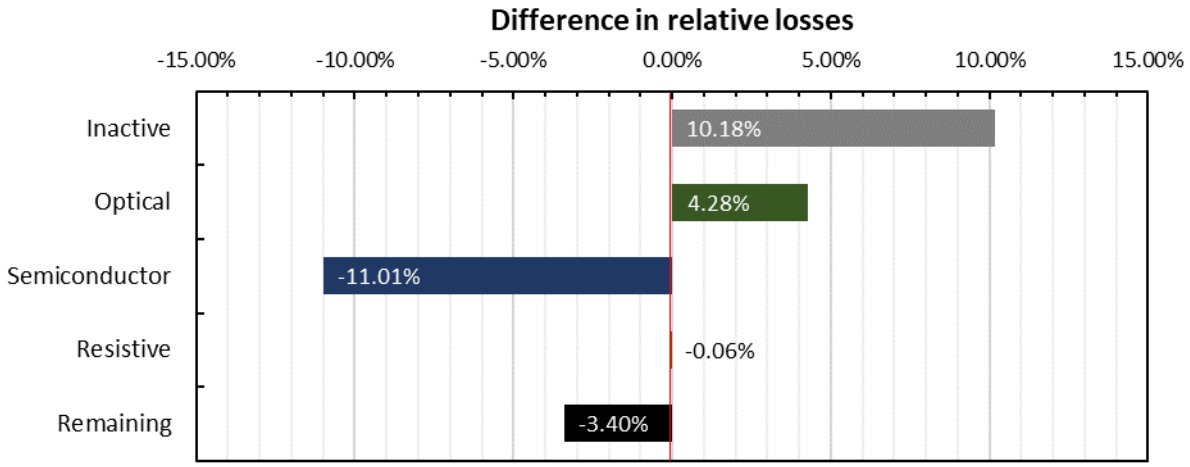

Figure 37: Summary of the difference in relative power losses between module and cell categorized by principal loses items. The difference in remaining power is also given.

With this calculation method, it is also possible to easily compare different module architectures. As an example, we propose to compare the reference module used until now, realized according to a glass / glass architecture, with a glass / backsheet module. This glass / backsheet module is similar to the reference module, except for the backsheet and the encapsulation on the back side of the module. This backsheet / encapsulant causes a gain of photo-generated current by reflection on inactive surfaces, as shown in Figure 38.

The inter-cell, inter-string and margins areas generate a gain of 1.35 % for the glass/encapsulant module. The losses by cell transmission are also decreased for this module compared to the reference case: the IR part of the spectrum is not totally lost when transmitted by the cell, because of the reflection of the backsheet / white encapsulant at the rear side of the cell, causing a gain of 2.19 %. This increase in irradiance absorbed by the cell produce semiconductor losses higher for the glass/backsheet module: 2.06 %. Finally, the higher I_{sc} in the glass/backsheet module generates higher Joule resistive losses. As a result, the glass/backsheet module has an efficiency 1.34 % higher than the reference glass/glass module: 19.38 % compared to 18.04 %.

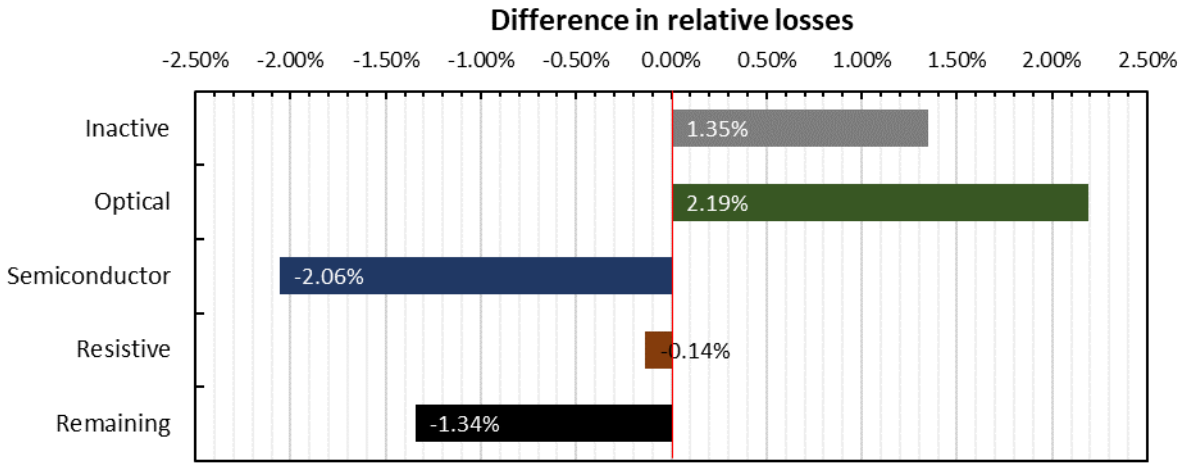

Figure 38: Summary of the difference in relative power losses between reference glass/glass module and glass/encapsulant module categorized by principal loses items.

Part II.B State-of-the art in module performance modelling and test of the CTMod simplified model

This part is a presentation of the main tools for PV module performance modelling and a comparison of CTMod with stat-of-the-art Sunsolve model.

II.B.1 Existing modelling tools of the PV module performance

There are many software packages available for the simulation of photovoltaic module performance. We will use the PVLighthouse nomenclature, which contains the following categories among others:

- Optics (sun position, solar spectrum calculation, cell optics and module optics)
- Electrical circuits (solar cells and modules)

Many programs are listed by PVLighthouse, which are mainly: software in executable form, online calculators, code to be executed, or spreadsheets. They can be free or paid for. If they are free, the code may be open-source, in which case, the software is called “open-source”. The software presented are based on scientific publications, described more or less completely.

Other programs are gathered in PVLighthouse for the analysis of experimental data (IV curves, electro-luminescence, photo-luminescence...), the analysis of production data on an industrial line. Software for system performance modelling is also available, as well as some cost analysis tools (cost model, learning curve, LCOE calculation...).

The first step for calculating the performance of a module is the study of optical phenomena.

II.B.1.a *Main approaches for PV module optical modelling*

Optics take place at several levels in the modelling of the performance of a photovoltaic device. The first is the modelling of the position of the sun position during the day, which was not considered during this PhD, limited to the case of a fixed illumination, type AM1.5g at normal incidence. However, there are several software capable of calculating the position of the sun: "Solar path calculator" [77], "SPosi" [78], "SMARTS: simple model for the atmospheric radiative transfer of sunshine" [33], [79], "Solar spectrum calculator" [80]. SMARTS and Solar spectrum calculator, with “SunCalculator” [81] can compute the incident spectrum on any position on earth.

But it is the module optics modelling programs that interest us the most. Three mains approaches exist to model optics in module:

- Ray-tracing modelling: the optics of the module is simulated by launching a large number of light rays onto the surface of the module at different wavelengths. Reflection and/or absorption are tracked for each ray. This method allows to process complex geometries in 3D, surface texture, geometrical optics and wave optics phenomena for thin films. This approach is time consuming, but by definition it includes all the optical couplings between the different elements of the module.

- Matrix formalism modelling: the optics of the module is simulated by multiplying the elementary transmission and reflection matrix for each of the layers of the module. These matrices depend on the wavelength but also on the angle of incidence of the rays. This method allows to treat essentially flat layers, thin or thick, with or without texture. It is faster in computation time than ray tracing, but is limited to 1D devices.

- Analytical modelling: this approach is the simplest of all, the main optical effects of reflection and absorption in the module are described by analytical equations. The optical coupling phenomena between the different elements are only taken into account afterwards by empirical corrective factors. It is therefore difficult to generalize without changing models.

Tracey from PVLighthouse

"Tracey" is a free open-source and downloadable spreadsheet that allows you to throw rays on three areas of a module simultaneously: the cell, the metallization, and the backsheet [82]. It has been developed by K. McIntosh from PVLightHouse, and the last update was in 2013. The surface of these three areas, and their reflectance (with a specularity factor to be chosen from 0 to 100 %) are filled in. These three areas can then be covered with a stack of thin layers / thick layers to simulate the ARC layers of the cell and the module layers (glass, encapsulant, ARC). These three areas (cell, metal, backsheet) are considered semi-infinite in thickness. It is possible to define the type of incident spectrum, in diffuse light or in direct light (with angle of incidence to be chosen). This program does not allow to model the front and the back of a module, and therefore does not allow to take into account the multiple reflections on the back of the cell / module. The results are presented as spectral or integrated losses, for the absorption and reflection of each element.

"Tracey" has been used in study of optical comparison of silicone and EVA as encapsulant of conventional silicon PV modules [83], under various spectra [84].

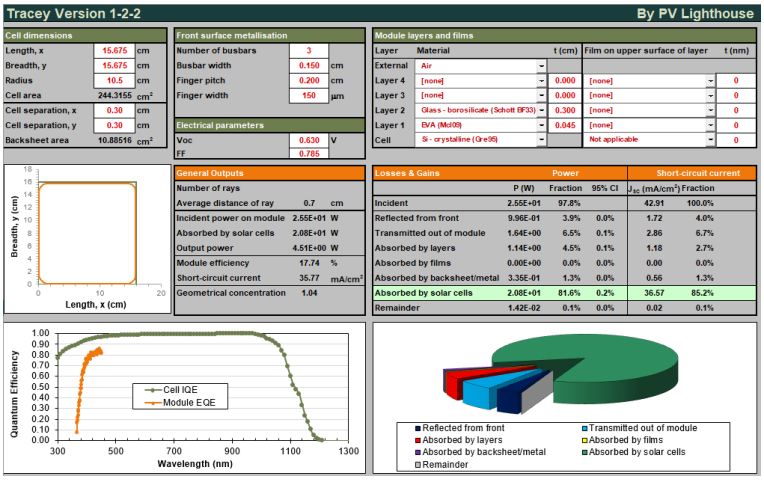

Figure 39: Overview of the main page for inputs parameters and results of the ray-tracing spreadsheet "Tracey"

Daidalos from ISFH

“Daidalos” in an online free ray-tracer for PV module, with premium capabilities extensions developed by the Institute for Solar Energy Research in Hamelin (ISFH) [85], [86]. It includes all the features of "Tracey", and adds others: both sides of the cell/module can be configured. In particular, it is possible to handle glass/glass or glass/backsheet module cases. Daidalos also includes optical modelling of cell interconnect ribbons. But the free version only allows to model ribbons with rectangular section (as of 21/01/2021). The default cell texture is random upright pyramids, and other kind of texture can be defined in the premium version. Only one encapsulant layer and one glass layer (or backsheet) can be simulated in the free version, and more layers are available for premiums. The results are presented similarly to “Tracey”. The particularity of this software is that it allows to treat optical phenomena for very large characteristic sizes: it uses a multi-scale approach to simulate the texture (a few micrometres) up to the complete module (a few meters) [87].

“Daidalos” has been applied in many research studies: comparison with LBIC measurements [88], for complete module [89], to prove the gain of PERCs compared with Al-BSF cells in term of module temperature [90], for multi-physic coupled model of PV module [91], for study of UV-induced degradation of PERC solar modules with transparent encapsulation materials [92], for study of cell-to-module efficiency ratio greater than 100 % [93], for module performance under realistic irradiance conditions [94], and many others..

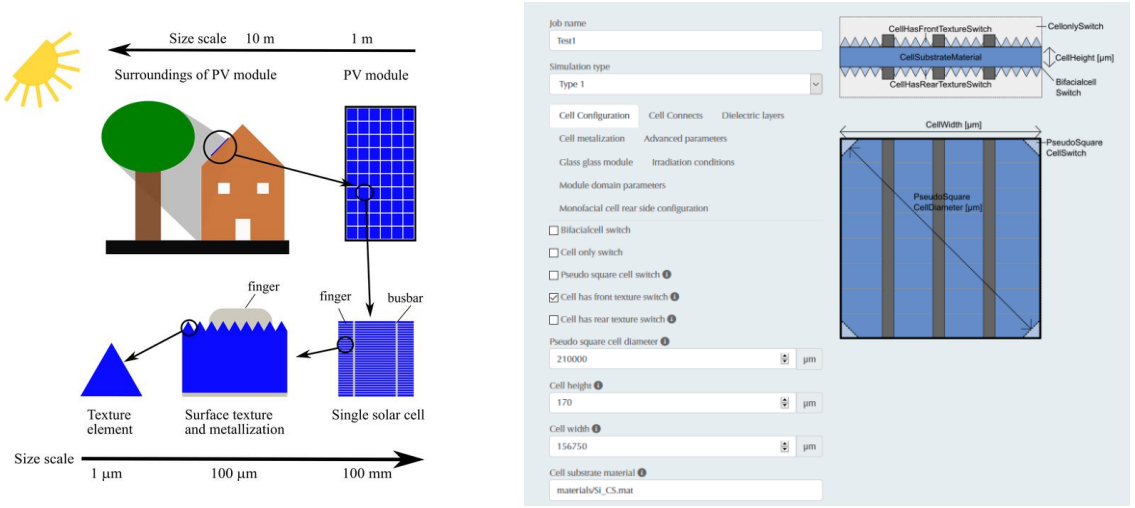

Figure 40: Overview of the principle of Daidalos (left) and example of the input parameters page for cell (right)

SunSolve from PVLighthouse

SunSolve is a ray tracing software specialized in modelling the performance of photovoltaic systems [95]. It is available online, paid and proprietary: developed by PVLighthouse. It is the historical evolution of "Tracey", with far superior functionalities. Each component is defined with its optical constants n & k. Each interface can be textured (pyramid, V-groove, spherical caps or cones...), and a Lambertian or Phong diffusion part can be chosen.

At the cell level, each of the faces can be defined, with an arbitrary number of thin layers. The fingers can be chosen in different types of section (rectangular, triangular, semi-elliptical, rounded rectangle). Busbar and soldering pads can be added, as well as cell-interconnection ribbons of different shapes (rectangular, rounded, circular, semi-elliptical and elliptical, pentagonal...). The optical material of metallization and cell interconnection can be selected. The shape of the cell can be square, circular or pseudo-square.

At the module level, optical layers can be added without limits, textured and with thin films. The number of cells, the space between the cells and between the strings, as well as the margins of the module must be filled in. A frame can be added to the module, with the hooks. Finally, information about the system can be given: number of modules, installation height, type of support, orientation of the module, presence of a tracker... All this information will be used in the ray tracing.

Several illumination sources can be applied, specular or diffuse, with a variable angle of incidence, at the front or rear of the module. It is possible to apply any spectrum other than AM1.5G. For all these reasons, Sunsolve is to date the most configurable and ergonomic ray tracing program for modelling PV performance. From 2016 to 2020, the Sunsolve model has been used more than 35 times in published research [96].

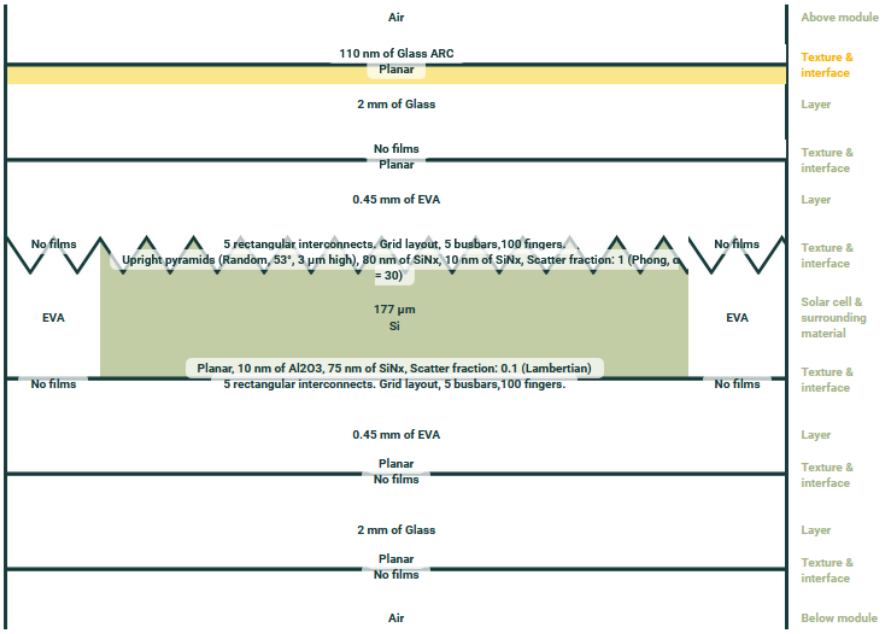

Figure 41: Example of the optical stack definition in Sunsolve, given here for a bifacial glass / glass module.

Optos from Fraunhofer ISE

OPTOS (for Optical Properties of Textured Optical Sheet) is a simulation program of the optical properties of plane-parallel structured interfaces developed by the Fraunhofer ISE [97]. It is based on a matrix formalism, and coded in Matlab, and released with the GNU licensing. It can process an arbitrary number of layers, as long as the transfer matrix of each interface is known. For each angle of incidence, this transfer matrix gives the intensity of the layer's

reflection or transmission for all possible angles of reflection or transmission. These interfaces can be planes, textures or anti-reflection layers. Thick layers (glass, encapsulant, silicon...) are also treated via transfer matrices. The transfer matrices of interfaces and layers must be pre-calculated by numerical optical methods (ray-tracing, rigorous coupled-wave analysis RCWA, finite difference time domain FDTD…) or determined experimentally by angle measurements (goniometer). It is a long step, but once these matrices have been calculated, they can be reused in other optical stacks. OPTOS does not integrate the effects of metallization and cell interconnections, nor the effects of intercellular spaces: each of the layers is considered infinite and homogeneous in both directions of their plane. Scattering effects of small texture can be tackle with this method.

Among twenty studies where "OPTOS" has been used, we can cite: the analyse of different cell texture in a module [98], [99], or current increase gratings at rear side of a solar cell [100], [101]. Theoretical study of pyramid sizes and scattering effects have been made, showing that for pyramid size over 600 nm, scattering effects are negligible [102]. OPTOS has also been used in a III-V nanowire array solar cell [103], or in perovskite silicon tandem solar cells for cell design optimization [104].

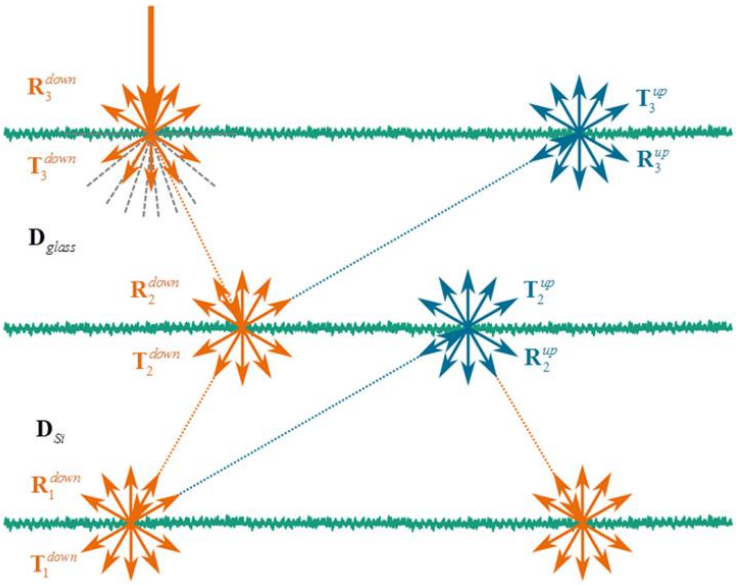

Figure 42: Overview of the working principle of OPTOS modelling. Each interface is described by 4 transfer matrix: reflexion and transmission for up and down directions.

Other optical programs for PV module modelling exists. "SMARTI", and open source Matlab ray tracing tool for solar cell and module optics has been only used once to our knowledge, and even if the Matlab code is available, a correct documentation is not provided [105]. "Ray-sim 6.0", a free geometrical ray tracing program for silicon solar cell and module, has been published in 2005 [106], but cannot be downloaded anymore. This is also the case of "SunRays", published in 1994. Many studies have also been done directly with professional optical software such as TracePro or ZeMax.

All these optical softwares model the cell up to the level of absorption in the cell, or photo-generation, via the IQE of the cell. To model the final electrical behaviour of a module in STCs, they must therefore be coupled with other cell physics modelling programs.

SmartCalc by Fraunhofer ISE

SmartCalc is a software for modelling losses and performance gains between a cell and a module, with obviously an optical part [107]. The software is fee-based and proprietary, but based on a large number of publications detailing its operation [54], [64], [108]–[111]. A free demo version exists. The optical approach is different from ray tracing or matrix formalism: it is largely an analytical method, where the gains and loss positions are described by analytical equations, fed by experimental measurements.Loss and gain modelling is standardized, based on 15 factors. They are presented in Figure 43. The optical factors of interest here are: losses due to module margins, losses due to intercell and inter-string gaps, reflection on the module cover, absorption in the covers, reflection between the cover and the encapsulant, absorption in the encapsulant, shading of the cell interconnect ribbons, index-coupled gains between the cell and the encapsulant, optical coupling of the fingers, optical coupling of the cell interconnect ribbons, optical coupling with the module backsheet.

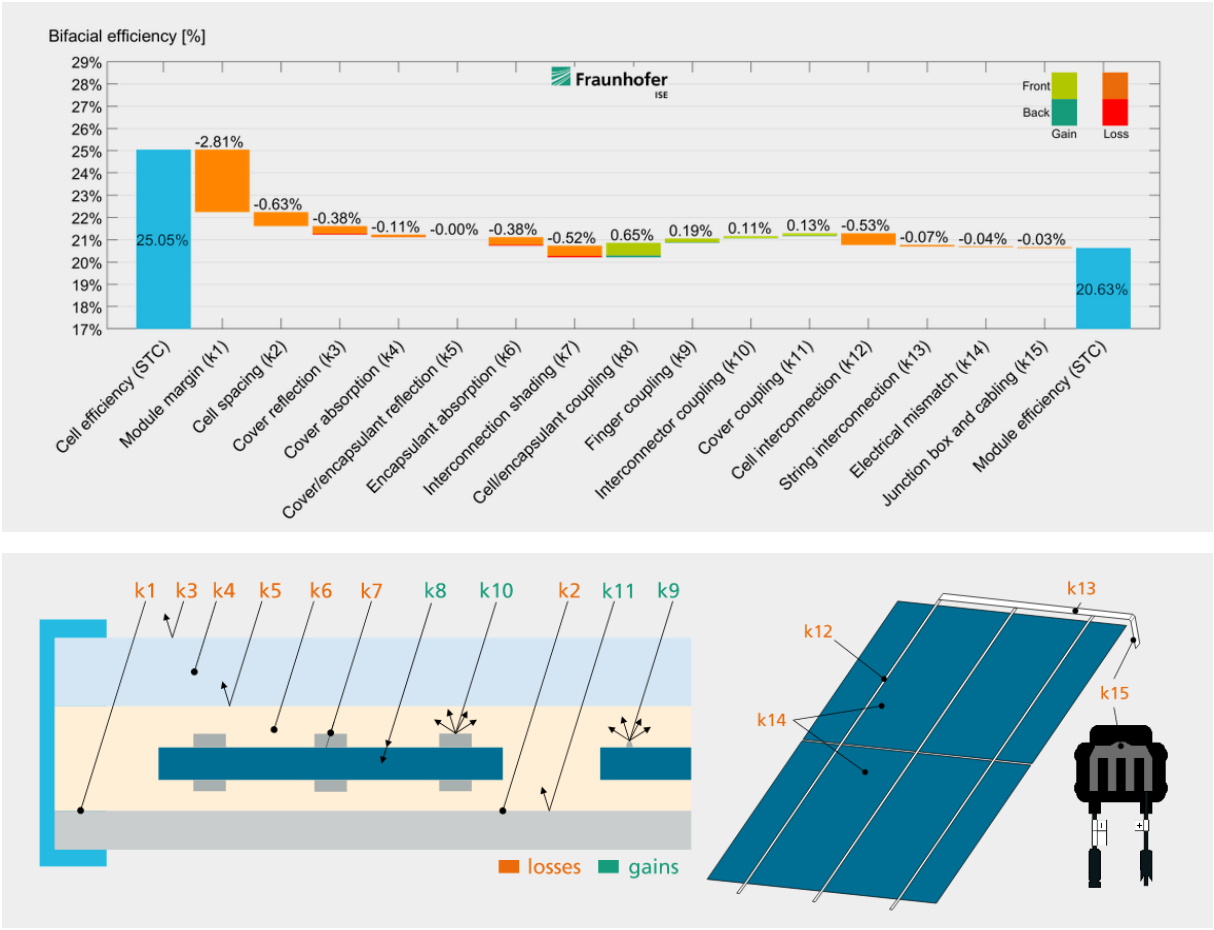

Figure 43: Calculation of 15 loss and gain factors based on material properties and module setup (top) and location of the losses (bottom). Taken from www.cell-to-module.com/software.

It is a relative loss approach that is chosen by SmartCalc, since it is a question of comparing the performance of the cell with that of the module. Hanifi *et al.*, also from the Fraunhofer ISE, have reused this analytical loss factor approach to calculate absolute power losses within a module [70]. This therefore also includes the losses in the cell and does not require too much information about the cell.

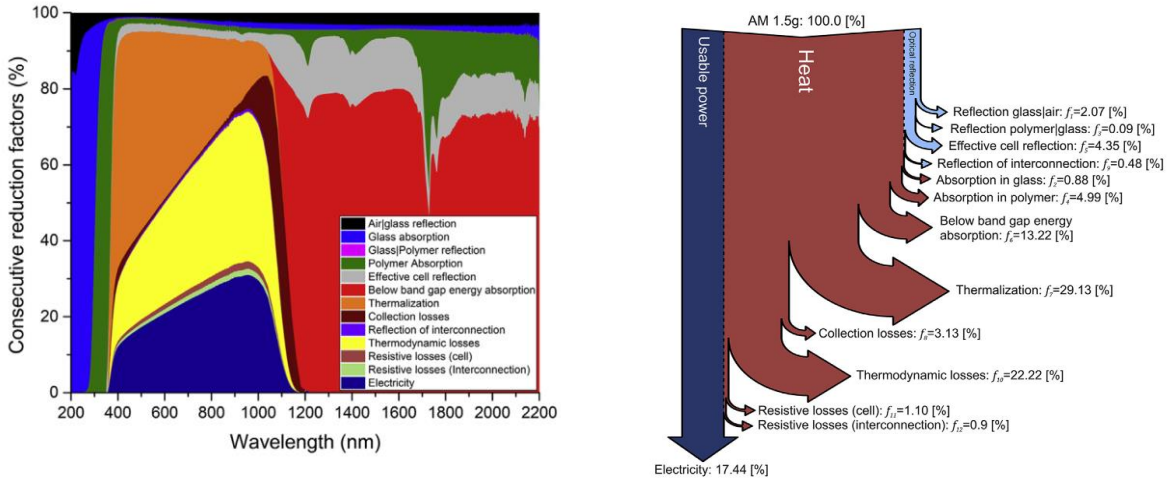

Figure 44: Loss analysis as a function of wavelength as done by Hanifi et al. (left). Corresponding integrted loss factor (optical, thermal).

In the case of the simplified modelling proposed in this thesis, we have chosen an analytical approach like SmartCalc™ and Hanifi *et al.* Ray-tracing modelling (or more rigorous methods: RCWA or FDTD) seemed too slow in computing time to be able to generate a large number of simulations necessary for the validation of the model and the analysis of the case studies. Our motivation was also to start with the simplest approaches to fully understand the physical phenomena involved.

II.B.1.b *Determination of the IV parameters of the module from optical computations.*

Many software programs exist to solve in detail the behaviour of solar cells. These are fundamentally multi-physical software because they combine optics with the physics of semiconductors and the thermal transport. The most complete ones deal with problems in 3D. They are often based on finite element / finite volume methods to deal with drift-diffusion equations, heat propagation, and optical phenomena. We give below some examples of the most used software.

Sentaurus (by SYNOPSYS™) is an advanced 1D, 2D & 3D device simulator for simulation of electrical, thermal and optical behaviour of silicon-base devices [112]. ATLAS (by Silvaco™) solves electrical, optical and thermal behaviour devices [113]. Quokka 3 (by Andreas Fell) is a software in 2D/3D specifically developed for silicon solar cells [114]. PC3D is the 3D version of the free open-source PC1D: it solves drift-diffusion equation in low and high injection level [115]. LAOSS (by Fluxim) is a large area organic semiconductor simulation specialized in organic devices, OLED and solar cells [116].

Other softwares are limited to 1D but are also widely used. PC1D is the standard 1D semiconductor device simulator, in steady state and transient regime [117]. SCAPS was originally designed for CuInSe2 and CdTe families but is now extended to silicon and amorphous devices [118]. ADEPT (by Jeffrey L. Gray) perform coupling of Poisson equation with continuity equation for various cell technologies [119]. AFORS-HET is a 1D software for simulation of steady state and transient physics of heterojunction structures [120]. This list is obviously not exhaustive.

Other models do not solve the semiconductor equations, but use an equivalent circuit approach. The equivalent circuit can describe the IV curve of the cell or module and thus the electrical power generated by the module. This is perfectly suited for our wish to easily integrate cutting losses in the module performance modelling (Chapter III).

The main advantage is that the cell is described by only a few parameters (7 for the classic model with two diodes with series resistance and shunt resistance). This contracts enormously with the tens, see hundreds of parameters necessary in the 3D finite element models. In addition, the resolution of these equivalent circuits is generally very fast. It necessarily follows that these models can poorly describe a cell or a module over wide operating ranges (variable lighting, variable temperature, variable voltage, etc.)

Sunsolve uses the cell's IQE to calculate the photo-generated current I_{ph}, which is then used in an equivalent circuit model. The equivalent circuit may be with one, two or three diodes, each of the recombination currents I_0 and ideality factor n being able to vary. It also includes the lumped series resistance and a shunt resistance (Figure 45). The distributed nature of the series resistance is not taken into account: this may lead to errors, particularly if the cell is not homogeneous. In particular, this may imply that this lumped series resistance may depend on the voltage at the terminals of the cell [121]–[123].

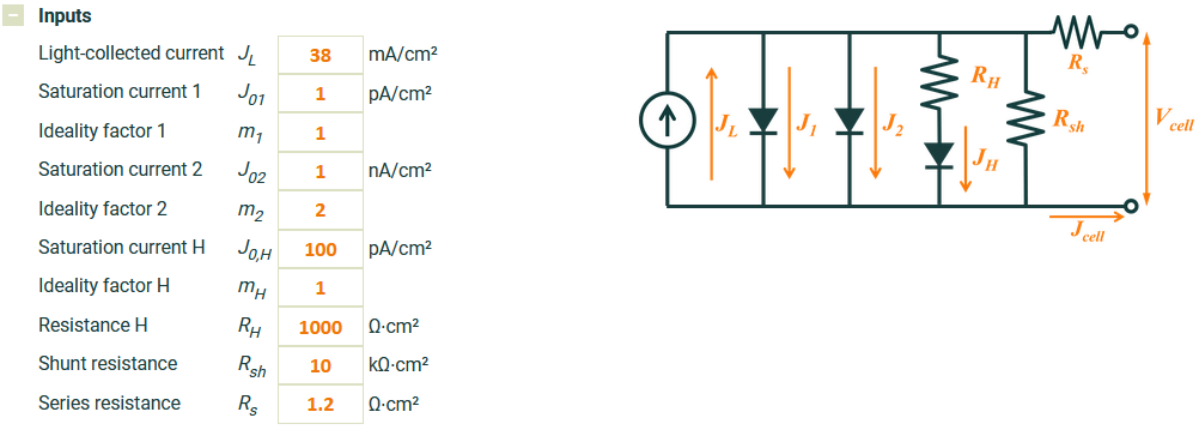

Figure 45: Example of the 1D equivalent circuit with lumped series resistance used in SunSolve, each elementary element can be activated or deactivated and parametrized with values on the left.

Griddler, and its extension for module "Module" is a 3D finite elements method that solve the voltage at every points of the front and rear side of the cell as a function of the resistivity of the different layers, metallization and cell interconnections [124], [125]. It

therefore does not use a single scalar value of lumped series resistance, but therefore fundamentally integrates its distributed behaviour. The core model of Griddler is presented on the Figure 46, taken from the Griddler user manual.

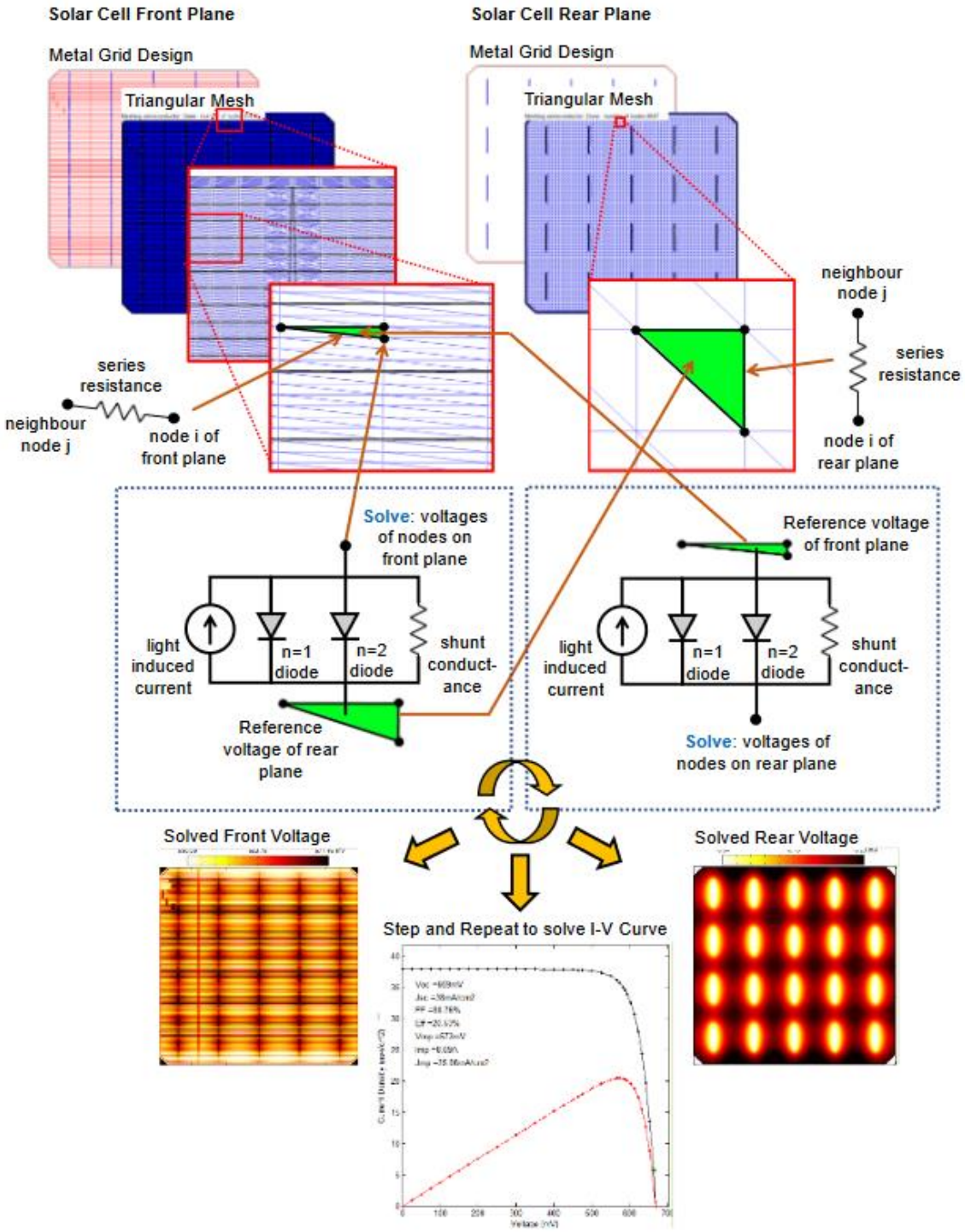

Figure 46: Griddler and module core model for determination of the IV curve of the solar cell from voltage distribution and local equivalent circuit with two-diodes and a shunt resistance. Picture taken From Griddler user manual.

Griddler can be used to analyze various module architecture using coupling voltage distribution solving at the cell level and Spice like simulation for the entire electric circuit of the module. Griddler is limited in his analysis of the optics of a module: only the photo-generated current is used, even if the effective shading of the fingers and of the interconnections of the cells is taken into account. For our case study, the main limitation of Griddler is that the model considers a PERC cell with front emitter and rear base, as a consequence the lateral parallel transport between front ITO and c-Si occurring in the a-Si:H/ c-Si heterojunction cells that we use is not taken into account.

In our simplified CTMod model, to avoid taking too much time to characterize the input parameters of the advanced semiconductor simulation models (Sentaurus, Atlas, Quokka, Laoss), and to avoid the significant calculation time that results from these models by finite elements, we have chosen an equivalent circuit approach. This allows us to reduce the number of parameters necessary for the modelling of the cell, while having a very short calculation time. The choice between a Sunsolve (equivalent circuit model with lumped resistance) or Griddler (distributed nature of series resistance included) approach lies in Griddler's limited ability to describe heterojunction cells. Griddler's computation time, although faster than semiconductor simulation software, is higher than a 1D model since it also requires the coupled resolution of a finite element model.

Choosing a 1D equivalent circuit model involves determining the lumped series resistance of the cell and module. The series resistance of the cell is calculated from the models of Mette *et al.* and of Basset *et al*., and correspond to a heterojunction cell. The modelling of the series resistance of the module is common to several works: Guo, Haedrich *et al.*, Hanifi *et al.*, Rodriguez *et al.*, Geipel *et al*. We have included the resistance of electro-conductive adhesive (ECA), specific to heterojunction technologies.

II.B.2 Comparison of CTMod simplified model with state-of-the-art Sunsolve model

As seen from the previous section of the chapter, our simplified model combines several approaches from many authors and software.

It is inspired by the work of Hanifi *et al.,* since it is based on a description of the absolute losses in a module. The semiconductor loss calculation methods we use (below bandgap, thermalization, cell collection, thermodynamic) are taken directly from their work.

CTMod is inspired by the work done in the SmartCalc software: the loss categories are standardized, making easier to compare different module architectures. The losses are also calculated for the front and rear faces of the module, which was not done by Hanifi. The losses by reflection and absorption in the covers, by absorption in the encapsulant, optical coupling with the backsheets are calculated in CTMod, as in SmartCalc. On the other hand, there is no notion of gains in CTMod, since we are dealing with the power losses compared to the incident solar power and not compared to the performance of the cells.

The consideration of semiconductor effects in the cells is based on the IQE coupled to an equivalent 1D circuit model with two diodes. This is also the choice made by SunSolve, which avoids dealing with the complexity of the 3D equations of the cell.

The resistive losses in the heterojunction cell is based on the models of Mette and Basset [68], [126]. The resistive losses in the cell interconnections are modeled in a similar way to what is done in Hanifi *et al.*, SmartCalc, Geipel *et al.*, or even SunSolve.

Our optical analytical model contains several questionable approximations. It is therefore important to compare the results it gives with more accurate software, and in particular the modelling of optical couplings, the effects of metallization and cell interconnections, and the optics of the cell. Sunsolve is been chosen for this benchmark, for its accuracy as well as for its ease of use.

The Sunsolve software integrates in fact the phenomena of multiple reflection. This is not the case of the simple analytical model developed in this thesis, apart from the phenomena of effective shading of the fingers and cell interconnection ribbons. It is therefore necessary to quantify the error resulting from this approximation. To this aim, we propose to compare the results of Sunsolve and CTMod, for module architectures of increasing complexity: a non-metallized cell in air, a metallized cell in air, an encapsulated cell without metallization, a non-metallized cell with encapsulant and glass, a metallized cell with encapsulant and glass and finally a metallized cell with cell interconnection, encapsulant and glass.

Checking the starting point on non-metallized cell in air and in encapsulant

The different layers of the cell have been described previously. The reflectance and the transmittance of the cell in the air are input parameters of our model. As seen previously, there is a difference at this stage between measurement and modelling (Figure 16). To overcome this and only compare the accuracy of the models, we use the values obtained by Sunsolve as input values of CTMod. The results should therefore be equivalent by definition. We also take care to use the same incident irradiance. The two study geometries (cell in air and cell encapsulated) are shown in Figure 47 (Sunsolve screenshot).

As can be seen in Table 3, the results between Sunsolve and CTMod are similar to within 0.01 % for the cell in air and the cell encapsulated. This value is therefore an upper limit of the numerical errors which could have occurred because of rounding, integration methods.

	Sunsolve		**CTMod**	
	Current density (mA/cm²)	Fraction of incoming (%)	*Current density (mA/cm²)*	Fraction of incoming (%)
Incoming	*46.32*	100.00	*46.32*	100.00
Escape front	*1.79 / 1.29*	3.86 / 2.78	*1.79 / 1.29*	3.86 / 2.78
Escape Rear	*2.53 / 3.04*	5.45 / 6.55	*2.53 / 3.04*	5.45 / 6.55
Absorbed cell	*42.00 / 41.97*	90.67 / 90.61	*42.00 / 41.99*	90.67 / 90.65
Photogenerated	***38.27 / 38.43***	**82.62 / 82.97**	***38.27 / 38.43***	**82.62 / 82.97**

Table 3: Numerical check of initial state: comparison of cell reflectance (lost front) / absorption and transmission (lost rear) for Sunsolve and CTMod are similar. Value in air / Value in encapsulant.

In the case of the cell in air, 3.86 % is of the current density is lost from the front face after multiple reflection in the cell. The transmission of the cell generates 5.45 % loss, and therefore 90.67 % of the irradiance is absorbed. In the case of the encapsulated cell, 2.78 % of the current density is lost from the front face after multiple reflection in the cell. This value is lower than for the cell in air due to the index adaptation between the encapsulant (n = 1.5) and the ITO. Transmission from the cell causes 6.55 % loss, higher than for the cell in air, for the same reason. The absorption in cell is 90.61 % much the same as in the case of the cell in air.

For an encapsulated cell, the gain on the reflection of the cell by index adaptation is therefore 1.08 %, but the transmission on the rear face of the cell is also favoured by 1.10 %. The absorption in both cases is similar. These phenomena can be seen in the right part of Figure 48. The reflectance for the encapsulated cell is much better, especially over the ranges between 300 and 500 nm and between 800 and 1050 nm. The transmission of the encapsulated cell is greater from 1000 nm. These two phenomena combine: the absorption of the encapsulated cell is better between 300 and 500 nm, but less good between 1000 and 1200 nm. By integrating on the spectrum, these two phenomena cancel each other out.

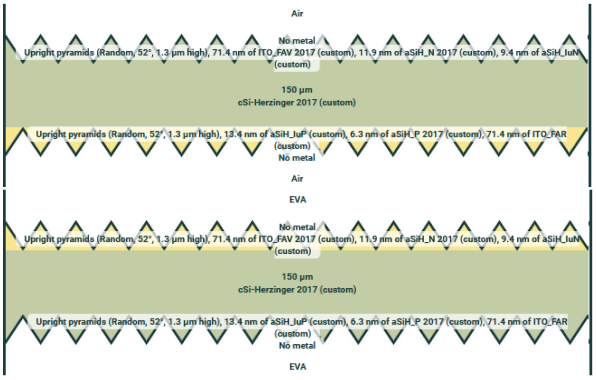

Figure 47: Sunsolve geometry of the two case considered: cell in air (top), cell in encapsulants (bottom). Sunsolve screenshot

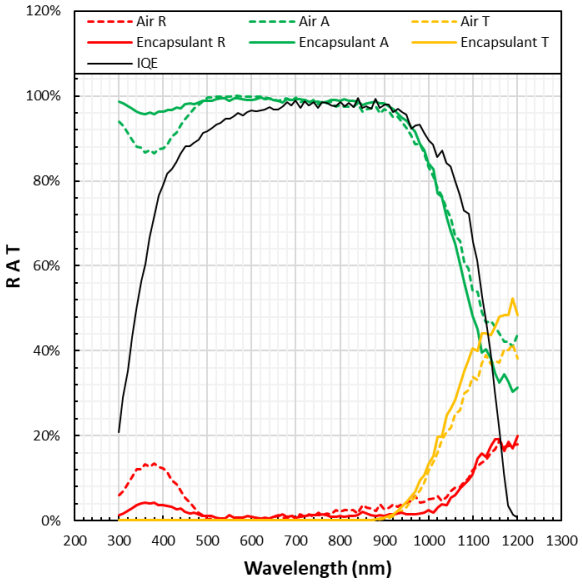

Figure 48: Reflectance, Absorption and Transmittance of the cell in air (dotted) and in encapsulants (full) as obtained by SunSolve. The internal quantum efficiency is also plotted.

On the other hand, for the calculation of the photo-generated current, the absorption is multiplied by the IQE. Since the IQE is greater in areas where there has been a gain in reflection than in areas where there has been an increase in transmission, the photo-generated current is therefore greater in the encapsulated cell than in the cell in the 'air. The difference is around 0.35 % (38.27 mA / cm² against 38.43 mA / cm²).

We were therefore able to verify the validity of the CTMod model for a non-metallized cell at the air / cell interface and the encapsulant / cell interface.

Impact of finger shading: Metallized cell in air

We are now interested in the impact of adding metallization on the cell (front and rear face, finger and busbar). SunSolve does not give the possibility of entering any type of profile for the fingers. The closest one is a triangular profile with a base 55 µm and a height of 18 µm. Optically, the fingers are made up of silver, with 80 % of the reflected light which is Lambertian [50]. As a reminder, the effective optical width measured in our case is 88 %.

The Table 4 summarizes the loss, cell absorption and photo-generated current comparison for Sunsolve and CTMod. What is counted as "Escape front" by Sunsolve is actually what was reflected either by the cell, or by the fingers, or by the busbars. This distinction is made in CTMod. Sunsolve indicates separately the part absorbed by the fingers. In CTMod, it is included in the notion of effective optical width. In the end, the losses by absorption in the fingers summed with the part that escapes from the module in Sunsolve represents the same thing as the losses by cell reflection and metallization calculated in CTMod.

The difference in Sunsolve between the light that escapes from the module (2.90 mA / cm²) and the same value for the non-metallic cell (1.79 mA / cm²) is 1.11 mA / cm². This therefore represents an effect of the fingers on the losses of current density of 1.16 mA / cm² by adding the 0.05 mA / cm² absorbed by the metal. This value is in perfect agreement with the reflectance generated by the metallization in CTMod (1.04 + 0.11 mA / cm²).

	Sunsolve		**CTMod**	
	Current density (mA/cm²)	Fraction of incoming (%)	*Current density (mA/cm²)*	Fraction of incoming (%)
Incoming	*46.32*	100.00	*46.32*	100 %
Escape front	*2.90*	6.26	*1.75 c* *1.04 f* *(2.89)* *0.11 bb*	3.77 2.24 (6.24) 0.23
Escape rear	*2.27*	4.91	*2.282*	4.93
Absorbed metal	*0.05*	0.11		
Absorbed cell	*41.06*	88.64	*41.15*	88.84
Photo-generated	***37.41***	**80.76**	***37.43***	**80.81**

Table 4: Comparison of Sunsolve and CTMod current densities losses in a metallised cell in air. Light escaping the module and absorption in cell are given. Absorption in metallisation is also mentioned.

Good consistency can be observed between the different losses. This means that the approximation made in Sunsolve with silver fingers with triangular section and 80 % Lambertian gives the correct values of effective shading of the cell by metallization. The part absorbed by the cell differs only by 0.2 % and the modelled photo-generated current differs

only by 0.05 % between Sunsolve and CTMod. The difference is made at wavelengths where the IQE is low, since the difference in absorption is greater than the difference between the photo-generated currents.

Impact of multiple reflections: cell in optical stack without metallisation

This part is dedicated to the study of the impact of multiple reflections into account on the module's modelling. Indeed, the developed model - CTMod - does not generally take into account the multiple reflections in the layers of the module. In particular, the impact of the air / glass interface is only taken into account during the first passage of the incident light. The results in terms of current density are summarized in the Table 5.

A case without metallization is considered here, removing the effect of the effective optical width of the fingers, which would complicate the comparison. A standard 450 µm thick UV-transmissive EVA is used on the front and back sides [127]. A 3 mm soda-lime glass without anti-reflective layer with an iron content of 0.01 $\%_{wt}$ is also used on the front and back [128].

	Sunsolve		**CTMod**	
	Current density (mA/cm²)	Fraction of incoming (%)	*Current density (mA/cm²)*	Fraction of incoming (%)
Incoming	*46.32*	100.00	*46.32*	100.00
Reflected Glass	*1.915*	4.13	*1.92*	4.15
Absorbed Glass	*0.445*	0.96	*0.39*	0.84
Absorbed EVA	*0.283*	0.61	*0.21*	0.45
Escape front	*0.872*	1.88	*1.21*	2.61
Escape Rear	*2.433*	5.25	*2.84*	6.13
Absorbed cell	*40.38*	87.18	*39.76*	85.83
Photo-generated	***36.79***	**79.43**	***36.43***	**78.65**

Table 5: Comparison of Sunsolve and CTMod current density losses in a cell with optical stack and no metallisation. Light escaping the module and absorption in cell are given. Glass reflection and absorption and EVA absorption are also mentioned.

A noticeable overestimation in CTMod exists on the part of the irradiance lost by the front face of the module (2.61 % for CTMod against 1.88 % for Sunsolve, ie 0.73 % of difference). An even greater overestimation is made by CTMod on the irradiance lost by the rear face of the module (6.13 % for CTMod against 5.25 % for Sunsolve, or 0.88 %).

This is explained precisely by the phenomena of multiple reflections. Light reflected by the cell is considered lost in CTMod when it can actually be reflected at the glass / air interface to be reabsorbed by the cell. This reflectance is all the more important as the light reflected by the cell is diffused by the surface texturing. Significant angles of incidence at the glass / air interface generate significant reflectance. Similarly, the light transmitted by the cell was

actually diffused twice: from the front side and from the back side. By the same phenomenon, it can be redirected to the rear face of the cell and then be absorbed.

The sum of the difference observed for the light escaping from the module between Sunsolve is CTMod is 1.61 % (0.88 + 0.73). This corresponds to the difference observed in the absorption of the cell (1.35 %) if we correct for the additional absorption in the glass and the EVA induced by the multiple reflections (0.28 %).

In Figure 39, we can see a comparison of the different spectral losses and cell absorption for Sunsolve and CTMod, expressed in photon flux. For the front glass (top left graphic), the reflectance is similar for both models. The absorption is similar from 300 to 1000 nm, but further in the IR, we see the underestimation of CTMod due to the absence of multiple reflections. For the EVA encapsulant (top right graph), the same underestimation of absorption in IR is visible. This is also the case for the part of the flow which escapes from the module via the front face and the rear face (graph below left). Finally, these differences translate into greater absorption in the cell for wavelengths greater than 1000 nm (abs graph on the right).

The effect of multiple reflections is therefore mainly visible on IR from 1000 nm. After applications of the IQE for the calculation of the photo-generated current, the difference between the two models is therefore only 0.78 %, lower than for absorption (1.35 %).

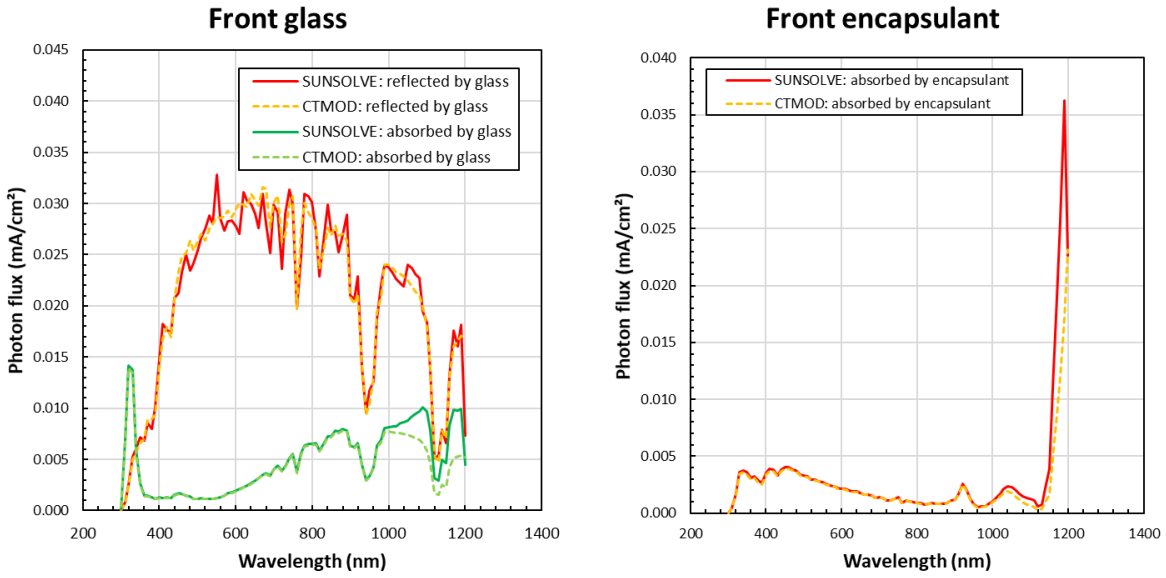

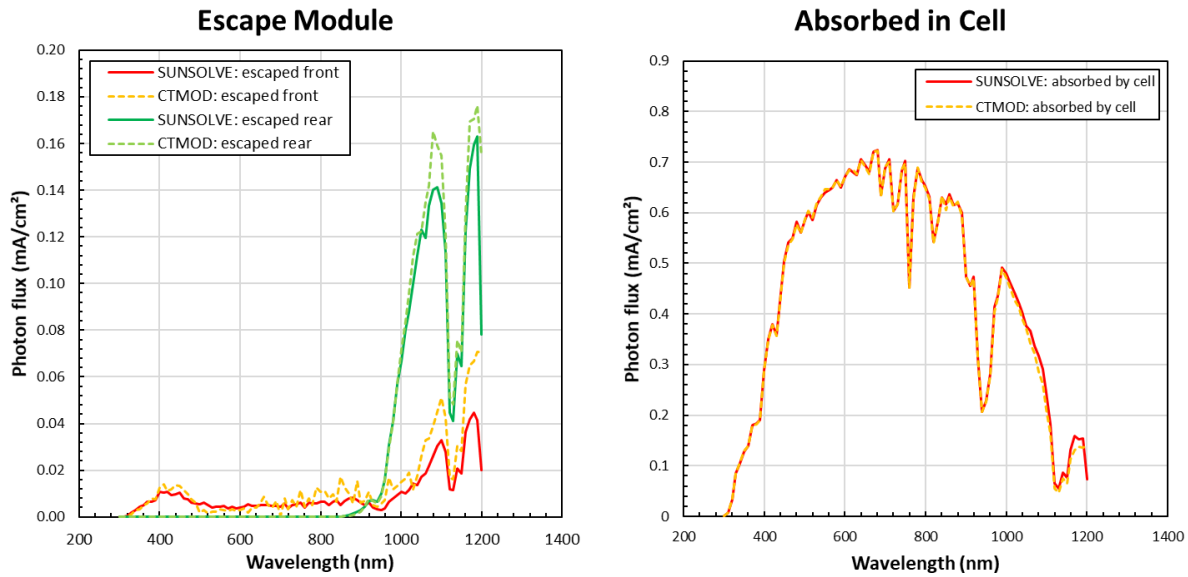

Figure 49: Comparison of photon flux spectral losses and cell absorption for different components of the module produced by SUNSOLVE simulation and by CTMOD simulation (this work). Front glass reflectance and absorption (top left), Front encapsulants absorption (top right), Photon flux escaped from module – front and rear (bottom left) and photon flux absorbed in cell (bottom right).

Finger optical effective width: cell with metallisation and optical stack

This part is dedicated to validate the values of the fingers optical width when the cell is encapsulated. We expect a difference between Sunsolve and CTMod at least as important as in the case of a cell in an optical stack but not metallized. The results are shown in Table 6. In the CTMod model, in the absence of multi-reflection, the values of reflectance on the glass and absorption in the glass and in the encapsulant are identical to the previous part without metallization. Considering Sunsolve, the reflectance on the glass is the same as the previous case. The absorption in the glass and in the EVA are slightly higher than the previous case, due to the greater reflectance of the fingers compared to the cell.

The error made in CTMod due to multiple reflections is still present. Indeed the difference between what is lost on the rear face of the module is 4.83 % in Sunsolve, against 5.61 % in CTMod. The difference of 0.78 % with metallization, against 0.88 % in the previous case without metallization. This is due to the rear face metallization density which limits transmission, therefore the possibilities of multiple reflections, and consequently the overestimation of losses in CTMod.

The share absorbed by the cell in Sunsolve is here 86.46 % against 85.30 % in CTMod. The difference is therefore 1.16 %, against 1.35 % in the previous case without metallization. We have just seen that this difference between 1.16 % and 1.35 % is due to 0.1 % at the transmission. The remaining 0.1 % is due to the front face of the metallized cell.

In Sunsolve, the part that escapes from the module in the present case is 2.70 %, against 1.88 % in the previous case without metallization. There is therefore 0.82 % additional loss here due to the presence of the fingers. By adding the 0.12 % absorption in the fingers, and the residual absorption in the glass and the EVA of the light reflected by the fingers (0.07 %

glass + 0.05 % EVA), we obtain 1.06 % of losses due to the fingers in Sunsolve. This corresponds well to the 1.11 % (1.02 % fingers + 0.09 % busbars) obtained with CTMod.

	Sunsolve		CTMod	
	Current density (mA/cm²)	Fraction of incoming (%)	*Current density (mA/cm²)*	Fraction of incoming (%)
Incoming	*46.32*	100.00	*46.32*	100 %
Reflected Glass	*1.920*	4.15	*1.920*	4.15
Absorbed Glass	*0.479*	1.03	*0.389*	0.84
Absorbed EVA	*0.306*	0.66	*0.209*	0.45
Escape front	*1.253*	2.70	*1.19 c* *0.47 f* *(1.70)* *0.04 bb*	2.57 1.02 (3.68) 0.09
Lost rear	*2.239*	4.83	*2.60*	5.61
Absorbed metal	*0.055*	0.12		
Absorbed cell	*40.05*	86.46	*39.51*	85.30
Photo-generated	***36.48***	**78.76**	***36.13***	**78.00**

Table 6: Comparison of Sunsolve and CTMod current density losses in a cell with optical stack and metallisation. Light escaping the module and absorption in cell, glass and encapsulant are given. Glass, cell and metallisation reflectance are also mentioned.

The difference between the two models for the photo-generated current in the present case of a metallized cell in the optical stack module is 0.76 %, roughly equivalent with the error made in the previous case (0.78 %).

Impact of ribbons optical effective width: cell with metallisation, cell interconnector and optical stack

In this last part of the comparison of the optical model, we are interested in the effect of cell interconnect ribbons on the performance of the module. The ribbons used are 800 µm wide and 200 µm thick, with a V-groove texturing as shown in the right Figure 23. The angle of the V-groove texturing makes the rays reflected on the ribbon are fully reflected at the glass/air interface.

The Sunsolve results are substantially the same as those given in Table 6. The absorption in the cell amounts to 40.04 mA / cm², or only 0.01 mA / cm² of difference with the case without interconnecting ribbons. However, the absorption in these ribbons is 0.05 mA / cm². It is therefore noted that this loss in the ribbons is not caused by a loss in the absorption of the cell. This is due to the very low losses generated by the V-groove texturing compared to the losses generated by the texturing of the cell which has been covered by the ribbons.

In the case of ribbons, all the beams are in total reflection at the glass / air interface, whereas when it comes to the texture of the cell, only a part is. The absorption loss in the ribbons (0.05 mA/cm²) is therefore compensated for by better reflection at the glass-air interface. The result is therefore almost identical total absorption in the cell. And a photo-generated current, after application of the IQE of 36.47 mA / cm², almost identical to the case without ribbons: 36.48 mA/cm². The effective optical width of the interconnect ribbons in Sunsolve is therefore close to 0 %.

This is only possible because the ribbons are considered in Sunsolve as perfectly textured, and not diffusing. This is not the case in reality: as measured experimentally, the effective width of the ribbons is closer to 27 % than to 0 %. There are two reasons for this: the hollows and bumps in the texturing are smoothed out and flat areas may appear, and the coating of the ribbons may be diffusing [57].

Conclusion of the Chapter II

In this chapter the main physical, optical and electronic phenomena, which influence the performance of a photovoltaic module have been presented. We did this through the presentation of our simplified model, the study of a reference case and the comparison to a literature software.

We have first presented the input parameters useful for modelling a module as a mean to describe main physical phenomenon in a PV module. The model starts with any spectrum on the front and rear face, with a normal angle of incidence. The reflectance of the cell, according to the material which covers it, is calculated with ray tracing software (SunSolve). The effective shading of the fingers has been determined by studying cells with a variable metallization pitch, in a range comparable with what is found in the literature (88 %). The interface between the glass and the air reflects towards the cell a part of the light reflected by the fingers and the ribbon (optical coupling). The effective shading of the V-groove textured ribbons (27 %) was determined via local EQE measurements on a mini-module, also in line with the values reported in the literature. Masks of different sizes made it possible to determine the photocurrent gains due to inter-cell spaces, in a similar way to that of SmartCalc: this corresponds to gains of 2.2 % for spaces of 3 mm in whole cell. The effects by reflection and absorption in the glass and in the encapsulant are determined from the optical constants of these materials (more details in chapter 4).

Next, the details of the performance calculations were presented. It is an analytical approach that was chosen, except for a numerical resolution of the equation of the equivalent circuit model. This makes it possible to standardize the categories of losses, like it is done in the SmartCalc software. In addition, such classification allows a comparison of the impact of different architectures, in particular in the analysis of cell to module losses.

A short review of the different cell / module performance modelling software has been done. Optical modelling by ray tracing is the most common approach, due to the diversity of architectures that can be modelled (Tracey, Daidalos, Sunsolve). But it is an analytical approach, similar to the SmartCalc software and to the work of Hanifi *et al*. that was chosen for CTMod: It is simpler to set up numerically, and faster in term of calculation time. To obtain the electrical performance of the module, advanced semiconductor physics models can be used (Sentaurus, Atlas, Laoss, PC3D ...). The compromise between the complexity of the modelling and the time of implementation / calculation has rather directed us towards a 1D model of circuit equivalent to two diodes, in the manner of Sunsolve. The calculation of a lumped series resistance follows, integrated for the cell from Mette *et al*. and Basset *et al*. For the series resistance of the module, the generic approach of Guo *et al.*, Geipel *et al*. and Haedrich *et al.* was used.

Finally, as the most important simplifications in the CTMod analytical model are the one made for the optical model, it is therefore necessary to assess its accuracy. A comparison with SunSolve from PVLighthouse, a ray tracing software, was performed. Sunsolve makes it easy to model various mainstream module architectures. It was concluded on the reference case that: the effective shading of the cell by the fingers was correctly taken into account by CTMod (difference <0.1 % on I_{ph}), as well as the absorptions and reflection in the optical stack. On the other hand, the comparison has revealed a phenomenon that was not taken into account by our model: multiple reflections between the cell and glass/air interface. Indeed, part of the

irradiance reflected by the cell can be further reflected at the glass/air interface and participate to the photo-generation. The absence of this effect leads to an underestimation of the current photo-generated 0.7/0.8 %.

Conclusion du Chapitre II

Dans ce chapitre, les principaux phénomènes physiques, optiques et électroniques, qui influencent les performances d'un module photovoltaïque ont été présentés. Nous l'avons fait à travers la présentation de notre modèle simplifié, l'étude d'un cas de référence et la comparaison avec un logiciel de la littérature.

Nous avons d'abord présenté les paramètres d'entrée utiles à la modélisation d'un module comme moyen de décrire les principaux phénomènes physiques dans un module PV. Le modèle commence par un spectre quelconque sur la face avant et arrière, avec un angle d'incidence normal. La réflectance de la cellule, en fonction du matériau qui la recouvre, est calculée avec un logiciel de traçage de rayons (SunSolve). L'ombrage effectif des doigts a été déterminé en étudiant des cellules avec un pas de métallisation variable, dans une gamme comparable à ce qui est trouvé dans la littérature (88 %). L'interface entre le verre et l'air réfléchit vers la cellule une partie de la lumière réfléchie par les doigts et le ruban (couplage optique). L'ombrage effectif des rubans texturés à rainures en V (27 %) a été déterminé par des mesures locales d'EQE sur un mini-module, également en accord avec les valeurs rapportées dans la littérature. Des masques de différentes tailles ont permis de déterminer les gains de photo courant dus aux espaces inter-cellules, de manière similaire à celle de SmartCalc : cela correspond à des gains de 2,2 % pour des espaces de 3 mm en cellule entière. Les effets par réflexion et absorption dans le verre et dans l'encapsulant sont déterminés à partir des constantes optiques de ces matériaux (plus de détails au chapitre 4).

Ensuite, les détails des calculs de performance ont été présentés. C'est une approche analytique qui a été choisie, à l'exception d'une résolution numérique de l'équation du modèle de circuit équivalent. Cela permet de standardiser les catégories de pertes, comme cela est fait dans le logiciel SmartCalc. De plus, cette classification permet de comparer l'impact de différentes architectures, en particulier dans l'analyse des pertes cellule-module.

Une brève revue des différents logiciels de modélisation des performances des cellules / modules a été effectuée. La modélisation optique par lancer de rayons est l'approche la plus courante, en raison de la diversité des architectures qui peuvent être modélisées (Tracey, Daidalos, Sunsolve). Mais c'est une approche analytique, proche du logiciel SmartCalc et des travaux de Hanifi et al. qui a été choisie pour CTMod : elle est plus simple à mettre en place numériquement, et plus rapide en terme de temps de calcul. Pour obtenir les performances électriques du module, des modèles avancés de physique des semi-conducteurs peuvent être utilisés (Sentaurus, Atlas, Laoss, PC3D ...). Le compromis entre la complexité de la modélisation et le temps de mise en œuvre / calcul nous a plutôt orienté vers un modèle 1D de circuit équivalent à deux diodes, à la manière de Sunsolve. Le calcul d'une résistance série groupée suit, intégré pour la cellule de Mette et al. et Basset et al. Pour la résistance série du module, l'approche générique de Guo et al., Geipel et al. et Haedrich et al. a été utilisée.

Enfin, comme les simplifications les plus importantes du modèle analytique CTMod sont celles effectuées pour le modèle optique, il est donc nécessaire d'évaluer sa précision. Une

comparaison avec SunSolve de PVLighthouse, un logiciel de lancer de rayons, a été effectuée. Sunsolve permet de modéliser facilement diverses architectures de modules. Il a été conclu sur le cas de référence que : l'ombrage effectif de la cellule par les doigts a été correctement pris en compte par CTMod (différence <0.1 % sur I_{ph}), ainsi que les absorptions et réflexions dans la pile optique. En revanche, la comparaison a révélé un phénomène qui n'a pas été pris en compte par notre modèle : les réflexions multiples entre la cellule et l'interface verre/air. En effet, une partie de l'irradiance réfléchie par la cellule peut être réfléchie à nouveau à l'interface verre/air et participer à la photo-génération. L'absence de cet effet conduit à une sous-estimation de la photo-génération actuelle de 0.7 / 0.8 %.

Chapter III

Modelling of the impact of heterojunction solar cells cutting on module performance

This chapter is dedicated to the modelling of performance losses and performance gains resulting from the cutting of the cells and the integration in a photovoltaic module made of silicon heterojunction solar cells. Gains and losses due to solar cell cutting are rarely included in module loss studies, and even less so in CTM studies.

Why cut photovoltaic cells that have previously been manufactured in their “full" version? By cutting the cells, the resistive losses in the cell interconnections are reduced. But cutting also generates recombination losses. What are the influential parameters and optimums? All the simulations made in this chapter are obviously based on the model described in the previous chapter.

Ce chapitre est consacré à la modélisation des pertes et des gains de performance résultant de la découpe des cellules et de leur intégration dans un module photovoltaïque composé de cellules solaires à hétérojonction en silicium. Les gains et les pertes dus à la découpe des cellules solaires sont rarement pris en compte dans les études de perte de module, et encore moins dans les études de CTM.

Pourquoi couper des cellules photovoltaïques qui ont été préalablement fabriquées dans leur version "entière" ? En coupant les cellules, les pertes résistives dans les interconnexions des cellules sont réduites. Mais la découpe génère également des pertes par recombinaison. Quels sont les paramètres influents et les optimums ? Toutes les simulations réalisées dans ce chapitre sont évidemment basées sur le modèle décrit dans le chapitre précédent.

Part III.A Limitation of resistive losses at the module level by dividing the current in cell interconnection ribbons

Why cut a full-cell into sub-cells? Why create large solar cells and then cut them out and not make small cells from scratch? At first glance, this seems to complicate the industrial process: a module manufacturing step is added, and the throughput of the production line is reduced by a factor as great as the number of sub-cells created. The main aim is to reduce resistive losses by Joule dissipation within the electrical interconnections of the module. Using N sub-cells in a module, instead of the full-cell, divides the generated current by N, and multiplies the operating voltage by N. The power of the sum of the individual cells does not change. However, a lower current implies even lower resistive losses since they are quadratically dependant on the current. The topic of this part is to explain this phenomenon in detail. In which resistive elements of the cell and module the gain is obtained and what value can be expected? What is the influence of the incident irradiance and in particular the influence of the part hitting the backside of a bifacial module? What is the influence of the initial geometry of full-cells? In this part, any loss of performance when cutting the cell is neglected. Due to this assumption, comparison with experiments is not possible.

The interest of integrating cells cut into modules is not only limited to resistive gains: It increases the CTM power when using with a backsheet or white EVA (but using a larger module) and it is also a path to reduce the shading and hot spot effect when used in combination of series-parallel electrical architecture of module [129] [130]. It results in efficiency gains at the system level, which are particularly interesting for desert conditions [131]. Keep in mind that different cell separation technologies can lead to a similar electrical performance of the half-cells, yet leading to an entirely different mechanical behaviour of the cells [132]. But half-cut cell modules can sometimes be less valuable compared to full-cell module using the same initial cell efficiency in term of efficiency and cost [133].

III.A.1 Origin of resistive gains, impact on module performance and on CTM ratio

In this section, the general concept of a module with cut-out cells will be presented. It will be recalled where the different resistive losses in a module are located, how they vary according to the number of cell cut-outs made, what is the impact on the module's performance and on the CTM. The principle and geometry of a cutting step is presented in Figure 50.

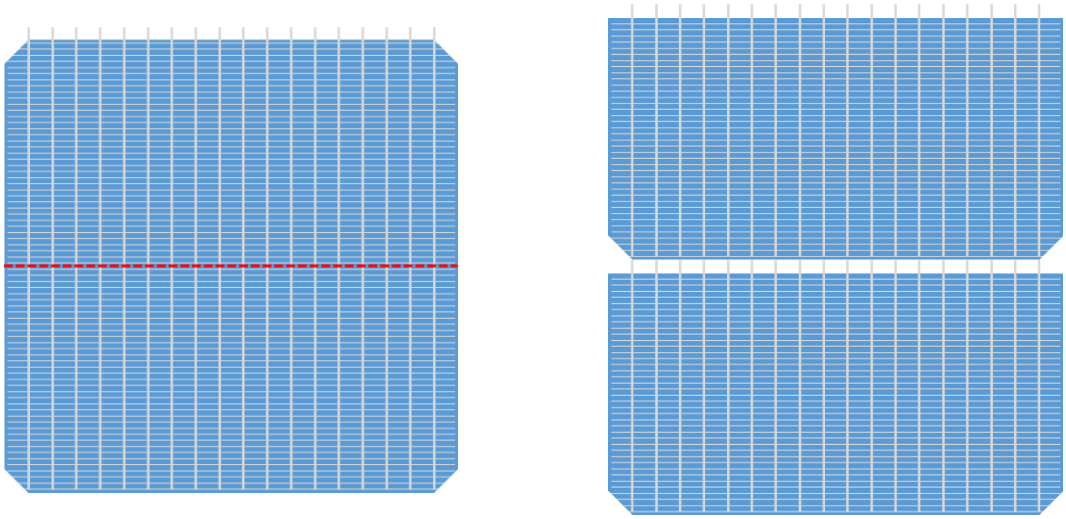

Figure 50: Cutting principle of a solar cell in direction parallel to the fingers (left) and interconnection of sub-cells (right).

III.A.1.a *Resistive losses in the cell and the module*

What does a module made of cut cells consist of? To illustrate this, we will take a reference module made up of full-cells and study the impacts of cutting these full-cells. This module will consist of 72 full-cells, divided into 6 strings of 12 cells. All the cells are connected in series. For the purpose of the study, we will neglect the impact of the inter-cell distance and the inter-string distance: they are initially assumed to be zero. We will also neglect the resistance of the junction box and the connection cables.

A two-diode model showed in the equation III.1 – whose parameters are given in the table 1 – describes the reference cell. This cell is busbarless and the cell interconnection of the module is made with wires of circular section. The format of the wafer is M2, which corresponds to a width of 15.675 cm for a surface area of 244.33 cm². The photo-generated current is calculated from an AM1.5g spectrum according to the absorption, reflection of the optical layers and the IQE of the cell. The series resistance r_s of the cell is calculated as indicated in chapter 2. It is here equal to 0.56 Ohm.cm² and does not include the resistive losses in the fingers of the cell. Thermal voltage V_{th} is 0.02569 mV.

$$J = J_{ph} - J_{01}\left(\exp\left(\frac{V + J.r_s}{n_1 . V_{th}}\right) - 1\right) - J_{02}\left(\exp\left(\frac{V + J.r_s}{n_2 . V_{th}}\right) - 1\right) - \frac{V + J.r_s}{r_{sh}} \qquad \text{III.1}$$

Two diodes model parameters	J_{01} [fA / cm²]	n_1	J_{02} [nA / cm²]	n_2	r_{sh} [Ohm.cm²]
Value	12.8	1	7.78	2	∞

Table 1: Two diodes models parameters of the reference cell for the study of cutting steps impact

The corresponding IV parameters are given in the Table 2:

IV Parameters	I_{sc} [A]	V_{oc} [V]	I_{mpp} [A]	V_{mpp} [V]	P_{mpp} [W]	FF %	η %
Value	9.30	0.729	8.71	0.612	5.33	78.6	21.7

Table 2 : IV parameters of the reference cell for the study of cutting steps impact

The series resistance of a module can be written as a contribution of the cell and a contribution of the module interconnections. The contribution of each of the components to the losses by Joule effect is different according to the number of cuts that are made. Some losses are dependent on the total cell area in the module and do not change with the number of cuts, whereas others losses items differ.

III.A.1.b *Impact of the number of cutting steps on the module performance*

The first step is to check the behaviour of the model when the cells of the module are split but not integrated into a module. For this, we are interested in an IV cell measurement that does not include the resistance of the fingers. The sum of the power of the 72 cut-up cells must remain constant, since the difference is only made at the level of the resistive losses in the cell interconnection strips. This is what is explained below.

Number of sub-cell N	**1**	**2**	**3**	**4**	**5**	**6**
Number of cutting steps	*0*	*1*	*2*	*3*	*4*	*5*
Number of sub-cell in module	72	144	216	288	360	432

Table 3: Correspondence between the number of sub-cells obtained in N cuts of a full-cell and the number of total sub-cells present in a module equivalent to 72 full-cells in series.

Since the parameters of the uncut two-diode cell model are considered homogeneous over the entire surface, decreasing the photo-generated current implies decreasing also the recombination currents by a similar factor, and the series and shunt resistances as well (as seen previously). By multiplying left and right the two-diode model equation III.1 by the surface area S_N of the elementary cell in $N-1$ cutting steps, we obtain equation III.2. This is because $I = j.S$ and $R_{sh} = \frac{r_{sh}}{S}$:

$$I_N = I_{ph,N} - I_{01,N}\left(\exp\left(\frac{V + J.r_s}{n_1 . V_{th}}\right) - 1\right) - I_{02,N}\left(\exp\left(\frac{V + J.r_s}{n_2 . V_{th}}\right) - 1\right) - \left(\frac{V + J.r_s}{R_{sh,N}}\right) \quad \text{III.2}$$

Because $J.r_s = (JS_N).(r_s/S_N) = I_N R_{s,N}$, we obtain the equation of the two-diode current model for the sub-area cell S_N (equation III.3)

$$I_N = I_{ph,N} - I_{01,N}\left(\exp\left(\frac{V + I_N.R_{s,N}}{n_1 .V_{th}}\right) - 1\right) - I_{02,N}\left(\exp\left(\frac{V + I_N.R_{s,N}}{n_2 .V_{th}}\right) - 1\right) - \left(\frac{V + I_N.R_{s,N}}{R_{sh,N}}\right) \quad \text{III.3}$$

It can be written according to the parameters of the full-cell:

$$I_N = \frac{I_{ph,F}}{N} - \frac{I_{01,F}}{N}\left(\exp\left(\frac{V + I_N.R_{s,F}.N}{n_1 .V_{th}}\right) - 1\right) - \frac{I_{02,F}}{N}\left(\exp\left(\frac{V + I_N.R_{s,F}.N}{n_2 .V_{th}}\right) - 1\right) - \left(\frac{V + I_N.R_{s,N}.N}{R_{sh,F} .N}\right) \quad \text{III.4}$$

which gives, by multiplying left and right by N, the exact two-diode current model equation for the full-cell:

$$I_F = I_{ph,F} - I_{01,F}\left(\exp\left(\frac{V + I_F.R_{s,F}}{n_1 .V_{th}}\right) - 1\right) - I_{02,F}\left(\exp\left(\frac{V + I_F.R_{s,F}}{n_2 .V_{th}}\right) - 1\right) - \left(\frac{V + I_F.R_{s,F}}{R_{sh,F}}\right) \quad \text{III.5}$$

The equations of the two-diode current models for each of the cells of area S_N are therefore perfectly equivalent: they generate a current I reduced by a factor N. Considering the sum of sub-cells, because all the sub-cells will be connected in series, the current remains the same, but voltages are added.

	$\mathbf{I_{sc}}$	$\mathbf{V_{oc}}$	$\mathbf{I_{mpp}}$	$\mathbf{V_{mpp}}$	**FF**	$\mathbf{P_{mpp}}$
One sub-cell	$\frac{I_{sc-F}}{N}$	V_{oc-F}	$\frac{I_{mpp-F}}{N}$	V_{mpp-F}	FF_F	$\frac{P_{mpp-F}}{N}$
Sum sub-cell	$\frac{I_{sc-F}}{N}$	$V_{oc-F}\ N$	$\frac{I_{mpp-F}}{N}$	$V_{mpp-F}\ N$	FF_F	P_{mpp-F}

Table 4: Value of IV parameters of the single sub-cell at N level, and value for the sum of the N sub-cell expressed as a function of IV parameters of the full-cell.

This is what is shown in Figure 51. The photo-generated current follows a power law in 1/N since it is proportional to the surface area of the cell, where N is the number of sub-cells obtained after cutting. The open circuit voltage V_{oc} and the MPP voltage V_{mpp} are proportional to N. The power P_{mpp} and the fill factor FF remains constant (386W and 78.6 %).

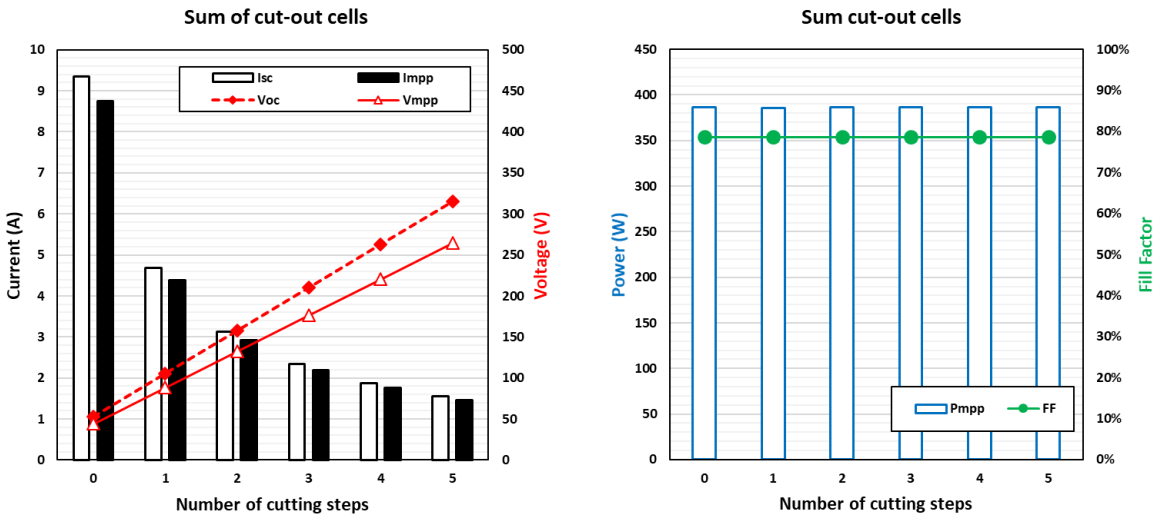

Figure 51: Evolution of the IV performance of the sum of cut-out cells as a function of the number of cutting steps: variable I_{sc}, V_{oc}, I_{mpp} and V_{mpp} (left) – and constant FF and P_{mpp} (right).

When the N x 72 sub-cells are interconnected in series, the resistive effect of the ribbons appears. According to Guo *et al.* [134], the power $P_{loss}(N)$ lost by Joule effect in the module interconnections as a function of the number of sub-cells N is given by the equation III.6 :

$$P_{loss}(N) = I_{mpp-F}^2 \left(R_{sc-F} + \frac{1}{N^2} R_{sm-F} \right) \quad \text{III.6}$$

The relative power loss reduction on ribbon can be calculated as follows (equation III.7):

$$R_N = \frac{P_{loss}(1) - P_{loss}(N)}{P_{loss}(1)} = 1 - \frac{1}{N^2} \quad \text{III.7}$$

This behaviour can be seen in Figure 52. The currents I_{sc} and I_{mpp} are decreasing in 1/N. The power of the panel consisting of full-cells is 360.5 W. The larger the number of sub-cells in the module is, the more the power of the module increases. The gain is higher for the first cut-outs, and decreases progressively: For 1 cut-out (half-cell), the power is 368 W. For five cuts, the power is only 371 W. This power gain is entirely explained by the gain in fill factor FF, which goes from 76.2 % for a full-cell to 77.9 % for a half-cell and then to 78.4 % with 5 cuts.

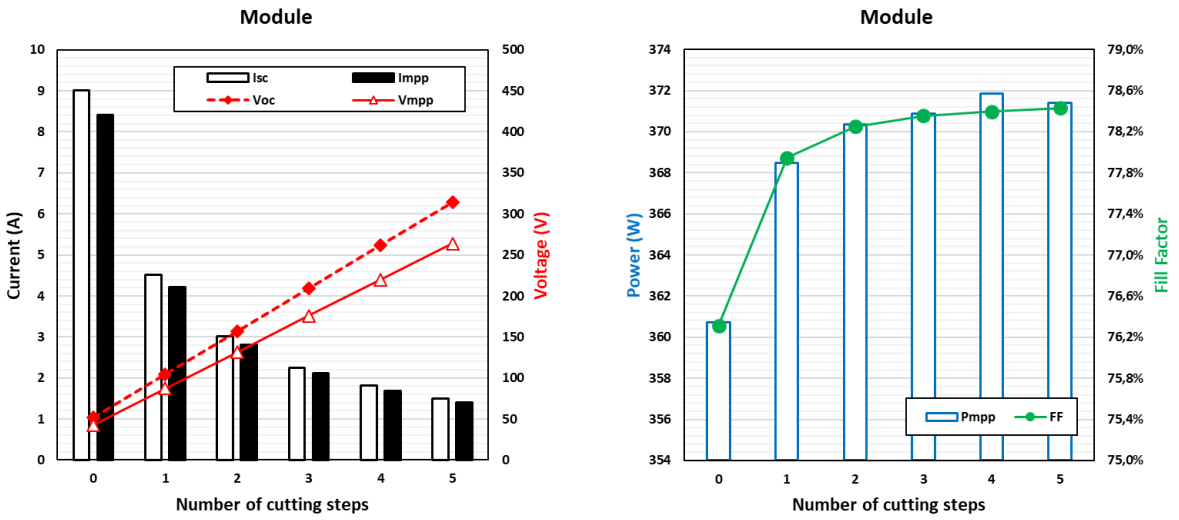

Figure 52: Evolution of module IV performance as a function of the number of cutting steps: I_{sc}, V_{oc}, I_{mpp} and V_{mpp} (left) - FF and P_{mpp} (right).

The Joule loss reduction factor of equation III.7 indicates that the resistive losses in a module made up of N sub-cells and normalised by the resistive losses in a full-cell, all as a function of the number of sub-cells N, follows a power law. The result of the model developed in the thesis is shown in the Figure 53. The exponent power law of -2 corresponds to what is expected: a multiplication by 2 of the number of sub-cells corresponds to a division of the losses by 4 (75 %). A multiplication by 4 corresponds to a decrease in resistive losses by 16 (93.7 %).

The loss of FF in the module interconnection is given by equation III.8 :

$$\Delta FF_F = \frac{R_{sm-F}\, I_{mpp-F}^2}{I_{sc-F}\, V_{oc-F}} \qquad \text{III.8}$$

The loss of FF in the module interconnection when cutting a full-cell into N sub-cells is given by the equation III.9 :

$$\Delta FF(N) = \frac{R_{sm-F}\, I_{mpp-F}^2}{I_{sc-F}\, V_{oc-F}} \frac{1}{N^2} = \frac{\Delta FF_F}{N^2} \qquad \text{III.9}$$

The impact of the number of cuts on the cell to module ratio is shown in the Figure 54. It can be seen that the CTM_{Voc} remains constant. The effect of reducing resistive losses is first visible on the CTM_{Vmpp}, which goes from 97.3 % in full-cell to 99.1% in half-cell (+1.8 %) then to 99.6 % (+ 2.3 %) in sixth of cell. The effect is more pronounced in the CTM_{FF} which goes from 97.1 % in full-cell to 99.1 % in half-cell (+ 2.0 %) then to 99.7 % in sixth of cell (2.6 %). Finally, it is visible on the CTM_{Pmpp}: 93.4 % in full-cell, 95.5 % in half-cell (+ 2.1 %) and 96.2 % in sixth cell (+ 2.8 %).

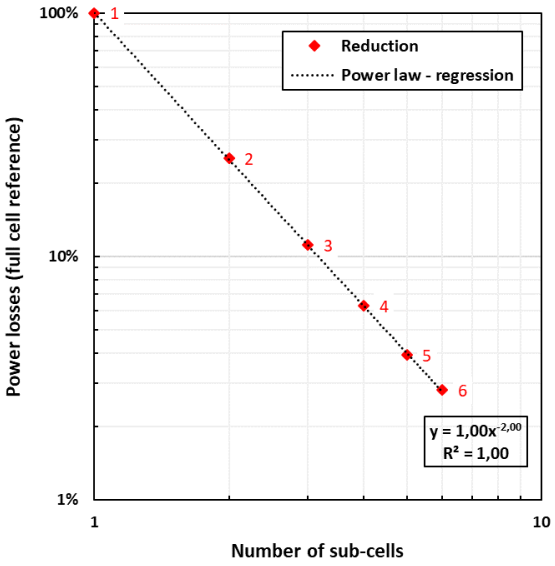

Figure 53: Resistive losses at the module level as a function of the number of sub-cells and normalized by the losses of the full-cell case.

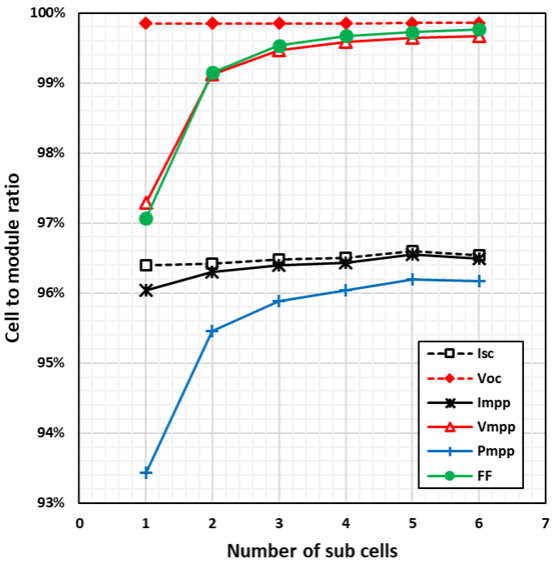

Figure 54: Impact of the number of sub-cells on the cell to module ratio (CTM) for the six IV parameters (Glass/glass module: no inter-cell I_{sc} power gains)

The effect on the CTM is greater for FF than for V_{mpp} because FF cumulates the effects of V_{mpp} and I_{mpp}. The slight increase in CTM_{Impp} is a consequence of the effect of the CTM_{Vmpp}. Because the voltage at the terminals of the diodes at the MPP is lower when the resistive losses are reduced, the recombination currents are also lower and the I_{mpp} is therefore higher.

The CTM_{Isc} should remain constant. However, it is not the case. The shading of the fingers on the cell is the cause. In the developed model, when cutting an entire cell in N sub-cells, the number of finger is divided by N. If this value is not integer, it is rounded. We can therefore have a current I_{sc} which does not exactly follow the decrease in 1 / N. This effect is also visible on the I_{mpp} and thus on the P_{mpp}. This is why the increase in CTM_{Pmpp} (+2.8 % for sixth cells) is greater than for FF (+2.6 %).

Thus, the power gain generated by a drop in resistive losses when the entire cells of a module are cut into N sub-cell is already 75 % of the max gain in half-cell and 90 % in third-cell. As cell cutting is an additional step compared to the classic full-cell module process, this represents an additional manufacturing cost. Moreover, cutting an entire cell in N sub-cell decreases the throughput of the production line by a factor of N. It is therefore not interesting to go to a very large number of cuts.

Comparison with literature

The gains that can be obtained by the integration of cut cells in a module is widely documented. Muller *et al.*, in 2015 show an increase of FF of 3.9 % when comparing a 9 full-cell module and an 18 half-cell module with PERC solar cell of 20 % efficiency [135]. Malik *et al.*, measured a gain of only 0.3 % on the FF between full and half-cell module [136]. Guo *et al.* mentioned a gain of +1.8 % on FF between a single cell multi-crystalline module and the corresponding half-cell module [134]. The cell have an efficiency of 17.3 %. The gain, much more limited than Muller *et al.*, could be explained by the number of cell in the module: the series resistance contribution of string interconnection ribbons doesn't vary linearly with the

number of cell. It has a smaller impact in module with a high number of cell by string. Tang *et al.*, compared a 32 full-cell module with a 64 half-cell module and a 128 quarter-cell module [137]. They found an increase in FF of 1.1 % for the half-cell module and an increase of 1.3 % for the quarter-cell configuration. They also characterize the losses due to the cutting step in term of FF around 0.6 % for both cut-cell configuration: this means the theoretical gain in FF without losses during the cutting process is +1.7 % for half-cells and +1.9 % for quarter size. Hanifi *et al.* found an increase of +1.5 % in FF [129]. Zhang *et al.*, have used 18.2 %, 18.4 % and 19.2 % PERC solar cell in glass-glass module and obtain a gain in FF of respectively 2.6 %, 2.0 % and 1.8 % [138].

Except for the extremum studies of Muller *et al.* and Malik *et al.*, the FF gain obtained by switching from full-cell to half-cell with our model is 1.6 % (Figure 52), in very good agreement with other studies on the subject.

All these different results come from the different kinds of cell interconnection and string interconnection used. The maximum FF gain corresponds to the loss observed on this parameter and generated by the series resistance of the module interconnections in a full-cell configuration. The lower this resistance is, the lower the gain expected when cutting the cells. Thus, the effect of other module parameters and environment is analysed in the next part.

III.A.2 Dependence of resistive gains on incident irradiance and module design

III.A.2.a *Impact of irradiance on the cutting gains of performance*

Dependence of IV parameters as a function of irradiance: generalities

The irradiance on the front face of the module has an effect on the IV parameters and therefore logically on the performance gains expected when cutting N sub-cells. The irradiance directly impacts the photo-generated current I_{ph} of the two-diode model, from which the IV parameters can be calculated. It is therefore necessary to first explain the variation of the IV parameters as a function of I_{ph} for an entire cell. The influence of I_{ph} is also dependent on the other parameters of the two-diode model, in particular the diffusion current I_{01}, the recombination current I_{02} and the series resistance r_s. This is shown in Figure 55. The parameters of the two-diode model are still those defined in Table 1. Three different cases are studied: (i) the influence of diode 1 only (I_{02} and r_s are zero) (ii) the influence of diode 1 and diode 2 simultaneously (addition of recombination: only r_s is zero) (iii) the influence of diode 1, diode 2 and the series resistance r_s. The shunt resistance is always considered infinite.

The short circuit current I_{sc} is equal to the photo-generated current as long as the shunt resistance is not too low and the series resistance is not too high. This is the case here. The influence of the I_{sc} on 4 IV parameters: V_{oc}, V_{mpp}, fill factor and efficiency is plotted. The current at P_{mpp} - I_{mpp} - is not plotted because it is proportional to the short circuit current I_{sc} and provides little information. A short circuit current of 9 A correspond to the standard test condition of 1000 W/m².

With only diode 1 (diffusion), the V_{oc} has a logarithmic dependence according to the I_{sc}, which is expected. It increases from a V_{oc} of 0.685 V at 1 A to 0.742 V at 9 A and then 0.749 V at 12 A. By adding diode 2 (recombination), the V_{oc} decreases logically. However, it decreases

more at low irradiance: we go from 0.659 V at 1A to 0.732 V at 9 A then to 0.741 V at 12 A. Asexpected, the addition of the r_s has no impact on the V_{oc}.

With only diode 1 (diffusion), the V_{mpp} has a logarithmic dependence according to the I_{sc}, like the V_{oc}. It increases from a V_{mpp} of 0.603 V at 1 A to 0.657 V at 9 A then 0.664 V at 12 A. By adding diode 2 (recombination), the V_{mpp} decreases but keeps a logarithmic dependence: from 0.549 V at 1A to 0.635 V at 9 A then 0.644 V at 12 A.

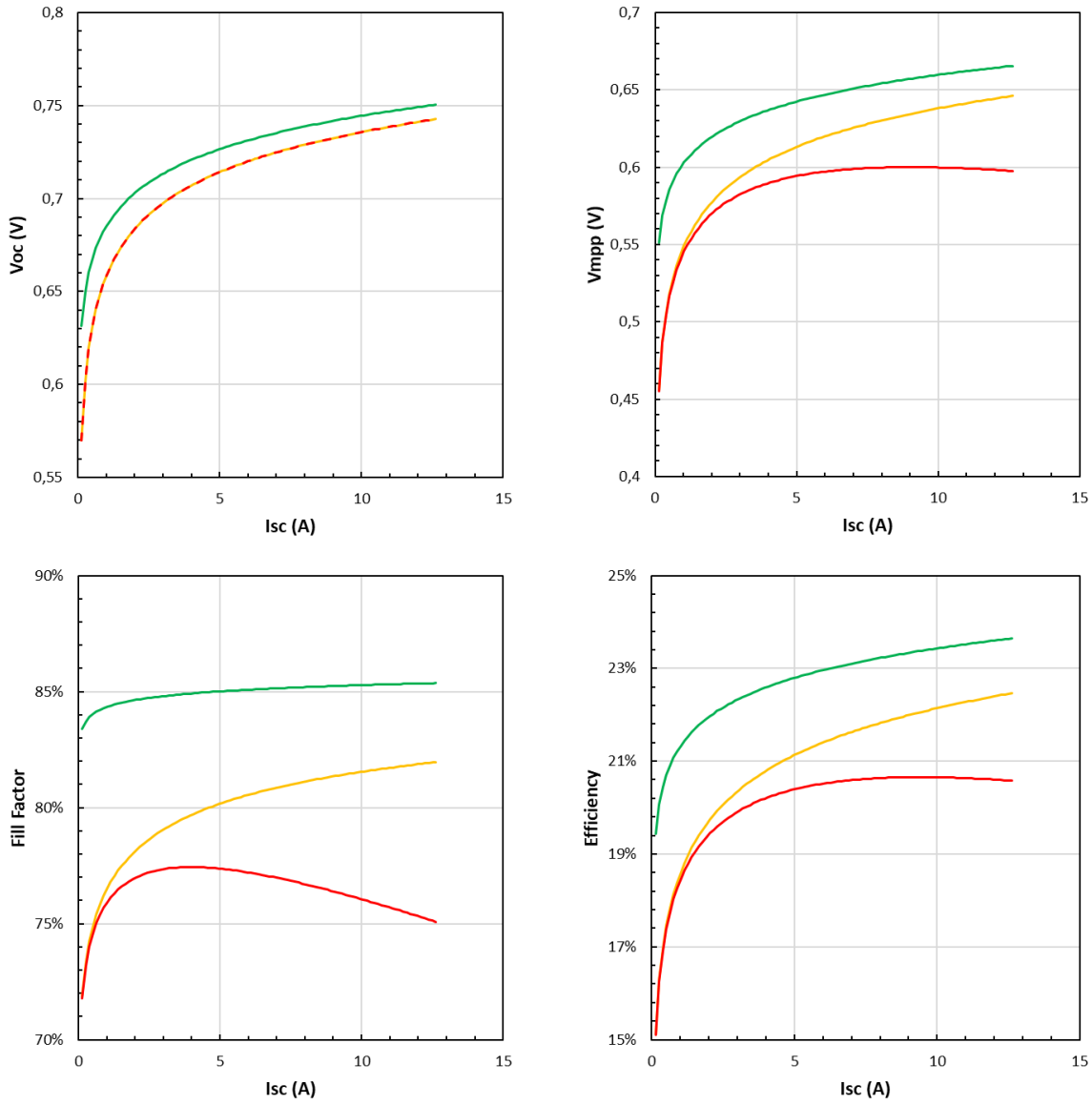

Figure 55: Variation of the IV Parameters V_{oc}, V_{mpp}, FF and efficiency as a function of I_{sc}. Progressive complexity of the 2-diodes model is plotted: only diode 1 with I_{01} = 12.8 fA/cm² and n1 = 1 (green), with diode 1 + diode 2 with I_{02} = 7.78 nA/cm² and n2 = 2 (orange) and diode 1 + diode 2 + serie resistance of 1.124 Ohm.cm² (red).

The addition of the r_s implies a drop in voltage quadratically dependent on the current I_{mpp}, itself proportional to the I_{sc}. We therefore go from 0.545 V at 1 A to 0.600 V at 9 A then 0.598 V at 12 A. We therefore see an optimum appear at 8.5 A and 0.600 V for the V_{mpp}: at too

low irradiance, the effect of the series resistance is negligible but the effect of the diodes is important. With too strong irradiance, it is the reverse.

The dependence of the fill factor on the photo-generated current is the addition of the effects of I_{sc}, V_{oc}, V_{mpp} and I_{mpp}. The fill factor has a weak logarithmic dependence when only diode 1 is considered. By adding diode 2, the logarithmic dependence is more marked. We can clearly see the impact of the series resistance on the FF: an optimum appears at I_{sc} of 4 A for a FF of 77.4 %.

The efficiency of the full-cell follows the same behaviour as the fill factor: a logarithmic behaviour with diodes one and two, and the presence of a maximum when the series resistance is included. The higher the series resistance, the better the optimum will be at low irradiances. Conversely, with a low series resistance, the optimum efficiency is shifted towards high currents. The optimum lies at different currents for the FF and for the efficiency. In fact, in the calculation of the efficiency, the P_{mpp} is divided by the incident power, proportional to the I_{sc}. In the case of the FF, P_{mpp} is divided by the I_{sc} and the V_{oc}. It is the logarithmic dependency of the V_{oc} that shifts the curve, producing an optimum of FF at a lower current than the one for optimal efficiency. These optimums in FF and efficiency mean that the module or cell must work at these respective irradiances to be most efficient, but it is obviously not at theses irradiances that it produces the most power.

Dependence of IV parameters as a function of irradiance: impact of cutting steps

The FF and the efficiency therefore depend on irradiance, and the expected gains on these parameters when cutting the cells therefore also depend on irradiance. Indeed, at low irradiance, resistive losses are expected to be negligible and the interest in cutting the cells is reduced. The results are presented in Figure 56.

The optimum FF for a full-cell module is therefore 400 W/m². For a given irradiance, as the number of sub-cells increases, the FF increases, as seen above. A limit value is reached which corresponds to FF where the series resistance of the cell interconnection ribbons has no influence. As the FF gains obtained by cutting are higher at higher irradiance, the optimum in FF is shifted at higher irradiance for a module consisting of several sub-cells. The FF optimum is 700 W/m² for sixths of a cell. 75 % of the FF gains are obtained at the first cut, whatever the irradiance on the front panel. This represents a FF gain for the module in question of 1.65 % under STC conditions (1000 W/m²) and only 0.35 % for an irradiance of 200 W/m². This corresponds to a gain of 0.44 % abs in efficiency at STC and 0.09 % abs at 200 W/m². FF gains are therefore linear with irradiance, as are efficiency gains.

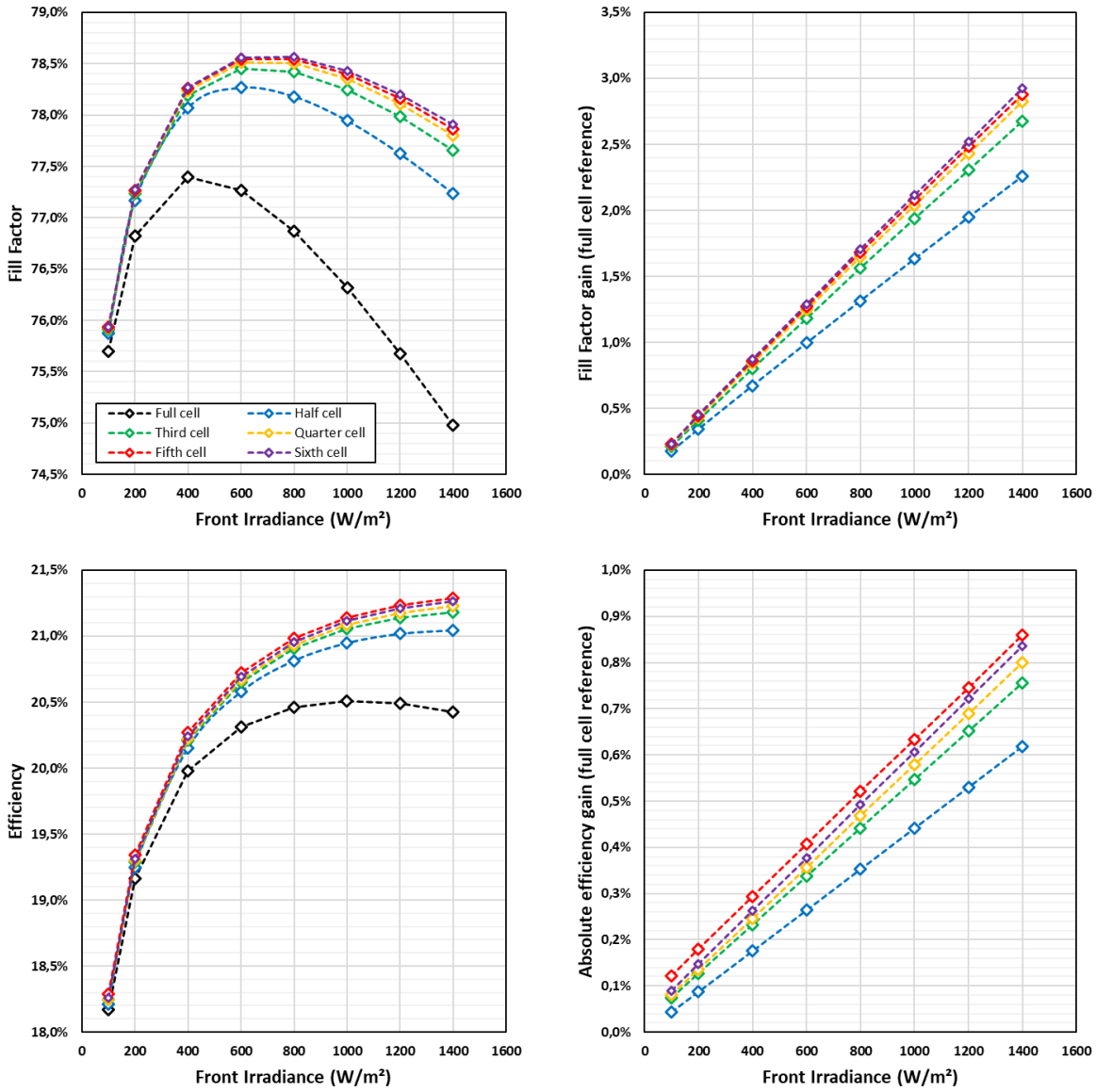

Figure 56: Evolution of the FF of the module as a function of irradiance, for increasing numbers of cut-out sub-cells (top left). FF gains compared to the reference case of uncut full-cells (top right). Evolution of efficiency as a function of irradiance (bottom left) and gains compared to full-cell case (bottom right).

.

If a back-side irradiance is present in addition to a front-side irradiance (bifaciality), the resulting current is higher and the FF gain due to cutting is greater. For example for a BIFI 10 situation (1000 W/m² front + 100 W/m² rear) with a 90 % bifacial module, the FF gain with a cut-out (half-cell) is obtained by looking at an incident irradiance of 1000 + 0.9*100 = 1090 W/m². The FF gain in this case is 1.8 %.

III.A.2.b *Impact of the parameters of the cell and module*

The power gain that can be obtained by cutting full-cells and limiting the resistive losses in module is obviously dependent on the module contribution to the total series resistance. As shown by equation III.9, the FF gain is linear with the share of series resistance of the cell interconnection ribbons.

Impact of the number of cell interconnection wires

The contribution of the module to the series resistance is mainly due to the cell interconnection wires. The series resistance varies quadratically with the wire diameter d_w. It is proportional to the wire length and inversely proportional to the number of wires n_w. This is given by the following equation III.10:

$$R_{sm} = \frac{\rho_{eff}.L}{S} = \frac{\rho_{eff}.L}{n_w\,\pi\left(\frac{d_w}{2}\right)^2} \qquad \text{III.10}$$

For a constant diameter and a constant effective resistivity, the more the number of wires in parallel increases, the more the total section increases and the more the resistance decreases. This can be seen on the left in Figure 57. But parallel to the increase in FF, the more wires there are, the higher the shading of the cell is. Here, the shading of the wires is fixed at 57 % of their width.

As a result, an optimum in efficiency can be found as a function of the number of cell interconnection wires (Figure 57 - right). Optimal number of wires for this configuration decreases with the number of cutting steps. In full-cell configuration, the optimal number in terms of efficiency is found to be 24, decreases to 15 in half-cell configuration, 14 in third-cell and 13 in half-cell. These results are closely linked to the other parameters of the module, and in particular: the diameter of the wires, the resistance of the metallization grid, the current I_{mpp} (and therefore all the parameters of the equivalent circuit of the module, in particular the optics and the recombination diodes).

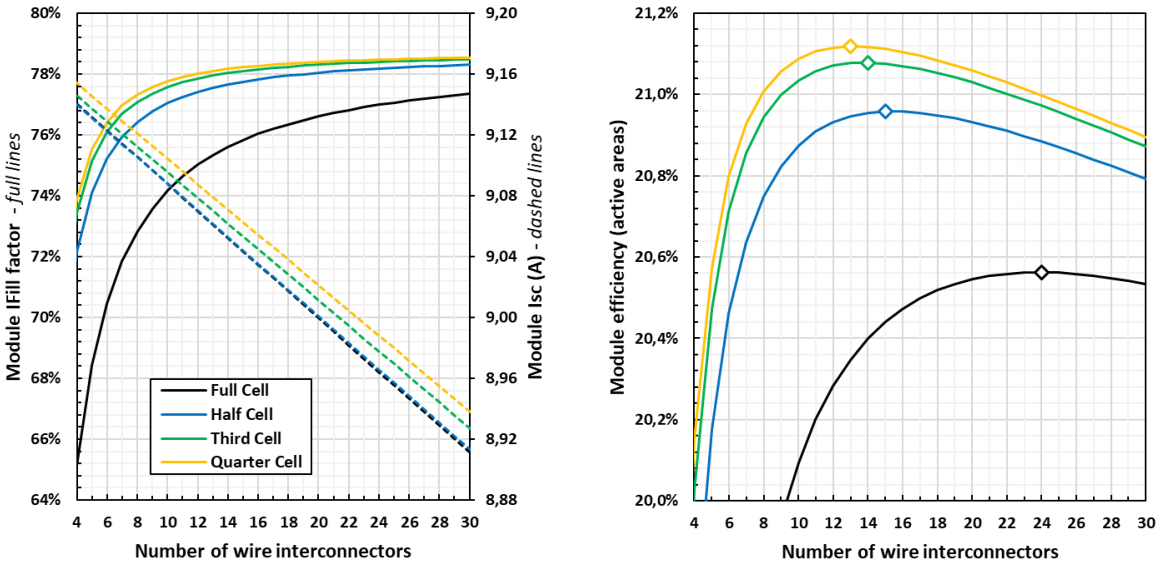

Figure 57: Dependence of the module fill factor FF (left figure, left axis) and short circuit current I_{sc} (left figure, right axis) and the module efficiency (right figure) on the number of cell interconnector wires for 1,2,3 and 4 sub-cell

Impact of the inter-cell distance

The previous results are valid for a zero inter-cell distance. In this part, we focus on a non-zero distance. In a string of full-cells, the total cell length does not vary when cut into sub-cells. On the other hand, the proportion of the total inter-cell space in relation to the total length of the string increases with the number of cuts. Can this effect change the previous conclusions of continued FF improvement as the number of cuts increases?

In a conventional architecture, the distance between the cells is necessary to pass the interconnection wires from the front face of one cell to the rear face of the next cell. This point is mechanically weak, and can cause cell breakage if they are too close together. Indeed, during thermal cycling peaks, the differential expansion of the materials will concentrate the stresses at this location. This distance increases the size of the module, and therefore the total length of interconnection wires. This results in more series resistance. This effect is all the more marked for a high number of cell cuts: twice as high for half-cells, three times for third cells, etc.

The effect of increasing the series resistance by an increase in the inter-cell distance is visible on the Figure 58. It can be noted that the FF decreases when the inter-cell distance increases. But we can clearly see that, regardless of the inter-cell distance, increasing the number of cuts is always a better choice in terms of electrical performance.

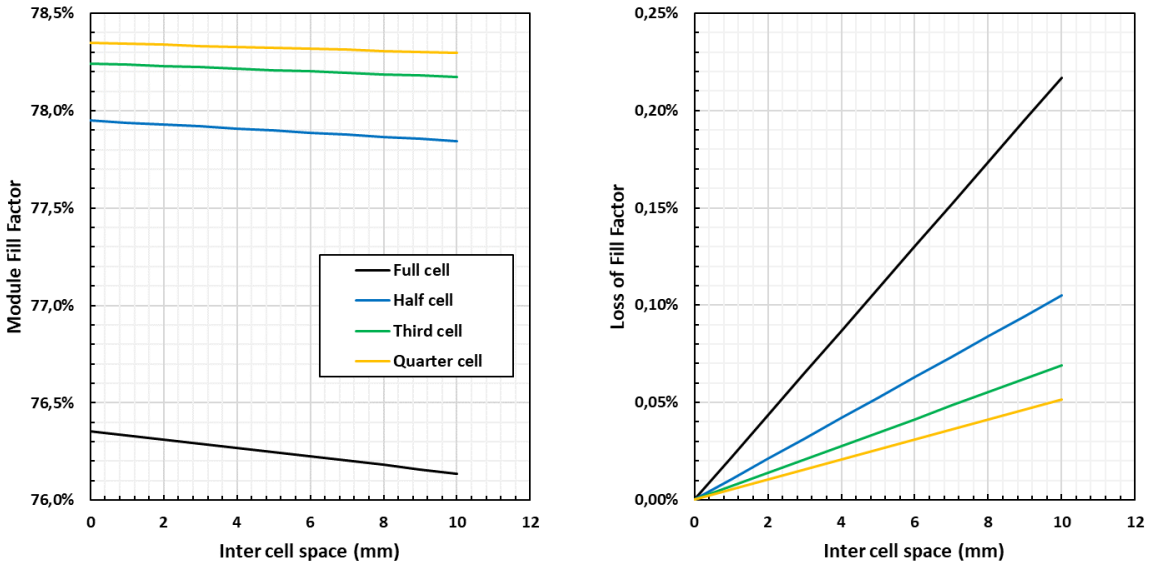

Figure 58: Dependence of module fill factor FF as a function of the inter-cell distance, considering an architecture of full-cell, half-cell, third-cell and quarter-cell.

This behaviour comes from the following observation: the FF gains due to the number N of sub-cells of an entire cell varies in (1 / N^2), as shown in equation III.9. On the other hand, the series resistance contribution of the inter-cell distance is linear depending on the number of cuts. This results in an ever decreasing trend of the FF losses as a function of the number of cuts. The total length L_F of a string made of full-cell can be written as:

$$L_F = n_{cell,F}\ (2\ L_{cell,F}. + d_{intercell}) \qquad \text{III.11}$$

And the generalisation of total length L_N of a string made of cell cut in N part is:

$$L_N = n_{cell,F}\ N\left(2\frac{L_{cell-F}}{N} + d_{intercell}\right) \qquad \text{III.12}$$

$$L_N = L_F + (N-1).n_{cell,F}\ d_{intercell} \qquad \text{III.13}$$

The loss of FF in the cell interconnections therefore has a 1 / N² component, due to the part of the ribbons on the cells, and another 1 / N component due to the inter-cell spaces. FF losses as a function of the inter-cell distance are therefore always greater for a reduced number of cuts. This can be seen in the graph to the right of Figure 58. For typical values of inter-cell distance - 3 mm - FF losses are 0.07 % in full-cell, and less than 0.02 % in quarter-cell. Negligible values in view of other phenomena.

The incompressible inter-cell space also has a direct impact on the total surface area of the module and therefore on its efficiency. This has two antagonistic effects: the more the number of cuts increases, the more the resistive losses in the cell interconnections decrease, but the more the share of inactive surface in the total surface of the module increases.

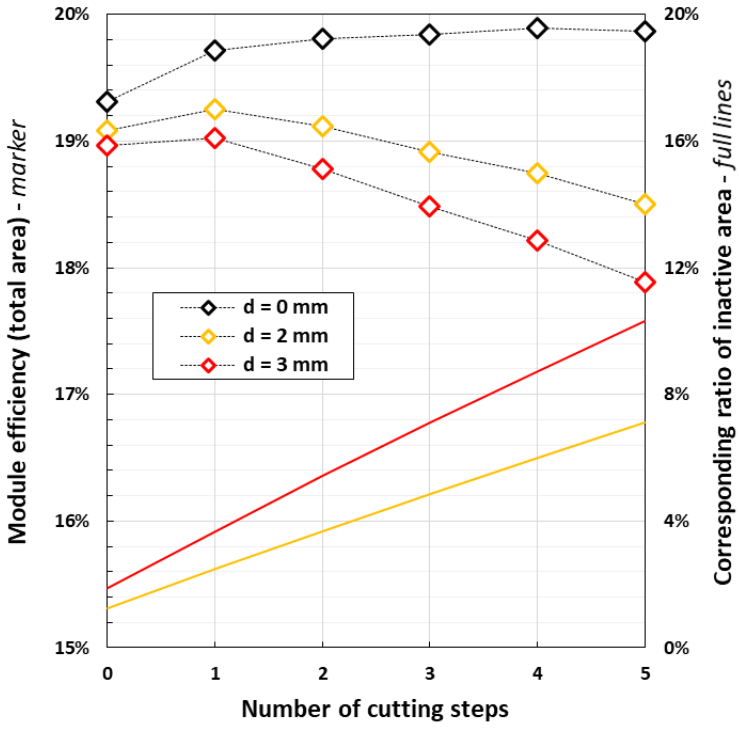

Figure 59: Impact of the number of cutting steps and the inter-cell distance d on the module efficiency, considering the total area of the module made of M2 wafer.

This phenomenon is highlighted in Figure 59. The efficiency gains increase with the number of cuts, when the inter-cell distance is neglected. When the inter-cell distance is taken into account, even as small as 2 mm, the efficiency increases to a maximum for one cut (half-cell configuration). It then decreases linearly, the faster the inter-cell distance is taken into account. As a reminder, the module always contains 72 cells in full-cell equivalent, so the total active surface is similar whatever the number of cut.

On the other hand, the size of the wafers is important. The results of Figure 59 are valid for M2 wafers with an area of 244.33 cm^2. For module made of bigger wafers the share of inactive area in the total area is lower. The impact of the inter-cell distance will therefore be less important, and the optimal efficiency depending on the number of cuts could be shifted to a higher number of cuts.

Conclusion of Part III.A:

In this introductory part, we were interested in the maximum performance gains expected by cutting the cells (without losses during this step). The resistive losses in the cell interconnection follow a law in $1/N^2$, where N is the number of sub-cells obtained after cutting a full-cell. The advantage obtained by cutting is therefore mainly due to the first cut. This effect, well known in literature and industry, allows us to validate the basic behaviour of our model when taking into account the cutting of full-cells. The effect of irradiance does not change its behaviour, even though the FF gains caused by cutting are weaker and weaker as the irradiance decreases. By taking into account the effect of an incompressible inter-cell distance, the trends are not changed: the law of variation of resistive losses is enriched with a term in 1/N. The effect of recombination will significantly modify these behaviours: this is the subject of Part III.B.

Part III.B Cut HJT cells: taking into account edge recombination losses in silicon HJT module performance

The process of cutting a cell generates losses on the cell itself. Cutting, whether done by laser, mechanical cleavage, or more advanced techniques, creates a new non-passivated edge on the cell. This edge is an additional recombination place that logically impacts its performance. This effect is more pronounced for high-performance cells, where initial passivation is very high: this is the case with heterojunction silicon solar cells. Cutting can also cause damage to the active layers and result in a drop in the photo current generated by the cell. A brief description of the non-passivated edge loss mechanisms and how they can be modelled within a cell described by an equivalent circuit model is proposed. The impact of these losses as a function of the cutting geometry and the cell geometry will also be discussed.

III.B.1 Characterization of HJT cell losses caused by the cutting process

Performance losses due to recombination on the edges of a cell have been studied for a long time. Indeed, these areas are unavoidable: they inevitably appear during the cutting of silicon ingots. Smaller cells are more affected because their perimeter-to-area ratio is higher: the defect density is higher. However, the industry is moving towards larger and larger wafers. From a 2012 standard, M0, with a 156 mm side, we are moving towards a standard that will probably be M6 (166 mm) in 2021. One might think that the problem is less and less important, but the cutting of cells for half-cell or shingle type architectures is also becoming a standard. Minimizing these losses is therefore more important than ever. A chronological presentation of the main studies on edge recombination is presented below.

As early as 1978, Henry *et al.* proved that a diode characteristic with ideality factor of two can be explained by surface recombination at the junction perimeter [139].

In 1995, Aberle *et al.* mentioned that unpassivated edges induce a high recombination activity. They used a strategy of masking the edges of the cell with an aluminium mask to make the edges of the cell inactive. Without this, the performance of the PERL laboratory cell of 2 cm side would have a reduced efficiency of 0.8 $\%_{abs}$ [140].

In 1996, Altermatt *et al.* analysed the reduction in efficiency due to perimeter losses as a function of the distance between the active cell area and the cut edge, and showed how the optimum distance depends on whether the cells in the panel are shingled or not [141].

In 2000, Khun *et al.* investigated by means of two-dimensional modelling the recombination mechanisms occurring in edge regions. It is shown that a poor quality of the surface passivation near the pn-junction borders is mainly responsible for the observed losses in fill factor and open-circuit voltages. They suggest that edge recombination current could not exceed 20 nA/cm [142].

In 2001, Breitenstein *et al.* used lock-in thermography to investigate edge leakage currents in silicon solar cells after laser scribing and cleavage [143]. The same year, McIntosh mention a new mechanism with recombination at the cell edge limited by series resistance [144]. He also concluded that unless the edge-recombination current is below 10 nA/cm, it significantly reduces the efficiency, even for medium-to-large area solar cells [145]. The next

year, Glunz *et al.* have designed cell for low illumination level, taking special care to keep efficiency high by analysing and optimizing cell border. They mention an edge recombination current of 13 nA/cm [146].

In 2003, Hermle *et al.* confirmed that at low illumination densities, solar cells are very sensitive to the recombination at the cell edges. Their modelling shows that at low illumination the main recombination channel at the perimeter is due to the surface recombination in the space charge region [147].

In 2010, Breitenstein *et al.* found that in order to obtain the high current-densities and ideality factors above 2 at a forward bias below 0.6 V, recombination in heavily defected regions must be modelled beyond the SRH approximation of independent defect states [27]. Same year, Kray *et al.* modelled and optimized the geometry and isolation of the edge region in silicon solar cells. They investigate the effect of 10 to 300 nA/cm edge current recombination on performance device [148].

In the 2010's, the theme of full-cell cutting appears, and losses due to unpassivated edges receive even more attention.

In 2014, Eiternick *et al.* proved that recombination plays the major role for an optimized laser separation process. Additionally they identify the laser scribing process as the major source of losses in comparison to the mechanical breaking. They found a J_{02} edge of 40 nA/cm, almost independent of the monocrystalline / multicrystalline characteristic of the wafer [149].

In 2015 Muller *et al.* performed a loss analysis on PV module made from half-cell silicon PERC and mentioned a loss in efficiency due to rear laser cut of 0.2% [135]. Chan *et al.*, used edge isolation with laser doping to separate peripheral shunted region from active area. They get an average improvement in FF of 1.7 $\%_{abs}$, and 0.5 $\%_{abs}$ efficiency increase. The J_{02} values achieved using this process ranges from 5.9 to 15.5 nA/cm [150]. The same year, Rühle *et al.* investigate the use of emitter windows with varying passivation layers in an intensity range between 1 and 10^{-3} suns. An aluminium oxide for passivation of the non-diffused region outside the emitter windows resulted in a reduction in edge recombination of a factor of 8 [151]. Still the same year, Eitnernick *et al.* used thermal laser separation (TLS) – a damage free and kerfless dicing technology – for cell splitting. It is found that the electrical properties of the TLS-half-cells are slightly better compared to the reference process and that compared to a classical laser separation there is no mechanical damage due to the TLS process [152]. Still in 2015, Wong *et al.* modelled M0 PERC and Al-BSF solar cell as a vast network of diodes. It is noted that the monocrystalline silicon PERC cells studied have significantly lower peripheral and second diode edge recombination compared with Al-BSF cells [153].

In 2017, Bertrand *et al.* studied two methods for modelling of edge recombination current in Al-BSF silicon solar cells. The first one is based on IV fitting and the second one on V_{oc} analysis. The second method is found to be more accurate and gives an edge recombination current of 20.6 nA/cm [154].

In 2018, [155] Fell *et al.* proposed a new approach to model edge recombination in silicon solar cells. The model accounts for recombination both at the edge of the quasi-neutral bulk as well as at an exposed space-charge-region (SCR), the latter via an edge-length-specific diode property with an ideality factor of 2: a localized J_{02} edge. A fitted value of ~19 nA/cm is

found, which is shown to be largely independent of device properties, including SHJ cells [155]. Mittag *et al.* used this value to perform techno-economic analysis of half-cell modules [109].

In 2019, Li *et al.* studied the J_{sc} loss of full area SHJ solar cells caused by edge recombination. They demonstrated that this J_{sc} loss effect can be suppressed effectively by simply controlling the gap between the edge of the transparent conductive oxide layer and that of the cell [156]. The J_{sc} can also be affected by the cutting process. The same year, Stolzenburg *et al.* found a J_{02} edge of 3 nA/cm by separating the contribution of the two relevant edge recombination losses: (i) recombination at the bulk edge, described by an effective surface recombination velocity, and (ii) recombination at the pn-junction edge described by an edge-length specific non-ideal recombination parameter J_{02} edge [157].

In all these studies, the experimental values of edge recombination current values vary from 3 nA/cm to over 70 nA/cm. This discrepancy between the lowest and the highest value implies losses on the IV parameters that are too dispersed to accurately model the performance of an SHJ module. The behaviour of the edge recombination current for SHJ cells has therefore not been deeply investigated. Due to their high level of passivation, the presence of amorphous layers and an emitter on the back side, it is necessary to question the value of J_{02} edge that can be obtained for this technology.

III.B.1.a *Experimental setup*

All the twenty solar cells in this work are made using the same process, based on M2 format n-type substrates (156.75 x 156.75 mm2) with a resistivity of 3 Ω.cm. Wafers are cleaned and textured, with a final thickness of 170 µm. Doped and intrinsic hydrogenated amorphous silicon (a-Si:H) layers are deposited on both sides, with a n-type/intrinsic stack (n/i) on the front side and a (p/i) stack on the rear, corresponding to the "rear-emitter" SHJ architecture [17,18]. Then, indium-tin oxide (ITO) layers are deposited on both sides by magnetron sputtering from an In_2O_3/SnO_2 target, under an Ar/O_2 gas mixture. Metal grids are screen-printed with a silver paste, and a 4-busbar pattern. Finally, the cells are annealed at 200 °C for 9 min in order to cure the silver paste. More details about the global cell process can be found in Ref. [18].

For the whole study, the cutting process is performed with an infrared pulsed laser (1064 nm wavelength, 10 ns pulses) commercialized by Rofin©. The cutting process can be optimized by tuning fluency (through laser input current), pulse frequency and cutting speed. All of these processes induce a trench in the wafer, deep enough to allow an easy mechanical cleaving (between 30 and 50 % of the cell's total thickness). Therefore, the levels of recombination losses induced by the laser process can differ from the "ideal" case of a clean, smooth and totally unpassivated edge, with a fixed theoretical value of 19 nA/cm for J_{02} edge, as calculated in a previous study [11]. In a non-ideal case, the value measured can be significantly different, and quantifies the overall quality of the cutting process. An example of the cut-cells put together is presented in the Figure 60.

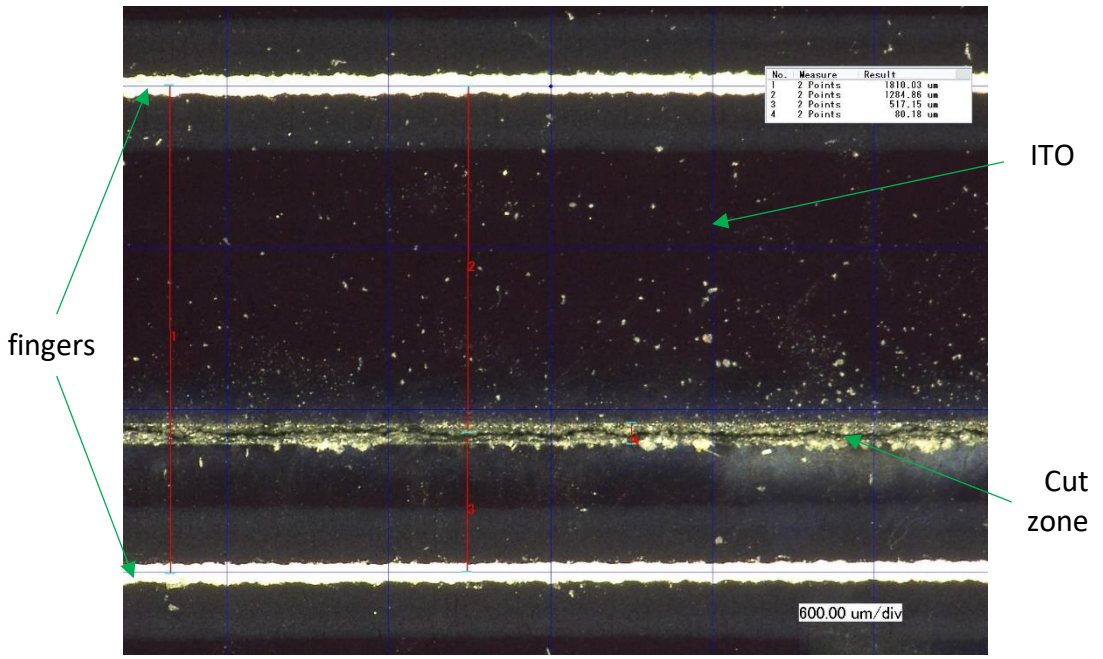

Figure 60: Example of the two half-cells put together. Here, the cutting process has created a trench of approximately 80 µm of optical width.

The characterization of recombination losses is entirely based on IV measurements, under illumination or in dark conditions. For this purpose, all solar cells are measured with an AAA-class solar simulator commercialized by Aescusoft™, with a halogen lamp and continuous illumination. Current and voltage are extracted on the front side through probe bars covering all the cell length, and on the rear side through a metal chuck with dedicated voltage probe. This chuck is regulated in temperature at 25 °C. The measurement repeatability has been determined through an intensive metrology study (tool qualification, including in particular many repeatability tests – cell positioning, calibration, different users involved). From this study, the repeatability of the different IV parameters has been estimated to 0.01 % for V_{oc}, 0.09 % for J_{sc}, 0.36 % for FF and 0.34 % for efficiency.

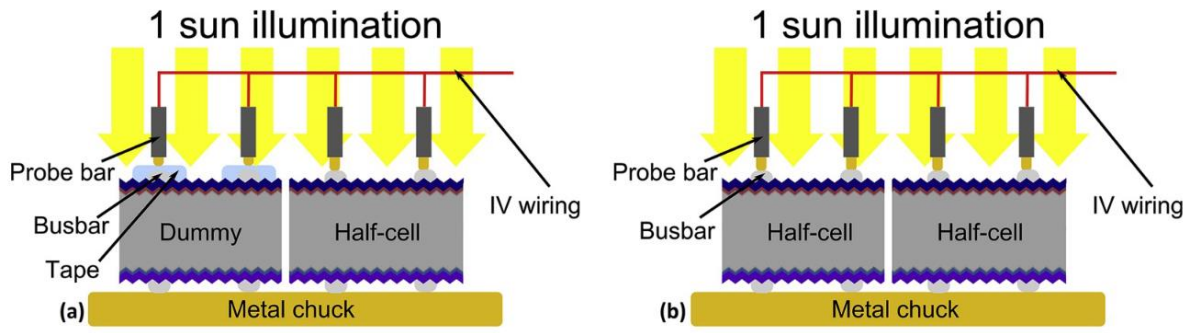

Figure 61: IV setup used to characterize half-cell after cleavage: separately (a), together (b)

The twenty solar cells used in this study are bifacial. Therefore, the voltage probe on the metal chuck is carefully placed in contact to a rear side busbar for an accurate voltage measurement. All cells, including the reference one used to calibrate the solar simulator, have identical sizes and metallization patterns, and are placed at the same position on the IV stage during measurement.

	J_{sc} *(mA/cm²)*	V_{oc} *(mV)*	V_{mpp} *(mV)*	J_{mpp} *(mA/cm²)*	**FF** *%*	**Eta** *%*
Initial	37.65 ± 0.04	732.2 ± 1.3	613.2 ± 2.3	35.54 ± 0.08	76.05 ± 0.21	21.79 ± 0.08
Relative losses after laser	$-0{,}34$ $\pm 0{,}05$ %	$-0{,}17$ $\pm 0{,}03$ %	$-0{,}37$ $\pm 0{,}09$ %	$-0{,}65$ $\pm 0{,}11$ %	$-0{,}55$ $\pm 0{,}06$ %	$-1{,}02$ $\pm 0{,}07$%
Relative losses after cleavage	$-0{,}51$ $\pm 0{,}05$ %	$-0{,}22$ $\pm 0{,}03$ %	$-0{,}47$ $\pm 0{,}07$ %	$-0{,}91$ $\pm 0{,}11$ %	$-0{,}65$ $\pm 0{,}06$ %	$-1{,}37$ $\pm 0{,}08$%

Table 5: Initial value of IV parameters of the 20 cells and relative losses after laser and after cleavage.

Five IV measurements are performed for each cell: before the laser shot (full-cell), after the laser shot (full-cell), after cleavage for half-cell 1, after cleavage for half-cell 2, after cleavage for both half-cells together. Figure 61 shows the adaptation of the measuring device for atypical cases of measuring a half-cell alone, and measuring the two half-cells together. When measured together, the two half-cell are electrically placed in parralel.

The mean IV parameters and dispersion of the twenty full-cell used in the study are summarized in the table 5. The losses between the initial state and the first cutting step (laser) are also mentionned, as well as the relative losses between the initial state and the end of the cutting process (after cleavage with half-cells measured together). The uncertainties are given for a confidence interval of 1 sigma: the losses have clearly a statistical significance.

The width of the trench created by the laser is 80 µm, which represents a destroyed area of 0.05 % of the total surface of the entire cell. A large part of the J_{sc} loss does not come from the loss of active surface but from the peripheral degradation of the cell layers (c-Si, a-Si, TCO).

III.B.1.b *Two-diode model equivalent circuit: parameter extraction*

The aim of the study is therefore to quantify the variation of the parameters of the 2-diode model before and after the different cutting steps. The central part of the module modelling presented in the previous chapter is the modification of the cell parameters of the two diodes equivalent circuit due to module manufacturing steps.

The parameter extraction is done by fitting the IV curve of the cell before and after the cutting step. The first step is to ensure that the quality of the fit is good enough to characterize difference due to cutting steps with a physical meaning.

Before adjusting any parameter, it is necessary to ensure that cutting steps produce a significant change in the IV curves. As mentioned in the table 5, this is a case for the IV parameters. For example, the IV and PV curves measurement of one of the 20 cells are given in the Figure 62. The full IV and PV curves are given for information is the left side. A zoom around the MPP is proposed on the right side. Changes in current and power density are clearly visible.

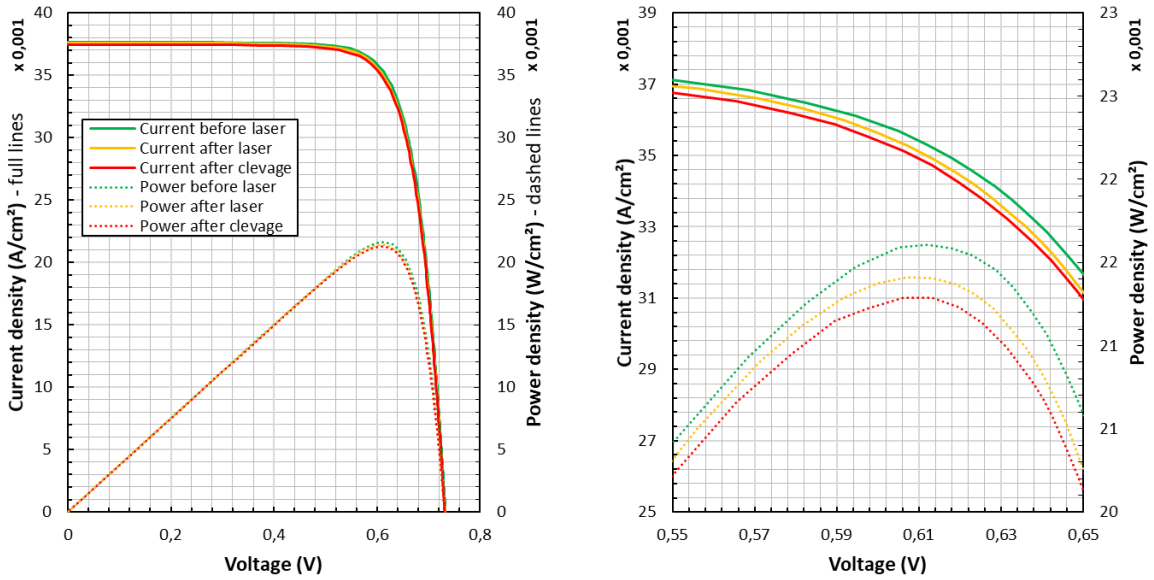

Figure 62: Example of IV and PV curve for the cell number 1 for the three steps of cutting process: before laser, after laser and after cleavage (left). Zoom on MPP (right).

Which parameters of the circuit model equivalent to two diodes can be adjusted during the fit?

The two-diode model has 7 parameters. The aim of the study is to characterize a change in recombination current caused by the cutting step. For this reason, the choice is made to set the ideality factors to n1 = 1 and n2 = 2. Indeed, if this were not the case, the differences in recombination currents J_{01} and J_{02} for different ideality factor values could not be compared. The heterojunction cells used do not have any shunts, in particular due to the TCO opening at the edges of the cell on the rear side. This is confirmed by Dark IV measurements and extraction of local ideality factor (Figure 63). The shunt resistance is therefore considered to be infinite. These two considerations reduce the number of free parameters to four: J_{ph}, J_{01}, J_{02} and r_s.

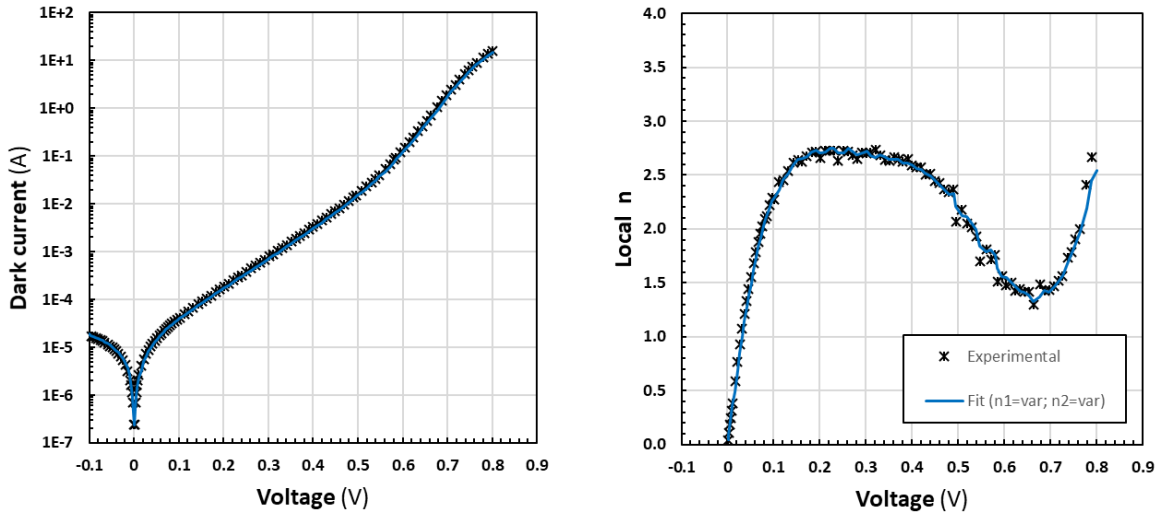

Figure 63: Dark IV measurement of current-voltage (left) and local ideality factor (right). Only in this case the ideality factor n1 and n2 are free to vary : n1 = 1.17, n2=2.67. The fitted value of Rshunt is extremely high: 2.3 MOhm.cm².

Does the fit of these experimental curves is accurate enough to quantify the observed differences. The experimental difference of current density before cutting and after (after laser, and after cleavage) are plotted in the Figure 64, on the left side. Because the voltage abscissa are not the same for all the measurements, a piecewise interpolation is made with 10000 points to compare current density for the same voltage. After laser, a loss of 0.08 mA/cm2 is observed between 0 and 0.5 V. The difference then increase exponentially to 0.74 mA/cm2 at a voltage of 0.720 V.

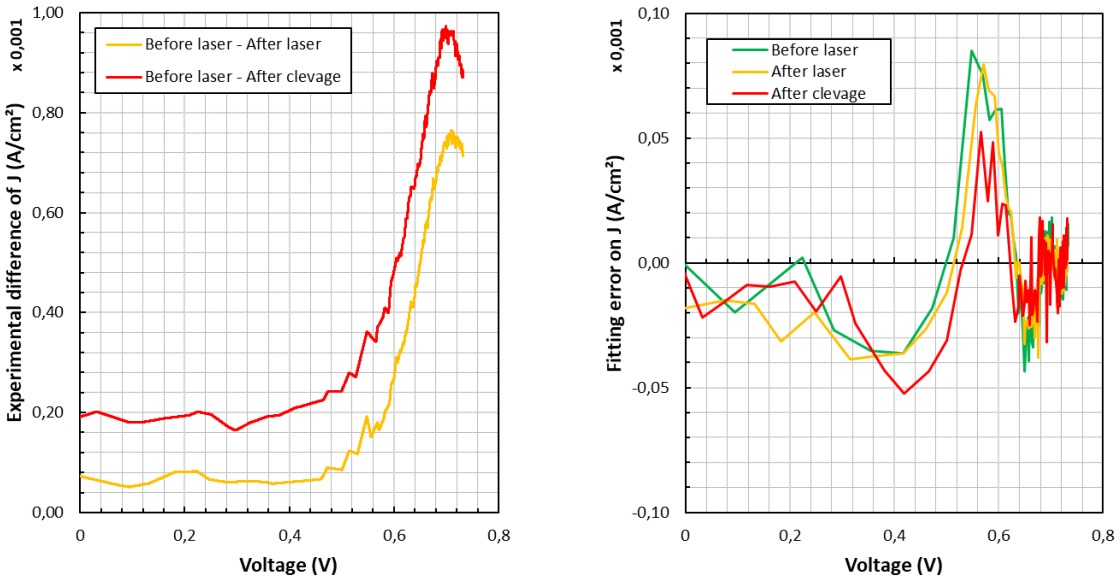

Figure 64: Difference in current density before and after cleavage as a function of voltage (left). Fitting error made on IV curves as a function of voltage (right).

This is a first clue that laser process affect the J_{sc} and the recombination: a difference exists at low voltage (J_{sc}) and added to an exponential contribution from 0.5V to the end of IV curve (recombination). After the cleavage, a greater loss of 0.20 mA/cm^2 is observed between 0 and 0.5 V, and an exponential increase to 0.96 mA/cm2 for 0.720 V.

The error in IV curve fitting for the IV curve before cutting, after laser and after cleavage are given in the Figure 64, on the right side. The mean value of the absolute error across all the voltage is 0.03 mA/cm2. A maximum in error fit of 0.08 mA/cm² can be noticed for the three curves at 0.55 V. It is clear that the fitting procedure is sufficiently accurate and can be used to quantify the difference in current density before and after cutting.

Hypothesis can be made to explain the not perfect fit procedure, resulting in a peak in error at 0.55V. The model of the two diode with fixed ideality factor of n1=1 and n2 = 2, constant r_s with voltage and infinite shunt resistance must not be the best one. The peak in fitting error can thus be due to an n1 value different from 1 and n2 value different from 2. It is also possible to add a third term of recombination which is specific to heterojunction technology [158]. The last hypothesis is the dependency of the r_s with voltage. It is a phenomenon well known, due to the distributed nature of the r_s [122], [159]–[162].

Figure 65 shows the evolution of the J_{01} parameters of the two-diode model after the laser step and after the mechanical cleavage step. The abscissa shows the value of the parameter before cutting and the ordinate axis shows the value after the cutting steps. The scales are identical, so the black dotted line represents an invariance at cutting.

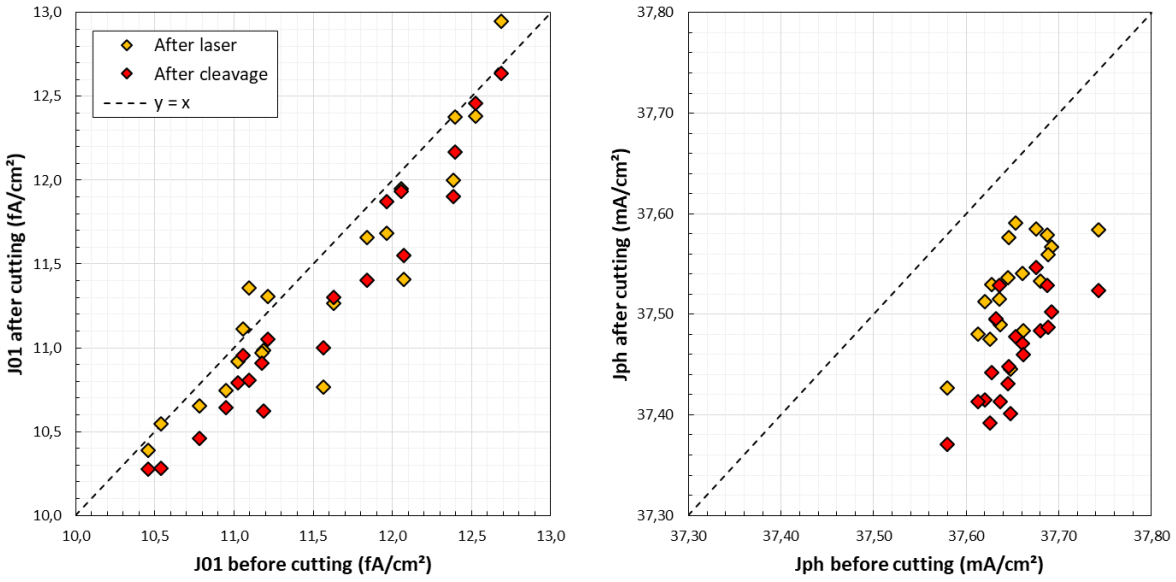

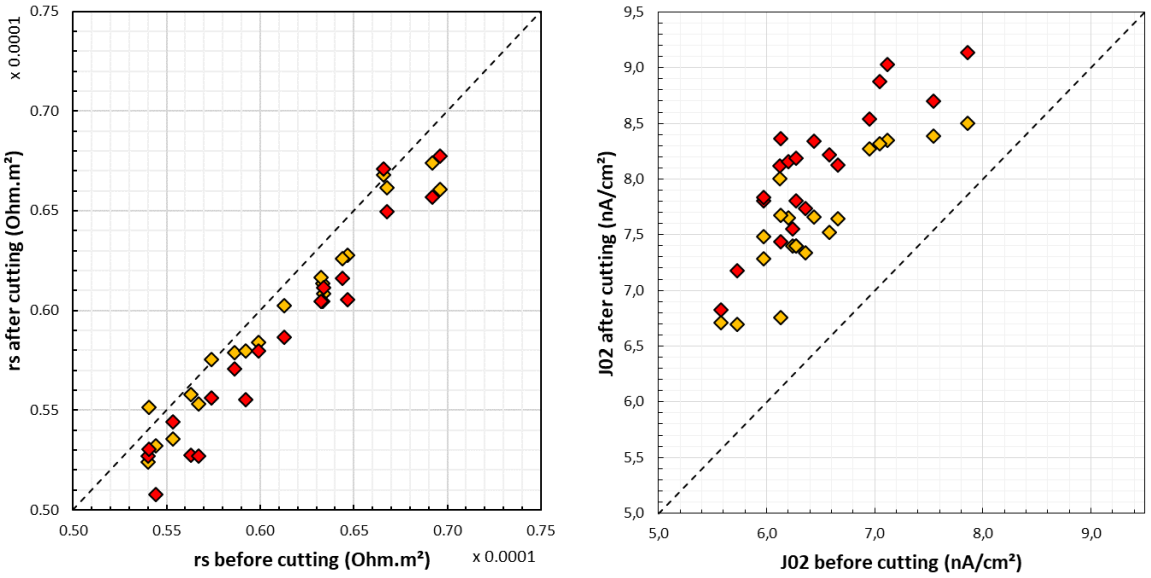

Figure 65: Evolution of the parameters of the two diode model before laser and after laser, before cutting and after cleavage (J_{01} top left, J_{ph} top right, r_s, bottom left, J_{02} top right)

The recombination current J_{01} before cutting ranges from 10.5 to 12.5 fA/cm2 and approximately the same values after laser cutting and after the additional mechanical cleavage (top left figure). These values are consistent with expected ones for highly passivated solar cells [30]. The difference analysis shows that the laser step produces a J_{01} loss of -0.16 ± 0.26 fA/cm2. The laser step plus mechanical cleavage produces a loss of -0.28 ± 0.15 fA/cm2. Two results seem strange: the J_{01} recombination current has no reason to decrease. This parameter is mainly related to the diffusion in the bulk of the cell which is not affected by the cutting. Moreover, it is difficult to understand how this parameter can decrease (and thus improve performance) when the cutting steps essentially produces defects. It is also hardly understandable to note that the difference of J_{01} after the laser shot is more dispersed than the same difference when we add an additional step: the mechanical cleavage. It would make more sense to expect an additional dispersion by adding a physical step.

For these two reasons, a non-parametric hypothesis test is carried out to determine whether the differences observed before and after cutting are statistically significant. A Wilcoxon test for 20 paired samples with a significance level of 1 % is done. The results are presented in the Table 7. The difference between J_{01} before the cutting (initial) and after the laser is not significant. The difference between initial and after the cleavage is significant. The difference between laser and cleavage is not significant.

The photo-generated current J_{ph} before cutting ranges from 37.58 mA/cm2 to 37.74 mA/cm2, and from 37.37 mA/cm2 to 37.60 mA/cm2 after cutting. The difference before and after laser seems significant: 0.12 ± 0.04 mA/cm2 as the difference before laser and after cleavage: 0.19 ± 0.04 mA/cm2. This is confirmed by the Wilcoxon test (Table 7): all the differences between cutting steps are statistically significant.

Statistical significance of difference	**Before laser** (initial) **/ After Laser**	**Before laser / After cleavage**	**After laser / After cleavage**
J_{01}	No *(-2.50)*	Yes *(-3.92)*	No *(-2.39)*
J_{ph}	Yes *(-3.92)*	Yes *(-3.92)*	Yes *(-3.81)*
J_{02}	Yes *(-3.92)*	Yes *(-3.92)*	Yes *(-3.81)*
r_s	Yes *(-3.55)*	Yes (-3.88)	Yes *(-3.30)*

Table 7: Results of Wilcoxon test of hypothesis of statistical difference of two diodes model parameters between the different cutting steps (at a significance level of 0.01). The Z value is given in brackets, and the critical z value for rejection of H0 hypothesis is -2.6.

The series resistance r_s before cutting ranges from 0.54 to 0.70 Ohm.cm² and from 0.50 to 0.68 Ohm.cm² after cleavage. The Wilcoxon test (Table 7) proves that all the differences between cutting steps are statistically significant for this parameters. This results is also surprising: how the cutting step can decrease series resistance and improve the related performance?

The recombination current J_{02} before cutting ranges from 5.5 to 7.9 nA/cm², and from 6.5 to 9.1 nA/cm after cutting. The difference between initial value and value after laser is 1.16 +-0.30 nA/cm² and the difference between initial value and value after cleavage is 1.64 +- 0.30 nA/cm². The Wilcoxon test (Table 7) proves that all the differences between cutting steps are statistically significant.

Because the recombination current J_{01} and the series resistance decrease despite any physical causes, we suppose this is a bias due to the fitting process. The last question that can be asked is the individual impact of these parameter changes on the IV performance of the cell. To do this, we look separately at the impact of the change of J_{01}, all other parameters remaining equal. Then, we focus on the change of J_{02}, J_{ph} and r_s. This is summarized in the Table 8.

Loss after cleavage	**I_{sc}**	**V_{oc}**	**I_{mpp}**	**V_{mpp}**	**eta**	**FF**
Experiment	-0.51 %	-0.22 %	-0.91 %	-0.47 %	-1.37 %	-0.55 %
STD 1 sigma	0.09 %	0.03 %	0.22 %	0.15 %	0.16 %	0.12 %
Only J_{01}	0.00 %	0.07 %	0.00 %	0.06 %	0.05 %	-0.03 %
Only r_s	0.00 %	0.00 %	0.03 %	0.13 %	0.14 %	0.14 %
Only J_{02}	0.00 %	-0.27 %	-0.34 %	-0.71 %	-1.06 %	-0.80 %
Only J_{ph}	-0.50 %	-0.03 %	-0.51 %	-0.02 %	-0.50 %	0.00 %
Sum of individual loss	-0.50 %	-0.23 %	-0.82 %	-0.53 %	-1.38 %	-0.68 %
Only J_{02} + J_{ph}	-0.50 %	-0.30 %	-0.85 %	-0.73 %	-1.56 %	-0.80 %

Table 8: Loss after cleavage: from experiments, computed with change of the two diodes model parameters separately.

Because the good quality of the fit, the experimental losses on IV parameters are consistent with the losses obtained by the sum of losses caused by the change in the four parameters of the two-diode model. But the variations of the parameters J_{01} and r_s cannot be neglected: considering the losses caused only by J_{02} and J_{ph}, the losses obtained on IV parameters are no longer compatible with the experimentally measured values, except on J_{sc} and J_{mpp} value.

It is therefore necessary to change the fit procedure. First, a fit with the 4 free parameters J_{01} J_{02} r_s and J_{ph} is performed on the IV curve of the cell before cutting. Then, the values of J_{01} and r_s are fixed for the IV curve fit after laser and after cleavage. For these two steps, only the parameters J_{ph} and J_{02} are free to vary. The quality of the fit remains similar, and the results of the extraction are presented on the Figure 66. On the left, the J_{02} extracted with the previous fitting process: J_{01} and r_s are free to vary. On the right, the J_{02} extracted with the current fitting process: J_{01} and r_s are fixed to the value obtained before laser (initial).

The results are consistent, but as expected, the method with fixed J_{01} and r_s produce less dispersion in the value of J_{02}. The mean value of the difference before / after cutting also seem to be smaller for the method with fixed J_{01} and r_s.

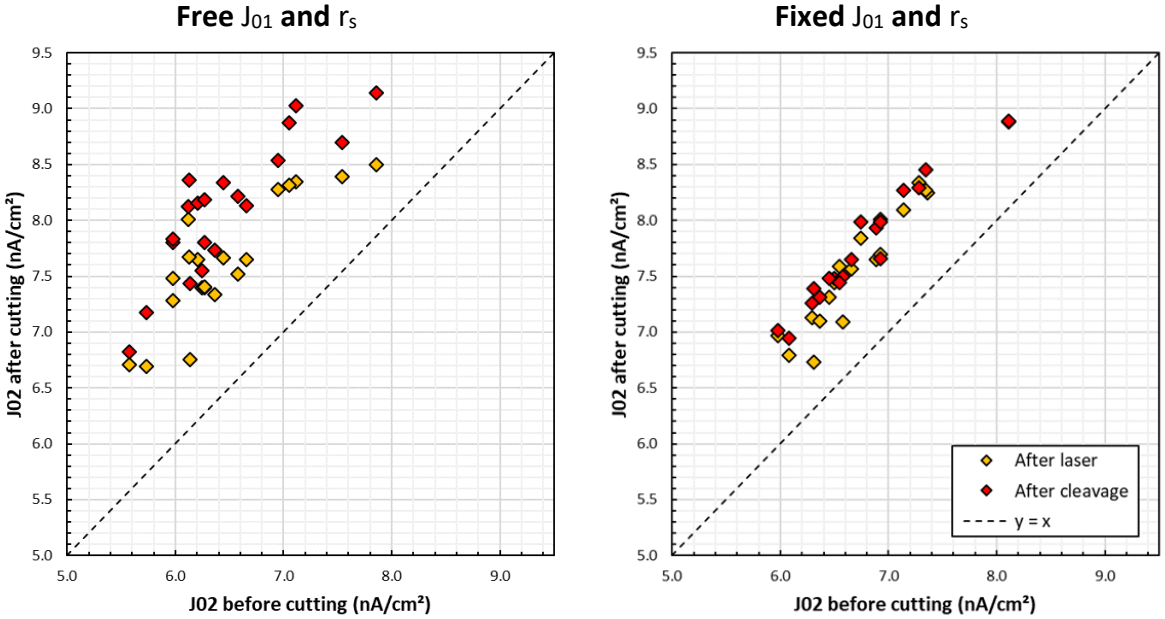

Figure 66: Fitted J_{02} before and after cutting (after laser & after cleavage) With J_{01} and r_s free to vary in all three steps (left). With J_{01} and r_s fixed after cutting to the value before cutting (right).

The quality of the fit with fixed J_{01} and r_s remains equal (R^2 of the fit over 0.998) compared to the quality of the fit with variable J01 and r_s. The physical behaviour is more coherent. The statistical dispersion on J_{02} is smaller. For these reasons, the second process of fitting with fixed J_{01} and r_s is used for the rest of the study.

III.B.1.c *Edge current recombination and photo-generated current losses*

From the extracted values of J_{02} and J_{ph}, the aim is to obtain loss values independent of the newly created stop length. Thus, the results can be extrapolated to any cell and cutting geometry. Before the cutting process, the IV curve can be described by the two-diode model:

$$J = J_{ph,F} - J_{01}\left(\exp\left(\frac{V + J.r_s}{n_1 . V_{th}}\right) - 1\right) - J_{02,F}\left(\exp\left(\frac{V + J.r_s}{n_2 . V_{th}}\right) - 1\right) - \frac{V + J.r_s}{r_{sh}} \qquad \text{III.14}$$

With a component coming from bulk recombination $J_{02,bulk}$ and a component coming from edge recombination of the full-cell $J_{02,edge}$:

$$J_{02,F} = J_{02,bulk,F} + J_{02,edge,F} \qquad \text{III.15}$$

When the cell is cut in two equal parts measured together, the expression of $J_{02,edge}$ is modified with a contribution of the newly created edge. The length of the new edge is $a = 15.675\ cm$, but two zones of additional recombination are created: one on each of the half-cell. The total length that must be taken into account is $L_H = 2a$.

The current density $J_{02,bulk,F}$ is supposed to remain the same. The $J_{02,H}$ measured is thus:

$$J_{02,H} = J_{02,bulk,F} + J_{02,edge,H}$$

With

$$J_{02,edge,H} = J_{02,edge,F} + J_{02L,edge}\ \frac{L_H}{S} \qquad \text{III.16}$$

Where $J_{02L,edge}$ is in nA/cm, and S in the area of the two half-cell together, which equal the area of the full-cell: $S = 244.33\ cm^2$. The difference between ΔJ_{02} before and after the cutting process is then:

$$\Delta J_{02} = J_{02,H} - J_{02,F} = J_{02L,edge}\ \frac{L_H}{S} \qquad \text{III.17}$$

A similar calculation provides the percentage of photo-generated current loss per unit of edge length exposed by the cut - $J_{phL,edge}$ (equation III.18). The loss is not defined in units of current, but as a percentage of the photo-generated current, which is more relevant to extrapolate losses to other values of J_{ph} (especially when the irradiance incident on the module varies, for example):

$$\frac{\Delta J_{ph}}{J_{ph}} = \frac{J_{02,H} - J_{02,F}}{J_{02,F}} = J_{phL,edge}\ L_H \qquad \text{III.18}$$

The Figure 67 shows the value of $J_{02L,edge}$ (left) and de $J_{phL,edge}$ (right) obtained after the laser process and after the mechanical cleavage. The final value of edge recombination is 7.6 +- 1.0 nA/cm at the end of the cutting process (after cleavage). But the main contribution comes from the laser process with 6.5 nA/cm and only 1.1 nA/cm from the cleavage. This point

is consistent with the work of Eiternick *et al.*: laser cutting produces the most loss compared to mechanical cleavage [149]. The values obtained are also consistent with the low range of studies that have calculated a recombination stop current on highly passivated cells [150] [157]. Moreover, the values obtained are well below the theoretical limit of 20 nA/cm determined for an edge intersecting a pn-junction with a p-type bulk [142].

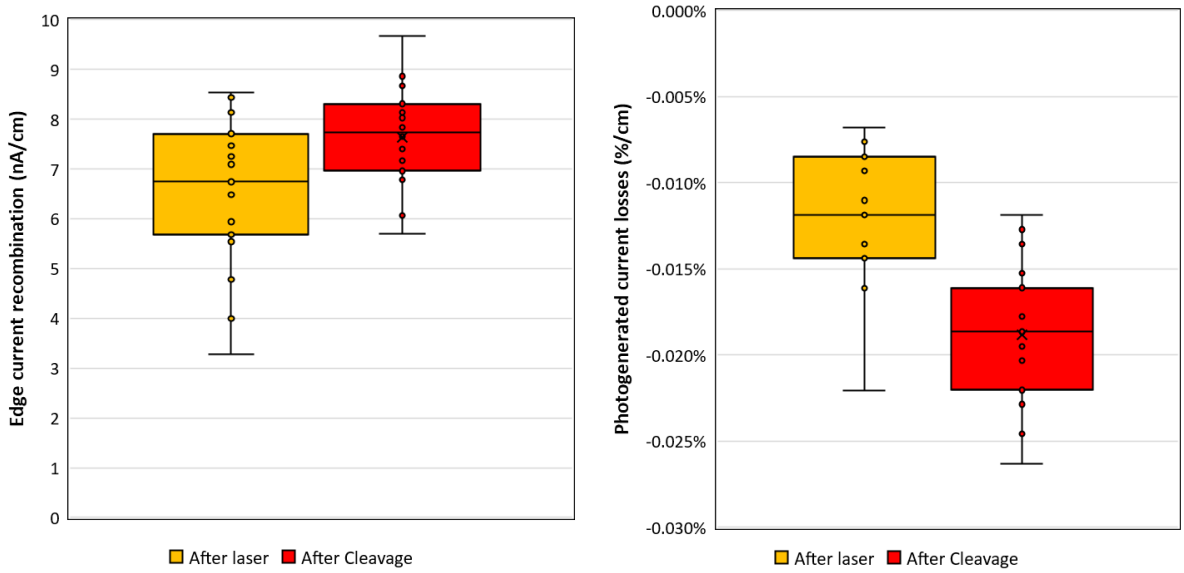

Figure 67: Edge current recombination (left) and photo-generated current losses (right) after laser and after cleavage.

The results of J_{sc} losses after laser are more dispersed than the losses after mechanical cleavage. The damages induce by the laser are sufficiently recombinant that the addition of further dangling bonds by mechanical cleavage will increase the recombination current of the edge only slightly. The laser cutting induce a loss on the photo-generated current of 0.013 %/cm, and the mechanical cleavage adds another loss of 0.007 %/cm. In total, the cut generates a loss of 0.02 % / cm.

Extrapolation to more cutting steps

The aim of this part is to study the variation of the IV parameters of the cell as a function of the number of cuts. At the moment, no module setting step is considered. For N cutting step, we consider the performances of the N+1 sub-cells together.

Initially, we are interested in the evolution of the parameters of the two-diode model as a function of the number of cuts. This is presented in Table 9. For a cut number N, and a cell of L = 15.675 cm side length, the newly created edge length is equal to L_{tot} = 2NL. We can therefore calculate the contribution of these new edges to the total J_{02} of the cell and to the photo-generated current J_{ph}. The initial J_{02} of the entire cell is 6.9 nA/cm² and the J_{ph} is 37.65 mA/cm². A half-cell configuration increases J_{02} by 14 ± 2 % and decreases J_{ph} by 0.6 ± 0.1 %. At the extreme, a sixth-cell configuration increases J_{02} by 71 ± 8 % and decreases J_{ph} by 2.8 ± 0.6 %.

Architecture	New edges length *(cm)*	J_{02} new edges *(nA/cm2)*	Increase in J_{02} *(%)*	J_{ph} edge loss *(mA/cm2)*	Loss on J_{ph} *(%)*
Full-cell	0	0	0	0	0
Half-cell	31.4	1.0 ± 0.2	14 ± 2	0.22 ± 0.05	0.6 ± 0.1
Third-cell	62.7	2.0 ± 0.3	28 ± 4	0.42 ± 0.09	1.2 ± 0.2
Quarter-cell	94.1	2.9 ± 0.4	43 ± 6	0.63 ± 0.14	1.8 ± 0.4
Fifth-cell	125.4	3.9 ± 0.5	57 ± 7	0.84 ± 0.18	2.4 ± 0.5
Sixth-cell	156.8	4.9 ± 0.6	71 ± 8	1.05 ± 0.23	2.8 ± 0.6

Table 9: Extrapolation of J_{02} and J_{ph} change with more cutting steps. The initial value of J_{02} is 6.9 nA/cm² and the initial value of J_{ph} is 37.65 mA/cm². The wafer is M2 with a side of 15.675 cm.

The evolution of these two parameters of the 2-diode model has a direct impact on the IV parameters. This can be seen in Figure 68 and Figure 69. The IV parameters have globally a linear decrease with the number of cuts made. The experimental uncertainty on the J_{02} edge and J_{ph} edge values propagates and the impact on the uncertainty of the IV parameters increases with the number of cuts.

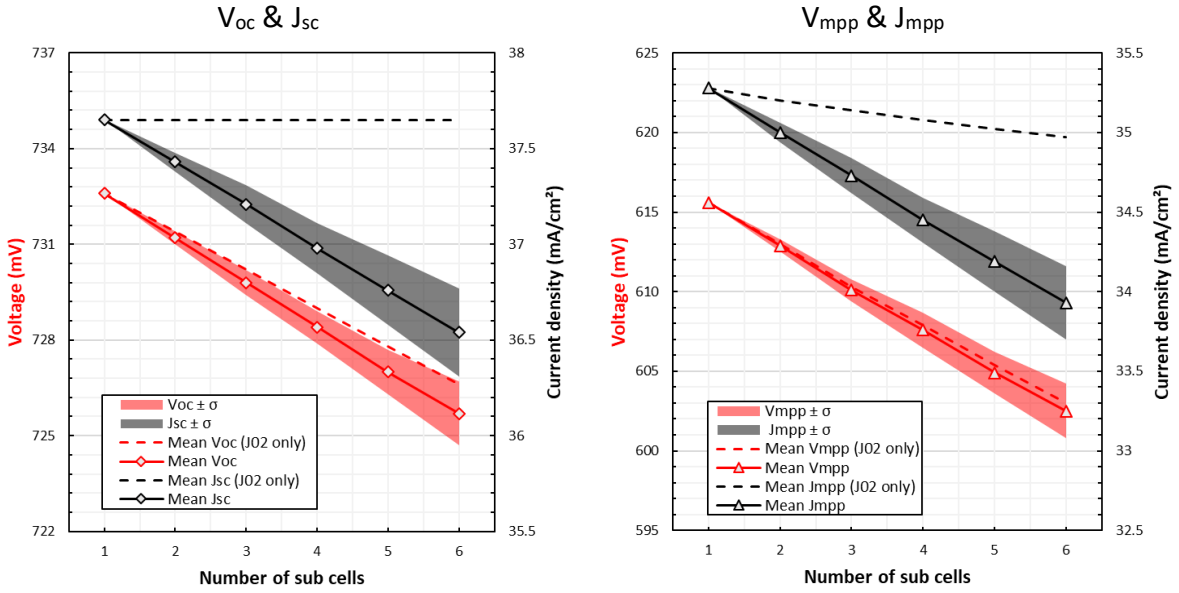

Figure 68: Evolution of modelled current and voltage IV cell parameters as a function of the number of cutting steps N. The N sub-cells are considered together. V_{mpp} and J_{mpp} on the left side, V_{oc} and J_{sc} on the right. The dotted lines show evolution of IV parameter with only a change in J_{02}, J_{ph} is kept constant.

When switching from full-cell to half-cell configuration, the efficiency loss is - 0.27 $\%_{abs}$ or -1.24 $\%_{rel}$. When switching from full-cell to six-cell configuration, the efficiency loss is much higher: -1.27 $\%_{abs}$ or -5.85 $\%_{rel}$. Regardless of the number of cuts, these losses are explained at 35 % by the drop in V_{mpp} and at 65 % by the drop in I_{mpp}. Another way of seeing this loss of

efficiency is to explain it at 15 % by the drop in V_{oc}, at 50 % by the drop in J_{sc} and at 35 % by the drop in FF.

The dashed lines correspond to the theoretical losses that would have been measured if only J_{02} were affected, and therefore if J_{ph} remained constant at 37.65 mA/cm². It can be seen that 90 % of the drop in V_{oc}, 20 % of the drop in J_{mpp} and 99 % of the drop in V_{mpp} comes from the increase in J_{02}, the rest of the losses is caused by J_{ph}. This corresponds to 100 % of the decrease in FF and 50 % of the decrease in efficiency which is due to the J_{02} edge.

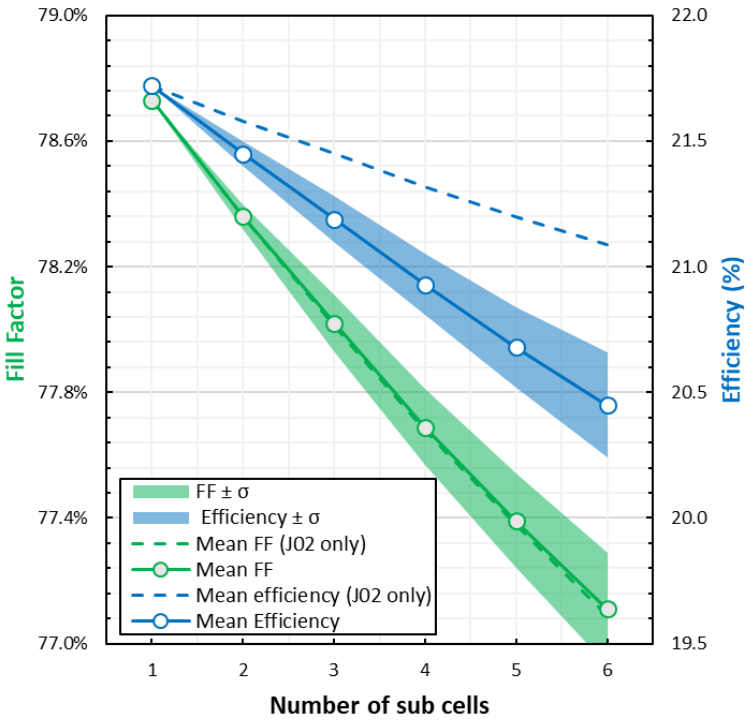

Figure 69: Evolution of fill factor and efficiency of the cell as a function of the number of cutting steps. The N sub-cells are considered together. The dotted lines show evolution of IV parameters with only a change in J_{02}, J_{ph} is kept constant

The decrease in J_{ph} and the increase in J_{02} therefore have a similar impact on the loss of cell performance after cutting steps. The increase in J_{02} comes from the existence of dangling bonds, which are traps for electron-hole pairs, especially at the intersection with the pn junction (SCR) and in the quasi-neutral zone. The drop of the J_{ph} has probably two mains origins: (i) destruction of the active surface by the laser. (ii) Layer damages over distances greater than the width of the laser spot.

The trench created by the laser is indeed 80 µm wide, compared to the 15.675 cm of the initial full-cell (see Figure 60). Thus, losses caused by active surface destruction are estimated at only 0.05 %. Layer damages over distances greater than the width of the laser spot is therefore more likely to be the reason of J_{ph} drop. The TCO may be damaged and its optical behaviour degraded: local EQE or LBIC measurements should be carried in the future.

The amorphous nature of the cell's passivation layers, which are sensitive to temperatures above 200°C, may have been degraded by the local heating produce by the

laser. As mentioned by Merten *et al.* and Stuckelberger *et al.*, the recombination in the amorphous layers can be expressed by a new term in the two diodes model, which produce a decrease of the J_{ph} even at zero voltage [158] [163]:

$$J_{recomb} = J_{ph} \frac{d_i^2}{(\mu\tau)_{eff}[V_{bi}-(V-IR_s)]} \quad \text{III.19}$$

In equation II.33, d_i is the thickness of the amorphous intrinsic layer, $(\mu\tau)_{eff}$ is the effective drift length in the intrinsic layer and V_{bi} is the built-in voltage. This could be a lead for further study. If the losses in J_{sc} is explained by damages of optical or amorphous layers, the passivation of the edge would result in only 50 % recovering of the total losses. The next section is dedicated to the module level: the combined study of cutting losses and resistive gains in module.

III.B.2 Impact of cutting on the performance of a module: resistive gain and cutting losses

This part aims to complete Part III.A by integrating cutting losses in the modelling of a module made up of cut cells cut into different numbers of sub-cells of equal size. The integration of cut cells makes it possible to gain in module power according to a law, as seen previously, in 1 - 1/N² where N is the number of sub-cells created per full-cell (Equation III.7). The power therefore increases continuously with N, but reaches a plateau when the current in the module interconnections is so low that the resistive losses no longer have any effect. Nevertheless, by integrating the active surface losses, we have shown that the optimum efficiency for an M2 glass/glass module of 72 equivalent full-cell with an inter-cell distance of 2 or 3 mm is in half-cell configuration.

III.B.2.a *Combination of resistive gains and edge losses: impact of wafer size*

On the other hand, the cutting losses cause recombination and photo-generation losses which generate a linear decrease in power with N. There is no counterbalancing phenomenon. This part is thus dedicated to the study of the impact of cutting losses on the previously found lossless architecture optimum. Figure 70 shows the evolution of the module IV parameters as a function of the number of sub-cells present in a module equivalent to 72 full-cells. The module is the same as the one presented in Part III.A. In contrast, parameters IV at the maximum operating point, I_{mpp} and V_{mpp}, are affected by cell losses and module gains.

The I_{sc} current and V_{oc} voltage suffer linear losses with the number of cuts. This is a direct consequence of the losses caused by J_{ph} and J_{02}, as studied for the cell only. In fact, the module creation affects the photo-generated current in the same for any number of cutting steps. This does not modify the behaviour of the losses recorded in the cell. The V_{oc} is logarithmically affected by the module manufacturing due to the variation of the I_{sc}. This variation is however indistinguishable for a current passing from 9.0 to 8.9 A. The drop in V_{oc} visible in the figure is therefore also completely caused by the increase of the J_{02} cell.

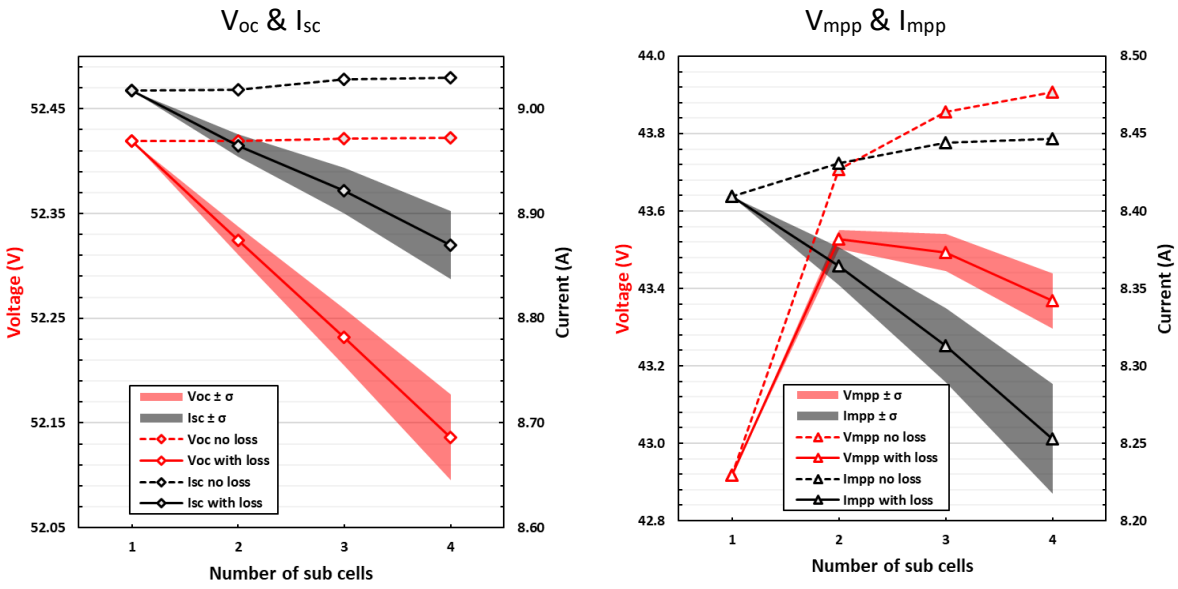

Figure 70: Evolution of the voltage and current IV parameters (V_{oc}, I_{sc}, V_{mpp}, I_{mpp}) of the module in equivalent full-cell design as a function of the number of sub-cell. Configuration from Full-cell to Quarter cell are considered. V_{oc} and I_{sc} (left), V_{mpp} and I_{mpp} (right).

The V_{mpp} increases indefinitely (following the law in $1 - 1/N^2$) with the number of sub-cells N in a no-cutting-loss case. Including the losses, it appears a maximum in half-cell configuration. The I_{mpp} decreases continuously when considering cutting losses: this is the direct impact of the aforementioned drop in I_{sc}.

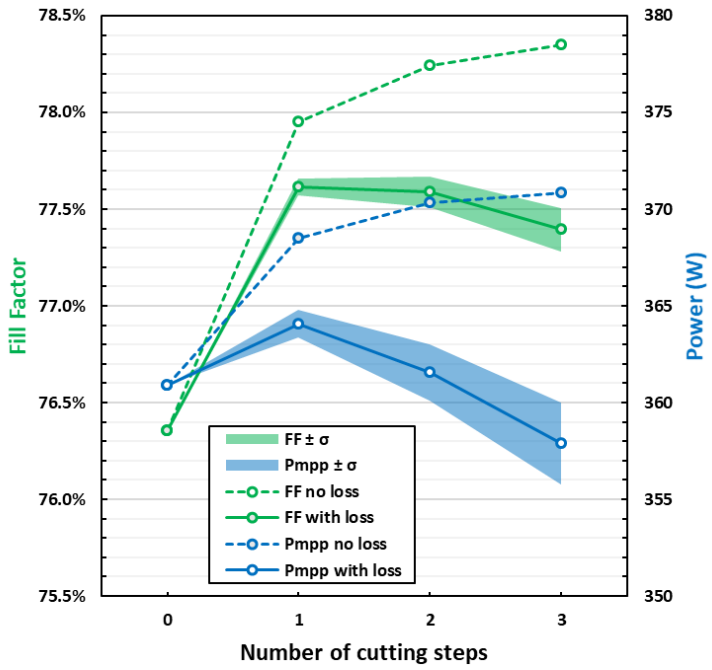

Figure 71: Evolution of the fill factor FF and the power at the MPP in equivalent full-cell design as a function of the number of cutting steps (M2 wafers).

The impact on FF and P_{mpp} is given in Figure 71. While both values increase in 1 - 1/N² in the lossless case, they pass through a maximum for a single cutting step (half-cell) at 77.6 $\%_{abs}$ FF for 364 Watt. The FF gain obtained by switching from full-cell to half-cell is 1.25 $\%_{abs}$ taking into account cutting losses, whereas it was 1.6 $\%_{abs}$ with no losses. The gain in Pmpp obtained by switching from full-cell to half-cell is 3 Watt (0.8 $\%_{rel}$) taking into account cutting losses, whereas it was 7.5 Watt (2.1 $\%_{rel}$) without loss.

The question that now arises is how this optimum in number of cuts varies according to the size of the wafer used for the full-cell. When the size of the wafer increases, two beneficial phenomena occur.

Firstly, the I_{sc} current produced by the cell increases for the same J_{sc} (it is assumed that the cell's surface performance does not change). The current flowing in the module interconnections is higher, and therefore the interest of integrating cells cut into modules is greater. Secondly, because the size of the wafer increases, the perimeter/surface ratio decreases, and the impact of cutting losses is reduced. These two reasons should result in a higher optimal cutting number when using larger wafers.

Table 10 summarizes the sizes of the different wafer standards. M2 wafers are still the industry standard of 2020, the first production with M12 wafers is expected to take place in 2021. The perimeter-to-area ratio for M2 wafers is 2.567 cm^{-1} compared to 1.905 cm^{-1} for an M12 wafer, a reduction of 25 %. This implies that the additional J_{02} produced by cutting, as well as the loss in J_{ph} will be 25 % lower in M12 than in M2.

Wafer standard	**Size** (cm)	**Area** (cm^2)	**Perimeter / area** (cm^{-1})
M2	15.67	244.3	2.567
M4	16.17	258.1	2.506
M6	16.60	274.1	2.422
M8	18.50	342.1	2.163
M12	21.00	441.0	1.905

Table 10: Main wafer size standards, corresponding size, area and ratio perimeter over area.

Figure 72 shows the evolution of the fill factor and the efficiency of a module made of M2 wafer and a module made of M12 wafer. The extensive parameters of the module (currents, voltages, powers) are not considered as they differ according to the size of the wafer. The M2 and M12 cells are considered to have a similar efficiency, only their size changes. The number of cell interconnection wires in M2 is taken at 18, and at 24 at M12. In this way, the spacing between the wires almost the same (8.71 mm in M2 against 8.75 mm in M12). This makes it possible to have equivalent shading of the cell in M2 and M12. This also makes it possible to generate the same resistive losses in the fingers of the metallization per unit area. The right graph presents this evolution for cutting losses including only J_{02}. On the left graph, the two losses, on J_{02} and J_{ph}, are included.

Let's first consider the case with the losses in J_{02} and J_{ph}. The initial efficiency of the M12 full-cell module (19.08 %) is logically lower than that of the M2 full-cell module (19.32 %). The

current generated by the M12 full-cell, 16.3 A, generates much higher resistive losses than the M2 module (Isc of 9.0 A). This can be seen on the FF value which is only 74.6 % in M12 against 76.4 % in M2.

Switching to half-cell reverses the trend: the efficiency of the M12 module (19.60 %) becomes higher than that of the M2 module (19.48 %). This is partly due to the decrease in module resistive losses, which corresponds to a greater gain for the M12 module by switching from full-cell to half-cell than for the M2 module. The FF gain between full and half-cell is 2.6 $\%_{abs}$ for the M12 module while it is only 1.2 $\%_{abs}$ for the M2 module: it is the combined effect of resistive losses and J02 cutting step losses that are both reduced from full to half-cell in a M12 module compared to a M2 module. But as we can see, this increase in FF from full to half-cell, which is more important for an M12 module than M2, is not enough to explain the better half-cell efficiency of the M12 module. Indeed, in half-cell, the M12 module has a FF of 77.25 % compared to 77.60 % in M2. One must push the cutting steps in third-cell or quarter-cell so that the FF of the M12 module exceeds that of the M2 module. But pushing the cutting steps in third-cell or quarter-cell implies a decrease in efficiency in the case of both M2 and M12. The optimum fill factor is in half-cell configuration for module M2, and in third-cell configuration for module M12. The optimum output remains in half-cell configuration, for both M12 and M2.

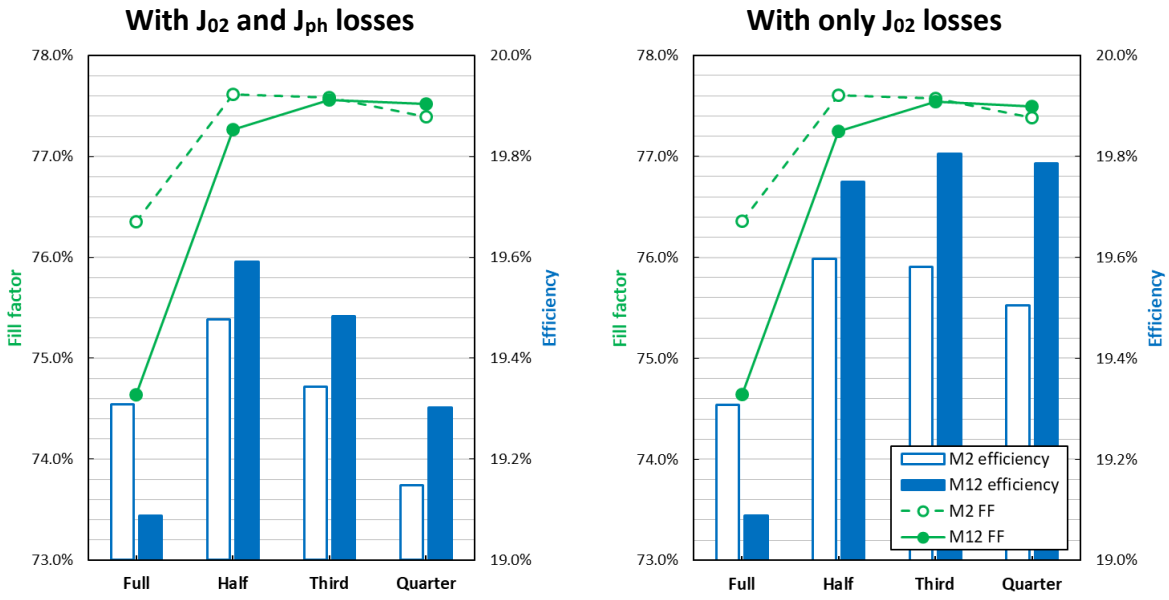

Figure 72: Evolution of the module fill factor and module efficiency as a function of the number of sub-cells used for M2 wafer and M12 wafer. In a case with both J_{02} and J_{ph} losses (left) and in the case of J_{02} losses only (right).

We now consider the case with only cutting losses on the J_{02} (Figure 72 – right). The variation of the FF is similar to the case with the losses on J_{02} and J_{ph}: the losses on J_{ph} have an indistinguishable impact on the FF. On the other hand, without a decrease in J_{ph}, the efficiency is less affected for a high number of cuts. This results in a change in the optimum efficiency in M12 module: it is now in third-cell with 19.8 %. But the efficiency values for half-cell (19.76 %) and quarter-cell (19.78 %) are very close.

For the configurations studied, it therefore does not seem useful to consider cut-outs larger than a half-cell configuration, even for modules made up of wafers as large as M12. The assumptions used are reminded. The module has a glass / glass architecture: the intercellular spaces do not participate in the increase of the photo-generated current by reflection at the air-glass interface. The cell used in these simulations is a cell corresponding to the average of those used to characterize the cutting losses (efficiency of 21.8 %, J_{mpp} of 35.54 mA/cm²).

This efficiency value is far from being a record for the INES pilot line. Cells at 23 % are common, with a record at 24.63 % on full size M2 wafer [164]. As these cells have a better passivation, the effect of cutting should be more marked. Indeed, the proportion of J_{02} brought by the cutting compared to the basic J_{02} (bulk + edge of the full-cell) will be higher. These cells also have a higher I_{sc} current. The expected resistive gain in module will therefore be higher. This is the goal of the next part: to study if the extracted J_{02} edge can be used to predict the performance of a real record module in half-cell configuration.

III.B.2.b *Prediction of the performance of a record module with 120 half-cells SHJ*

The goal is to know if the integration of the losses in cutting in modelling makes it possible to predict in a sufficiently precise way the IVs parameters of the final module. Indeed, the re-measurement of the cells after cutting is not a very common step. It requires the addition of a process step, and may require flash testers of a different design than those used for the characterization of full-cells. The Figure 73 is an electroluminescence image of the record module manufactured. We see the two sub-modules built in parallel (top and bottom), and a very good matching of the cells, which suggests a negligible electrical mismatch. There are no broken cells.

Electroluminescence at 3 A

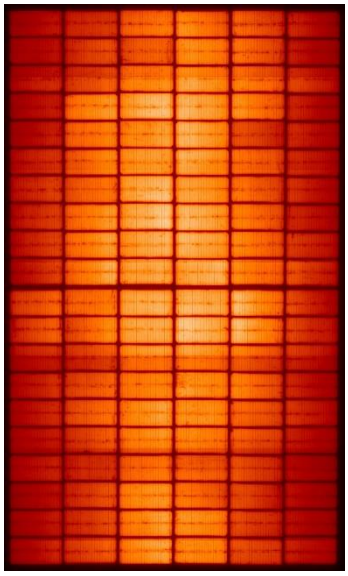

Electroluminescence at 300 mA

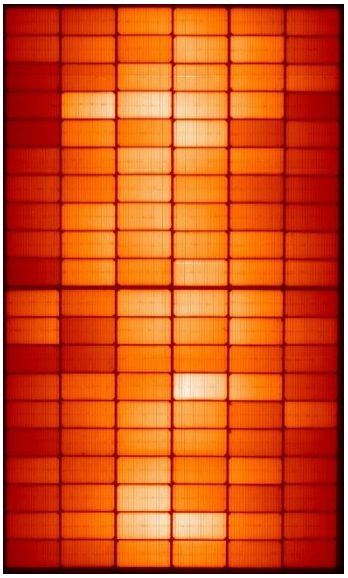

Figure 73: Electroluminescence images of the record module at high current (3A / left) and low current (0.3A / right).

The average cell used for this record module has a front pitch of 2.12 mm and a rear pitch of 0.2 mm. The line width measured automatically by optical contrast (ZEISS© instrument) is 42 µm, corrected to 36 µm. The effective shading of the fingers in the cell is 88 %. These have a line resistance of 4.5 Ohm/cm. The 60 full-cells were measured after manufacturing, then light-soaked and re-measured. They were then cut and the 120 half-cells were re-measured. As no light-soaking effect is included in our model, the IV cell measurements after light-soaking were chosen as the starting point of the module study. The mean IV parameters of the 23.68 % efficiency SH cells before and after cutting are given in the Table 11.

The initial mean cell IV are best fitted with J_{ph} of 38.22 mA/cm², J_{01} of 10.65 fA/cm², J_{02} of 0.25 nA/cm² and r_s of 0.3532 Ohm.cm². After the cutting step, J_{ph} decreases to 38.12 mA/cm² and J_{02} increases to 1.25 nA/cm². As can be seen, the fit errors on the full-cell IV parameters and the prediction errors with the modification of J_{ph} and J_{02} are at least an order of magnitude below the variation of the IV parameters due to cutting. This reinforces the idea that the use of J_{ph} edge and J_{02} edge also applies to much better performance cells (23.69 % efficiency) than those used to determine these values (21.79 %).

	I_{sc} *(A)*	**V_{oc}** *(mV)*	**FF** *(%)*	**Eta** (%)
Mean of measured 60 full-cells	9.338	742.60	83.42	23.68
Initial Fit	9.338	742.4	83.47	23.68
Fitting error	0.01%	0.03 %	- 0.06 %	0.00 %
Mean of measured 120 half-cells	9.313	740.9	82.89	23.41
Predicted with J_{02} and J_{ph} losses	9.314	741.1	82.82	23.40
Prediction error	-0.01 %	-0.03 %	0.08 %	0.04 %
Difference before / after cutting	0.27 %	0.23 %	0.64 %	1.14 %

Table 11: IV parameters measured experimentally and predicted by the 2-diode model for the 60 full-cells and the corresponding 120 half-cells after cutting.

The module created uses low-iron glass with anti-reflective coating on its outside, and without anti-reflective coating on its side in contact with the encapsulant. The glass is 3.2 mm thick, 1.669 m high and 0.998 m wide. The encapsulant on the front side is a 450 µm thick low UV cut-off EVA. The electrical interconnection of the cells is realized with 18 wires of 250 µm diameter for their copper core. The inter-cell distance is 2.5 mm and the inter-string distance is 5 mm. The encapsulant on the back side is a white EVA to maximize the inter-cell I_{sc} gain.

The IV parameters of the module measured on a SPIRE class AAA+ flash tester, as well as the parameters of the module predicted by the model developed in this thesis are given in Table 12.

	I_{sc} *(A)*	**V_{oc}** *(V)*	**FF** *(%)*	**Power** (W)	**Impp** (A)	**Vmpp** (V)
Measure raw	9.410	44.30	80.24	334.5	8.873	37.70
Measure corrected	9.405	44.30	80.28	334.5	8.873	37.70
Predicted with CTMod	9.446	44.49	81.94	344.3	9.018	38.19
Prediction error	0.44 %	0.43 %	2.07 %	2.9 %	1.63 %	1.30 %
Predicted with CTMod with Isc correction	9.405	44.48	81.94	342.8	8.979	38.18
Prediction error	0 %	0.41 %	2.07 %	2.48 %	1.19 %	1.27 %

Table 12: IV parameters of the record module measured on SPIRE AAA+ flash-tester and predicted with the CTMod model.

The error on the I_{sc} current is acceptable (0.4 %) in view of the number of phenomena that can affect photo generation. As a reminder, the following process are taken into account: inactive surface losses, reflection at the air-glass interface, absorption in the glass and in the encapsulant, effective shading of fingers and ribbons, reflection at the encapsulant-cell interface, transmission of the spectrum on the rear side of the cell and its possible reflection on the metallization and the backsheet, photo-generation via the IQE of the cell, but also inter-cell gains by lambertian reflection on the white encapsulant and then the glass-to-glass interface.

The error made on the V_{oc} (0.4 %) is not due to an error on the I_{sc}, nor can it be due to to an error in taking into account the series resistance component of the cell and string interconnection. It can be due to a modification of parameters J_{01} and J_{02} of the cells when they have been transported and then integrated into the module. An additional shunt could also have appeared when the module was created.

On the other hand, the error made on the fill factor (2.1 %) is high. Like the V_{oc}, this error can be due to a modification of J_{01} and J_{02} of the cells apart from transport and / or integration, but also by the appearance of a shunt during the manufacture of the PV module. By keeping the same parameters of the 2-diode model but adding a shunt of 780 Ohm.cm² to fit the FF, the V_{oc} goes to 44.44 V, i.e. a modelling error reduced to 0.3 %. By keeping the same parameters of the 2 diode model but by adding an additional J_{02} of 2.85 nA/cm² to fit the FF, the error on the V_{oc} is reduced to 0.14 %. It would seem that it is therefore rather a modification of J_{02} during the manufacture of the module that is in question.

In order to remove the impact of the I_{sc} modelling error on the other parameters, the modeled I_{sc} is adjusted to match the experimental value. But even with this adjustment, the error made on V_{oc} (0.41 %), V_{mpp} (1.27 %) and I_{mpp} (1.19 %) is not acceptable. The sum of the absolute value of the error on the four IV parameters (I_{sc}, V_{oc}, I_{mpp} V_{mpp}) is 2.87 %. The contribution of the error on the V_{oc} to the error made on the FF is 14.3 %. It is 41.5 % for the I_{mpp} and 44.2 % for the V_{mpp}.

In the formalism of the 2-diode model with $n_1 = 1$ and $n_2 = 2$, the error made on the V_{oc} can be due only to three causes: a modification of J01 and / or J02 and / or the presence of a shunt additional. The modification of J01 seems unlikely, since for heterojunction cells, this parameter is strongly related to the bulk of the cell. The bulk should not be affected during the module manufacturing. We choose to ignore it.

The IV curve of the module is fitted by setting the following parameters: J_{ph} = 38.49 mA/cm² (I_{ph} = 9.405 A), J_{01} = 10.65 fA/cm², $n_1 = 1$ and $n_2 = 2$ and the series resistance value obtained by the model r_s = 0.5365 Ohm.cm² (R_s module = 0.5285 Ohm). The quality of the obtained fit is thus highly satisfying (R^2 = 0.9999), as shown by the reconstruction of parameters IV (Table 13). The values obtained by the fit therefore give R_{shunt} = 3.425 kOhm.cm² and an additional J02 of 2 nA / cm² (ie 3.25 nA / cm² in total).

	I_{sc} *(A)*	**V_{oc}** *(V)*	**FF** *(%)*	**Power** (W)	**I_{mpp}** (A)	**V_{mpp}** (V)
Measure corrected	9.405	44.30	80.28	334.5	8.873	37.70
Predicted with Isc correction Rshunt (3.425 kOhm.cm²) and additional J02 (+2 nA/cm²)	9.405	44.32	80.42	335.2	8.867	37.80
Prediction error	0.00 %	0.05 %	0.17 %	0.21 %	- 0.07 %	0.27 %

Table 13: IV parameters of the module: measurement and reconstructed with IV curve fitting where J_{ph}, J_{01} n_1, n_2 and r_s are set to the modelled values, and only J_{02} and R_{shnt} are free to vary.

These results have several possible explanations. First, it seems very unlikely that the estimate of the J02 edge is bad and that the true value is the sum of the value extracted experimentally (+1 nA/cm²) with the additional value found by the fit of the module curve (+3 nA/cm²). Indeed, if this were the case, the prediction of the performance of the cells after cutting from the performance of the cells before the cutting would not be good (Table 11).

Then, it is also very unlikely that the estimate of the performance of the module due to the half-cells (with the reduction of the resistive losses compared to a full-cell case) is bad. Indeed, the developed model fits perfectly with the expectations of the theory (see Part III.A).

The presence of a shunt in the module is not surprising. This is a phenomenon easily observable on an IV curve and whose origin is known: the passage of the cell interconnection ribbons from the front face of one cell to the rear face of the next can generate a shunt via the ECA (cells with busbar). It can also be caused by the melting of the coating of the wires during lamination (multi-wire technology, as is the case with the module studied).

The presence of an additional J02 could be a physical reality. The transport of cells, their manipulation in the stringer and during the creation of the module, or even the lamination could generate defects in the cell, and therefore as many recombination centres.

But it is also possible that this additional J02 is not physical reality: the difference in calibration of the two devices used could make this j02 artificial. Indeed, a first piece of equipment is used for measuring the cell IVs curves, which are used to extract the basic parameters of the model diodes (J01 and J02). A second IV measuring equipment is then used to obtain the experimental IV curve of the module, which one attempts to compare with the predicted IV curve. Additional studies must be carried out to understand the origin of the divergence between experimental measurement and model prediction for the case of half-cell modules. The uncertainties on each piece of equipment can combine to give very uncertain results.

As an example only, one of the cell certification institutes (ISFH CalTec) gives the following expanded uncertainties (k=2) on the IV parameters of heterojunction cells: 1.07 % for I_{sc}, 0.29 % for V_{oc}, 0.80 % for FF, and 1.31 % for the P_{mpp}. The uncertainties on the IVs parameters of a module are even greater, including by specialized laboratories. Dirnberger *et al*. showed in 2013 that the expanded uncertainties on a standard crystalline silicon module are: 1.3 % for I_{sc}, 0.6 % for V_{oc}, 1.2 % for FF and 1.6 % for the P_{mpp} [165]–[167]. These results are valid for primary standards from organizations specializing in certification. The uncertainty of INES equipment is necessarily greater because of the use of secondary standards. It would therefore be very interesting to create combined monitoring systems for cell and module flash-test equipment to characterize systematic deviations and reduce the uncertainties on the experimental CTMs.

Another hypothesis to explain the differences in FF lies in the width of the metallization lines used. The residual losses in the fingers in a multi-wires configuration are very low. For record modules without an important objective of reliability, the width of the metallization lines is reduced to a minimum. This limits the shading of the cell without affecting the FF too much. However, very fine lines can cause line breaks, completely preventing current from flowing. These interruptions are barely visible during cell measurements, because a 36-wire network is used. In module, 18 wires are used, which multiplies the impact of this interruptions. This effect has not been precisely quantified.

Conclusion of the Chapter III

In the first part of this chapter, we were interested in the maximum performance gains expected by cutting the cells (without losses during this step). The resistive losses in the cell interconnection follow a law in $1/N^2$, where N is the number of sub-cells obtained after cutting a full-cell. The advantage obtained by cutting is therefore mainly due to the first cut. This effect, well known in literature and industry, allows us to validate the basic behaviour of our model when taking into account the cutting of full-cells. The effect of irradiance does not change its behaviour, even though the FF gains caused by cutting are weaker and weaker as the irradiance decreases. The effect of an incompressible inter-cell distance does not change the trends: the law of variation of resistive losses is enriched with a term in 1/N. Taking into account the inactive surfaces of the module significantly modifies the variation in efficiency depending on the number of cuts made. The optimum in module efficiency is obtained in half-cell configuration for an M2 module with standard inter-cell distances.

However, the effect of recombination can significantly decrease the efficiency of the cells and thus, of the module. As the cutting of the cells is considered first to reduce the resistive losses in module, it is necessary to include this step in the CTM analysis. The second part of the chapter therefore focused on the characterization of the recombination current induced at the edges newly created by the cut. This has never been done previously for heterojunction solar cells. Twenty cells were characterized before and after cutting. The J_{02} edge current obtained is 7.63 nA / cm, consistent with the experimental values obtained for other technologies, and lower than the theoretical value of a completely passivated edge (20 nA / cm). It has been shown that a decrease in the I_{sc} must also be included to reproduce the total losses after cutting: 0.020 % / cm of loss on the I_{ph} was measured. The bulk of these losses occur from the laser fire. These values imply a drop of 0.5 % on the I_{sc}, of 0.22 % on the V_{oc}, of 0.65 % on the FF and 1.37 % on the efficiency. These results were obtained for cells of 21.8 % average efficiency.

These losses were therefore integrated into the overall module performance model to predict the IV parameters of a record module. The cells of this record module were measured before and after cutting. The losses of J_{02} and J_{ph} edge made it possible to correctly predict the performance of the cells after cutting, even though these cells have a better efficiency than those used for the initial characterization (23.43 % vs 21.8 %). On the other hand, this did not make it possible to correctly predict the performance of the complete module, due to the error made on the optical prediction (I_{sc}), and the presence of an additional J_{02} of 2 nA / cm, whose origin is unknown. Further studies would be welcome to understand it.

Conclusion du Chapitre III

Dans la première partie de ce chapitre, nous nous sommes intéressés aux gains de performance maximums attendus par la découpe des cellules (sans pertes lors de cette étape). Les pertes résistives dans l'interconnexion des cellules suivent une loi en $1/N^2$, où N est le nombre de sous-cellules obtenues après découpe d'une cellule complète. L'avantage obtenu par la découpe est donc principalement dû à la première découpe. Cet effet, bien connu dans la littérature et l'industrie, nous permet de valider le comportement de base de notre modèle en prenant en compte la découpe des cellules complètes. L'effet de l'irradiance ne modifie pas

son comportement, même si les gains de FF dus à la découpe sont de plus en plus faibles lorsque l'irradiance diminue. L'effet d'une distance inter-cellules incompressible ne change pas les tendances : la loi de variation des pertes résistives s'enrichit d'un terme en 1/N. La prise en compte des surfaces inactives du module modifie significativement la variation du rendement en fonction du nombre de coupes réalisées. L'optimum du rendement du module est obtenu en configuration demi-cellule pour un module M2 avec des distances inter-cellules standard.

Cependant, l'effet de la recombinaison peut diminuer significativement le rendement des cellules et donc du module. Comme la découpe des cellules est considérée en premier lieu pour réduire les pertes résistives dans le module, il est nécessaire d'inclure cette étape dans l'analyse CTM. La deuxième partie du chapitre est donc axée sur la caractérisation du courant de recombinaison induit au niveau des arêtes nouvellement créées lors de la découpe. Ceci n'a jamais été fait auparavant pour des cellules solaires à hétérojonction. Vingt cellules ont été caractérisées avant et après la découpe. Le courant de bord J_{02} obtenu est de 7,63 nA/cm, cohérent avec les valeurs expérimentales obtenues pour d'autres technologies, et inférieur à la valeur théorique d'un bord complètement passivé (20 nA/cm). Il a été démontré qu'il faut également inclure une diminution de l'I_{sc} pour reproduire les pertes totales après découpe : 0,020 % / cm de perte sur l'I_{ph} a été mesuré. La majeure partie de ces pertes provient du tir laser. Ces valeurs impliquent une baisse de 0,5 % sur l'I_{sc}, de 0,22 % sur le V_{oc}, de 0,65 % sur le FF et de 1,37 % sur le rendement. Ces résultats ont été obtenus pour des cellules de 21,8 % de rendement moyen.

Ces pertes ont donc été intégrées dans le modèle de performance globale du module pour prédire les paramètres IV d'un module record. Les cellules de ce module record ont été mesurées avant et après découpe. Les pertes de bord J_{02} et J_{ph} ont permis de prédire correctement les performances des cellules après découpe, même si ces cellules ont un meilleur rendement que celles utilisées pour la caractérisation initiale (23,43 % vs 21,8 %). En revanche, cela n'a pas permis de prédire correctement les performances du module complet, en raison de l'erreur faite sur la prédiction optique (I_{sc}), et de la présence d'un J_{02} supplémentaire de 2 nA/cm, dont l'origine est inconnue. Des études complémentaires seraient les bienvenues pour la comprendre.

Chapter IV

Characterization of UV-Vis-NIR optical constants of encapsulant for accurate determination of absorption and backscattering losses in photovoltaics modules

Introduction

Encapsulation materials serve multiple purposes, such as mechanical coupling between cells and glass, electrical insulation and moisture barrier. In addition, they must present good optical properties [168]. The optical properties of encapsulants influences the cell performance in several ways.

Firstly, the refractive index of the encapsulant impacts the amount of reflected light at each interface: air / encapsulant and encapsulant / cell. Indeed, photo-generated current measurements of a cell are typically performed without encapsulant, in an air/cell configuration. Since the refractive index of the encapsulant is higher than the one of air, light reflections are weaker at the encapsulant/cell interface, leading to a photocurrent gain of the module relative to the cell. Secondly, the extinction coefficient k impacts the level of absorption (and in some cases, as detailed later, light scattering) in the encapsulant bulk. Obviously, this extinction coefficient should be as small as possible in the solar spectral range. Moreover, as UV light is known to degrade both modules and cells, the knowledge of the spectral absorbance in the UV range is also a prerequisite for durability studies [169], [170]. Encapsulants in PV are thus classified in terms of behaviour in near-UV, with low to high UV cut-off. An encapsulant with a high-UV cut-off has near-zero optical transmission below 400 nm. Conversely, an encapsulant with a low UV cut-off absorbs very little UV rays.

In consequence, optical constants are necessary input parameters for module simulation and digital prototyping to find optimal design of module using tools such as ISFH Daidalos™ [85], [88], PVLightHouse Sunsolve ™[171], Optos matrix formalism [100], and others.

A large range of encapsulating materials are currently available. Historically, the first PV module were laminated with polymethyl siloxane (PDMS) [172]. Nowadays, ethylene vinyl acetate copolymer (EVA) is the most used encapsulant material, representing more than $90\ \%$ of market share in 2018 [20], thanks to its low price, good adhesion with glass, and good moisture barrier properties. However, it suffers from non-negligible degradation mechanisms [173] due to acetic acid, can lead to potential induced degradation (PID) and is not well-suited for some specific cell-technology (such as Heterojunction with Intrinsic Thin-Layer (HIT) solar cell) or module architecture (glass-glass) [174]. Other families of polymer can be used: polyvinyl butyral (PVB), thermoplastic polyolefin (TPO), polyolefin elastomer (POE), ionomers [168], [172]. Each family has its own optical properties, governed by the nature of the polymer chains, the additive (adhesion promoter, UV absorber …), and the degree of crystallinity. Moreover, the lamination process also influences the optical properties, which can be used to control the process quality and the level of curing state for EVA [23]. The reduction of the cooling time of the module after lamination, for example via a cooling press, allows a limitation of light scattering by TPOs [24].

In this context, it appears necessary to be able to characterise accurately the optical properties of such encapsulating materials.

Several standards exist for the determination of optical properties of transparent layer. Determination of refractive index of transparent organic plastic with a refractometer method is proposed in ASTM D542-14 [175]: it is based on the total reflection angle determination. Haze measurement is detailed in ASTM D1003 and D1044 [176], [177], is supposed to quantify

the amount of light scattering. Some producers apply modified standards of glass building solar weighted transmittance [178]. But the most relevant standard is the IEC 62788-1-4 [179], which provides optical transmittance measurement methods for PV encapsulants and calculation of the solar-weighted photon transmittance, yellowness index, and UV cut-off wavelength.

Characterization of optical properties of transparent polymer have been investigated for a long time [180]. However, most of the method and measurements proposed so far give only partial information. Light absorption is commonly characterized by the encapsulant transmittance, but it is not representative of real losses in module due to light reflections at the air/layer interface. Coarse characterization of scattering is possible by haze measurement, but is generally not a spectrally resolved measurement [181]. Moreover, some studies characterize absorption ignoring the effect of light scattering at short wavelengths [83], [127], [182], [183], leading to upper estimation of absorption and under estimation of the amount of light reaching the cell. It is, however, an important value: for example, evaluation of the damp-heat aging test impact on optical performance of silicon and EVA encapsulants can be tricky without taking into account scattering by moisture ingress [169].

To address this issue, recent studies apply the four-flux model to account for collimated and diffuse light [184], [185], but the optical parameters obtained in these works were not spectrally resolved. Oreski *et al*. have used a four-flux model to determine spectrally resolved absorption and scattering coefficients of encapsulants, but values of refractive index were not mentioned in their work [186]. Kempe *et al*. has characterized the spectral absorption in eleven encapsulants of different nature (PDMS, POE, EVA, Ionomer..), without differentiation between absorption and scattering [187]. Other methods like photo-thermal deflection spectroscopy has also been used to determine absorption and scattering coefficients in low-loss polymer optical waveguides [188]. French *et al*. have used ellipsometry and spectroscopy to determine absorption coefficient, refractive index and haze of several polymer for optics of CPV system, but no scattering coefficient is extracted [189]. In conclusion, no study proposes the simultaneous determination of spectrally resolved value of refractive index, absorption coefficient and scattering coefficient simultaneously and consistently. Moreover, if the optical constants of standards encapsulant like EVA and silicon can be easily found in literature, values for new encapsulants, needed for simulation tools calibration, are not easily available, to our knowledge.

The aim of this work is thus to propose a reliable method allowing to determine spectrally resolved value of refractive index, absorption coefficient and scattering coefficient in the UV, visible and NIR spectral range, and to apply it to innovative encapsulants for solar module application.

Part IV.A Experimental method

IV.A.1 Sample preparation and lamination

Encapsulant samples are laminated using a membrane laminator. The samples are placed between two isolating and non-adhesive ultra-smooth (root mean square roughness around 50nm) PTFE thermoplastic film with high melting point (> 250°C) and covered by two non-textured glass plates of 10 x 10 cm (see Figure 74). Using the same lamination process, the temperature measured at the centre of these small optical samples can be at least 5 degrees higher than the one measures in standard size modules (60 cells). This is caused by border effects. Temperature influences the crystallinity of samples, and therefore their optical behaviour. The optical constants extracted on these small encapsulant samples may not be the same as those obtained for a sample from a large module carried out with the same lamination process. Consequently, in order to correctly predict the performance of a large module from the optical constants determined on a small sample, the lamination process of the large module will have to be adapted so that the encapsulant that constitutes it undergoes the same temperature cycle as the encapsulant used for optical measurements. To this aim, the edges of the laminated {glass / PTFE / encapsulant / PTFE / glass} are closed with a strip of ribbon. Hence, the encapsulant does not flow and keeps the same thickness as it would have in a real module.

Once laminated, the samples are separated from glass and non-adhesive film and cut into four pieces of 5x5 cm which can fit the spectrophotometer sample compartments (Figure 74). The thickness is recorded at four points around the middle of the sample with an electronic micrometre FOWLER of 1 µm resolution. Thickness measurement is performed after optical measurement, to prevent deterioration of the surface. Samples are kept in an opaque, airtight bag to prevent from photo-oxidation. Handling of samples is done with disposable gloves to prevent surface contamination with organic compounds.

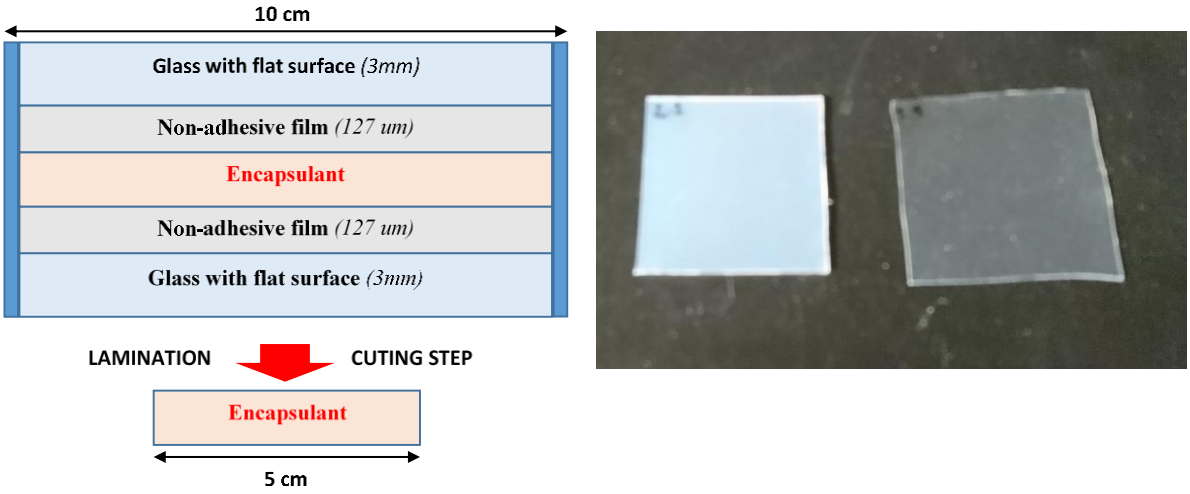

Figure 74 : (Left) Composition of sample for lamination process. The sample need to be held between glass and PTFE sandwich during process, to maintain a uniform surface state. The encapsulant sheet alone is used for spectrophotometric measurement. (Right) Picture of a high and low diffusive encapsulants sample on a black background

IV.A.2 Spectral reflectance and transmittance measurements

In this work, a spectrophotometer instrument, allowing specular and diffuse measurements, has been used. It is a high accuracy UV-Vis-NIR PERKINELMER Lambda 950. A deuterium lamp is used for UV measurements between 280 and 320 nm, and a tungsten lamp is used for the remaining wavelengths. The double holographic grating monochromator switches at 860 nm. The beam splitting system for correction of lamp deviation is a chopper wheel with 46+Hz cycle: dark sample / sample / dark reference / reference and a chopper segment signal correction. The temperature of the room is controlled and ranges from 20.5 to 21.5 °C. The samples are brought into the room one hour before the measurement to ensure the correct thermalization.

The first module - an InGaAs integrating sphere (IS) of 150 mm in diameter - is used for reflectance and transmittance, in total and diffuse mode. It is referred to as "IS 150mm" in the following. The detector is a photomultiplier R6872 for high energy in the whole UV/vis wavelength and a Peltier cooled detector for NIR, the switching occurring at 860 nm. The UV/Vis resolution is less than 0.05 nm and the NIR resolution is less than 0.20 nm. The back aperture for reflectance measurement is a 25 mm diameter hole. The front side aperture for diffuse reflectance measurement is a 30 mm side square. For diffuse transmittance and reflectance measurement, a light trap guarantees a transmittance lower than 0.1 %, eliminating errors due to back reflectance. The diffuse spectralon has been calibrated by LabSphere™. The incident light beam hits the sample with an angle of 8°; the geometry of measurements is thus 8°:d. The size of the spot is 3 mm wide and 12 mm high.

At the beginning of each series of measurements, a baseline is made to correct from any instrument deviation. Measurements are made between 280 nm and 2450 nm with 10 nm steps as recommended by the IEC standard 62788-1-4:2016. The spectralon is systematically placed in the same position, to minimize uncertainty due to its potential inhomogeneity. At the beginning of each series of measurements, the baseline is measured (100 % transmittance in transmittance measurements, and spectralon reflectance in reflectance measurements) and compare with a same measure at the end of the series of measurements to check for deviation. A check of the dark level is systematically made after baseline measurement, using a light trap at the back hole of the integrating sphere. It ensures that the spot of the spectrophotometer is correctly aligned with the sample aperture. All the geometry of the measurements are illustrated in Figure 75. Let us define the physical quantities measured by the apparatus:

- The **Total transmittance $\mathbf{T_t}$:** in this case, the sample is located at the front hole of the integrating sphere and the back hole is closed with the LabSphere™ spectralon.

- The **Diffuse transmittance $\mathbf{T_{cd}}$:** (also denoted as “collimated-to-diffuse” transmittance). In this case, the sample is located at the front hole of the integrating sphere and the back hole is closed with the light trap. Due to aperture of back hole with a radius $r_{ht} = 12.5\ mm$, and diameter of the sphere $d_s = 150\ mm$, rays with an angle $\theta_d > 4.8°$ are included in diffuse measurement. The aperture represents a solid angle Ω_{ht} of $0.35\ \%$ of the $2\pi\ sr$ of the half sphere (1):

$$\frac{\Omega_{ht}}{2\pi} = \frac{1}{2}\left(\frac{r_{ht}}{d_s}\right)^2 = 0.35\ \% \quad (1)$$

- The **Total reflectance $\mathbf{R_t}$:** In this case, the sample is located at the back hole of the sphere, the specular light port at 16° from the front port is closed. The light trap is located at the back of the sample.

- The **Diffuse reflectance $\mathbf{R_{cd}}$:** (also denoted as the "collimated-to-diffuse" reflectance) in this case, the configuration is the same than for measuring the total reflectance, but the specular port is open. Due to aperture of specular light port with a side $a_{hr} = 30\,mm$, and the incident angle $\theta_i = 8°$, rays with angle $\theta_d > 6.7°$ are included in diffuse measurement. The aperture represents a solid angle of $0.66\,\%$ of the 2π sr of the half-sphere (2):

$$\frac{\Omega_{hr}}{2\pi} = \frac{1}{2\pi\cos(2\theta_i)}\left(\frac{a_{hr}}{d_s}\right)^2 = 0.66\,\% \qquad (2)$$

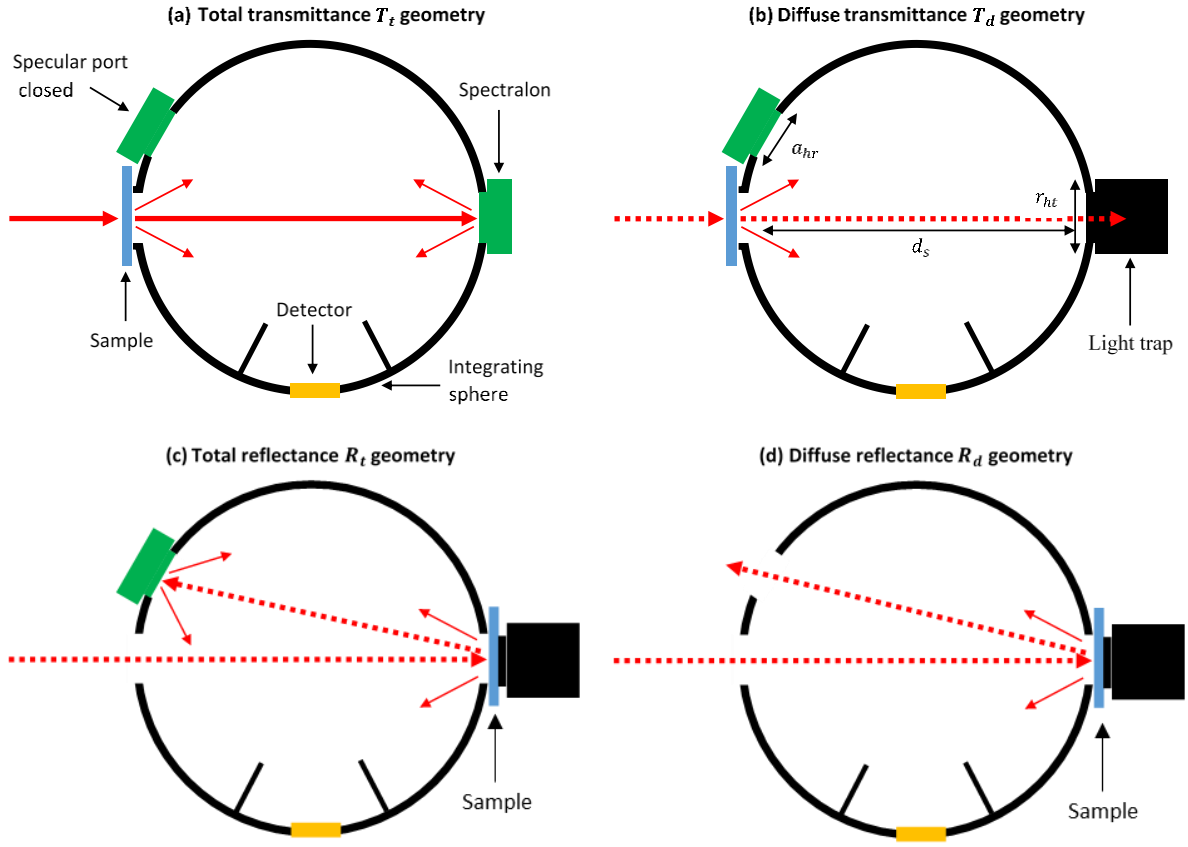

Figure 75: Four measurement geometries used in the work: (a) Total transmittance. (b) Diffuse transmittance. (c) Total reflectance. (d) Diffuse reflectance; depending on the position of sample, presence or absence of the light trap, specular port open or closed

The collimated-to-collimated transmittance T_{cc} and the collimated-to-collimated reflectance R_{cc} are computed afterwards as: $T_{cc} = T_t - T_{cd}$ and $R_{cc} = R_t - R_{cd}$.

A second spectrophotometer Lambda 950 is used with an ARTA module (automatic reflectance and transmittance measurement system) [190]. It will be referred to as "ARTA" in the following. This goniometer has 2 degree of freedom: the sample can rotate on one axis, and the detector can rotate around the same axis independently. The detector is a 60mm integrating sphere with PMT and InGaAs detectors. This spectrophotometer is less accurate than the previous one due to the reduced size of the integrating sphere. The width of the window of the integrating sphere can range from 20 mm to 0 mm, for a fixed height of 10 mm: by reducing this IS aperture, it is possible to better select the collimated part of the beam in relation to the diffuse part. Details are given in the following section. This spectrophotometer cannot perform measurement of collimated-to-diffuse or total transmittance or reflectance. It is only used to obtain value of collimated-to-collimated R & T. The principle of operation of the second spectrophotometer (ARTA) is schematized on Figure 76.

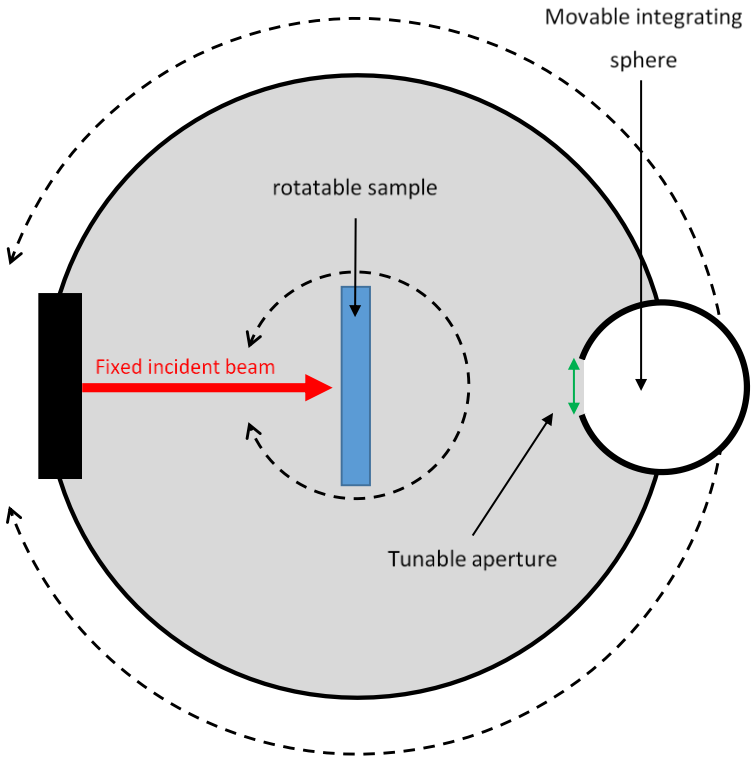

Figure 76: Operating principle of the second spectrophotometer (ARTA). Depending on the angle of the sample and the angle of the integrating sphere, a measurement of the collimated flux can be performed in transmittance or reflectance.

IV.A.3 Impact of specular port aperture and of the reference sample

Some experimental bias may occur in the measurement of diffuse reflectance and transmittance due to aperture size of the specular port of the spectrophotometer IS 150 mm. To illustrate this effect, we compare the collimated-to-collimated transmittance in two configurations: (i) the measurement on IS 150 mm obtained as the difference of total and collimated-to-diffuse transmittance (ii) the direct measurement on ARTA. The ARTA

measurement is done for three acceptance angles, corresponding to detector aperture a_{ARTA} of 20 mm, 5 mm, and 1 mm. Ideally, the real collimated contribution should be obtained when the aperture tends to zero ($\theta_d \approx 0°$). However, with aperture smaller than 1 mm, the too low signal to noise ratio becomes prejudicial. The difference between $T_{cc,SI}$ and $T_{cc,ARTA}$ for the three acceptance angles are plotted on the Figure 78 , for a highly diffusive sample (TPO).

The smaller the aperture of ARTA's detector, the closer we get to the true value of collimated-to-collimated transmittance: aperture of 1 mm gives a good approximation of the true value. Conversely, the larger the aperture, the greater the portion of the diffuse flow counted as collimated. The difference between the T_{cc} value obtained on the IS 150mm and that measured on the ARTA for the 1mm aperture show that measurements of T_{cc} on the IS 150 mm spectrophotometer are overestimated by 4 to 7 % in the UVs and Visible. This value decreases in the IR region, where the diffusion of the sample becomes smaller.

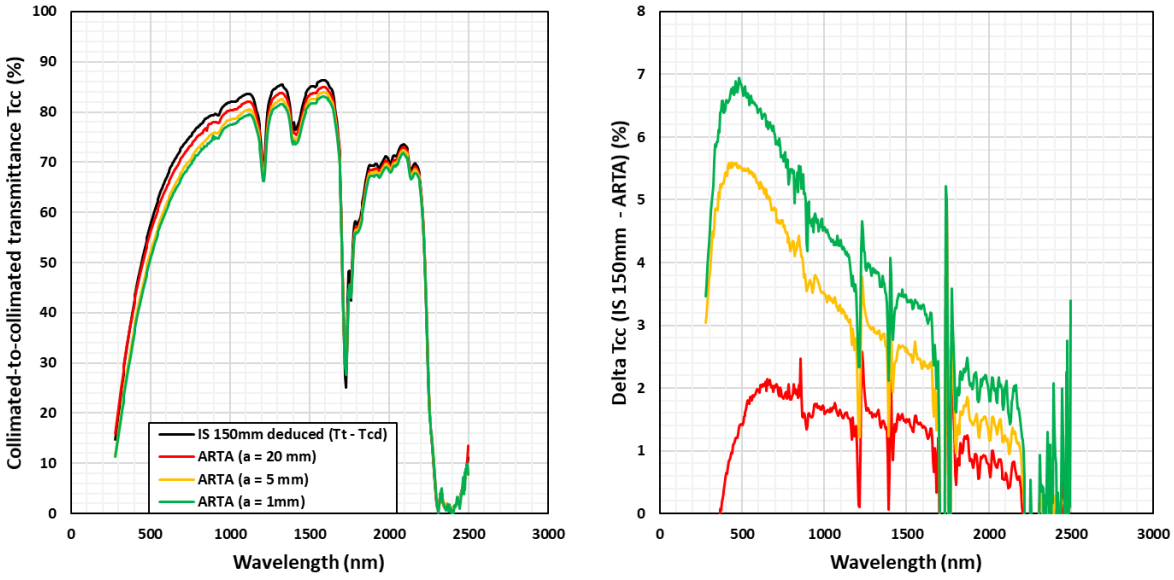

Figure 77 : (Left) Collimated-to-collimated transmittance for IS 150 mm spectrophotometer (deduce from Tt and Tcd) and for ARTA spectrophotometer for three aperture a of the detector: 20mm, 5mm & 1mm. (Right) Difference between Tcc deduced from IS 150mm measurements and Tcc obtain with ARTA for the three aperture.

The reflectance measurements require to perform a baseline measurement on a calibrated sample. Two calibrated references are available. A lambertian reflectance standard spectralon by LabSphere™ and a calibrated OMT™ reference mirror. The spectralon is preferred when measuring a “mostly diffusive” sample and the reference mirror is used for a “mostly specular” sample. The encapsulants characterized in this study are highly specular within the range of 1500-2500 nm, but some present a highly diffusive behaviour within the range of 280-1500 nm, which raises the question of the impact of the nature (lambertian or specular) of the reference standard on the determination of diffuse and total reflectance.

To investigate it, we measured a diffusive sample (TPO) in total and diffuse reflectance, with calibration with the reference mirror and with the spectralon sample. The results are presented in Figure 78. We notice a difference of 0.2 to 0.6 % in the UV region, and almost no

difference from 500 nm to 2500 nm. Firstly, the shift seems to be independent of the geometry of the measure (total vs diffuse). Indeed, the difference between measurements with mirror calibration and spectralon calibration is almost the same for total reflectance or diffuse reflectance for both samples. This means that the difference does not come from the collimated part of the flow, but from the diffuse part.The explanation for this difference has not been found.

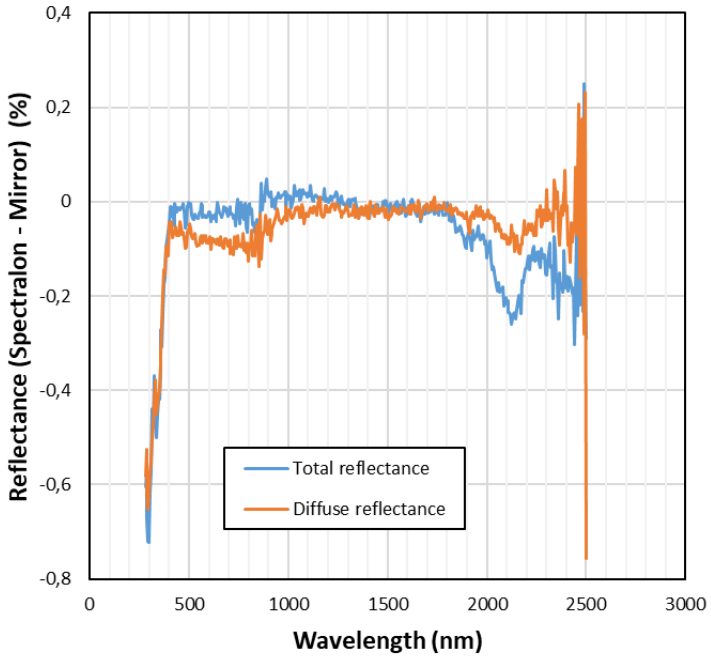

Figure 78: Impact of the nature of the standard reflectance sample on the measure of diffuse and total transmittance for a highly diffusive material (TPO)

The extraction of optical parameters of the PV encapsulant are valid under certain hypothesis, which are reviewed in the following.

First of all, the sample must not be photo-luminescent, because the spectrophotometer is not equipped with a monochromator between sample and detector, and the formulation of the four-flux model does not include bulk emission. In a more general view, there must be no change in wavelength of the incoming beam (due to potential inelastic scattering for example).No polarisation effect has been taken into account, as the specular light is at normal incidence, and because of the depolarization induced by the scattering [191].

Part IV.B Theory: overview of the optical four-flux model

IV.B.1 Model of Maheu *et al*. with Rozé *et al*., interpolation and bi-hemispherical reflectance

IV.B.1.a *The formalism of the four-flux model*

This section is dedicated to a brief presentation of the 4-flow model of Maheu *et al.*, 1984, the starting point of the approach used in this work. It describes the propagation of light through a thick and homogeneous layer, accounting for absorption, reflectance and refraction at the interfaces and scattering (in the Lambertian approximation). Coherence, polarization and non-linearity effects are neglected.

In the case of a slab composed of randomly homogeneously distributed particles, with perpendicular illumination of unpolarised light, the propagation of light in a medium that absorbs and scatters light is governed by the radiative transfer equation [192], [193]:

$$\mu \frac{dI(\tau,\mu)}{d\tau} = -I(\tau,\mu) + \frac{\omega_0}{2}\int_{-1}^{+1} p(\mu,\mu')I(\tau,\mu') - \frac{\omega_0}{4\pi}S(\tau,\mu) \quad (3)$$

where $I(\tau,\mu)$ is the luminance (or specific intensity) of the diffuse radiation at an optical depth τ and the direction of propagation μ. The optical depth is $\tau = (s+a)d$, with s the scaterring coefficient, a the absorbtion coefficient, and d the thickness of the film. The single scattering albedo is defined as $\omega_0 = s/(s+a)$. $p(\mu,\mu')$ is the scattering phase function, i.e. the probability that a scattering event change the light direction from μ to μ'. Finally, $S(\tau,\mu)$ is the intensity of the collimated beam in the direction μ.

The four-flux model is an approximation of the radiative transport equation, assuming that forward I_d and outward J_d diffused irradiances are Lambertian. Contrary to the two-flux (or Kulbelka-Munk model), it also considers the propagation of the collimated (or ballistic) forward I_c and outward J_c irradiance and its coupling with diffused flux.

Several formulations of the four-flux model exist. Maheu *et al.* [194], [195] proposed a four flux model for a scattering layer, accounting for reflectance and transmittance of the interface. Vargas *et al.*, [196] have generalized the expression of Maheu *et al.*, taking into account different value for forward scattering ratio in up and down direction. Expression of diffuse and collimated reflectance are given in function of light transport parameters, namely:

- The **absorption coefficient a (m-1):** the fraction of irradiance absorbed by a layer of infinitesimal thickness dz is $a\ dz$.

- The **scattering coefficient s (m-1):** the fraction of irradiance scattered by a layer of infinitesimal thickness dz is $s\ dz$.

- The **average crossing parameter ϵ** is defined as the average path travelled by the diffuse radiation, which cross the layer perpendicular. If the collimated beam crosses the infinitesimal dz, the diffuse radiation crosses $\epsilon\ dz$.

- The **forward scattering ratio ζ** is the ratio of irradiance scattered by the particle in the forward hemisphere divided by the total scattered energy. The ratio of energy back scattered is thus $1-\zeta$. This value is defined for a collimated beam, and is an approximation for the diffuse radiation.

According to the previous definitions, the collimated and diffused irradiance of an infinite environment without interface obey to the coupled balance differential equations (4) to (7):

$$\frac{dI_c}{dz} = (a+s)\, I_c \tag{4}$$

$$\frac{dJ_c}{dz} = -(a+s)J_c \tag{5}$$

$$\frac{dI_d}{dz} = \epsilon(a+(1-\zeta)s)I_d - \epsilon(1-\zeta)sJ_d - \zeta sI_c - (1-\zeta)sJ_c \tag{6}$$

$$\frac{dJ_d}{dz} = \epsilon(1-\zeta)sI_d - \epsilon(a+(1-\zeta)s)J_d + (1-\zeta)sI_c + \zeta sJ_c \tag{7}$$

The reflectance of the interface between the air and the scattering layer are also included in the following form: r_c is the reflectance coefficient of the collimated beam, r_d^e is the reflectance coefficient of the diffuse radiation flowing inward the layer and r_d^i for the diffuse radiation flowing outward the slab. Reflectance coefficient of the collimated beam is expressed as a function of the incidence angle, and the complex value of the relative refractive index $= n_2/n_1$:

$$r_c = (n-1)^2/(n+1)^2 \tag{8}$$

Reflectance coefficient r_d of the diffuse radiation, called bi-hemispherical reflectance factor, is described below in a dedicated section.

The solution of these equations requires boundary conditions. In the original model of Maheu *et al.*, a reflective background is added behind the sample. The sample and the layer are not in optical contact and are separated by a thick layer of air. The geometry used by Maheu *et al.* is presented in Figure 79. In the present study, no background is used: its effect is therefore not taken into account in the model presented. The reflectance values of the background are therefore zero and the transmittance values are unity.

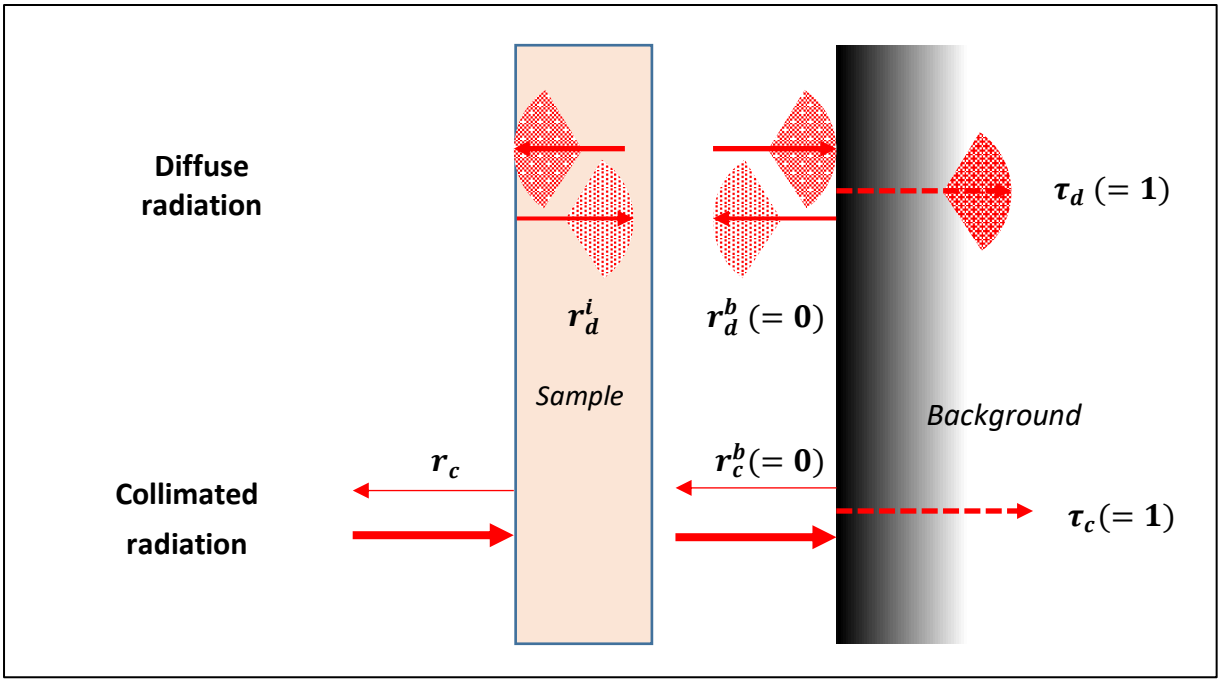

Figure 79: Geometry of the system as studied in Maheu et al. The layer of the sample is place above a background and separated by a thick layer of air. The reflectance of the collimated beam at the air/sample interface is r_c, and at the air/background interface is r_c^b. The reflectance of the diffuse beam at the air/sample interface is r_d^i for the flux going outward of the layer. At the air/background the diffuse reflectance is r_d^b. The background has a diffuse transmittance of τ_d and a collimated transmittance of τ_c. In the geometry of this study, no background is used: in brackets, the corresponding values of reflectance and transmittance are mentioned.

Following Maheu *et al.*, the collimated to collimated transmittance T_{cc} , the collimated to diffuse transmittance T_{cd}, the collimated to collimated reflectance R_{cc}, and the collimated to diffuse reflectance R_{cd} are given by :

$$T_{cc} = \frac{(1-r_c)^2 \exp(-(a+s)h)}{-r_c^2 \exp(-2(a+s)h)} \tag{9}$$

$$T_{cd} = \frac{\left(1-r_d^i\right)(1-r_c)\ \exp(-(a+s)h)}{(A_1-(a+s)^2)(1-r_c^2 \exp(-2(a+s)h))} \cdot \frac{N_T}{D_T} \tag{10}$$

$$R_{cc} = r_c + \frac{(1-r_c)^2 r_c \exp(-2(a+s)h)}{-r_c^2 \exp(-2(a+s)h)} \tag{11}$$

$$R_{cd} = \frac{\left(1-r_d^i\right)(1-r_c) \exp(-(a+s)h)}{(A_1-(a+s)^2)(1-r_c^2 \exp(-2(a+s)h))} \cdot \frac{N_R}{D_R} \tag{12}$$

With:

$$
\begin{aligned}
N_T = \sqrt{A_1}\left[r_d^i A_3 - A_2 + r_c\left(r_d^i A_2 - A_3\right)\right] ch\left(\sqrt{A_1}h\right) \\
+ \left[\left(A_5 - r_d^i A_4\right)\left(A_3 + A_2 r_c\right)\right. \\
\left. - \left(A_4 - r_d^i r_c\right)\left(A_2 + A_3 r_c\right)\right] sh\left(\sqrt{A_1}h\right) \\
+ \sqrt{A_1}\left\{\left(A_2 - r_d^i A_3\right)\exp\left((a+s)h\right)\right. \\
\left. + r_c\left(A_3 - r_d^i A_2\right)\exp(-(a+s)h)\right\}
\end{aligned}
\tag{13}
$$

$$
D_T = \sqrt{A_1}\left(r_d^{i\,2} - 1\right) ch\left(\sqrt{A_1}h\right) + \left[r_d^i\left(A_5 - r_d^i A_4\right) + r_d^i A_5 - A_4\right] sh\left(\sqrt{A_1}h\right) \tag{14}
$$

$$
\begin{aligned}
N_R = (\sqrt{A_1}\left[A_3 + A_2 r_c - r_d^i\left(A_2 + A_3 r_c\right)\right] \\
+ \left\{\sqrt{A_1}\left(A_2 r_d^i - A_3\right) ch\left(\sqrt{A_1}h\right)\right. \\
+ \left[A_2\left(A_5 - A_4 r_d^i\right)\right. \\
\left.\left. + A_3\left(A_5 r_d^i - A_4\right)\right] sh\left(\sqrt{A_1}h\right)\right\}\exp\left((a+s)h\right) \\
+ r_c\left\{\sqrt{A_1}\left(A_3 r_d^i - A_2\right) ch\left(\sqrt{A_1}h\right)\right. \\
+ \left[A_3\left(A_5 - A_4 r_d^i\right)\right. \\
\left.\left. + A_2\left(A_5 r_d^i - A_4\right)\right] sh\left(\sqrt{A_1}h\right)\right\}\exp(-(a+s)h)
\end{aligned}
\tag{15}
$$

$$
D_R = \sqrt{A_1}\left(r_d^{i\,2} - 1\right) ch\left(\sqrt{A_1}h\right) + \left[2A_5 r_d^i - A_4\left(1 + r_d^{i\,2}\right)\right] sh\left(\sqrt{A_1}h\right) \tag{16}
$$

Where the constant A_i are given by:

$$A_1 = \epsilon^2 a[a + 2(1-\zeta)s] \tag{17}$$
$$A_2 = s[\epsilon a\zeta + \epsilon s(1-\zeta) + \zeta(a+s)] \tag{18}$$
$$A_3 = s(1-\zeta)(a+s)(\epsilon - 1) \tag{19}$$
$$A_4 = \epsilon[a + (1-\zeta)s] \tag{20}$$
$$A_5 = \epsilon(1-\zeta)s \tag{21}$$

To summarize, the Maheu *et al.* model allows to calculate four measurable quantities (namely T_{cc}, T_{cd}, R_{cd}, R_{cc}) as a function of five unknown quantities describing the layer optical properties (namely a, s, ϵ, ζ, n), knowing the sample thickness h. A diagram of the possible transfers between the collimated incident flux and the reflected and transmitted, collimated and diffuse fluxes is given on Figure 80.

In order to reduce the number of unknown layer optical parameters, Rozé *et al.* [197] have proposed a procedure, described in more details in the following section, allowing to express the average crossing parameter ϵ and the forward scattering ratio ζ as a function of the other parameters, and one additional unknown quantity, the asymmetry parameter g of the Henyey-Greenstein phase function. Consequently, the number of unknown optical parameters are now four, namely a, s, g and n.

A fitting algorithm is used to solve the system of four equations and four unknowns, by minimising the following objective function $RMSE$ wavelength by wavelength (Equation (22)). The Matlab® function "*fmincon*" has been used, with a sequential quadratic programing algorithm "SQP" described in Nocedal *et al*. [198]. The possibility to fit several samples of the

same nature but different thickness is added. In this study, for each encapsulant material, we use two samples of different thickness. The first one is made of a simple sheet of thickness h_1, the second one is made with two sheets for a total thickness $h_2 \approx 2h_1$. The details of the steps of the optimization routines are given in the Figure 84.

$$RMSE = \sqrt{\frac{\sum_{i=1}^{N}(Tcc_n^i - Tcc_e^i)^2 + (Tcd_n^i - Tcd_e^i)^2 + (Rcc_n^i - Rcc_e^i)^2 + (Rcd_n^i - Rcd_e^i)^2}{4\,N}} \quad (22)$$

Four experimental measurements are carried out per sample, and four parameters are to be determined. Two reasons led us to use two samples rather than one. First, using more data than necessary increases the reliability of the fit procedure. Second, it ensures that the optical constants are valid for a range of thicknesses, rather than a single thickness. Finally, if the fit is good for both samples, it is an important indication of volume diffusion rather than surface diffusion. Indeed, the thicker the sample, the greater the volume diffusion. This is not the case for surface diffusion, whose importance is independent of the thickness of the sample.

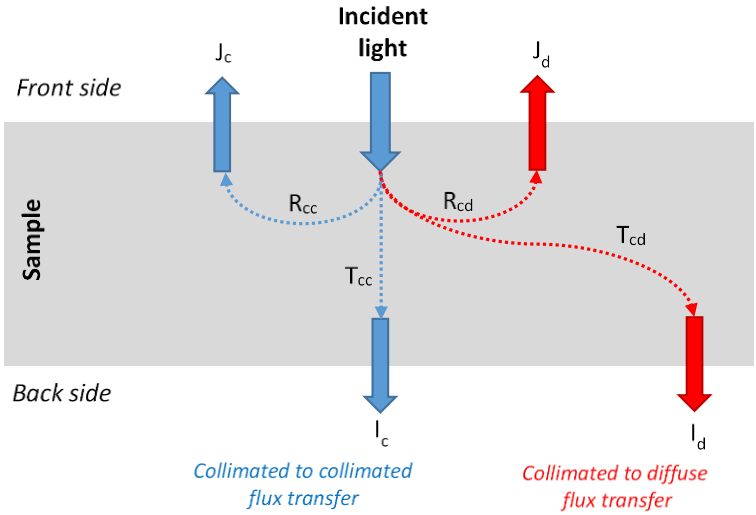

Figure 80: Diagram of the possible transfers between the collimated incident flux and the reflected and transmitted, collimated and diffuse fluxes.

IV.B.1.b *Rozé et al. interpolation of the average crossing parameter* ϵ *and the forward scattering ratio* ζ

In this section, details are given about the model of Rozé at al. They computed from Monte Carlo simulations the average crossing parameter ϵ and the forward scattering ratio ζ of the four-flux model as a function of the single scattering albedo $\omega_0 = s/(a+s)$, the optical depth $\tau = (a+s)h$ and the asymmetry factor g of the Henyey-Greenstein phase function [199].

The Henyey-Greenstein phase function is an angular distribution introduced by Louis Henyey and Jesse Greenstein in 1941 to represent anisotropic measurements with the help of an easily manipulated analytical function. The phase function has azimuthal symmetry: it is therefore a function of the cosine of the colatitude angle θ. The function is expressed in the

form given in Equation (23). The function is plotted in the Figure 81. The closer g is to 1 (respectively -1), the more diffusion occurs forward (respectively backward). For a value of zero g, the diffusion is isotropic. The physically plausible values of g are between -0.25 and 1, explaining why the tabulation is performed for these g values. The range of optical depth values from 0 to 8.

$$P_{HG}(cos\theta) = \omega_0(1-g^2) \,/\, (1+g^2-2g\,cos\theta)^{\frac{3}{2}} \tag{23}$$

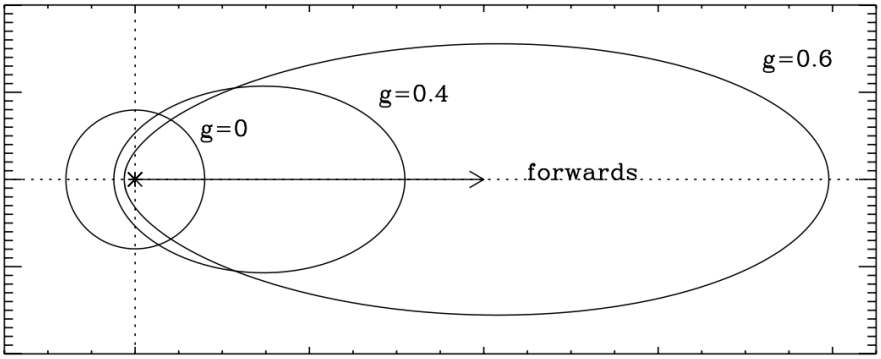

Figure 81: Polar plot of the Henyey-Greenstein phase function for different value of asymmetry parameter g: 0 0.4 and 0.6. Figure taken from Bethell et al. 2011 [200]

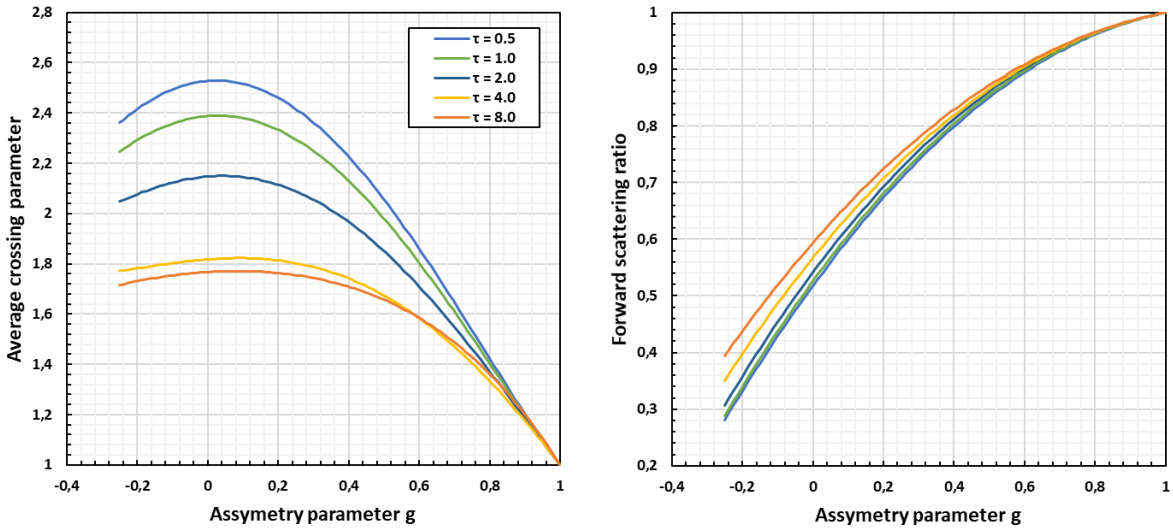

Figure 82: Interpolated average crossing parameter (left) and forward scattering ratio (right) from Rozé et al. tabulation, for asymmetry parameter g in [-0.25, 1], optical depth τ between 0.5 and 8.0, and single scattering albedo ω_0 of 0.6.

IV.B.1.c *Improved bi-hemispherical reflectance of the diffuse flux at interfaces*

The model boundary condition requires a value of the bi-hemispherical reflectance r_d^i of the diffuse flux going outward the layer.

Assuming a Lambertian diffuse flux, the bi-hemispherical reflectance is typically computed by integration of the Fresnel coefficient $R_{i-p/s}$ for polarization p and s over all the direction:

$$r_{d-p/s}^{i}(n) = \frac{\int_{\theta=0}^{\frac{\pi}{2}} R_{i-p/s}(\theta, n)\ \sin(2\theta)\, d\theta}{\int_{\theta=0}^{\frac{\pi}{2}} \sin(2\theta)\, d\theta} \tag{24}$$

The total bi-hemispherical reflectance is given by :

$$r_{d}^{i} = \frac{r_{d-p}^{i} + r_{d-s}^{i}}{2} \tag{25}$$

Duntley and Walsh found an analytical solution of this integral, giving the reflectance as a function of the refractive index, as mentioned in Equation (26) [201].

$$r_{d}^{i} = \frac{1}{2} + \frac{(n-1)(3n+1)}{6(n+1)^2} + \frac{n^2(n^2-1)^2}{(n^2+1)^3}\ln\left(\frac{n-1}{n+1}\right) - \frac{2n^3(n^2+2n-1)}{(n^2+1)(n^4-1)} + \frac{8n^4(n^4+1)}{(n^2+1)(n^4-1)^2}.\ln(n) \tag{26}$$

However, even for a highly diffusing layer, the assumption of Lambertian diffuse flux is questionable when scattering is highly anisotropic. Indeed, for a strong anisotropy (g = ±1), the diffuse flux is in fact collimated. In consequence, the reflectance factor of the inward and the outward should be equal to the well-known specular normal incidence analytical Fresnel coefficients. This issue illustrates one of the limitations of the 4 flux approach in case of anisotropic scattering, anisotropy being included in the bulk equations but not in the boundary conditions. Such issue would not be present in a full radiative transport equation model.

In order to address this issue in an approximated way, we propose to replace the conventional bi-hemispherical reflectance by the following expression, which account for anisotropy:

$$r_{d-p/s}^{i}(n, g) = \frac{\int_{\theta=0}^{\frac{\pi}{2}} R_{i-p/s}(\theta, n)\ P_{HG}(\theta, g) \sin(2\theta)\, d\theta}{\int_{\theta=0}^{\frac{\pi}{2}} P_{HG}(\theta, g) \sin(2\theta)\, d\theta} \tag{27}$$

This new formulation of the bi-hemispherical reflectance accounts for the anisotropy factor g and maintains a continuity between the Fresnel reflectance factor for the collimated case ($g = \pm 1$) and the conventional bi-hemispherical reflectance factor in the limit case of isotropic diffusion (g = 0). Indeed, the variation of the improved bi-hemispherical reflectance factor as a function of g and n is given on the Figure 83. For information and validation, even if only the value of the reflectance for the flux flowing outward the encapsulant sheet is needed, the value of the reflectance for the flux flowing inward r_d^e is also plotted.

As expected, for a strong anisotropy ($g = \pm 1$), as the diffuse flux is in fact collimated, the improved bi-hemispherical reflectance factor of the inward and the outward flux for $n = 1.5$ are the same and correspond well to the expected value of 4 % given by the analytical Fresnel coefficients. For a perfect isotropy ($g = 0$) and the same value of refractive index n,

the improved bi-hemispherical reflectance factor is $r_d^i = 59.6\ \%$, which is the same value as the one obtained by equation (26).

As there is no obvious analytical solution for the improved bi-hemispherical reflectance, its values are all pre-calculated and interpolated by a fifth-degree polynomial as a function of n and g.

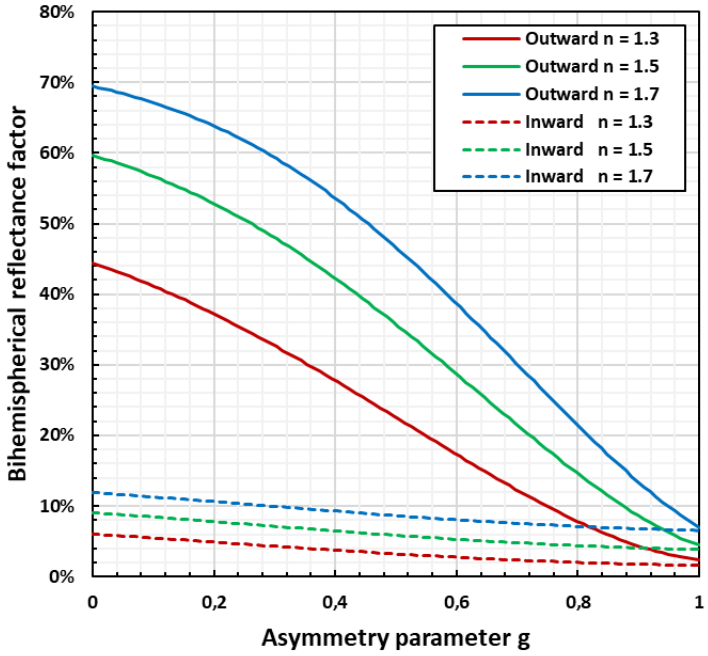

Figure 83: Bi-hemispherical reflectance of the diffuse flux as a function of the asymmetry parameter g of the Henyey-Greenstein phase function for refractive index n=1.3, 1.5, and 1.7. Plotted for both case: flux flowing outward and inward the encapsulant sheet.

However, this approach is not completely accurate. Indeed, using the equations (27), we only integrate the frontal lobe of the Henyey-Greenstein phase function. This is therefore representative of the forward propagating diffuse flow intercepting the second interface. On the other hand, the backscattered flux in the volume at the first beam pass, which then intercepts the first interface, has an angular distribution given by the back lobe of the phase function. If g=0, the phase function is isotropic and the problem does not arise. Similarly, if g is close to 1, the flux is almost collimated and the backscatter is negligible. On the other hand, for intermediate values of g, the angular distributions of the front and back lobe are different, and thus the bi-hemispherical reflectance should be different. This is not the case in the model used: the front and rear interfaces are considered to be identical. This weakness may result in an error in the extraction of parameters.

IV.B.1.d *Initialization: first guess and boundaries of parameters to optimize*

The optimization routine requires guess values of the extracted parameters. Also, it can be helpful for the numerical extraction to provide a range where each fitting parameter should be found.

For the absorption coefficient, the total absorption $A_t = 1 - R_t - T_t$ can give a good first estimation: $a_0 = -\ln(1 - A_t)/h$, where h is the thickness of the encapsulant. The main error made here comes from multi-reflections and scattering, both of which increase the optical path in the encapsulant, which is therefore actually larger than h.

Concerning the scattering coefficient, it is assumed that the attenuation of the collimated beam gives a good indication: $A_{cc} = 1 - R_{cc} - T_{cc}$. It is due to both absorption and diffusion: $a_0 + s_0 = -\ln(1 - A_{cc})/h$, which imply $s_0 = -\ln((1 - A_{cc})/(1 - A_t))/h$. The first guess of the refractive index is computed from the sum of the first two reflections in the process of multiple reflections. The collimated reflectance is approximated by $R_{cc} \approx r_{c0}\left(1 + t_0^2(1 - r_{c0})\right)$, where r_{c0} is the first guess of the reflectance coefficient of the interface for collimated light and t_0 is the first guess of transmission coefficient for collimated light: $t = \exp(-(a_0 + s_0)h)$. By inverting the above approximation of collimated reflectance: $r_{c0} = \left(1 + t_0^2 - \sqrt{(1 + t_0^2)^2 - 4t_0^2 R_{cc}}\right)/2t_0^2$. The first estimate of n is therefore: $n_0 = -(1 + \sqrt{r_{c_0}})/(\sqrt{r_{c_0}} - 1)$. The guess value of the asymmetry parameter g is set uniform and equal to 0.7 for all wavelength.

Fitted parameter	First guess	Minimum bound	Maximum bound
Absorption coefficient a $[m^{-1}]$	$-\ln(1 - A_t)/h$	$-\ln(1 - L)/h$	$-\ln(L)/h$
Scattering coefficient s $[m^{-1}]$	$-\ln((1 - A_{cc})/(1 - A_t))/h$	$-\ln(1 - L)/h$	$-\ln(L)/h$
Asymmetry parameter g	0.7	-0.25	1
Refractive index n	$-(1 + \sqrt{r_{c_0}})/(\sqrt{r_{c_0}} - 1)$	$(1 + \sqrt{L})/(1 - \sqrt{L})$	1.8

Table 14: Initial guess and boundaries of the fitting algorithm.

The optimization routine also requires boundaries for the parameters to optimize. The absorption coefficient can vary numerically from 0 to infinity, as well as the scattering coefficient. But because the spectrophotometer has an uncertainty of $L = \pm 0.1$ %, the value below the level L, and over the level $1 - L$, are considered as not significant.

If all the transmittance losses is explained by either absorption or scattering, we can write: $a_{min} = s_{min} = -\log(1 - L)/h$ and $a_{max} = s_{max} = -\log(L)/h$, which are also function of the thickness of the measured layer h. With the same rational, supposed all the reflectance is due to an interface between slowly absorbing media: $n_{min} = (1 + \sqrt{L})/(1 - \sqrt{L})$, equal 1.06 with $L = 0.1$ %. Because samples are polymer, maximum value for n is put to $n_{max} = 1.8$. Even if the asymmetry parameter g can range theoretically from -1 (collimated reflectance) to 1 (collimated transmission), value with a physical meaning range from -0.25 to 1. First guess and boundaries are sum up in the Table 14.

The main steps of the algorithm are summarized in Figure 84. In few words, this software determines by iteration the four parameters (a, s, g, n) that best match theoretical and

experimental reflectance and transmittance (wavelength by wavelength) using an "SQP" optimisation algorithm provided by Matlab®.

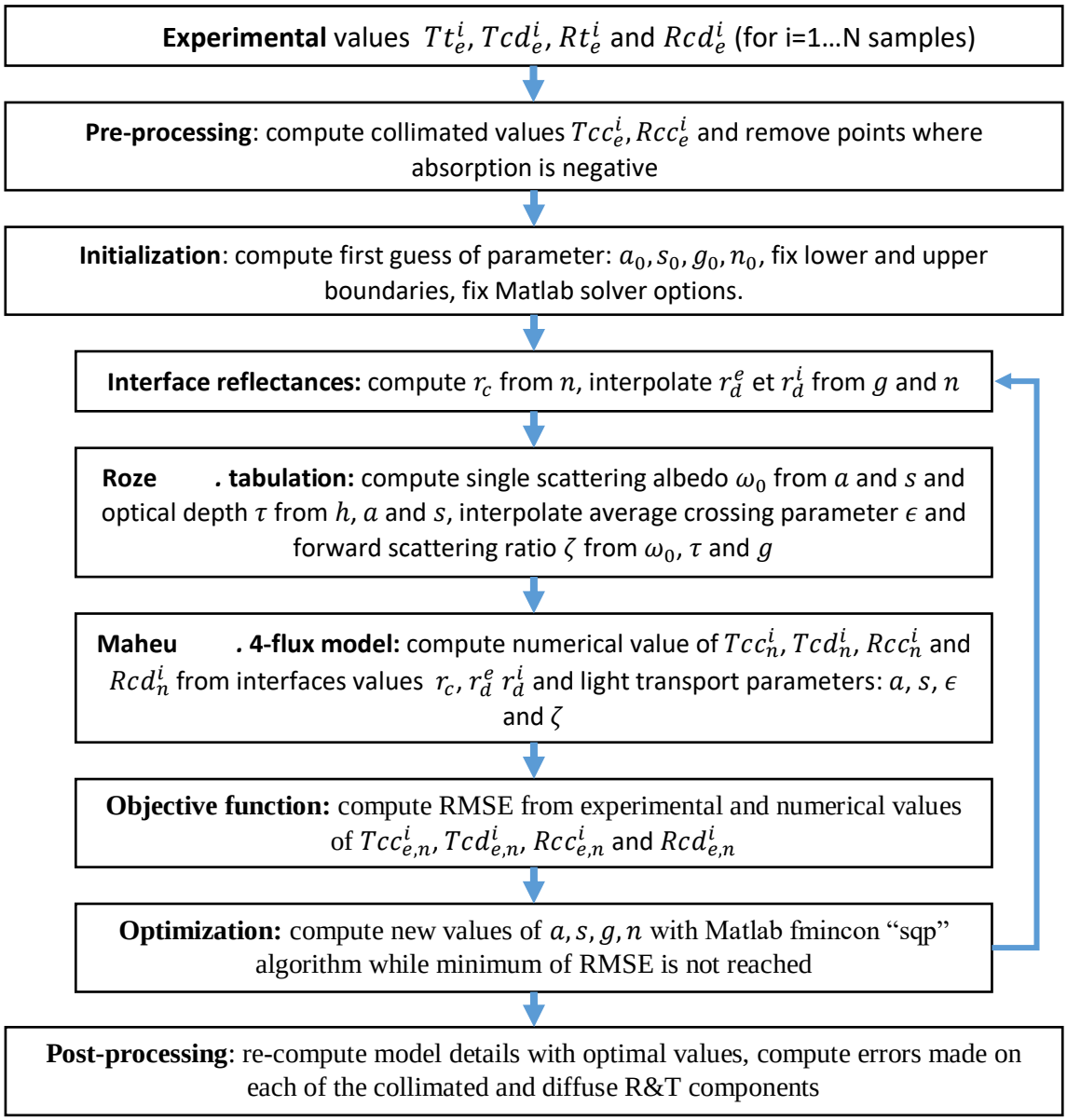

Figure 84: Steps of the optimization routine to obtain best value of absorption a, and scattering coefficient s, asymmetry parameter g and refractive index n ,from the diffuse and collimated measurements of transmittance and reflectance.

IV.B.2 Model validation on a known case: BK7 glass and EVA encapsulants

For the two following cases, the scattering parameters of the model are forced to 0 for the scattering coefficient s and to 1 for the asymmetry factor g. In this way, the model of this study is forced to use the same assumption as the one used for the determination of the optical constants of the BK7 glass and the EVA encapsulant (collimated beams only). The influence of these assumptions on the results is analysed in the part IV.C.1.

IV.B.2.a *Comparison with literature for a BK7 reference glass*

The model is applied on a 4.953 mm thick reference glass: the n-BK7 glass from SCHOTT. The refractive index n and absorption coefficient a of this material are well known (Schott Datasheets [202]). Extracted refractive index and extinction coefficient are plotted in Figure 85 : Absorption coefficient a (left) and refractive index n (right) of a SCHOTT glass n-BK7 obtained from the literature (black) and from the four-flux model used in this study (blue). The agreement is very good between SCHOTT refractive index (which are values fitted with a Sellmeier model), and the raw value (wavelength by wavelength – no dispersion model) obtain with the four-flux model of this study (Figure 85). SCHOTT gives the absorption coefficient data for only a few wavelengths. The two data sets are quasi-identical, except for one measuring point at 1500 nm.

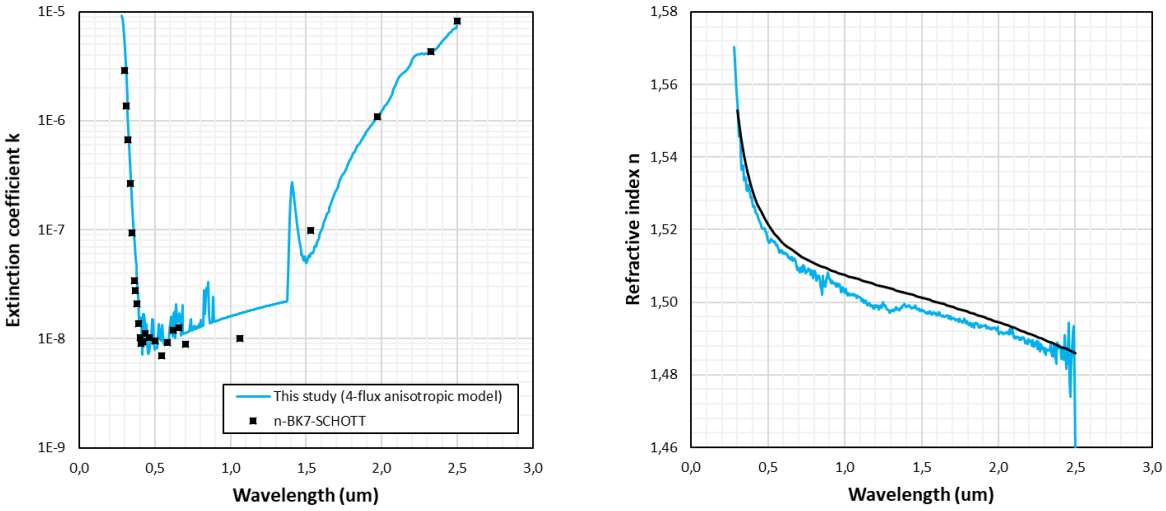

Figure 85 : Absorption coefficient a (left) and refractive index n (right) of a SCHOTT glass n-BK7 obtained from the literature (black) and from the four-flux model used in this study (blue).

The experimental values of collimated-to-collimated and collimated-to-diffuse transmittance and reflectance are given on the Figure 86. The modelled values are also given on the figure, and are completely superimposed to the experimental values: the fitting error (RMSE) is smaller than 0.04 % for every wavelength. These results validate our approach, at least for the collimated 2-flux form, as the considered sample is very weakly scattering.

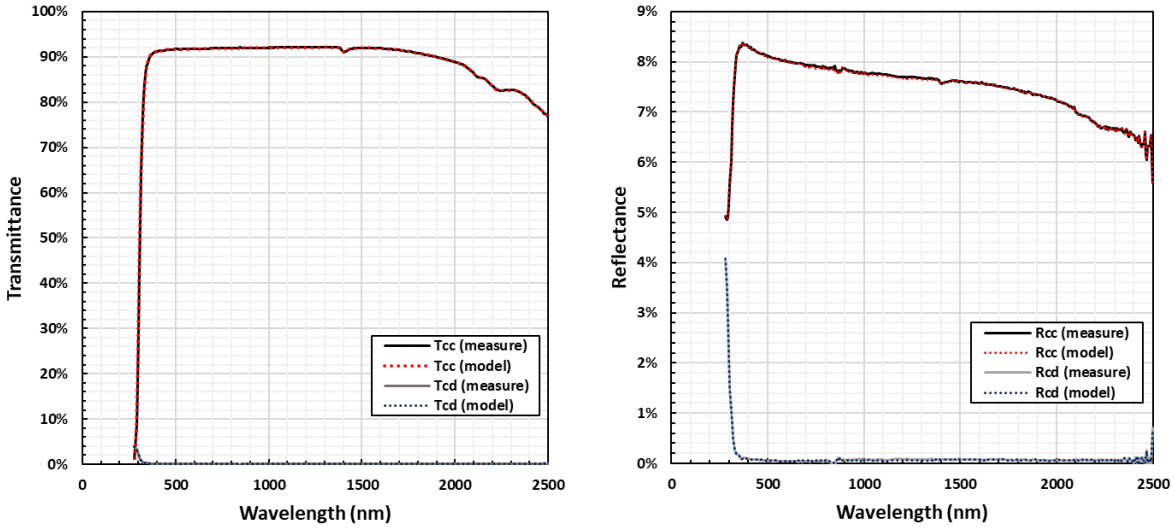

Figure 86: Comparison of experimental measurement of collimated-to-collimated (cc) and collimated-to-diffuse (cd) transmittance (T) on the left and reflectance (R) on the right with the value obtain with the model and extraction of optical constant after fitting procedure for a SCHOTT glass n-BK7.

IV.B.2.b *Comparison with literature for encapsulants of the EVA family*

The model was also applied to a UV-transmissive encapsulant from the family of EVAs, which are known to be low-diffusing. The supplier is First Solar. The two samples are 387 and 598 µm thick. The values obtained are compared to the measurements published by Vogt *et al*. on a Bridgestone EVASKY S87 with 25 layers of EVA laminated together, to obtain more precision on the absorption coefficient [127]. The total thickness of the 25-layers sample is 10.2 mm, corresponding to a thickness of single layer of 400 µm.

The results for the refractive index differ from app. 1 % in the visible range. This difference could be due to scattering from surface state which lower the reflectance of collimated beam, or by an interface consisting of an effective porous medium. This corresponds to a difference in the reflectance coefficient of 0.6 % absolute at an air / encapsulants interface. But this configuration never occurs in a real module: the encapsulant is always covered with glass. The reflectance coefficient at a glass/encapulant is 0.001 % for a glass with refractive index of 1.5 and encapsulants with refractive index of 1.47. It becomes 0.01 % if the encapsulants has a refractive index of 1.47. Both reflectance coefficients can be considered as negligible.

The refractive index of the encapsulant also plays on the optical coupling with the cell. The reflectance of a heterojunction cell encapsulated in an EVA with an index of 1.49 at 550 nm is 0.89 % (obtained with Sunsolve). If a material with an index of 1.47 at 550 nm is now used, the reflectance is 0.90 %. It can therefore be concluded that the 1 % difference between the refractive index value obtained by Vogt *et al.* and obtained in this study has no impact either on the optical coupling between the encapsulant and the cell.

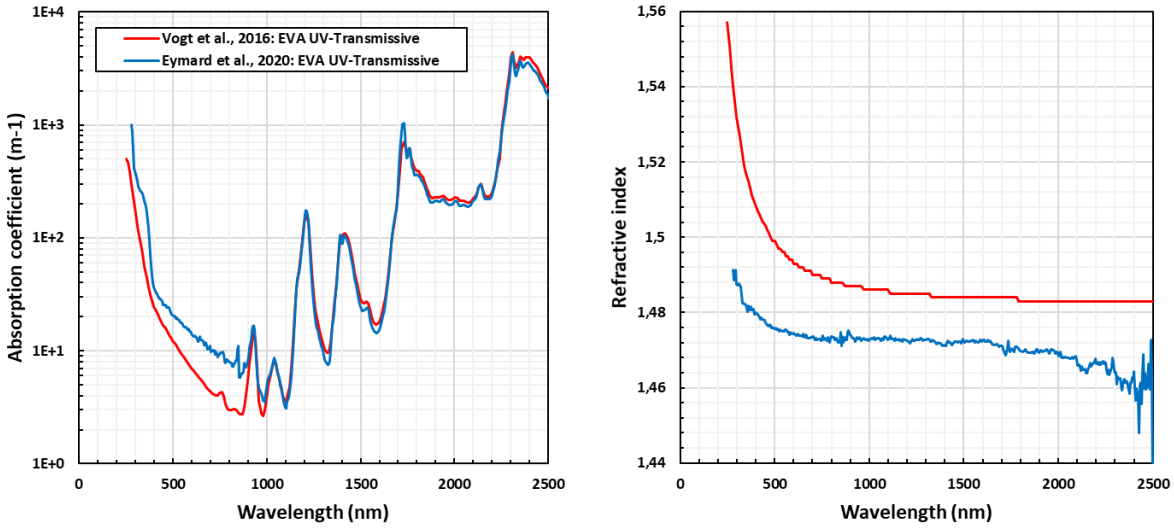

Figure 87 : Absorption coefficient a (left) and refractive index n (right) of a UV-Transmissive non-scattering glass n-BK7 obtained from the literature (red) and from the present four-flux model.

The absorption coefficient is similar throughout the 1000-2500 nm range: the peak of absorption are linked to the common bond C-H , C-O and N-H and their overtones [188]. Below 1000 nm, the difference is more pronounced, but it may be attributed to sample differences. Indeed, in this spectral range, the nature of additives may impact the absorption, and it is known that these additives and their proportions may differ among producers.

In conclusion, even if minor differences have been observed, the absorption and refractive index on low diffusing EVA encapsulant have been found in good agreements with literature data.

IV.B.3 Application of a dispersion model based on Lorentz spectral oscillator

IV.B.3.a *Complex dielectric function and Lorentz oscillator*

In the previously described approach, the physical parameter (a, s, g, n) have been extracted from experiments for each wavelength. However, it is usually recommended in the literature to apply “spectral models”, i.e. to extract parameters of a spectral law for the optical index rather than their value. This approach allows to reduce the number of extracted parameters, and to force the extracted physical parameter to satisfy to a fundamental physical law. For example, the refractive indices and the absorption coefficient are related to the real and imaginary part of the dielectric permittivity. The complex dielectric function $\tilde{\epsilon}$ is linked to the succeptibility $\tilde{\chi}$ by the relation:

$$\tilde{\epsilon} = 1 + \tilde{\chi} \tag{28}$$

The susceptibility is the response (polarizability P) of the material to an oscillating electric field E:

$$\tilde{P} = \epsilon_0 \tilde{\chi} \tilde{E} \tag{29}$$

The complex refractive index of the material is related to the complex dielectric function $\tilde{\epsilon}$ according to :

$$\tilde{n} = \sqrt{\tilde{\epsilon}} = n + i\kappa \tag{30}$$

$$\tilde{\epsilon} = (n + ik)^2 = n^2 - k^2 - 2ink \tag{31}$$

$$|\tilde{\epsilon}|^2 = (n^2 - k^2)^2 + 4n^2k^2 = (n^2 + k^2)^2 \tag{32}$$

$$|\tilde{\epsilon}| = n^2 + k^2 \tag{33}$$

The real part of the refractive index is then :

$$n = \sqrt{\frac{|\tilde{\epsilon}| + Re(\tilde{\epsilon})}{2}} \tag{34}$$

and the extinction coefficient k, the imaginary part, is given by:

$$k = \sqrt{\frac{|\tilde{\epsilon}| - Re(\tilde{\epsilon})}{2}} \tag{35}$$

Moreover, n and k are linked to the real and imaginary parts of the same function, they are not independent but linked by Kramers-Kronig relations. For a given complex analytic function f, $f(\omega) = f_1(\omega) + if_2(\omega)$, the relation gives:

$$f_1(\omega) = +\frac{2}{\pi}\int_0^\infty \frac{\Omega f_2(\Omega)}{\Omega^2 - \omega^2} d\Omega \tag{36}$$

$$f_2(\omega) = -\frac{2}{\pi}\int_0^\infty \frac{\omega f_1(\Omega)}{\Omega^2 - \omega^2} d\Omega \tag{37}$$

In theory, it is thus possible to obtain the spectral variation of one (f_2 for instance) from the behaviour of the second (f_1). In practice however, this requires to know the variation of one over the full spectral range, because the integration is performed on all frequencies ω. In the case of optical indices, it is never possible to measure n (or k) on the full spectral range. However, by making assumptions about variations outside the range measured, the application of Kramers-Kronig formula may allow to deduce k from n, when they have values of the same order of magnitude.

Another approach to determine n and k consists in using a fitting model that intrinsically respects Kramers-Kronig formula. This is usually done using the Lorentz oscillator model, relevant for a dielectric material. In this model, the complex dielectric function is given by the sum of N oscillators:

$$\tilde{\epsilon}(\omega) = \epsilon_\infty + \sum_{j=1}^{N} \frac{f_j\, \omega_{0j}^2}{\omega_{0j}^2 - \omega^2 + i\gamma_j\omega} \tag{38}$$

where each oscillator j is characterized by its resonant frequency ω_{0j}, its “strength of the oscillator” f_j, and its peak broadening factor γ_j. When f_j increases, the peak amplitude

increases, and the peak width decreases. Finally, a global parameter exists, ϵ_∞, which represents the value of the high-frequency dielectric function. The refractive index n and the extinction coefficient k are deduced via the previous relationships (34) and (35).

IV.B.3.b *Application to the extraction of optical index (n, κ)*

Once the optical parameters have been extracted wavelength by wavelength as described in part "Model of Maheu *et al.* with Rozé *et al.*, interpolation and bi-hemispherical reflectance", a fitting procedure of the values of n and the absorption coefficient:

$$\alpha = \frac{4\pi\,\kappa}{\lambda} \tag{39}$$

is performed. To initialize the fit a good estimation of the peak positions and their width at mid-height is necessary. The search for the inflection points of the curve allows to obtain these first guesses, as described in Rosas-Roman *et al.*, 2017 [203]. For a peak of Lorentzian shape:

$$L(x) = \frac{h}{\left(\frac{x - x_0}{\frac{\gamma}{2}}\right)^2 + 1} \tag{40}$$

where h is the maximum height, x_0 is the porition of the peak and γ is the width at half height. We can obtain the position of some stationary points: the maximum of the peak, related to the first derivative, is at the abscissa x_0 and the ordinate h, and the right and left inflection points, related to the second derivative, are at the abscissa $x_0 \pm \frac{\gamma}{2\sqrt{3}}$ and the ordinate $\frac{3}{4}\ h$. An automatic search can therefore be performed, setting the detection threshold values correctly. As some peaks are partially superimposed, the estimation of their parameters. A procedure of simultaneous height adjust is necessary as described in [203]. Finally, a fitting procedure of least square adjust is performed. The fit procedure carried out does not include the optical constants s (scattering coefficient) and g (asymmetry parameter): for these quantities, the values extracted during the wavelength-by-wavelength optimisation are retained. The results of the fit on a low UV cut-off TPO are shown on the Figure 88.

The results of the fit are obtained using 48 oscillators. The fit on the absorption coefficient is good in the range of 600 to 2500 nm. From 300 to 600 nm, parasitic oscillators are present, causing these artificial oscillations. As the absorption values are low in this range, the consequences on reflectance and transmittance prediction are negligible.

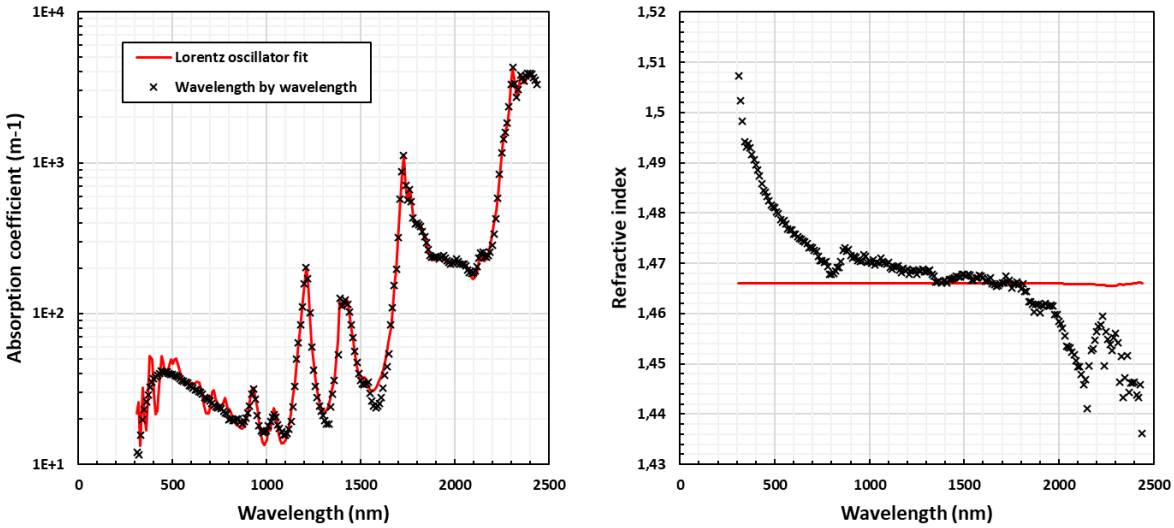

Figure 88: Results of the spectral fitting procedure with Lorentz oscillator on the absorption coefficient and the refractive index.(TPO low UV-cut off)

However, the refractive index results are not good: in the dipole extraction model, the refractive index is found almost constant (no dispersion), contrary to the literature results and to the result of the extraction performed by the previous approach. It is thus likely that none of the oscillators in the spectral range can explain the variation of the refractive index. Their amplitudes are too small and only the ϵ_∞ parameter allows to obtain an average value over the whole spectral range. The visible variations in the refractive index are therefore likely due to oscillators outside the spectral range, with much higher amplitudes. This removes much of the interest in using a Lorentz oscillator model consistent with Kramer Kroning's relationships in a spectral range where absorption is negligible. The two parameters n and a may therefore be fitted with separate models. For example, a Lorentzian sum for α and a Sellmeier model for n.

Part IV.C Results of the model for diffusing encapsulant

This part demonstrates the usefulness of a four-flow model, taking into account both the transport of both specular and diffuse contribution to adequately describe the behaviour of a diffusing encapsulant. To make a comparison, four different approaches are considered to perform optical index extractions.

The first two approaches are applications of the extraction model in its purely specular version (diffusion is neglected, a = 0). However, the experimental values on which the model is applied are different. In the first approach, the measured diffuse components are fixed at 0: the total and collimated components are therefore merged (see Table 15). In the second approach, the diffuse components are left as measured. The following two approaches are applications of the extraction model in its specular and diffuse version. The third approach is the application of isotropic diffusion (g = 0), while the fourth approach is the application of anisotropic diffusion. Experimental values are as measured.

The particularities of each model are presented in the first part IV.C.1, and the results of the extraction on experiments are compared in the second part IV.C.2.A sample of encapsulant from the TPO family is chosen for its highly diffusing nature, recognizable at glance by its milky appearance. A sample with a low UV cut-off is preferred. In this way, the absorption in UVs does not mask the diffusion, and the analysis of the relevance of a model including the diffusion is facilitated. Two samples of the same material but of different thickness are used: as mentioned previously, this procedure allows to minimize uncertainties. The first sample “TPO low UV cut-off 1” is obtained by laminating a simple sheet of encapsulant: its thickness (667 µm after lamination) is therefore representative of the thickness that would be obtained when manufacturing a reference PV module. The second sample “TPO low UV cut-off 2” is 1141 µm thick, obtained by laminating two sheets. The experimental points where the absorption is found negative are simply removed from the data, as they are problematic for the extraction procedure. These aberrant measurements may occur when the encapsulants are very transparent, as the uncertainty of the measurement of R & T can cause a negative A, which is calculated by subtraction (A = 1 - R - T). The experimental measurements are presented in the Figure 89.

Sample 1: Transmittance measurements show typical absorption peaks at 1200, 1400, 1700 and 2300 nm. Total transmittance decreases in UVs compared to the 92 % plateau at 1000 nm: it is only 80 % at 300 nm. As mentioned above, the chosen encapsulant is highly diffusive in UV light. Sample 1 reaches 50 % diffuse transmittance at 300 nm, and this value decreases according to a power law with wavelength, reaching only 4 % at 1300 nm and zero at 2300 nm. As a consequence, the collimated transmittance, obtained as a subtraction of the two previous values, is low in the UVs (30 %), increases up to 1600 nm and is then confused with the total transmittance. The total reflectance is 19 % at 300 nm and decreases to 3.5 % at 2500 nm, interspersed with absorption peaks. Diffuse reflectance is 15 % at 300 nm and decreases to 0 % at 2500 nm. The effect of absorption peaks can also be seen, but less markedly. As a consequence, the collimated reflectance is 4.5 % at 300 nm, reaching a maximum of 6.5 % at 1600 nm and a minimum of 3.5 % at 2500 nm.

Sample 2: As expected, the total transmittance is smaller than in Sample 1, because of the longer path of light through the sample. The diffuse transmittance is greater on the whole spectrum (58 % at 300 nm). Thus, the collimated transmittance is much smaller in the UVs (14 % at 300nm because of the higher scattering), and the absorption peaks are more pronounced because of the greater thickness. The total reflectance is greater in the UV region because of the higher diffuse part. The collimated reflectance is similar to the one of the Sample 1, with the exception of more pronounced absorption peaks.

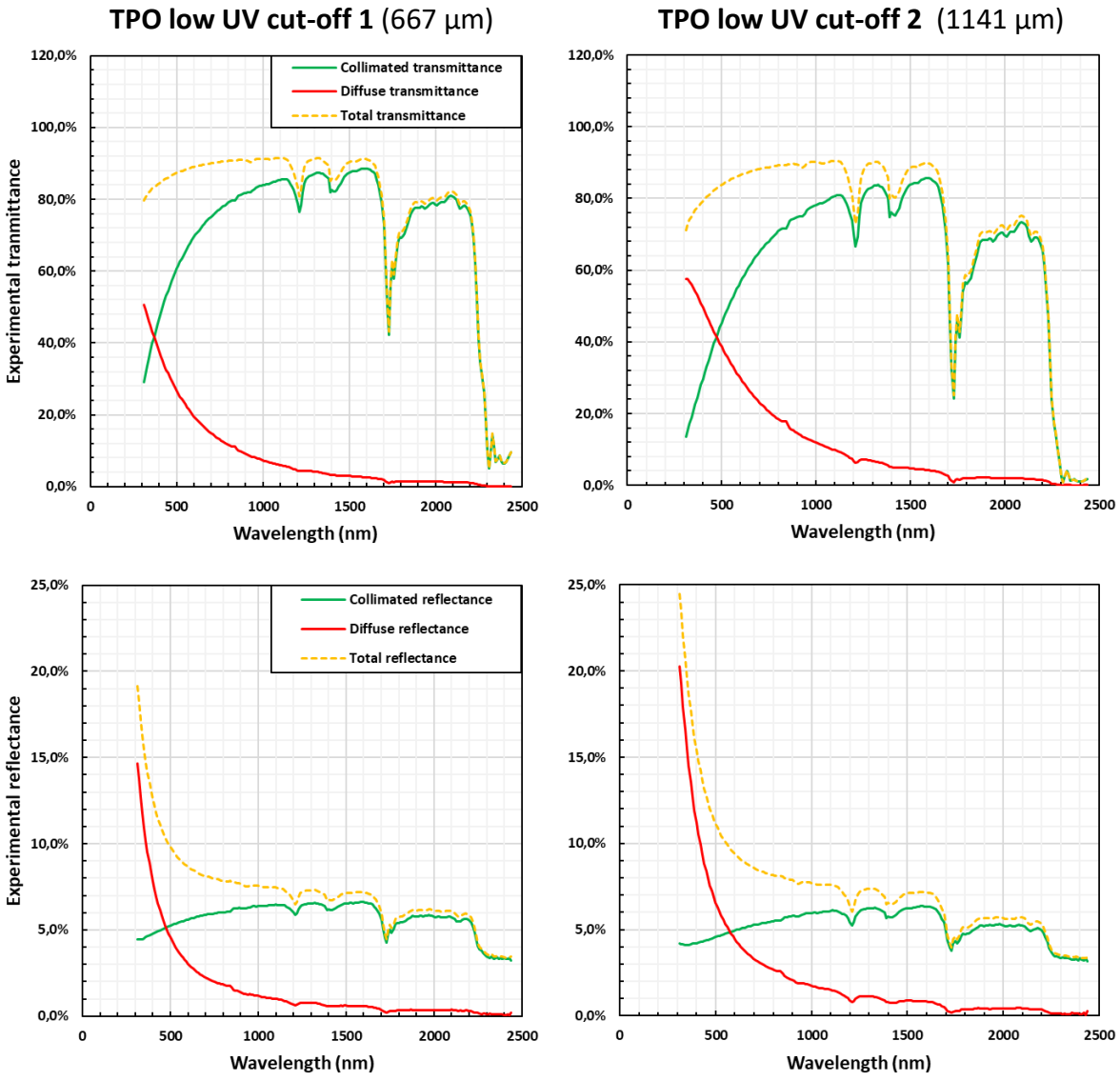

Figure 89: Experimental measurements of R&T of sample 1 (left) and sample 2 (right). The collimated, diffuse and total transmittance are plotted at the top, the equivalent for reflectance are plotted below

Absorption peak of polymer are mainly due to C-H bond at 3390nm and all high order overtones with decreasing amplitude: double peak at 1725 / 1760 nm, 1190 and 920nm. Double bond C=O is responsible for absorption peaks at 1830, 1380 and 1130 nm (hidden) [204]. All polymers present this similar peak position, between 500 and 2500nm.

IV.C.1 Description of four different approaches to extract optical index in scattering encapsulants

IV.C.1.a *Approach 1: Collimated two-flux model applied only on specular components of transmission and reflectance*

The first approach consists in the standard procedure used for the extraction of optical constant of transparent materials with spectrophotometer. In this approach, the 4-flux model is simplified in a two-flux model with only collimated components, the first flux propagates forward and the second propagates backward. The absorption coefficient a is considered to have any spectrally resolved value between zero and infinity, as well as the refractive index n. On the other hand, the scattering coefficient s is set to zero over the entire spectral range. To ensure that the scattering is zero, the asymmetry parameter of the Hervey-Greenstein function g is set to 1 for all wavelengths, which means that the scattering is confused with the specular part. This is a numerical precaution, since any value of g should result in a zero scattering component since the scattering coefficient is zero.

As a consequence of the previous values: the optical depth od is only related to the absorption a and thickness h of the sample: $od = (a + s)\, h = ah$. The single scattering albedo ssa is zero across the entire spectral range: $ssa = s/(a + s) = 0$. Since g is 1 and ssa is 0, the tabulated average crossing parameter ϵ and forward scattering ratio ζ are unity over the entire spectral range. The reflectance of the collimated light is governed by the common Fresnel coefficients. This model is applied to experimental values of transmission and reflectance that have been deliberately modified. Measurements of the diffuse components are forced to be zero. This implies that transmission and total reflectance are confused with the specular component.

This corresponds to the often assumed approach that the measurement of total transmission and total reflectance is sufficient to characterize the encapsulant sample with a specular model.

	T_{cc}	T_{cd}	R_{cc}	R_{cd}
Value	*T_t exp*	*Fix to 0*	*R_t exp*	*Fix to 0*

Table 15: Modification of the experimental value for approach 1. Collimated-to-diffuse transmittance and reflectance are set to 0.

IV.C.1.b *Approach 2: Collimated two-flux model applied on specular and diffuse components of transmission and reflectance*

The second approach uses the same theoretical model as approach 1, but no modification of the experimental values is made. In particular, the reflectance and diffuse transmittance values are non-zero.. This method is wrong in principle, but may be performed in practice where it is not possible to measure separately diffuse and specular contributions. As the model cannot explain diffuse behaviour, the error on these components will be necessarily large. However, such comparison remains interesting, as it allows a more rigorous

comparison of the modelling errors between the specular model and the diffuse models 3 and 4 (next approaches). Indeed, as the specular approach 1 forces the experimental diffuse components to zero, the corresponding error on these components will necessarily be zero in the fitting procedure. Once the experimental diffuse measurements have been made, this information must be included. This approach is therefore relevant to evaluate the real error which is made by the application of a specular model on experimental values with diffusion.

IV.C.1.c *Approach 3: Collimated and isotropic diffuse four-flux model applied on specular and diffuse components of transmission and reflectance*

The third approach uses a four-flux model: one collimated and one diffuse flow propagating forward, and their symmetrical flux propagating backward. The diffuse fluxes are considered isotropic: diffusion is equal in all directions. This implies in particular that the forward scattered part is the same as the backward scattered part. The absorption coefficient a can take any value between zero and infinity, as can the scattering coefficient s. The asymmetry parameter of the Henyey-Greenstein phase function g is fixed to 0, which corresponds almost to the approach of the Rayleigh scattering phase function. The refractive index n can take any value between 1.0 and 2.0.

As a consequence, the optical depth od is related to the absorption a, scattering coefficicent s and thickness h of the sample: $od = (a + s)\, h$. The single scattering albedo ssa is free to vary between 0 and 1. Since g is 0 and ssa and od are free to vary, the tabulated average crossing parameter ϵ can take values between 1 and 3 – around 2.5 where the absorption is negligible. The forward scattering ratio can take values between 0 and 1, and should be around 0.5 where the absorption is negligible. The reflectance of the collimated light is governed by the common Fresnel coefficients. The refection at interfaces of the diffuse part is computed as a function of n and g. This approach corresponds almost to the standard four-flux model of Maheu *et al.*, 1984, where the forward scattering ratio is fixed to 0.5 and the average crossing parameter is 2.5.

IV.C.1.d *Approach 4: Collimated and anisotropic diffuse four-flux model applied on specular and diffuse components of transmission and reflectance*

The fourth approach also uses a four-flux model, but the scattering can be anisotropic. The absorption coefficient, diffusion coefficient and refractive index are limited by the same values as in the previous approach. The asymmetry parameter g can take values between -0.25 (mainly backscattering) and 1 (collimated beam). This approach can therefore theoretically approach the anisotropic phase functions of Mie's theory.

The values and boundaries of parameters to optimize are sum up in the Table 16.

	Absorption coefficient a	Scattering coefficient s	Asymmetry parameter g	Refractive index n
Approach 1	0 / Inf	0	1	1.0 / 2.0
Approach 2	0 / Inf	0	1	1.0 / 2.0
Approach 3	0 / Inf	0 / Inf	0	1.0 / 2.0
Approach 4	0 / Inf	0 / Inf	-0.25 / 1	1.0 / 2.0

Table 16: Boundaries (lower / upper) used in the fitting procedure for each approach.

IV.C.2 Comparison of the four approaches: need of a four-flux model with anisotropic scattering

In this part, the four approaches are compared in terms of their ability to reproduce the experimental measurements, i.e. in terms of the quality of the fit obtained. The root mean square error, as presented in the Part IV.B, is a spectral value, because each wavelength is processed independently. Because of the normalization aforementioned, the root mean square error is independent of the number of samples used for fitting. The value corresponds to the mean error made on one components of the foursome diffuse / collimated - transmittance /reflectance. The values are shown in the Figure 90.

It can be observed that the four models have a similar behaviour: the error is higher in the UVs than in the infrared. The RMSE curve seems to follow the same decreasing trend as the transmittance or diffuse reflectance curves, which would suggest that the fit error is mainly due to a poor consideration of scattering. All models show a zero fit error (< 0.2 %) beyond 2300 nm, where scattering is negligible. Errors can therefore be compared in terms of their values at 300 nm. Approach 1 generates an error of 2.2 %, approach 2 an error of 28.5 %, approach 3 an error of 14 % and approach 4 an error of 0.6 %. Approach 2 of a two-flux collimated model is the one that generates the biggest error among the models that take into account the experimental values of diffuse transmittance and reflectance, as expected. Approach 3, an isotropic collimated / diffuse 4-flux model, gives better results than approach 2, but the error generated is still huge. Finally, approach 4, an anisotropic collimated/diffused 4-flux model gives the best results since the error is reduced by a factor of 20. Over the whole spectral range, the error of approach 4 is less than 0.6 %, an outstanding result. Indeed, even if the uncertainty of the spectrometer is estimated at 0.1 %, other uncertainties are added to the fit procedure. For instance, the tabulation of ϵ and ζ proposed by Rozé *et al.*, which is done by performing the fit of curves obtained by Monte-Carlo simulation, is done with an accuracy of 0.5 %. Moreover, as mentioned is the part IV.A.3, the difference between a spectralon and mirror as reference sample for reflectance ca be as high as 0.6 % in the UV spectral range.

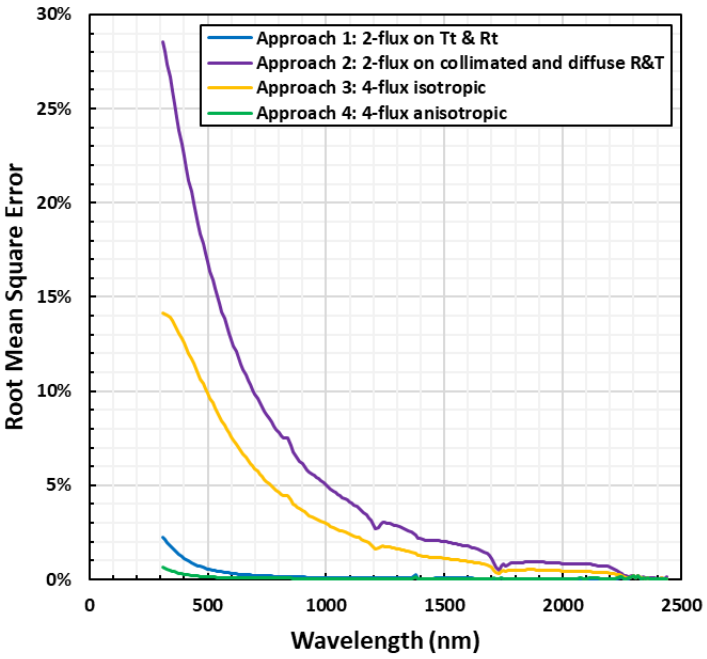

Figure 90: Root mean square error (RMSE) of the fitting procedure for each of the four approaches.

The spectral RMSE values, on the other hand, do not give any information on the origin of the error: is it rather the diffuse transmittance or the reflectance? To answer this question, the errors on each of the components, for sample 1 and sample 2 are plotted in Figure 91. The results of the optimisation: the absorption coefficient a, the scattering coefficient s, the asymmetry parameter g and the refractive index n are plotted on the Figure 92.

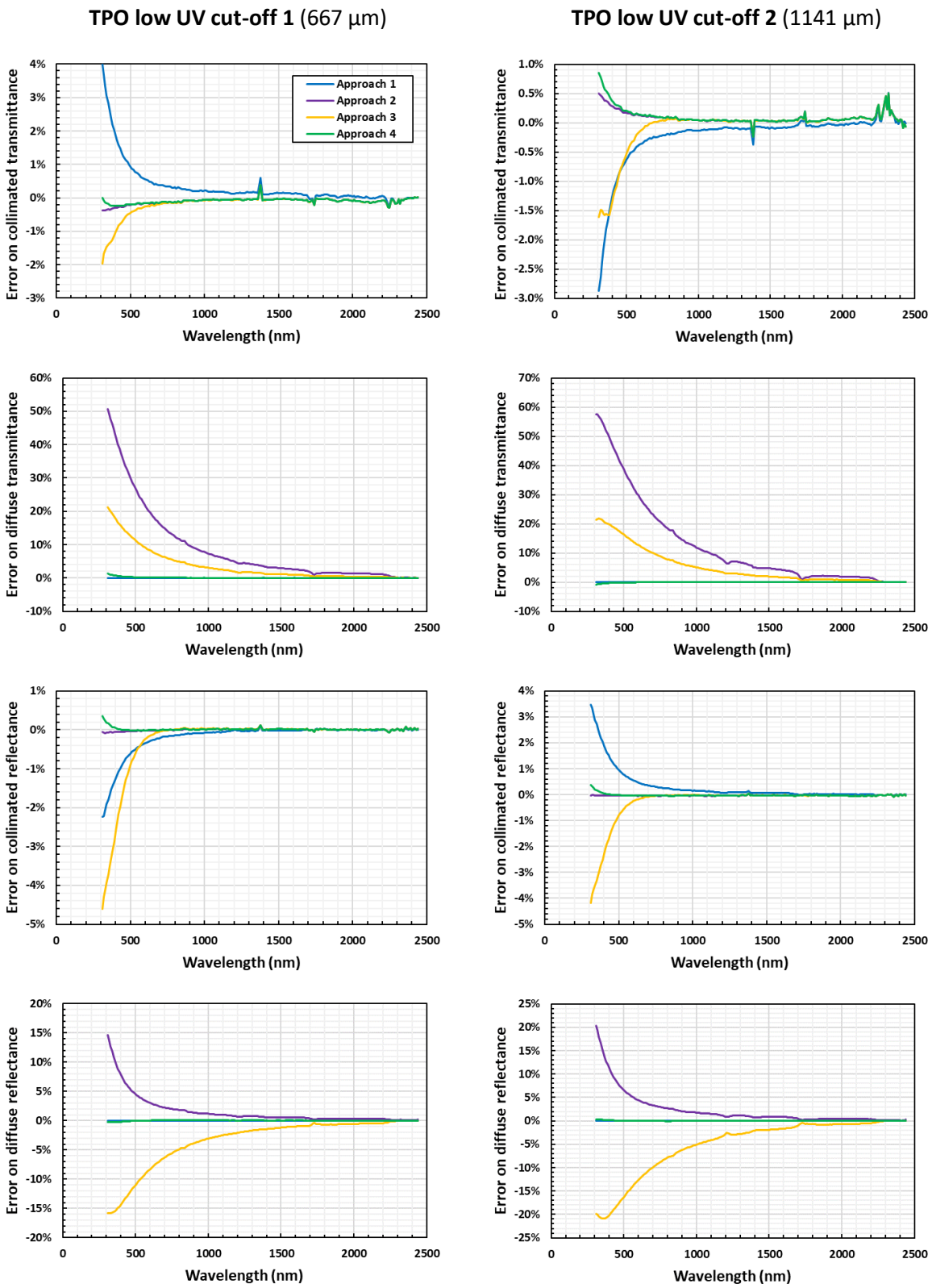

Figure 91: Details of the error made on collimated and diffuse transmittance and reflectance for the four approaches, for sample 1 (left) and sample 2 (right).

IV.C.2.a *Analysis of the results for each approach*

Regarding approach 1, the error on the diffuse values is obviously zero. The collimated transmittance is underestimated for sample 1 and overestimated for sample 2. The opposite is true for collimated reflectance. Without diffusion, the model explains the high reflectance values in the UVs by a high value of refractive index (Figure 92). The result of a refractive index higher than 2 is questionable, as even high index polymer cannot reach such high value. This may also explain the decrease in transmittance over this spectral range for a single sample. On the other hand, these phenomena are related to interfaces, and should therefore be similar whatever the thickness of the sample. This is not the case: the total reflectance of sample 2 is higher in the UVs. The fit procedure therefore finds a compromise between the two values. As an indication, we can see that the difference between the total reflectance of sample 1 and sample 2 is 5.5 % at 300 nm, which corresponds approximately to the fit error of 2.2 % for this wavelength.

Regarding approach 2, the model cannot explain the diffuse transmission and diffuse reflectance, so the associated error affects the entire diffuse measurement. The model therefore tries to get as close as possible to the collimated components: well below 0.5 % for transmittance and reflectance, for both samples. A more precise interpretation of the error behaviour for values below 0.5 % would be difficult to make in view of the uncertainties. The low value of collimated transmittance and reflectance in the UVs region, in reality due to diffusion, are attributed within this model to absorption. Thus, in this model, the absorption coefficient a is actually an extinction coefficient $k = a + s$. In this model, the refractive index n has plausible physical behaviour: between 1.51 at 300 nm to 1.44 at 2400 nm. It can be described by a Sellmeier model.

Approach 3 overestimates the collimated transmittance by 1.5 % for sample 1 and 2 % for sample 2 and underestimates the diffuse transmittance by 20 % for both samples. Collimated reflectance is also overestimated by more than 4.5 % for sample 1 and 4 % for sample 2, and diffuse reflectance is overestimated by 15 % for sample 1 and 20 % for sample 2. In this model, the scattering is isotropic, there is as much light scattered backwards as forwards. This is not what is observed: the diffuse transmittance is higher than the diffuse reflectance for both sample: the model finds a compromise by overestimating one and underestimating the other. Moreover, at the interfaces, the diffuse reflectance coefficient between the encapsulant and the air is very high, as expected for Lambertian illumination. The reflectance coefficient increases with the angle of incidence. There is even a critical angle from which there is total internal reflectance. In this configuration, for a refractive index of 1.44, 55.8 % of the light is reflected. At an index of 1.8, 73 % of the light is reflected. Due to the high internal reflectance, the effective path of the light in the encapsulant is higher than in the other model: the computed absorption coefficient needs to be smaller than in other model to explain the same total absorbance. The reason why the model converges to high value of refractive index in the UVs region has not been found. The scattering coefficient s shows a plausible behaviour.

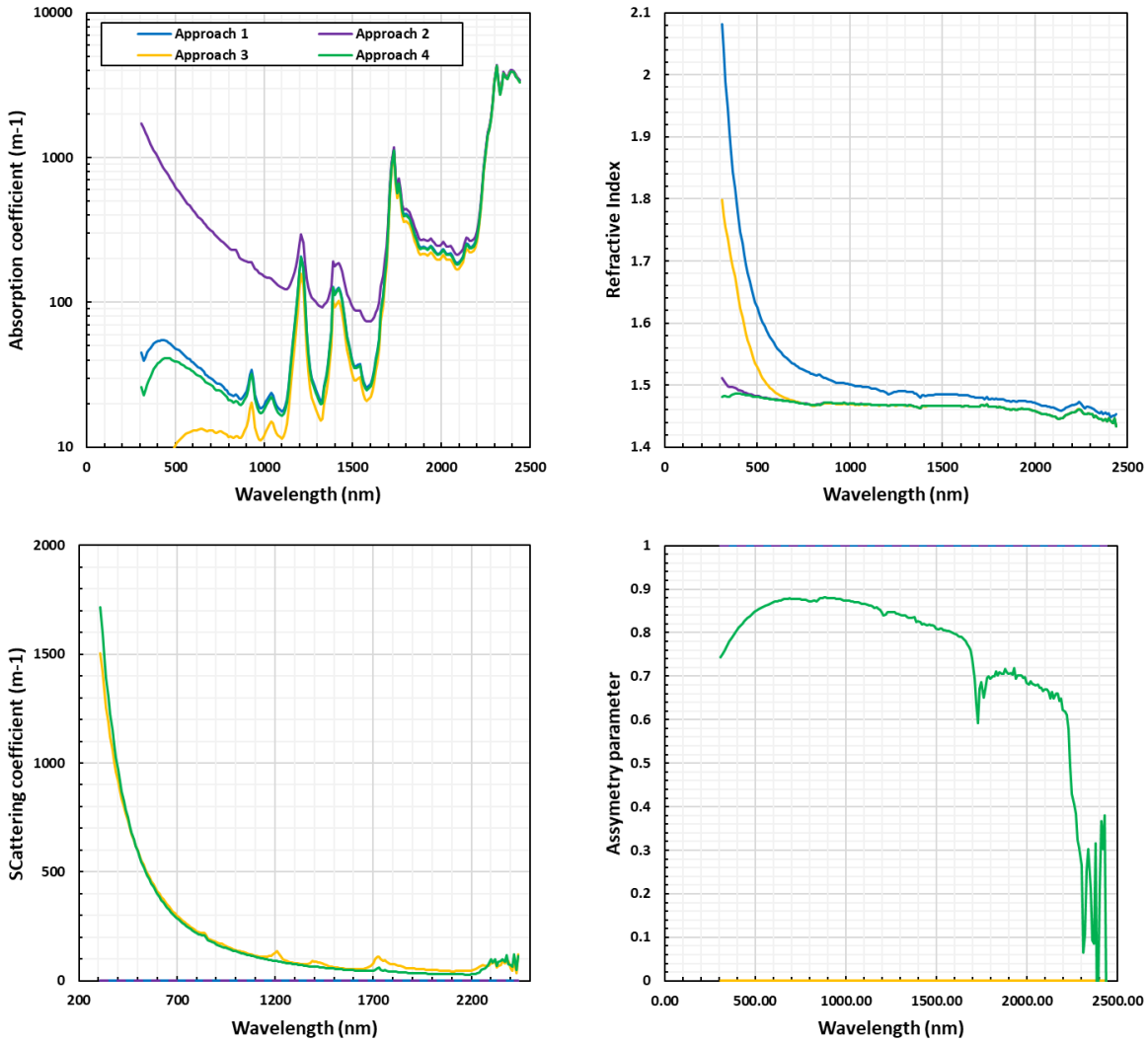

Figure 92: Results of the optimization for each approach: absorption coefficient, refractive index, scattering coefficient and asymmetry parameter.

Approach 4 is the best one in term of RMSE. It is also the most homogeneous approach: the errors on each of the R & T components, and for both samples, are always less than 0.5 % for any wavelength. The trend of the optimized parameters is physically plausible: the asymmetry parameter g, in particular, takes values between 0.7 and 0.9 over the whole spectral range. In IRs, the scattering is low, so it can be assumed that the g values beyond 1500 nm are overfitting. On the other hand the variation of g in the UVs and in the visible is necessary: if g is fixed at 0.8 over the whole spectral range, the RMSE in the UVs rises to 2 %, and the refractive index becomes high (1.7) for a polymer.

The Table 17 summarizes the root mean square error, and the error on each component for sample 1 and sample 2. The values are not spectrally resolved, but instead, the mean of the error on the whole spectral range is computed. With this indicator, the conclusions remain the same, in a more succinct and readable way.

Mean on Wavelength (%)	Approach 1	Approach 2	Approach 3	Approach 4
RMSE	0.20	5.38	3.08	0.08
Collimated transmittance	+0.33 / -0.22	-0.10 / +0.09	-0.19 / -0.08	-0.09 / +0.10
Collimated reflectance	-0.18 / +0.30	-0.00 / -0.04	-0.26 / -0.27	+0.01 / -0.02
Diffuse transmittance	+0.00 / +0.00	+8.50 /+12.26	+3.50 / +5.08	+0.10 / -0.06
Diffuse reflectance	+0.00 / +0.00	+1.63 / +2.32	-3.39 / -5.03	+0.02 / -0.01

Table 17: Summary of the total error of fit for each approach (RMSE) and details on each quantities for sample 1 / sample 2

IV.C.2.b *Impact of each model on the calculation of the photo-generated current of a PV module*

This part is dedicated to the analysis of the impact of each approach on the photo-generated current I_{sc} of a module. The reference module as described in chapter II is used. The encapsulant is replaced by the low UV cut-off TPO analyzed in this study. Only the 667 µm thick encapsulant sample is considered here. This corresponds to a single sheet of encapsulant, which is the case in module.

As a reminder, in the complete module model used, multiple reflectances are not taken into account. We therefore consider here the effect of the encapsulant during a single passage of light through. The index coupling between the cell and the encasulant is taken into account extrinsically by SunSolve simulations. This coupling is indeed very dependent on the architecture of the cell and it is rather calculated in advance and considered constant in the model developed in this thesis. Thus, in this part, we will only be interested in losses by absorption in the encapsulant and by backscattering. The gain and / or losses by index coupling are considered identical between the 4 approaches. This is a substantial simplification, since for example in approach 1 and 3, the refractive index becomes much greater than 1.5 in UVs. However, this does not play a role in determining the absorption and backscattering of the encapsulant on the first pass of light. Finally, the scattering of light by the encapsulant changes the angle of incidence of the rays on the cell and can theoretically modify the reflectance at the cell / encapsulant interface independently of the refractive index. This effect is also overlooked. We focus on the volume phenomena in the encapsulant. The results are summarized in the Table 18.

Effect on I_{sc}	Approach 1	Approach 2	Approach 3	Approach 4
Only absorption (%)	- 2.16 %	- 21.33 %	-0.79 %	-1.86 %
Only backscattering (%)	0 %	0 %	-10.10 %	-0.81 %
Remaining (%)	97.84 %	78.67 %	89.11 %	97.30 %

Table 18: Losses on photo-generated current due to absorption and backscattering for each of the four approaches.

The quality of the fit of the four R & T quantities and the prediction of the photo-generated current after the encapsulant has been passed through are not completely correlated, for two main reasons. The first is that the fit is made to explain the behaviour of the encapsulant sheet, with its interfaces with the air. In PV modules, it is not this configuration that matters, but only the behaviour of the encapsulant in volume. Indeed, multiple reflections are strongly limited: the glass/encapsulant interface is very poorly reflective, and the reflectance of the cell is another CTM loss item not addressed in this study (although it depends on the refractive index of the encapsulant). The loss items due to the encapsulant can therefore be summed up as follows: (i) absorption during a simple passage through the encapsulant and (ii) backscattering losses in its volume.

However, considering the quality of the fit produced by approach 4 (RMSE < 1 % over the whole spectral range) with the anisotropic scattering model, one can legitimately think that the most accurate model in terms of fit error also gives the best accuracy on the photo-generated current. It is thus reasonable to think that the encapsulant studied in this part causes a loss on the I_{sc} by absorption of 1.86 % and a loss by backscattering of 0.81 %.. This corresponds to -0.34 $\%_{abs}$ in efficiency of the module from absorption, and -0.15 $\%_{abs}$ from backscattering.

It would have been possible to gain in accuracy by performing a fit on R&T measurements weighted by the solar spectrum and by the EQE of a cell. However, the optical constants obtained would not only be related to the encapsulant, but also to the thickness, the incident spectrum and the EQE, which is not necessarily desirable for the characterization of a material. It could nevertheless be the subject of future investigations.

IV.C.3 Impact of the choice of diffuse reflectance factor of interfaces

The most appropriate model is therefore the one with anisotropic diffusion. In this model, the improved bi-hemispherical reflectance coefficient is calculated as a function of the asymmetry parameter g and the refractive index n. In the study, we realized that the definition for the reflectance coefficient of diffuse radiation can produce very different results of the fitting procedure, and thus different optical constants. To illustrate it, we will therefore analyse 3 approaches:

1. **Collimated approach:** the bi-hemispherical reflectance factor is reduced to the Fresnel coefficient for normal incidence described by the equation (8): $r_d^i = r_c(n)$. This approach can be relevant if the diffuse radiation is highly anisotropic, with the forward hemisphere of the phase function highly directed toward the propagation direction of the collimated beam.

2. **Isotropic approach:** the bi-hemispherical reflectance factor does not take into account the anisotropy of the diffuse radiation, which is considered isotropic ($g = 1$). The variation of the refractive index is taken into consideration: $r_d^i = r_d^i(n, g = 1)$.

3. **Anisotropic approach:** the bi-hemispherical reflectance factor takes into account the anisotropy of the diffuse radiation and the variation of the

refractive index: $r_d^i = r_d^i(n, g)$. This is the standard behaviour of the algorithm, how it is described by the equation (27) and the Figure 83.

The quality of the fit for the three hypotheses on the extraction of optical constants is presented on the Figure 93. The application of the Fresnel coefficient (Approach 1) on the diffuse radiation produces a quality of the fitting procedure as high as the application of the improved anisotropic bi-hemispherical reflectance factor (approach 3). The result is even a little better for the approach 1 in the UV region, but for RMSE values below one percent, uncertainties make it impossible to conclude on the existence of a better approach. In contrast, the application of the isotropic bi-hemispherical reflectance factor (approach 2) produces bad quality of the fit: RMSE up to 3 % for a wavelength of 500 nm, and a value greater than 1 % from 300 nm to 1600 nm. It therefore seems that diffuse radiation is strongly anisotropic, close to being collimated, so that Fresnel coefficient can be applied without losing accuracy of the optical constant. This is due to the fact that Fresnel coefficients of unpolarised light are almost constant up to angle value of 60°.

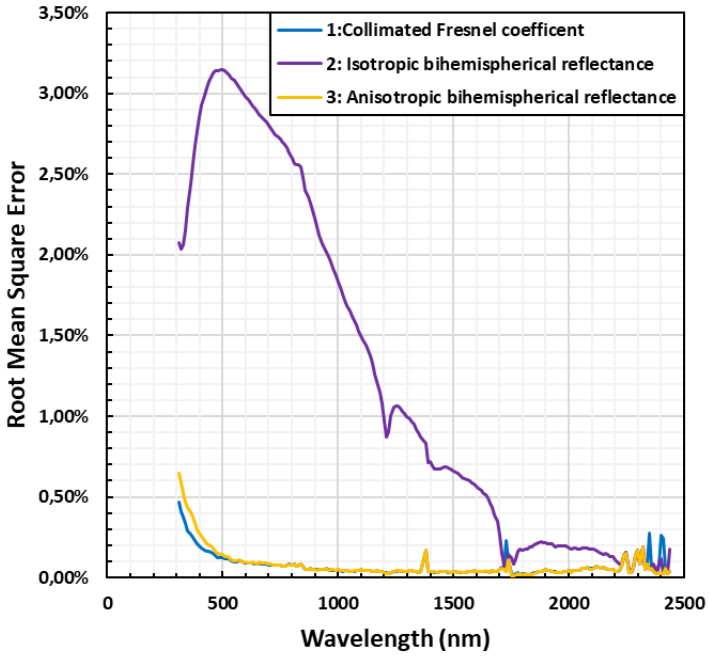

Figure 93: Impact of the choice of bi-hemispherical reflectance factor of the diffuse radiation on the root mean square error (RMSE) of the fitting procedure for extraction of optical constant with a four-flux model.

The results of the extraction of optical constant are presented in the Figure 94. The approach 2 (isotropic bi-hemispherical reflectance factor) produces unphysical results, especially on the refractive index and on the asymmetry parameter. In this approach, the reflectance factor is overestimated because the contribution of high incident angle is non-negligible. The fitting procedure has no other choice than lowering the refractive index to explain the experimental value of collimated-to-diffuse reflectance and transmittance.

The approach 1 (collimated approach with Fresnel coefficient) gives results of absorption coefficient, refractive index and scattering coefficient similar to the approach 3 where anisotropy is taken into account. A difference can be observed in the asymmetry parameter g, which is smaller in the approach 1. As the reflectance factor is underestimated for approach 1 because high incident angle is not taken into account, the diffuse transmittance is overestimated and the diffuse reflectance is underestimated. To compensate for this effect, the asymmetry parameter g is smaller than in approach 3: if g is smaller, then the forward scattering ratio is also smaller, which increases intensity of backscattering (and diffuse reflectance) and decreases intensity of forward scattering (and diffuse transmittance).

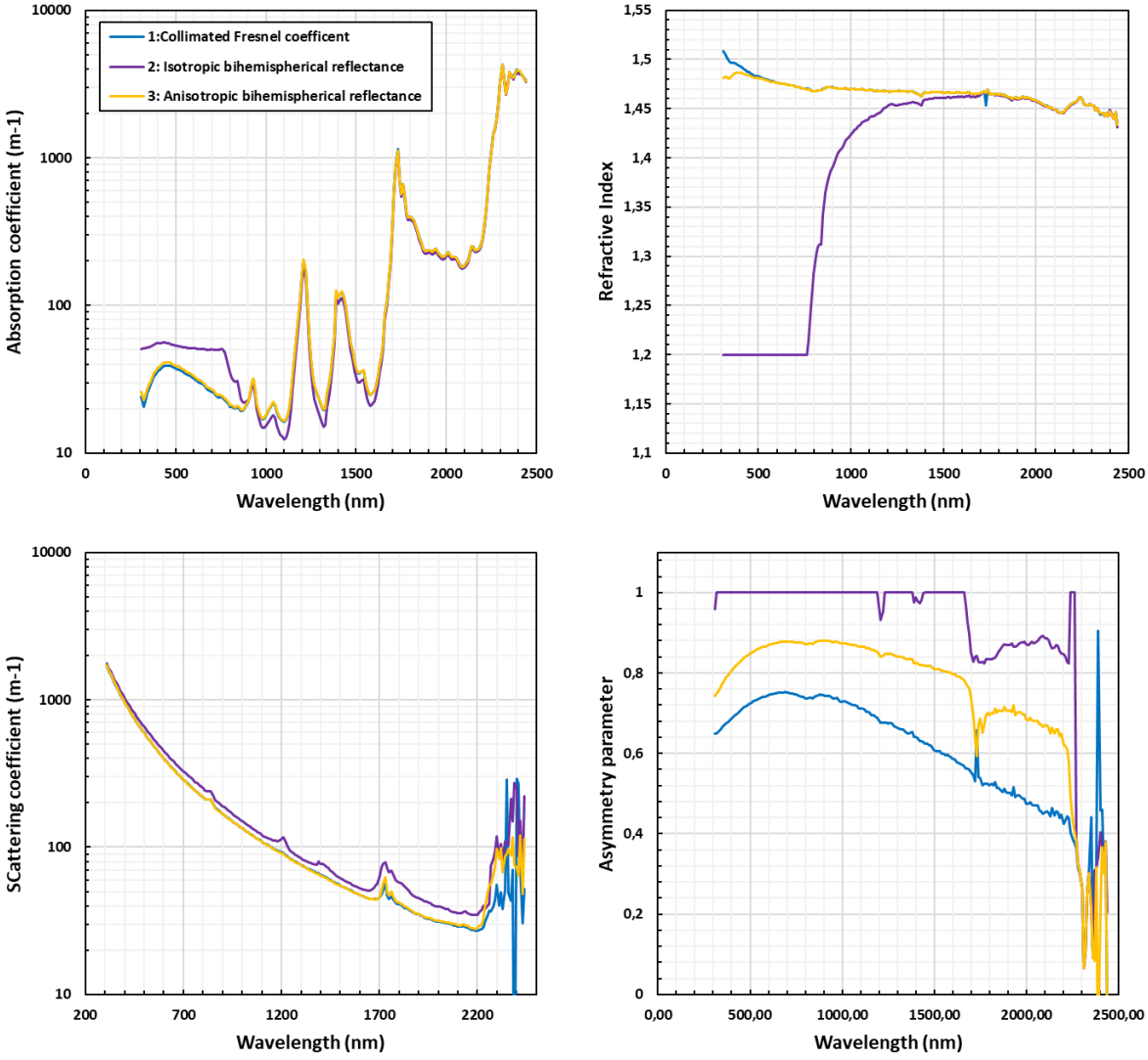

Figure 94: Results of optical constants for the three different approaches in the choice of the bi-hemispherical reflectance factor of the diffuse radiation: absorption coefficient, refractive index, scattering coefficient and asymmetry quantities.

The error made during the fitting procedure should not be the only reason to prefer a model. In the present approach, the implementation of approach 3 as the standard behaviour of the model is justified not only by the better RMSE, but also for a question of coherence of

the model. In fact, it is inconsistent to consider that volume scattering can be anisotropic - with angle distribution, but to ignore this effect for reflectance at interfaces.

IV.C.4 Optical constants of high and a low UV cut-off highly diffusive TPO

This part is devoted to the presentation of the results of two diffusive encapsulants of the TPO's family. The first one absorbs UVs (high UV cut-off) and the second one lets them pass through (low UV cut-off).. This part will be used to compare the coherence of the results on the spectral ranges outside UVs. The thickness of the two encapsulants is set at 600 µm. This is the thickness announced by the manufacturer.

The quality of the fit for both encapsulants is shown in Figure 95. In the Visible-Infrared range, the error on both samples is similar, on average less than 0.1 %. In the visible range, the error increases as expected, because diffusion is important. For the high UV cut-off encapsulant, the error in the UVs drops to 0.1 %, because the diffuse flux is completely absorbed. For both samples the maximum error remains low, at 0.6 %. The results of the optimization are given in Figure 96. The absorption coefficient a is found similar for the two samples from 450 to 2500nm. This result is expected and shows that the optimization is reliable: different samples give the same results over the spectral range where their difference in chemical composition has no impact.

The results on the refractive index are also similar, it decreases from 1.49 in the UVs to 1.44 in the infrared at 2500 nm. A Sellmeier model, representative of transparent materials in the visible-infrared range, can describe the spectral variation of the index. The local decrease present at 2100 nm is probably a measurement artefact. The refractive index is the real part of the complex index, and the absorption coefficient is related to the imaginary part. These two parts are linked by the Kramers-Kronig relations: a local variation of the optical index must be associated with a local variation of the coefficient, in a way that can be described by the Lorentz oscillator model. However, the absorption at 2100 nm is not the strongest of the spectral range, there is no reason why it should cause a local variation of the index.

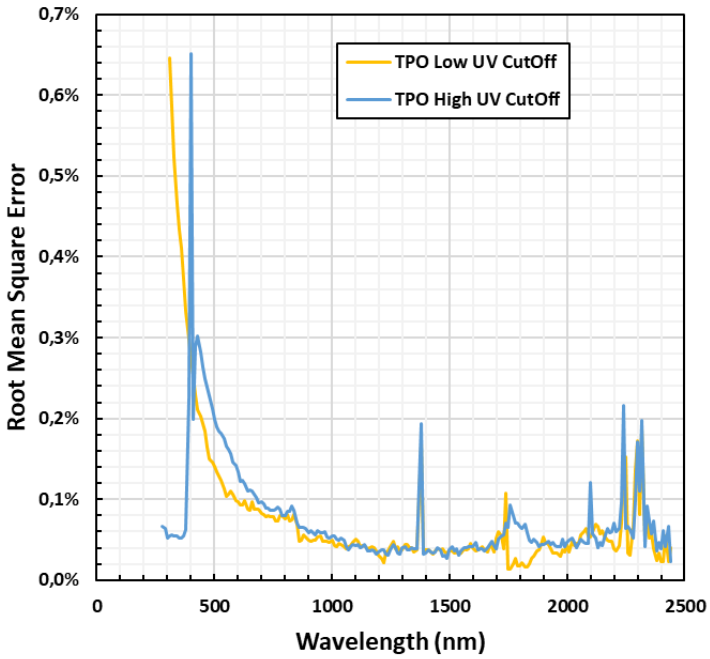

Figure 95: *Root mean square error for high and low UV cut-off TPO samples.*

The scattering coefficient shows a similar variation in power law for both samples. It is more important for high-cut-off TPO, due to the presence of additional scattering particle (UV absorber). Especially in UVs, where it becomes ten times higher than for low cut-off TPO. Although it appears to be more diffusive, the diffusion lobe is slightly more specular for high cut-off TPO, as shown by the higher values of the g-asymmetry factor. However, the overall trend is similar for both samples: a more specular lobe in the UV-Visible (average g = 0.85) and which becomes more and more isotropic in the infrared (g=0.2 at 2400nm).

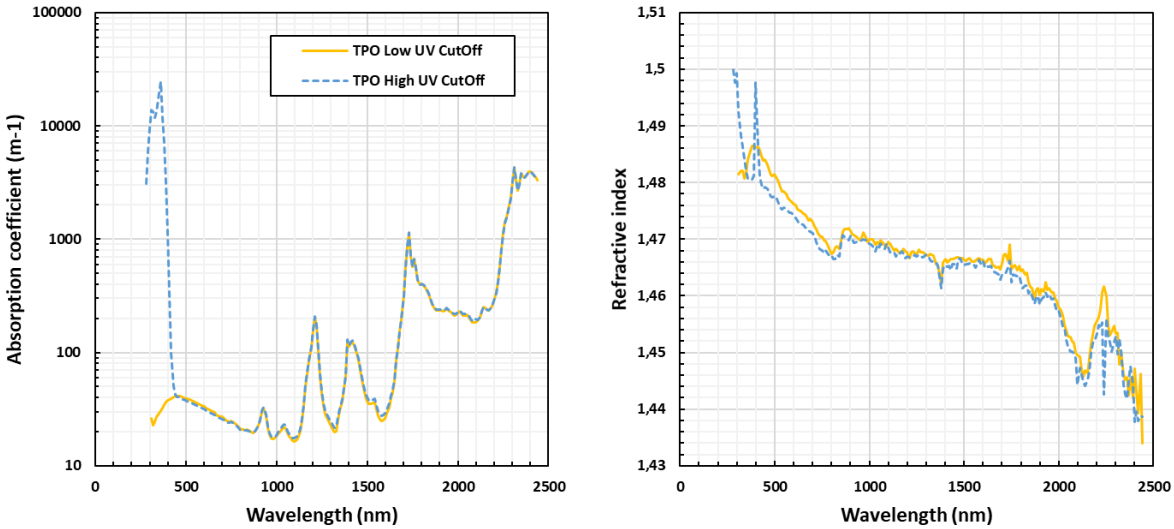

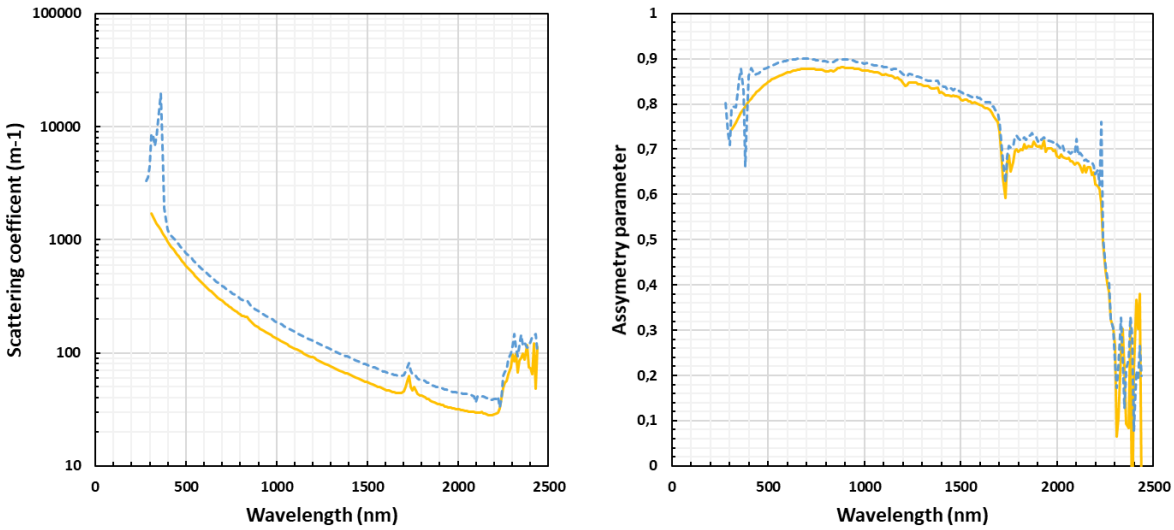

Figure 96: Optimization results of the optical constant of low and high UV cut-off TPO: absorption coefficient (top left), refractive index (top right), scattering coefficent (bottom left) and asymmetry parameter (bottom right).

For the two 600µm thick encapsulants, the effect on the photo-generated current is shown in the Table 19. The absorbed part represents a loss of 1.67 % in the approach of low cut-off TPO, and rises to 3.81 % loss for low cut-off TPO: this represents an additional 2.1 % loss. The backscattered portion is about 0.7-0.8 % for both encapsulants, which is consistent with the values of nearly similar scattering coefficients.

Effect on I_{sc}	TPO High UV Cut-off	TPO Low UV Cut-off
Only absorption (%)	-3.81 %	-1.67 %)
Only backscattering (%)	-0.77 %	-0.73 %
Remaining (%)	95.48 %	97.58 %

Table 19: Effect of optical constants on the photo-generated current (absorption and backscattering) for both sample of TPO (high and low UV cut-off).

In conclusion, the application of the extraction model to two encapsulants of the same nature (TPO) but with a behaviour in different UVs in terms of absorption leads to similar values of optical constants (a, s, n, g) for wavelengths greater than 500 nm. This is proof of the reliability of the extraction model. In UVs, the absorption coefficient of the high UV cut-off encapsulant is much higher than the low UV cut-off sample. This results in 2.1 % higher photo-generated current losses I_{sc}. The scattering coefficients being similar, the associated losses on the I_{sc} are similar. For comparison, a UV-Transmissive EVA would cause an absorption loss of only 0.5 %. Characterized TPOs are therefore much more absorbent than EVA, and in addition generate backscattering.

Conclusion of the Chapter IV

Some of the new encapsulants used in PV modules are much more volume diffusive than the historical EVAs, such as the TPO and POE families. Characterisation of the optical constants of these materials is important for simulation, numerical prototyping and loss analysis of PV modules. However, until now, light scattering effects were not included in the simulation of module performance losses.

Our study shows that in order to correctly reproduce the measurements of reflectances and transmittances - both collimated and diffuse - a 4-flux model is required, 4-flux meaning that two collimated and two diffuse fluxes propagating in opposite directions are considered. To this aim, we use the historical model of Maheu *et al.*, 1984, completed by the tabulation of Rozé *et al.*, 2001. This later work makes possible to overcome the fit of the average crossing parameter and forward scattering ratio, the two parameters being expressed as a function of a single one, the asymmetry parameter of the Henyey-Greenstein phase function. The number of parameters to extract is reduced, and an approximation of the shape of the scattering lobe is obtained. Moreover, we have proposed an approximated procedure to calculate more precisely the bi-hemispherical reflectance coefficient of the diffuse flux accounting for anisotropy. Using this model, a numerical procedure of optimisation has been implemented to extract a the absorption coefficient (m^{-1}), related to the imaginary part of the optical index κ, s the scattering coefficient (m^{-1}), g the asymmetry factor and n the refractive index from the measurement of the total transmittance T_t, the diffuse transmittance T_{cd}, the total reflectance R_t and the diffuse reflectance R_{cd}. This procedure, for accuracy, combines experiments performed on two samples of different thickness. The results obtained with this innovative approach have been compared with other neglecting diffusion or assuming scattering isotropic, both on specular and diffusing encapsulants : it turns out that the improved 4 flux models is the best approach to reproduce accurately experimental data and obtained reasonable values of the optical index.

Moreover, our analysis has shown that the fluxes have to be anisotropic: the diffusion is mainly forward, the total flux remains globally very specular.

The proposed 4-flux model allows the accurate calculation of the absorption and backscattering that will take place in a module encapsulant, and the associated losses on photo generated current weighted by the EQE and the AM1.5 spectrum. This investigation concludes to the existence of a new source of loss when encapsulating cells with diffusing polymer, not due to absorption or refraction, but due to backscattering. To the best of our knowledge, such backscatter loss has never been mentioned in CTM analyses until now. As an example, results on two 600 µm thick TPO encapsulants (one high UV cut-off and the other low UV cut-off) show a backscatter loss of 0.75 % on average, and a loss on the I_{sc} by absorption of 1.67 % for the low cut-off against 3.81 % for the high cut-off, a difference of more than 2 %.

Characterized TPOs are therefore much more absorbent than EVA, and in addition generate backscattering. Future studies should focus on the characterization of different types of encapsulant (EVA, POE, Ionomer, etc.) to characterize the diffusive behaviour, the impact on the extraction of optical constants and therefore on the performance of the module of these materials. It would also be interesting to analyse the behaviour of the extraction model

using samples of very different thicknesses. For each material used, add a sample of very low thickness (a few tens of microns), and a sample of much greater thickness (several millimetres). A low thickness would make it possible to increase the precision of the extraction for wavelengths where the absorption is great. A significant thickness would make it possible to gain in precision on the extraction of the scattering coefficients.

Conclusion du Chapitre IV

Certains des nouveaux encapsulants utilisés dans les modules PV sont beaucoup plus diffusants en volume que les EVA historiques, comme les familles TPO et POE. La caractérisation des constantes optiques de ces matériaux est importante pour la simulation, le prototypage numérique et l'analyse des pertes des modules PV. Cependant, jusqu'à présent, les effets de diffusion en volume de la lumière n'étaient pas inclus dans la simulation des pertes de performance des modules.

Notre étude montre que pour reproduire correctement les mesures de réflectances et de transmittances - collimatées et diffuses - un modèle 4-flux est nécessaire, 4-flux signifiant que deux flux collimatés et deux flux diffus se propageant dans des directions opposées sont considérés. Dans ce but, nous utilisons le modèle historique de Maheu et al., 1984, complété par la tabulation de Rozé et al., 2001. Ce travail ultérieur permet de s'affranchir de l'ajustement du paramètre de croisement moyen et du ratio de diffusion vers l'avant, les deux paramètres étant exprimés en fonction d'un seul, le paramètre d'asymétrie de la fonction de phase de Henyey-Greenstein. Le nombre de paramètres à extraire est réduit, et une approximation de la forme du lobe de diffusion est obtenue. De plus, nous avons proposé une procédure approchée pour calculer plus précisément le coefficient de réflectance bi-hémisphérique du flux diffus en tenant compte de l'anisotropie. En utilisant ce modèle, une procédure numérique d'optimisation a été mise en œuvre pour extraire a le coefficient d'absorption (m-1), lié à la partie imaginaire de l'indice optique, s le coefficient de diffusion (m-1), g le facteur d'asymétrie et n l'indice de réfraction à partir de la mesure de la transmittance totale T_t, de la transmittance diffuse T_{cd}, de la réflectance totale R_t et de la réflectance diffuse R_{cd}. Cette procédure, pour plus de précision, combine des expériences réalisées sur deux échantillons d'épaisseur différente. Les résultats obtenus avec cette approche innovante ont été comparés avec d'autres approches négligeant la diffusion ou supposant la diffusion isotrope, à la fois sur des encapsulants spéculaires et diffusants : il s'avère que le modèle amélioré à 4-flux est la meilleure approche pour reproduire avec précision les données expérimentales et obtenir des valeurs raisonnables de l'indice optique.

De plus, notre analyse a montré que les flux doivent être anisotropes : la diffusion se fait principalement vers l'avant, le flux total reste globalement très spéculaire.

Le modèle à 4-flux proposé permet de calculer précisément l'absorption et la rétrodiffusion qui auront lieu dans l'encapsulant d'un module, et les pertes associées sur le courant photo-généré pondéré par l'EQE et le spectre AM1.5. Cette étude conclut à l'existence d'un nouveau poste de perte lors de l'encapsulation de cellules avec un polymère diffusant, non pas due à l'absorption ou à la réfraction, mais à la rétrodiffusion. À notre connaissance, cette perte par rétrodiffusion n'a jamais été mentionnée dans les analyses CTM jusqu'à présent. A titre d'exemple, les résultats sur deux encapsulants TPO de 600 µm d'épaisseur (l'un à haut seuil de coupure UV et l'autre à bas seuil de coupure UV) montrent une perte par

rétrodiffusion de 0,75 % en moyenne, et une perte sur l'I_{sc} par absorption de 1,67 % pour le bas seuil de coupure UV contre 3,81 % pour le haut seuil de coupure UV, soit une différence de plus de 2 %.

Les TPOs caractérisés sont donc beaucoup plus absorbants que l'EVA, et génèrent en plus de la rétrodiffusion. Les études futures devraient se concentrer sur la caractérisation de différents types d'encapsulant (EVA, POE, Ionomer, etc.) afin de caractériser le comportement diffusif, l'impact sur l'extraction des constantes optiques et donc sur les performances du module de ces matériaux. Il serait également intéressant d'analyser le comportement du modèle d'extraction en utilisant des échantillons d'épaisseurs très différentes. Pour chaque matériau utilisé, ajouter un échantillon de très faible épaisseur (quelques dizaines de microns), et un échantillon d'épaisseur beaucoup plus importante (plusieurs millimètres). Une faible épaisseur permettrait d'augmenter la précision de l'extraction pour les longueurs d'onde où l'absorption est importante. Une épaisseur importante permettrait de gagner en précision sur l'extraction des coefficients de diffusion.

General Conclusion

The role of photovoltaic energy in the context of global warming.

We are responsible for a major crisis of life on Earth: IPBES reports show a collapse in species diversity and numbers of individuals. This crisis is mainly linked to our unstable way of occupying and transforming space: we have already exceeded 3 of the 11 planetary limits identified by Steffen *et al.* [7]. We are currently following a systemic trajectory close to the collapse scenarios modelled by the "Limits to Growth" report [8]. The exponential development of our societies has been made possible by the use of more and more primary energy, both in quantity and quality: primary energy production has been multiplied by more than 30 since 1800, with each new energy source being added to the previous ones. In particular, the use of fossil fuels (coal, gas, and oil), with a high energy return rate, has enabled us to ensure high societal functions for a large number of people (arts, health, education...). But they are high emitters of greenhouse gases and therefore have a significant impact on climate change. The social, economic and biological destabilization that it carries with it if we follow the current trajectory towards +3.5°C thus pushes us to decarbonize our energy production [9]. Electricity consumption is a significant part of the world's energy consumption: about 20% in 2020. This share, coupled with the increasing electrification of new uses, also pushes the use of decarbonized energy - hydro, wind, nuclear and photovoltaic - for electricity. The International Energy Agency predicts that photovoltaic energy will increase from around 700 GW to 3200 GW of global installed capacity between 2020 and 2040 [19]. This growth, past and future, is closely linked to the falling costs of this technology: the price of modules has been divided by 25 in the last 20 years [20]. The total cost of a PV installation (LCOE) has been divided by 4 in 10 years, reaching $69/MWh in 2019 [21]. This cost reduction is due to the huge economies of scale, but also to the increased performance of the devices at constant cost.

The need for computer experiments in the optimisation of module performances.

The analysis of electrical power losses within a photovoltaic system is therefore essential to enable its improvement. Photovoltaic cells, today mainly made of semiconductor silicon, are a basic component of the system. They convert light energy into electrical energy, but they are fragile. To protect them mechanically and chemically, and thus guarantee their durability, they have to be integrated into modules: the cells are electrically interconnected to obtain the desired current and voltage, and then encapsulated in polymers and/or glass to isolate them from the environment. These interconnection and encapsulation steps generate power losses: part of the incident irradiance can be reflected, absorbed, or transmitted by these layers and therefore does not participate in the photo-generation of current. Similarly, the electrical interconnections of the cells generate resistive losses by Joule effect.

Experiments, combined with *computer* experiments, are necessary to understand the influence of each component on the global performance of a module, and therefore constitute the basis for the development of more efficient architectures.

This is why numerical models, tools or software for PV module performance are widely used: they are complementary to experience and allow to accelerate studies by limiting the number of physical experiments to be performed, while improving the understanding of the phenomena involved.

These module performance simulation softwares are numerous (Part II.B). Some of these model optics, other model semiconductor physics or the electrical circuit that constitutes a module, few of them model combinations of these categories.

Optical modelling can be done by a combination of ray tracing and wave optic methods (Tracey, LAOSS, Daidalos, Sunsolve...): such tools are precise but expensive in computing time. Other models use the transfer matrix methods to assess the coupling of flat layers (OPTOS): fast in computation time, they require more rigorous numerical methods (RCWA, FDTD...) or complex experimental methods (BRDF) to calibrate the transfer matrices of complex interfaces. Finally, some optical models are analytical (SmartCalc, Hanifi *et al., …*): they are even faster, but may omit some couplings between the elements of the module.

To compute the electrical performance (I-V curves) of the module from the optics, some models use a finite element approach and solve semiconductor equations (Sentaurus, Atlas, Quokka 3, LAOSS, PC3D, AFORS-HET...). In 1D or 3D, they offer a detailed understanding of the physics of the cell. Other tools use an equivalent circuit approach to describe the cell electrically (Sunsolve, Rodriguez *et al.*, Griddler & Module). The most commonly used approach is a one-dimensional two-diode model: a current generator, two diodes to model recombinations in the cell, a shunt resistance and a lumped series resistance.

CTMOD: an innovative and efficient module performance modelling tool for silicon heterojunction modules.

The model CTMod developed during this thesis (Part II.A) uses essentially analytical approaches to model optical and electrical issues in module, with a particular emphasis on silicon heterojunction modules.

The analytical optical model at normal incidence is inspired by the approach of SmartCalc and Hanifi *et al.*: it takes into account the reflection on the front of the module, the absorption in the glass, in the encapsulant and in the foil (if present), the effective shading of the metallization and the interconnection ribbons, the reflection and the optical transmission of the cell as well as the gain of photo-current by the reflective inter-cell spaces.

CTMod adopts a two diodes equivalent circuit in one dimension to calculate the curve and IV parameters from the optics of the module, similarly to Sunsolve. The resistive losses in the module are treated analytically, mainly as in Geipel *et al.* and Guo *et al*. It is used to deal with the case of a glass / backsheet or glass / glass module. The interconnection between cells can be based on ribbons or of the “shingle” type. The calculation of the absolute power losses is based on the classification proposed by Hanifi *et al.*: it allows the comparison of module architecture by the term-to-term difference of the power losses. It also makes possible to analyse the effects of combined changes in metallization and cell interconnections, as carried out by Rodriguez *et al.*

The main technology developed at INES - silicon heterojunction modules - makes it necessary to adapt these previous approaches. Because of the parallel transport of the current between the ITO and the bulk of silicon on the front face of the cell, a change of metallization design forces to consider all the series resistance components of the cell. This point is therefore included in the model, thanks to the work of Basset *et al.* (who completed his thesis at INES).

Application of CTMOD to investigate the performance of modules based on cut cells.

In the quest for performance gains, the inclusion of cut cells has been widely studied, and adopted industrially. Limiting the current flowing in the cell interconnections makes it possible to limit resistive losses: the more the number of cuts N increases, the higher the CTM FF and the more powerful the module. The resistive losses follow a law in $1 / N^2$, as envisaged by the literature. However, the more the number of cuts increases, the more the inter-cell spaces occupy a significant proportion of the total surface of the module, and thus limit the yield. These two effects generate an optimum for a single cutting step (half-cell architecture) for a module made up of M2 cells with 18 wires of 250 µm diameters and a standard inter-cell space of 2 or 3 mm. For this architecture, the FF gain has been found close to 1.6% when going from full-cell to half-cell, consistent with literature.

However the process of cutting the cells also generates losses. The creation of new non-passivated edges causes recombinations, to which high efficiency HJT cells are more sensitive. Since the integration of cut cells aims at reducing the resistive losses in module, it seemed relevant to us to include also the effect of the cutting in the loss analysis, which is not explicitly done by the current CTM analysis tools. This loss item is generally described by its impact on the parameters of a two-diode model, which corresponds perfectly to the description chosen in CTMod: integration is thus facilitated. All cell technologies taken together, the additional recombination current - J_{02} edge - has been measured by previous works in the literature between 3 and 70 nA/cm, with a theoretical maximum value of 20 nA/cm. This large dispersion of experimental values makes it impossible to integrate simply these values taken from litterature in CTMod. Moreover, to our knowledge, no experimental study has treated the case of HJT cells yet.

Thus, twenty HJT cells with an average efficiency of 21.8% were measured before and after cutting by a pulsed infrared laser (1064 nm, 10 ns pulse) commercialized by Rofin. We obtained a J_{02} edge value of 7.63 nA/cm, and a photo-generated current loss J_{ph} of 0.02 %/cm. These values allow us to faithfully reproduce the decrease of 0.5 % on the I_{sc}, 0.22 % on the V_{oc}, 0.65 % on the FF and 1.37 % on the efficiency. Two fitting procedures were tested. The first one consists in leaving all the parameters of the 2-diodes model variable before and after cutting. This method has the major disadvantage of producing lower J_{01} and r_s values after cutting, which is difficult to interpret physically. We therefore preferred a second method: the parameters J_{ph}, J_{01}, J_{02} and r_s are free before cutting. After cutting, J_{01} and r_s are fixed and only J_{ph} and J_{02} can vary. These values were therefore integrated into the overall module performance model to predict the IV parameters of a record module. The cells of this record module were measured before and after cutting. The losses of J_{02} and J_{ph} edge made it possible to correctly predict the performance of the cells after cutting, even though these cells have a better efficiency than those used for the initial characterization (23.43 % vs 21.8 %). On the other hand, this did not make it possible to correctly predict the performance of the complete

module due the presence of an additional J_{02} of 2 nA / cm, whose origin is unknown. Further studies would be welcome to understand it.

Application of CTMOD to investigate the performance of diffusing encapsulants.

Another improvement in module performance prediction models has been made for encapsulants. Some of the new encapsulants used in PV modules – and particularly HJT module – are much more diffusive in volume than the historical EVAs, such as the TPO and POE families. However, until now, volume light scattering effects were not included in the simulation of module performance losses.

Our study shows that in order to correctly reproduce the measurements of reflectances and transmissions - both collimated and diffuse - a 4-flux model with anisotropic scattering is required. To this aim, we use the historical model of Maheu *et al.*, 1984, completed by the tabulation of Rozé *et al.*, 2001. We have proposed an approximated procedure to calculate more precisely the bi-hemispherical reflectance coefficient of the diffuse flux accounting for anisotropy. Using this model, a numerical procedure of optimisation has been implemented to extract a the absorption coefficient (m^{-1}), related to the imaginary part of the optical index κ, s the scattering coefficient (m^{-1}), g the asymmetry factor and n the refractive index from the measurement of the total transmittance T_t, the diffuse transmittance T_{cd}, the total reflectance R_t and the diffuse reflectance R_{cd}. This procedure, for accuracy, combines experiments performed on two samples of different thicknesses. The results obtained with this innovative approach have been compared with other neglecting diffusion or assuming scattering isotropic, both on specular and diffusing encapsulants: it turns out that the improved 4-flux model is the best approach to reproduce accurately experimental data and obtain reasonable values of the optical index.

Moreover, our analysis has shown that the fluxes have to be anisotropic: the diffusion is mainly forward, the total flux remains globally very specular. The proposed 4-flux model allows the accurate calculation of the absorption and backscattering that will take place in a module encapsulant. This investigation concludes to the existence of a new source of loss when encapsulating cells with diffusing polymer, not due to absorption or refraction, but due to backscattering. To the best of our knowledge, such backscatter loss has never been mentioned in CTM analyses until now.

As an example, results on two 600 µm thick TPO encapsulants (one high UV cut-off and the other low UV cut-off) show a backscatter loss of 0.75 % on average, and a loss on the I_{sc} by absorption of 1.67 % for the low cut-off against 3.81 % for the high cut-off, a difference of more than 2 %. Characterized TPOs are therefore much more absorbent than EVA, and in addition generate backscattering. Future studies should focus on the characterization of different types of encapsulant (EVA, POE, Ionomer, etc.) to characterize the diffusive behaviour, the impact on the extraction of optical constants and therefore on the performance of the module of these materials.

It would also be interesting to analyse the behaviour of the extraction model using samples of very different thicknesses. For each material used, add a sample of very low thickness (a few tens of microns), and a sample of much greater thickness (several millimeters). A low thickness would make it possible to increase the precision of the extraction

for wavelengths where the absorption is great. A significant thickness would make it possible to gain in precision on the extraction of the scattering coefficients.

Perspectives of improvement of the CTMOD models

Several points for improvement are still to be considered. The model could obviously be improved on its optical part. The main flaw is to take into account multiple interactions afterwards, via corrective factors.

A simple corrective factor should account for the part of the light reflected by the cell encapsulating interface, which is re-reflected at the glass-to-air interface and can therefore participate to the photo-generation.

We believe that this improvement would avoid the 0.8% difference found comparing Sunsolve and CTMod. Then, a major limitation of the model is that it is only valid at normal incidence. To consider a prediction of the performance at any angle, a ray tracing or transfer matrix method seems to be necessary.

One of the advantages of analytical models like CTMod is its speed of execution. It allows for example to calculate in a few tens of minutes hundreds of thousands of different module configurations. It also allows sensitivity analysis to input parameters, and therefore also to analyse the propagation of uncertainties on these input parameters. Such analysis require a much longer time with ray tracing models. A matrix approach, such as OPTOS, could therefore offer a good trade-off between accuracy and speed, if it is improved to account for the optical impact of the metallization and interconnection of the cells.

The model was mainly used under standard irradiance and temperature conditions (STC): normal incidence, AM1.5g spectrum, and 25°C for the module and cells. The consideration of temperature has been mentioned in CTMod: it is based on the temperature coefficients of the cell. It could be considered to develop a model of equivalent thermal resistance to quickly address the issue of temperature distribution in the module placed in any environment. Including the electrical effects of junction boxes and bypass diodes could be another desirable improvement.

We have therefore precisely characterized two new loss items for the HJT modules. However, the comparison of the final model results (parameters or curve IV) with experimental values on a solar simulator is still incomplete, as shown by the attempt to model the record 120 half-cell module. Future work should certainly focus on a thorough characterization of the uncertainties on the model input parameters, in order to obtain the influence of these uncertainties on the CTMod IV results. Comparison of these numerical values with the IV results of solar simulators, obviously associated with their experimental uncertainties, is now essential. In this sense, preliminary studies were launched in 2020, but aborted due to the pandemic crisis. It will be highly desirable to continue them.

Conclusion Générale

Le rôle de l'énergie photovoltaïque dans le contexte du réchauffement climatique.

Nous sommes responsables d'une crise majeure de la vie sur Terre : les rapports de l'IPBES montrent un effondrement de la diversité des espèces et du nombre d'individus. Cette crise est principalement liée à notre mode instable d'occupation et de transformation de l'espace : nous avons déjà dépassé 3 des 11 limites planétaires identifiées par Steffen et al. [7]. Nous suivons actuellement une trajectoire systémique proche des scénarios d'effondrement modélisés par le rapport " Limits to Growth " [8]. Le développement exponentiel de nos sociétés a été rendu possible par l'utilisation de toujours plus d'énergie primaire, tant en quantité qu'en qualité : la production d'énergie primaire a été multipliée par plus de 30 depuis 1800, chaque nouvelle source d'énergie s'ajoutant aux précédentes. En particulier, l'utilisation des énergies fossiles (charbon, gaz et pétrole), à fort taux de rendement énergétique, a permis d'assurer des fonctions sociétales élevées pour un grand nombre de personnes (arts, santé, éducation...). Mais elles sont fortement émettrices de gaz à effet de serre et ont donc un impact important sur le changement climatique. La déstabilisation sociale, économique et biologique qu'il entraîne si nous suivons la trajectoire actuelle vers +3,5°C nous pousse donc à décarboner notre production énergétique [9]. La consommation d'électricité représente une part importante de la consommation énergétique mondiale : environ 20% en 2020. Cette part, couplée à l'électrification croissante des nouveaux usages, pousse également à l'utilisation des énergies décarbonées - hydraulique, éolienne, nucléaire et photovoltaïque - pour l'électricité. L'Agence internationale de l'énergie prévoit que l'énergie photovoltaïque passera d'environ 700 GW à 3200 GW de capacité installée mondiale entre 2020 et 2040 [19]. Cette croissance, passée et future, est étroitement liée à la baisse des coûts de cette technologie : le prix des modules a été divisé par 25 au cours des 20 dernières années [20]. Le coût total d'une installation photovoltaïque (LCOE) a été divisé par 4 en 10 ans, pour atteindre 69 $/MWh en 2019 [21]. Cette réduction des coûts est due aux énormes économies d'échelle, mais aussi à l'augmentation des performances des dispositifs à coût constant.

La nécessité d'expériences informatiques pour l'optimisation des performances des modules.

L'analyse des pertes de puissance électrique dans un système photovoltaïque est donc essentielle pour permettre son amélioration. Les cellules photovoltaïques, aujourd'hui principalement constituées de silicium semi-conducteur, sont un composant de base du système. Elles transforment l'énergie lumineuse en énergie électrique, mais elles sont fragiles. Pour les protéger mécaniquement et chimiquement, et ainsi garantir leur pérennité, elles doivent être intégrées dans des modules : les cellules sont interconnectées électriquement pour obtenir le courant et la tension souhaités, puis encapsulées dans des polymères et/ou du verre pour les isoler de l'environnement. Ces étapes d'interconnexion et d'encapsulation génèrent des pertes de puissance : une partie du rayonnement incident peut être réfléchie, absorbée ou transmise par ces couches et ne participe donc pas à la photo-génération de courant. De même, les interconnexions électriques des cellules génèrent des pertes résistives par effet Joule.

Des expériences physiques, combinées à des expériences informatiques, sont nécessaires pour comprendre l'influence de chaque composant sur la performance globale d'un module, et constituent donc la base du développement d'architectures plus performantes.

C'est pourquoi les modèles, outils ou logiciels numériques pour la performance des modules PV sont largement utilisés : ils sont complémentaires à l'expérience physique et permettent d'accélérer les études en limitant le nombre d'expériences physiques à réaliser, tout en améliorant la compréhension des phénomènes en jeu.

Ces logiciels de simulation de la performance des modules sont nombreux (partie II.B). Certains d'entre eux modélisent l'optique, d'autres la physique des semi-conducteurs ou le circuit électrique qui constitue un module, peu d'entre eux modélisent des combinaisons de ces catégories.

La modélisation optique peut se faire par une combinaison de méthodes de traçage de rayons et d'optique ondulatoire (Tracey, LAOSS, Daidalos, Sunsolve...) : de tels outils sont précis mais coûteux en temps de calcul. D'autres modèles utilisent les méthodes de matrice de transfert pour évaluer le couplage de couches planes (OPTOS) : rapides en temps de calcul, ils nécessitent des méthodes numériques plus rigoureuses (RCWA, FDTD...) ou des méthodes expérimentales complexes (BRDF) pour calibrer les matrices de transfert d'interfaces complexes. Enfin, certains modèles optiques sont analytiques (SmartCalc, Hanifi et al., ...) : ils sont encore plus rapides, mais peuvent omettre certains couplages entre les éléments du module.

Pour calculer les performances électriques (courbes I-V) du module à partir de l'optique, certains modèles utilisent une approche par éléments finis et résolvent les équations des semi-conducteurs (Sentaurus, Atlas, Quokka 3, LAOSS, PC3D, AFORS-HET...). En 1D ou 3D, ils offrent une compréhension détaillée de la physique de la cellule. D'autres outils utilisent une approche par circuit équivalent pour décrire électriquement la cellule (Sunsolve, Rodriguez et al., Griddler & Module). L'approche la plus utilisée est un modèle unidimensionnel à deux diodes : un générateur de courant, deux diodes pour modéliser les recombinaisons dans la cellule, une résistance shunt et une résistance série globale.

CTMOD : un outil innovant et efficace de modélisation des performances des modules à hétérojonction de silicium.

Le modèle CTMod développé au cours de cette thèse (partie II.A) utilise des approches essentiellement analytiques pour modéliser les phénomènes optiques et électriques des modules, avec un accent particulier sur les modules à hétérojonction de silicium.

Le modèle optique analytique à incidence normale est inspiré de l'approche de SmartCalc et de Hanifi et al. il prend en compte la réflexion sur la face avant du module, l'absorption dans le verre, dans l'encapsulant et dans le foil (si présent), l'ombrage effectif de la métallisation et des rubans d'interconnexion, la réflexion et la transmission optique de la cellule ainsi que le gain de photo-courant par les espaces inter-cellules réfléchissants.

CTMod adopte un circuit équivalent à deux diodes en une dimension pour calculer les paramètres de la courbe IV à partir de l'optique du module, de manière similaire à Sunsolve. Les pertes résistives dans le module sont traitées analytiquement, principalement comme dans

Geipel et al. et Guo et al. Il est utilisé pour traiter le cas d'un module verre/backsheet ou verre/verre. L'interconnexion entre les cellules peut être basée sur des rubans ou du type "shingle". Le calcul des pertes de puissance absolue est basé sur la classification proposée par Hanifi et al : il permet de comparer l'architecture des modules par la différence terme à terme des pertes de puissance. Elle permet également d'analyser les effets des modifications combinées de la métallisation et des interconnexions des cellules, comme l'ont fait Rodriguez et al.

La principale technologie développée à l'INES - les modules à hétérojonction de silicium - nécessite d'adapter ces approches précédentes. En raison du transport parallèle du courant entre l'ITO et le bulk de silicium sur la face avant de la cellule, un changement de conception de la métallisation oblige à considérer toutes les composantes de résistance série de la cellule. Ce point est donc inclus dans le modèle, grâce aux travaux de Basset et al. (qui a réalisé sa thèse à l'INES).

Application du modèle CTMOD pour étudier les performances des modules basés sur des cellules découpées.

Dans la recherche de gains de performance, l'inclusion de cellules découpées a été largement étudiée, et adoptée industriellement. Limiter le courant circulant dans les interconnexions des cellules permet de limiter les pertes résistives : plus le nombre de coupes N augmente, plus le CTM FF est élevé et plus le module est performant. Les pertes résistives suivent une loi en 1 / N^2, comme prévu par la littérature. Cependant, plus le nombre de découpes augmente, plus les espaces inter-cellules occupent une proportion importante de la surface totale du module, et limitent donc le rendement. Ces deux effets génèrent un optimum pour une seule étape de coupe (architecture demi-cellule) pour un module composé de cellules M2 avec 18 fils de 250 µm de diamètre et un espace inter-cellule standard de 2 ou 3 mm. Pour cette architecture, le gain FF a été trouvé proche de 1,6 % en passant de la cellule complète à la demi-cellule, ce qui est cohérent avec la littérature.

Cependant, le processus de découpe des cellules génère également des pertes. La création de nouveaux bords non passivés provoque des recombinaisons, auxquelles les cellules HJT à haut rendement sont plus sensibles. Puisque l'intégration de cellules découpées vise à réduire les pertes résistives dans le module, il nous a semblé pertinent d'inclure également l'effet de la découpe dans l'analyse des pertes, ce qui n'est pas explicitement fait par les outils d'analyse CTM actuels. Ce poste de perte est généralement décrit par son impact sur les paramètres d'un modèle à deux diodes, ce qui correspond parfaitement à la description choisie dans CTMod : l'intégration est ainsi facilitée. Toutes technologies de cellules confondues, le courant de recombinaison additionnel - J_{02} d'arête - a été mesuré par des travaux antérieurs dans la littérature entre 3 et 70 nA/cm, avec une valeur maximale théorique de 20 nA/cm. Cette grande dispersion des valeurs expérimentales rend impossible la simple intégration de ces valeurs issues de la littérature dans CTMod. De plus, à notre connaissance, aucune étude expérimentale n'a encore traité le cas des cellules HJT.

Ainsi, vingt cellules HJT d'un rendement moyen de 21,8% ont été mesurées avant et après découpe par un laser infrarouge pulsé (1064 nm, impulsion de 10 ns) commercialisé par Rofin. Nous avons obtenu une valeur de J_{02} d'arête de 7,63 nA/cm, et une perte de courant photo-généré J_{ph} de 0,02 %/cm. Ces valeurs nous permettent de reproduire fidèlement la diminution de 0.5 % sur l'I_{sc}, 0.22 % sur le V_{oc}, 0.65 % sur le FF et 1.37 % sur le rendement. Deux procédures d'ajustement numérique ont été testées. La première consiste à laisser tous les paramètres du

modèle 2-diodes variables avant et après la coupe. Cette méthode présente l'inconvénient majeur de produire des valeurs de J_{01} et r_s plus faibles après découpe, ce qui est difficile à interpréter physiquement. Nous avons donc préféré une deuxième méthode : les paramètres J_{ph}, J_{01}, J_{02} et r_s sont libres avant la coupe. Après la coupe, J_{01} et r_s sont fixes et seuls J_{ph} et J_{02} peuvent varier. Ces valeurs ont donc été intégrées dans le modèle de performance globale du module pour prédire les paramètres IV d'un module record. Les cellules de ce module d'enregistrement ont été mesurées avant et après la coupe. Les pertes de J_{02} d'arête et J_{ph} ont permis de prédire correctement les performances des cellules après découpe, même si ces cellules ont un meilleur rendement que celles utilisées pour la caractérisation initiale (23,43 % vs 21,8 %). En revanche, cela n'a pas permis de prédire correctement les performances du module complet en raison de la présence d'un J_{02} supplémentaire de 2 nA/cm, dont l'origine est inconnue. Des études complémentaires seraient les bienvenues pour la comprendre.

Application du modèle CTMOD pour étudier les performances des encapsulants diffusants.

Certains des nouveaux encapsulants utilisés dans les modules PV sont beaucoup plus diffusants en volume que les EVA historiques, comme les familles TPO et POE. La caractérisation des constantes optiques de ces matériaux est importante pour la simulation, le prototypage numérique et l'analyse des pertes des modules PV. Cependant, jusqu'à présent, les effets de diffusion en volume de la lumière n'étaient pas inclus dans la simulation des pertes de performance des modules.

Notre étude montre que pour reproduire correctement les mesures de réflectances et de transmittances - collimatées et diffuses - un modèle 4-flux est nécessaire, 4-flux signifiant que deux flux collimatés et deux flux diffus se propageant dans des directions opposées sont considérés. Dans ce but, nous utilisons le modèle historique de Maheu et al., 1984, complété par la tabulation de Rozé et al., 2001. Ce travail ultérieur permet de s'affranchir de l'ajustement du paramètre de croisement moyen et du ratio de diffusion vers l'avant, les deux paramètres étant exprimés en fonction d'un seul, le paramètre d'asymétrie de la fonction de phase de Henyey-Greenstein. Le nombre de paramètres à extraire est réduit, et une approximation de la forme du lobe de diffusion est obtenue. De plus, nous avons proposé une procédure approchée pour calculer plus précisément le coefficient de réflectance bi-hémisphérique du flux diffus en tenant compte de l'anisotropie. En utilisant ce modèle, une procédure numérique d'optimisation a été mise en œuvre pour extraire a le coefficient d'absorption (m-1), lié à la partie imaginaire de l'indice optique, s le coefficient de diffusion (m-1), g le facteur d'asymétrie et n l'indice de réfraction à partir de la mesure de la transmittance totale T_t, de la transmittance diffuse T_{cd}, de la réflectance totale R_t et de la réflectance diffuse R_{cd}. Cette procédure, pour plus de précision, combine des expériences réalisées sur deux échantillons d'épaisseur différente. Les résultats obtenus avec cette approche innovante ont été comparés avec d'autres approches négligeant la diffusion ou supposant la diffusion isotrope, à la fois sur des encapsulants spéculaires et diffusants : il s'avère que le modèle amélioré à 4-flux est la meilleure approche pour reproduire avec précision les données expérimentales et obtenir des valeurs raisonnables de l'indice optique.

De plus, notre analyse a montré que les flux doivent être anisotropes : la diffusion se fait principalement vers l'avant, le flux total reste globalement très spéculaire.

Le modèle à 4-flux proposé permet de calculer précisément l'absorption et la rétrodiffusion qui auront lieu dans l'encapsulant d'un module, et les pertes associées sur le courant photo-généré pondéré par l'EQE et le spectre AM1.5. Cette étude conclut à l'existence d'un nouveau poste de perte lors de l'encapsulation de cellules avec un polymère diffusant, non pas due à l'absorption ou à la réfraction, mais à la rétrodiffusion. À notre connaissance, cette perte par rétrodiffusion n'a jamais été mentionnée dans les analyses CTM jusqu'à présent. A titre d'exemple, les résultats sur deux encapsulants TPO de 600 µm d'épaisseur (l'un à haut seuil de coupure UV et l'autre à bas seuil de coupure UV) montrent une perte par rétrodiffusion de 0,75 % en moyenne, et une perte sur l'I_{sc} par absorption de 1,67 % pour le bas seuil de coupure UV contre 3,81 % pour le haut seuil de coupure UV, soit une différence de plus de 2 %.

Les TPOs caractérisés sont donc beaucoup plus absorbants que l'EVA, et génèrent en plus de la rétrodiffusion. Les études futures devraient se concentrer sur la caractérisation de différents types d'encapsulant (EVA, POE, Ionomer, etc.) afin de caractériser le comportement diffusif, l'impact sur l'extraction des constantes optiques et donc sur les performances du module de ces matériaux. Il serait également intéressant d'analyser le comportement du modèle d'extraction en utilisant des échantillons d'épaisseurs très différentes. Pour chaque matériau utilisé, ajouter un échantillon de très faible épaisseur (quelques dizaines de microns), et un échantillon d'épaisseur beaucoup plus importante (plusieurs millimètres). Une faible épaisseur permettrait d'augmenter la précision de l'extraction pour les longueurs d'onde où l'absorption est importante. Une épaisseur importante permettrait de gagner en précision sur l'extraction des coefficients de diffusion.

Perspectives d'amélioration du modèle CTMOD

Plusieurs points d'amélioration sont encore à considérer. Le modèle pourrait évidemment être amélioré sur sa partie optique. Le principal défaut est de prendre en compte les interactions multiples a posteriori, via des facteurs correctifs.

Un simple facteur correctif devrait permettre de prendre en compte la partie de la lumière réfléchie par l'interface d'encapsulation des cellules, qui est re-refléchie à l'interface verre-air et peut donc participer à la photo-génération.

Nous pensons que cette amélioration permettrait d'éviter la différence de 0,8% constatée en comparant Sunsolve et CTMod. Ensuite, une limitation majeure du modèle est qu'il n'est valable que pour une incidence normale. Pour envisager une prédiction de la performance à n'importe quel angle, une méthode de lancer de rayon ou de matrice de transfert semble nécessaire.

L'un des avantages des modèles analytiques comme CTMod est sa vitesse d'exécution. Il permet par exemple de calculer en quelques dizaines de minutes des centaines de milliers de configurations différentes de modules sur un ordinateur de bureau standard. Il permet également de réaliser des analyses de sensibilité aux paramètres d'entrée, et donc d'analyser la propagation des incertitudes sur ces paramètres d'entrée. De telles analyses nécessitent un temps beaucoup plus long avec les modèles de lancer de rayons. Une approche matricielle, telle qu'OPTOS, pourrait donc offrir un bon compromis entre précision et rapidité, si elle est

améliorée pour tenir compte de l'impact optique de la métallisation et de l'interconnexion des cellules.

Le modèle a été principalement utilisé dans des conditions d'irradiation et de température standard (STC) : incidence normale, spectre AM1.5g, et 25°C pour le module et les cellules. La prise en compte de la température a été mentionnée dans CTMod : elle est basée sur les coefficients de température de la cellule. Il pourrait être envisagé de développer un modèle de résistance thermique équivalente pour aborder rapidement la question de la distribution de la température dans le module placé dans un environnement quelconque. L'inclusion des effets électriques des boîtes de jonction et des diodes de dérivation pourrait être une autre amélioration souhaitable.

Nous avons donc caractérisé avec précision deux nouveaux éléments de perte pour les modules HJT. Cependant, la comparaison des résultats finaux du modèle (paramètres ou courbe IV) avec les valeurs expérimentales sur un simulateur solaire est encore incomplète, comme le montre la tentative de modélisation du module record de 120 demi-cellules. Les travaux futurs devraient certainement se concentrer sur une caractérisation approfondie des incertitudes sur les paramètres d'entrée du modèle, afin d'obtenir l'influence de ces incertitudes sur les résultats IV de CTMod. La comparaison de ces valeurs numériques avec les résultats IV des simulateurs solaires, évidemment associés à leurs incertitudes expérimentales, est maintenant essentielle. En ce sens, des études préliminaires ont été lancées en 2020, mais avortées en raison de la crise pandémique. Il sera hautement souhaitable de les poursuivre.

Bibliography

[1] S. Díaz *et al.*, "Summary for policymakers of the global assessment report on biodiversity and ecosystem services of the Intergovernmental Science-Policy Platform on Biodiversity and Ecosystem Services," p. 45.

[2] J. Fourier, *Remarques Generales sur les Temperatures Du Globe Terrestre et des Espaces Planetaires*. 1824.

[3] J. Tyndall, *Heat, considered as a mode of motion; from the second London ed., rev., with additions embracing the author's latest researches*. New York, Appleton, 1873.

[4] S. Arrhenius, "On the Influence of Carbonic Acid in the Air upon the Temperature of the Earth," *Publications of the Astronomical Society of the Pacific*, vol. 9, p. 14, Feb. 1897, doi: 10.1086/121158.

[5] D. Lin *et al.*, "Ecological Footprint Accounting for Countries: Updates and Results of the National Footprint Accounts, 2012–2018," *Resources*, vol. 7, no. 3, Art. no. 3, Sep. 2018, doi: 10.3390/resources7030058.

[6] W. Steffen, W. Broadgate, L. Deutsch, O. Gaffney, and C. Ludwig, "The Trajectory of the Anthropocene: The Great Acceleration," *The Anthropocene Review*, Mar. 2015, doi: 10.1177/2053019614564785.

[7] W. Steffen *et al.*, "Planetary boundaries: Guiding human development on a changing planet," *Science*, vol. 347, no. 6223, Feb. 2015, doi: 10.1126/science.1259855.

[8] D. H. Meadows, D. L. Meadows, and J. Randers, "The limits to growth."

[9] R. K. Pachauri, L. Mayer, and Intergovernmental Panel on Climate Change, Eds., *Climate change 2014: synthesis report*. Geneva, Switzerland: Intergovernmental Panel on Climate Change, 2015.

[10] G. H. Brundtland, M. Khalid, S. Agnelli, S. Al-Athel, and B. Chidzero, "Our common future," *New York*, p. 8, 1987.

[11] G. Turner, *Is Global Collapse Imminent? An Updated Comparison of The Limits to Growth with Historical Data*. 2014.

[12] J. D. Ward, P. C. Sutton, A. D. Werner, R. Costanza, S. H. Mohr, and C. T. Simmons, "Is Decoupling GDP Growth from Environmental Impact Possible?," *PLOS ONE*, vol. 11, no. 10, p. e0164733, Oct. 2016, doi: 10.1371/journal.pone.0164733.

[13] J. Ellul, *La Technique ou l'Enjeu du siècle*. Paris, France: Armand Colin, 1954.

[14] S. Latouche, *La mégamachine. Raison techno-scientifique, raison économique et mythe du progrès. Essais à la mémoire de Jacques Ellul*. La Découverte, 1995.

[15] H. Ferreboeuf, "Pour une sobriété numérique," *Futuribles*, vol. N° 429, no. 2, p. 15, 2019, doi: 10.3917/futur.429.0015.

[16] P. Bihouix, *L'Âge des low tech. Vers une civilisation techniquement soutenable*. Le Seuil, 2014.

[17] R. P. Feynman, R. B. Leighton, and M. Sands, "The feynman lectures on physics; vol. i," *American Journal of Physics*, vol. 33, no. 9, pp. 750–752, 1965.

[18] J. G. Lambert, C. A. S. Hall, S. Balogh, A. Gupta, and M. Arnold, "Energy, EROI and quality of life," *Energy Policy*, vol. 64, pp. 153–167, Jan. 2014, doi: 10.1016/j.enpol.2013.07.001.

[19] International Energy Agency, Ed., "World Energy Outlook 2019," *World Energy Outlook*, p. 11, 2019.

[20] VDMA, “International Technology RoadMap for Photovoltaic (ITRPV),” Tenth Edition, Mar. 2019.
[21] Inernational Renewable Energy Agency, “Renewable power generation costs in 2019,” p. 144, 2020.
[22] “p–n junction,” *Wikipedia*. Dec. 22, 2020, Accessed: Jan. 25, 2021. [Online]. Available: https://en.wikipedia.org/w/index.php?title=P%E2%80%93n_junction&oldid=995709128.
[23] W. Shockley and W. T. Read, “Statistics of the Recombinations of Holes and Electrons,” *Phys. Rev.*, vol. 87, no. 5, pp. 835–842, Sep. 1952, doi: 10.1103/PhysRev.87.835.
[24] R. N. Hall, “Germanium rectifier characteristics,” in *Physical Review*, 1951, vol. 83, no. 1, pp. 228–228.
[25] P. Auger, “Sur les rayons β secondaires produits dans un gaz par des rayons X.,” *CR Acad. Sci.(F)*, vol. 177, p. 169, 1923.
[26] L. Meitner, “Über die entstehung der β-strahl-spektren radioaktiver substanzen,” *Zeitschrift für Physik*, vol. 9, no. 1, pp. 131–144, 1922.
[27] O. Breitenstein, J. Bauer, P. P. Altermatt, and K. Ramspeck, “Influence of Defects on Solar Cell Characteristics,” *Solid State Phenomena*, 2010. https://www.scientific.net/SSP.156-158.1 (accessed May 25, 2018).
[28] “Spectral Response | PVEducation.” https://www.pveducation.org/pvcdrom/solar-cell-operation/spectral-response (accessed Jan. 25, 2021).
[29] “Quantum Efficiency | PVEducation.” https://www.pveducation.org/pvcdrom/solar-cell-operation/quantum-efficiency (accessed Jan. 25, 2021).
[30] O. Breitenstein, “Understanding the current-voltage characteristics of industrial crystalline silicon solar cells by considering inhomogeneous current distributions,” *Opto-Electron. Rev.*, vol. 21, no. 3, pp. 259–282, Sep. 2013, doi: 10.2478/s11772-013-0095-5.
[31] “Best Research-Cell Efficiency Chart.” https://www.nrel.gov/pv/cell-efficiency.html (accessed Jan. 26, 2021).
[32] C. Roux, A. Danel, W. Favre, J. Hotel, J. Dahan, and R. Varache, “Mastering the Defectivity: Prerequisite for High Efficiency Silicon Heterojunction Solar Cells,” *37th European Photovoltaic Solar Energy Conference and Exhibition*, pp. 252–255, Oct. 2020, doi: 10.4229/EUPVSEC20202020-2CO.13.5.
[33] C. Gueymard, “Simple Model for the Atmospheric Radiative Transfer of Sunshine (SMARTS2) Algorithms and performance assessment,” p. 84.
[34] “Wafer ray tracer.” https://www2.pvlighthouse.com.au/calculators/wafer%20ray%20tracer/wafer%20ray%20tracer.html (accessed Dec. 23, 2020).
[35] V. Magnin, J. Harari, M. Halbwax, S. Bastide, D. Cherfi, and J.-P. Vilcot, “Angle-dependent ray tracing simulations of reflections on pyramidal textures for silicon solar cells,” *Solar Energy*, vol. 110, pp. 378–385, Dec. 2014, doi: 10.1016/j.solener.2014.09.025.
[36] T. H. Fung *et al.*, “Improved Ray Tracing on Random Pyramid Texture via Application of Phong Scattering,” *IEEE Journal of Photovoltaics*, vol. 9, no. 3, pp. 591–600, May 2019, doi: 10.1109/JPHOTOV.2019.2894688.
[37] A. Schneider, R. Harney, and S. Koch, “Impact of Cell Texturing Quality on Cell to Module Losses,” *Energy Procedia*, vol. 77, pp. 414–419, Aug. 2015, doi: 10.1016/j.egypro.2015.07.058.
[38] Y. Du, W. Tao, Y. Liu, Z. Le, and M. Zhang, “Cell-to-Module Variation of Optical and Photovoltaic Properties for Monocrystalline Silicon Solar Cells with Different Texturing

Approaches," *ECS J. Solid State Sci. Technol.*, vol. 6, no. 5, pp. P332–P338, Jan. 2017, doi: 10.1149/2.0341705jss.
[39] I. Haedrich *et al.*, "How cell textures impact angular cell-to-module ratios and the annual yield of crystalline solar modules," *Solar Energy Materials and Solar Cells*, vol. 183, pp. 181–192, Aug. 2018, doi: 10.1016/j.solmat.2018.04.006.
[40] L. Basset, W. Favre, D. Muñoz, and J.-P. Vilcot, "Series Resistance Breakdown of Silicon Heterojunction Solar Cells Produced on CEA-INES Pilot Line," *35th European Photovoltaic Solar Energy Conference and Exhibition*, pp. 721–724, Nov. 2018, doi: 10.4229/35thEUPVSEC20182018-2DV.3.21.
[41] M. Wolf and H. Rauschenbach, "Series resistance effects on solar cell measurements," *Advanced Energy Conversion*, vol. 3, no. 2, pp. 455–479, Apr. 1963, doi: 10.1016/0365-1789(63)90063-8.
[42] C. Berthod, R. Strandberg, G. H. Yordanov, H. G. Beyer, and J. O. Odden, "On the Variability of the Temperature Coefficients of mc-Si Solar Cells with Irradiance," *Energy Procedia*, vol. 92, pp. 2–9, Aug. 2016, doi: 10.1016/j.egypro.2016.07.002.
[43] O. Dupré, R. Vaillon, and M. A. Green, "Temperature Coefficients of Photovoltaic Devices," in *Thermal Behavior of Photovoltaic Devices*, Cham: Springer International Publishing, 2017, pp. 29–74.
[44] A. W. Blakers, "Shading losses of solar-cell metal grids," *Journal of Applied Physics*, vol. 71, no. 10, pp. 5237–5241, May 1992, doi: 10.1063/1.350580.
[45] M. F. Stuckings and A. W. Blakers, "A study of shading and resistive loss from the fingers of encapsulated solar cells," *Solar Energy Materials and Solar Cells*, vol. 59, no. 3, pp. 233–242, Oct. 1999, doi: 10.1016/S0927-0248(99)00024-0.
[46] S. W. Glunz, M. Hoerteis, and R. Woehl, "Determination of the Effective Optical Width of Screen-Printed and Aerosol-Printed and Plated Fingers," *23rd European Photovoltaic Solar Energy Conference and Exhibition, 1-5 September 2008, Valencia, Spain*, pp. 1377–1382, Nov. 2008, doi: 10.4229/23rdEUPVSEC2008-2CV.4.16.
[47] J. Levrat *et al.*, "High-performance hetero-junction crystalline silicon photovoltaic technology," in *2014 IEEE 40th Photovoltaic Specialist Conference (PVSC)*, Jun. 2014, pp. 1218–1222, doi: 10.1109/PVSC.2014.6925134.
[48] M. Galiazzo, M. Bertazzo, M. Martire, M. Zamuner, E. Bortoletto, and A. Voltan, "Double Printing Feasibility of 35um Printed Ag Finger Width," *29th European Photovoltaic Solar Energy Conference and Exhibition*, pp. 1387–1391, Nov. 2014, doi: 10.4229/EUPVSEC20142014-2CV.4.40.
[49] C. Rodríguez *et al.*, "Analysis And Performance Of Dispensed And Screen Printed Front Side Contacts At Cell And Module Level," 2015, p. 8.
[50] R. Witteck *et al.*, "Optimizing the Solar Cell Front Side Metallization and the Cell Interconnection for High Module Power Output," *Energy Procedia*, vol. 92, pp. 531–539, Aug. 2016, doi: 10.1016/j.egypro.2016.07.137.
[51] R. Witteck *et al.*, "Optimized Interconnection of Passivated Emitter and Rear Cells by Experimentally Verified Modeling," *IEEE Journal of Photovoltaics*, vol. 6, no. 2, pp. 432–439, Mar. 2016, doi: 10.1109/JPHOTOV.2016.2514706.
[52] M. Pospischil *et al.*, "Optimizing Fine Line Dispensed Contact Grids," *Energy Procedia*, vol. 55, pp. 693–701, 2014, doi: 10.1016/j.egypro.2014.08.046.
[53] T. Geipel, D. Eberlein, and A. Kraft, "Lead-free solders for ribbon interconnection of crystalline silicon PERC solar cells with infrared soldering," Perak, Malaysia, 2019, p. 020015, doi: 10.1063/1.5125880.

[54] M. Mittag, T. Zech, M. Wiese, D. Blasi, M. Ebert, and H. Wirth, “Cell-to-Module (CTM) Analysis for Photovoltaic Modules with Shingled Solar Cells,” in *2017 IEEE 44th Photovoltaic Specialist Conference (PVSC)*, Washington, DC, Jun. 2017, pp. 1531–1536, doi: 10.1109/PVSC.2017.8366260.
[55] G. C. Glaeser, L. Hamann, and L. Proenneke, “Structured Ribbons For Short Circuit Current Gain In Modules,” p. 3, 2010.
[56] J. Schneider, M. Turek, M. Dyrba, I. Baumann, B. Koll, and T. Booz, “Combined effect of light harvesting strings, anti-reflective coating, thin glass, and high ultraviolet transmission encapsulant to reduce optical losses in solar modules: Optical loss reduction by combining innovative solar module technologies,” *Progress in Photovoltaics: Research and Applications*, vol. 22, no. 7, pp. 830–837, Jul. 2014, doi: 10.1002/pip.2470.
[57] H. Holst *et al.*, “Increased Light Harvesting by Structured Cell Interconnection Ribbons: An Optical Ray Tracing Study Using a Realistic Daylight Model,” *Energy Procedia*, vol. 92, pp. 505–514, Aug. 2016, doi: 10.1016/j.egypro.2016.07.134.
[58] W. Muehleisen *et al.*, “Comparison of output power for solar cells with standard and structured ribbons,” *EPJ Photovoltaics*, vol. 7, p. 70701, 2016, doi: 10.1051/epjpv/2016003.
[59] S. Braun, G. Micard, and G. Hahn, “Solar Cell Improvement by using a Multi Busbar Design as Front Electrode,” *Energy Procedia*, vol. 27, pp. 227–233, Jan. 2012, doi: 10.1016/j.egypro.2012.07.056.
[60] T. Söderström, J. Ufheil, and P. Papet, “Smart Wire Connection Technology,” *28th European Photovoltaic Solar Energy Conference and Exhibition*, pp. 495–499, Nov. 2013, doi: 10.4229/28thEUPVSEC2013-1CV.2.17.
[61] K. R. McIntosh, M. D. Abbott, M. B. Edwards, R. Evans, and Y. Yao, “Optical Evaluation of Multi-Wire Modules,” *32nd European Photovoltaic Solar Energy Conference and Exhibition*, pp. 15–19, Jul. 2016, doi: 10.4229/EUPVSEC20162016-1AO.2.1.
[62] R. Witteck, “Analysis of cell to module losses and UV radiation hardness for passivated emitter and rear cells and modules,” doctoralThesis, München : Verlag Dr. Hut, 2019.
[63] B. Commault *et al.*, “Module Integration Of SHJ Cells By Soldering,” *36th European Photovoltaic Solar Energy Conference and Exhibition*, p. 20, 2020.
[64] I. Haedrich, U. Eitner, M. Wiese, and H. Wirth, “Unified methodology for determining CTM ratios: Systematic prediction of module power,” *Solar Energy Materials and Solar Cells*, vol. 131, pp. 14–23, Dec. 2014, doi: 10.1016/j.solmat.2014.06.025.
[65] S. Ponce-Alcántara, A. V. Arangú, and G. S. Plaza, “The importance of optical characterization of PV backsheets in improving solar module power,” in *Proceedings of the 8th International Photovoltaic Power Generation Conference Exhibition, Shanghai, China*, 2014, vol. 20.
[66] A. Pfreundt, M. Mittag, M. Heinrich, and U. Eitner, “Rapid Calculation of the Backsheet Coupling Gain Using Ray Groups,” p. 7.
[67] O. Dupré, J. Levrat, J. Champliaud, M. Despeisse, M. Boccard, and C. Ballif, “Reassessment of cell to module gains and losses: Accounting for the current boost specific to cells located on the edges,” in *AIP Conference Proceedings*, 2018, vol. 1999, no. 1, p. 090001.
[68] L. Basset, “Contact Electrodes for Heterojunction Silicon Solar Cells: Evaluation and Optimization of the Electron Contact,” 2020.
[69] H. Hanifi, D. Dassler, J. Schneider, M. Turek, S. Schindler, and J. Bagdahn, “Optimized Tab Width in Half-cell Modules,” *Energy Procedia*, vol. 92, pp. 52–59, Aug. 2016, doi: 10.1016/j.egypro.2016.07.009.

[70] H. Hanifi, C. Pfau, M. Turek, and J. Schneider, “A practical optical and electrical model to estimate the power losses and quantification of different heat sources in silicon based PV modules,” *Renewable Energy*, vol. 127, pp. 602–612, Nov. 2018, doi: 10.1016/j.renene.2018.04.060.
[71] C. Kittel, P. McEuen, and P. McEuen, *Introduction to solid state physics*, vol. 8. Wiley New York, 1996.
[72] C. Schinke *et al.*, “Uncertainty analysis for the coefficient of band-to-band absorption of crystalline silicon,” *AIP Advances*, vol. 5, no. 6, p. 067168, Jun. 2015, doi: 10.1063/1.4923379.
[73] M. A. Green and M. J. Keevers, “Optical properties of intrinsic silicon at 300 K,” *Progress in Photovoltaics: Research and Applications*, vol. 3, no. 3, pp. 189–192, 1995, doi: https://doi.org/10.1002/pip.4670030303.
[74] J. Wagner and J. A. del Alamo, “Band-gap narrowing in heavily doped silicon: A comparison of optical and electrical data,” *Journal of Applied Physics*, vol. 63, no. 2, pp. 425–429, Jan. 1988, doi: 10.1063/1.340257.
[75] W. Shockley and H. J. Queisser, “Detailed balance limit of efficiency of p-n junction solar cells,” *Journal of applied physics*, vol. 32, no. 3, pp. 510–519, 1961.
[76] L. C. Hirst and N. J. Ekins-Daukes, “Fundamental losses in solar cells,” *Progress in Photovoltaics: Research and Applications*, vol. 19, no. 3, pp. 286–293, 2011, doi: https://doi.org/10.1002/pip.1024.
[77] “Solar path calculator.” https://www2.pvlighthouse.com.au/calculators/solar%20path%20calculator/solar%20path%20calculator.aspx (accessed Jan. 20, 2021).
[78] “SPosi.” https://www.pvlighthouse.com.au/cms/simulation-programs/sposi (accessed Jan. 20, 2021).
[79] “SMARTS.” https://www.pvlighthouse.com.au/cms/simulation-programs/smarts (accessed Jan. 20, 2021).
[80] “Solar spectrum calculator.” https://www2.pvlighthouse.com.au/calculators/solar%20spectrum%20calculator/solar%20spectrum%20calculator.aspx (accessed Jan. 20, 2021).
[81] “SunCalculator.” https://www.pvlighthouse.com.au/cms/simulation-programs/sun-calculator (accessed Jan. 20, 2021).
[82] “Tracey.” https://www.pvlighthouse.com.au/cms/simulation-programs/tracey (accessed Jan. 21, 2021).
[83] K. R. McIntosh, J. N. Cotsell, J. S. Cumpston, A. W. Norris, N. E. Powell, and B. M. Ketola, “An optical comparison of silicone and EVA encapsulants for conventional silicon PV modules: A ray-tracing study,” in *2009 34th IEEE Photovoltaic Specialists Conference (PVSC)*, Jun. 2009, pp. 000544–000549, doi: 10.1109/PVSC.2009.5411624.
[84] K. R. McIntosh, J. N. Cotsell, A. W. Norris, N. E. Powell, and B. M. Ketola, “An optical comparison of silicone and EVA encapsulants under various spectra,” in *2010 35th IEEE Photovoltaic Specialists Conference*, 2010, pp. 000269–000274.
[85] ISFH, *Daidalos*. .
[86] H. Holst, P. P. Altermatt, and R. Brendel, “Daidalos – A Plugin Based Framework For Extendable Ray Tracing,” 2010, p. 4.
[87] M. Winter, M. R. Vogt, H. Holst, and P. P. Altermatt, “Combining structures on different length scales in ray tracing: analysis of optical losses in solar cell modules,” *Opt Quant Electron*, vol. 47, no. 6, pp. 1373–1379, Jun. 2015, doi: 10.1007/s11082-014-0078-x.

[88] H. Holst *et al.*, “Application of a New Ray Tracing Framework to the Analysis of Extended Regions in Si Solar Cell Modules,” *Energy Procedia*, vol. 38, no. Supplement C, pp. 86–93, Jan. 2013, doi: 10.1016/j.egypro.2013.07.253.
[89] M. R. Vogt *et al.*, “Ray Tracing of Complete Solar Cell Modules,” in *OSA Advanced Photonics Congress (AP) 2019 (IPR, Networks, NOMA, SPPCom, PVLED)*, 2019, p. PW2C.1, doi: 10.1364/PVLED.2019.PW2C.1.
[90] M. R. Vogt *et al.*, “Reduced Module Operating Temperature and Increased Yield of Modules With PERC Instead of Al-BSF Solar Cells,” *IEEE Journal of Photovoltaics*, vol. 7, no. 1, pp. 44–50, Jan. 2017, doi: 10.1109/JPHOTOV.2016.2616191.
[91] M. R. Vogt, H. Holst, M. Winter, R. Brendel, and P. P. Altermatt, “Numerical Modeling of c-Si PV Modules by Coupling the Semiconductor with the Thermal Conduction, Convection and Radiation Equations,” *Energy Procedia*, vol. 77, no. Supplement C, pp. 215–224, Aug. 2015, doi: 10.1016/j.egypro.2015.07.030.
[92] R. Witteck *et al.*, “UV-induced degradation of PERC solar modules with UV-transparent encapsulation materials,” *Progress in Photovoltaics: Research and Applications*, vol. 25, no. 6, pp. 409–416, 2017, doi: https://doi.org/10.1002/pip.2861.
[93] M. R. Vogt *et al.*, “Boosting pv module efficiency beyond the efficiency of its solar cells – a raytracing study with daidalos now available to the scientific community,” p. 7.
[94] M. Ernst, H. Holst, M. Winter, and P. P. Altermatt, “SunCalculator: A program to calculate the angular and spectral distribution of direct and diffuse solar radiation,” *Solar Energy Materials and Solar Cells*, vol. 157, pp. 913–922, Dec. 2016, doi: 10.1016/j.solmat.2016.08.008.
[95] “SunSolve.” https://www.pvlighthouse.com.au/sunsolve (accessed Jan. 21, 2021).
[96] “Publications sunsolve.” https://www.pvlighthouse.com.au/cms/publications/sunsolve (accessed Jan. 21, 2021).
[97] “OPTOS – Determination of Reflection and Absorption of Solar Cells with Surfaces Textured on Both Sides - Fraunhofer ISE,” *Fraunhofer Institute for Solar Energy Systems ISE*. https://www.ise.fraunhofer.de/en/research-projects/optos.html (accessed Jan. 21, 2021).
[98] N. Tucher *et al.*, “Optical simulation of photovoltaic modules with multiple textured interfaces using the matrix-based formalism OPTOS,” *Opt. Express, OE*, vol. 24, no. 14, pp. A1083–A1093, Jul. 2016, doi: 10.1364/OE.24.0A1083.
[99] N. Tucher *et al.*, “Optical performance of the honeycomb texture – a cell and module level analysis using the OPTOS formalism,” *Solar Energy Materials and Solar Cells*, vol. 173, Jul. 2017, doi: 10.1016/j.solmat.2017.06.004.
[100] N. Tucher *et al.*, “3D optical simulation formalism OPTOS for textured silicon solar cells,” *Opt. Express, OE*, vol. 23, no. 24, pp. A1720–A1734, Nov. 2015, doi: 10.1364/OE.23.0A1720.
[101] J. Eisenlohr *et al.*, “Matrix formalism for light propagation and absorption in thick textured optical sheets,” *Optics Express*, vol. 23, Jun. 2015, doi: 10.1364/OE.23.00A502.
[102] O. Höhn, N. Tucher, and B. Bläsi, “Theoretical study of pyramid sizes and scattering effects in silicon photovoltaic module stacks,” *Optics Express*, vol. 26, p. A320, Mar. 2018, doi: 10.1364/OE.26.00A320.
[103] Y. Chen, O. Höhn, N. Tucher, M.-E. Pistol, and N. Anttu, “Optical analysis of a III-V-nanowire-array-on-Si dual junction solar cell,” *Optics Express*, vol. 25, p. A665, Aug. 2017, doi: 10.1364/OE.25.00A665.

[104] "(PDF) Energy yield analysis of textured perovskite silicon tandem solar cells and modules," *ResearchGate*. https://www.researchgate.net/publication/335760858_Energy_yield_analysis_of_textured_perovskite_silicon_tandem_solar_cells_and_modules (accessed Jan. 21, 2021).
[105] N. Reiners and U. Blieske, "SMARTI - An Open Source Matlab Ray Tracing Tool for Solar Cell and Module Optics," in *2018 7th International Energy and Sustainability Conference (IESC)*, May 2018, pp. 1–6, doi: 10.1109/IESC.2018.8440001.
[106] J. E. Cotter, "RaySim 6.0: a free geometrical ray tracing program for silicon solar cells," in *Conference Record of the Thirty-first IEEE Photovoltaic Specialists Conference, 2005.*, Jan. 2005, pp. 1165–1168, doi: 10.1109/PVSC.2005.1488345.
[107] "Powerful Cell-To-Module Analysis." // (accessed Jan. 21, 2021).
[108] T. Zech, A. J. Beinert, P. Romer, S. Hoffmann, C. Kutter, and M. Mittag, "Electrical and Thermal Modeling of Junction Boxes," *33rd European Photovoltaic Solar Energy Conference and Exhibition*, pp. 1501–1506, Nov. 2017, doi: 10.4229/EUPVSEC20172017-5DO.5.5.
[109] M. Mittag, "Techno-Economic Analysis of Half Cell Modules - the Impact of Half Cells on Module Power and Costs," p. 8, 2019.
[110] M. Heinrich, M. Mittag, and J. Shahid, "A Multidimensional Optimization Approach to Improve Module Efficiency, Power and Costs," *35th European Photovoltaic Solar Energy Conference and Exhibition*, pp. 1106–1112, Nov. 2018, doi: 10.4229/35thEUPVSEC20182018-5DO.8.3.
[111] M. Mittag and M. Ebert, "Systematic PV-module optimization with the cell-to-module (CTM) analysis software," *Solar Cells*, vol. 4, no. 2, p. 585, 2014.
[112] "Sentaurus Device - Technology Computer Aided Design (TCAD) | Synopsys." https://www.synopsys.com/silicon/tcad/device-simulation/sentaurus-device.html (accessed Jan. 21, 2021).
[113] "Silvaco." https://www.pvlighthouse.com.au/cms/simulation-programs/atlas (accessed Jan. 21, 2021).
[114] "Quokka 3." http://quokka3.com/Features.html (accessed Jan. 21, 2021).
[115] P. A. Basore, "Multidimensional Fourier-Series Solution of the Quasi-Neutral Drift–Diffusion Equations," *IEEE Journal of Photovoltaics*, vol. 10, no. 3, pp. 905–911, May 2020, doi: 10.1109/JPHOTOV.2020.2966831.
[116] "Simulation Software for Upscaling to Large-Area OLEDs and Solar Cells," *Fluxim*. https://www.fluxim.com/laoss (accessed Jan. 21, 2021).
[117] "PC1D," *SourceForge*. https://sourceforge.net/projects/pc1d/ (accessed Jan. 21, 2021).
[118] M. Burgelman, P. Nollet, and S. Degrave, "Modelling polycrystalline semiconductor solar cells," *Thin solid films*, vol. 361, pp. 527–532, 2000.
[119] J. Gray, X. Wang, R. V. K. Chavali, X. Sun, A. Kanti, and J. R. Wilcox, "ADEPT 2.1," 2011.
[120] R. Varache, C. Leendertz, M. E. Gueunier-Farret, J. Haschke, D. Muñoz, and L. Korte, "Investigation of selective junctions using a newly developed tunnel current model for solar cell applications," *Solar Energy Materials and Solar Cells*, vol. 141, pp. 14–23, 2015.
[121] J.-M. Wagner, A. Schütt, J. Carstensen, and R. Adelung, "Linear-response Description of the Series Resistance of Large-area Silicon Solar Cells: Resolving the Difference between Dark and Illuminated Behavior," *Energy Procedia*, vol. 92, pp. 255–264, Aug. 2016, doi: 10.1016/j.egypro.2016.07.072.

[122] J.-M. Wagner, S. Rißland, A. Schütt, J. Carstensen, and R. Adelung, “Distributed series resistance in a one-dimensional two-diode model revisited,” *Energy Procedia*, vol. 124, pp. 197–206, Sep. 2017, doi: 10.1016/j.egypro.2017.09.313.

[123] J.-M. Wagner, M. Hoppe, A. Schütt, J. Carstensen, and H. Föll, “Injection-level Dependent Series Resistance: Comparison of CELLO and Photoluminescence-based Measurements,” *Energy Procedia*, vol. 38, pp. 199–208, Jan. 2013, doi: 10.1016/j.egypro.2013.07.268.

[124] J. Wong, “Griddler: Intelligent computer aided design of complex solar cell metallization patterns,” in *2013 IEEE 39th Photovoltaic Specialists Conference (PVSC)*, Jun. 2013, pp. 0933–0938, doi: 10.1109/PVSC.2013.6744296.

[125] “Griddler Solar,” *Griddler Solar*. http://griddlersolar.com/ (accessed Jan. 22, 2021).

[126] D. Pysch, A. Mette, and S. W. Glunz, “A review and comparison of different methods to determine the series resistance of solar cells,” *Solar Energy Materials and Solar Cells*, vol. 91, no. 18, pp. 1698–1706, Nov. 2007, doi: 10.1016/j.solmat.2007.05.026.

[127] M. R. Vogt *et al.*, “Optical Constants of UV Transparent EVA and the Impact on the PV Module Output Power under Realistic Irradiation,” *Energy Procedia*, vol. 92, no. Supplement C, pp. 523–530, Aug. 2016, doi: 10.1016/j.egypro.2016.07.136.

[128] M. R. Vogt *et al.*, “Measurement of the Optical Constants of Soda-Lime Glasses in Dependence of Iron Content and Modeling of Iron-Related Power Losses in Crystalline Si Solar Cell Modules,” *IEEE Journal of Photovoltaics*, vol. 6, no. 1, pp. 111–118, Jan. 2016, doi: 10.1109/JPHOTOV.2015.2498043.

[129] H. Hanifi, J. Schneider, and J. Bagdahn, “Reduced Shading Effect On Half-Cell Modules – Measurement And Simulation,” *31st European Photovoltaic Solar Energy Conference and Exhibition*, p. 6.

[130] S. Guo *et al.*, “Investigation of the short-circuit current increase for PV modules using halved silicon wafer solar cells,” *Solar Energy Materials and Solar Cells*, vol. 133, pp. 240–247, Feb. 2015, doi: 10.1016/j.solmat.2014.11.012.

[131] H. Hanifi, D. Dassler, M. Turek, and J. Schneider, “Evaluation and Comparison of PV Modules With Different Designs of Partial Cells in Desert and Moderate Climates,” *IEEE Journal of Photovoltaics*, vol. 8, no. 5, pp. 1266–1273, Sep. 2018, doi: 10.1109/JPHOTOV.2018.2841515.

[132] F. Kaule, M. Pander, M. Turek, M. Grimm, E. Hofmueller, and S. Schoenfelder, “Mechanical damage of half-cell cutting technologies in solar cells and module laminates,” *AIP Conference Proceedings*, vol. 1999, no. 1, p. 020013, Aug. 2018, doi: 10.1063/1.5049252.

[133] M. Chiodetti, J. Dupuis, D. Boublil, K. Radouane, and P. Dupeyrat, “Half-Cell Module Behaviour And Its Impact On The Yield Of A PV Plant,” Sep. 2019, doi: 10.4229/EUPVSEC20192019-5DO.3.3.

[134] S. Guo, J. P. Singh, I. M. Peters, A. G. Aberle, and T. M. Walsh, “A Quantitative Analysis of Photovoltaic Modules Using Halved Cells,” *International Journal of Photoenergy*, 2013. https://www.hindawi.com/journals/ijp/2013/739374/ (accessed May 25, 2018).

[135] J. Muller *et al.*, “Resistive Power Loss Analysis of PV Modules Made From Halved 15.6 × 15.6 cm^2 Silicon PERC Solar Cells With Efficiencies up to 20.0%,” *IEEE Journal of Photovoltaics*, vol. 5, no. 1, pp. 189–194, Jan. 2015, doi: 10.1109/JPHOTOV.2014.2367868.

[136] S. Malik, D. Dassler, J. Fröbel, J. Schneider, and M. Ebert, “Outdoor Data Evaluation Of Half- / Full-Cell Modules With Regard To Measurement Uncertainties And The

Application Of Statistical Methods," *29th European Photovoltaic Solar Energy Conference and Exhibition*, p. 5.

[137] T. Tang, C. Gan, Z. Hu, H. Niu, J. Si, and X. Luo, "A Quantitative Comparison Between Double Glass Photovoltaic Modules Using Half-Size Cells and Quarter-Size Cells," *IEEE Journal of Photovoltaics*, vol. 7, no. 5, pp. 1298–1303, Sep. 2017, doi: 10.1109/JPHOTOV.2017.2730358.

[138] H.-X. Zhang, H. Zhuang, X.-F. Gou, Q.-S. Huang, L.-K. Jiang, and Z.-Y. Chen, "Study on the Benefit of Half-Cut Cells towards Higher Cell-to-Module Power Ratio," *DEStech Transactions on Environment, Energy and Earth Sciences*, vol. 0, no. epee, Art. no. epee, 2017, doi: 10.12783/dteees/epee2017/18123.

[139] C. H. Henry, R. A. Logan, and F. R. Merritt, "The effect of surface recombination on current in AlxGa1−xAs heterojunctions," *Journal of Applied Physics*, vol. 49, no. 6, pp. 3530–3542, Jun. 1978, doi: 10.1063/1.325265.

[140] A. G. Aberle *et al.*, "Limiting loss mechanisms in 23% efficient silicon solar cells," *Journal of Applied Physics*, vol. 77, no. 7, pp. 3491–3504, Apr. 1995, doi: 10.1063/1.358643.

[141] P. P. Altermatt, G. Heiser, and M. A. Green, "Numerical quantification and minimization of perimeter losses in high-efficiency silicon solar cells," *Progress in Photovoltaics: Research and Applications*, vol. 4, no. 5, pp. 355–367, 1996, doi: https://doi.org/10.1002/(SICI)1099-159X(199609/10)4:5<355::AID-PIP145>3.0.CO;2-X.

[142] R. Kuhn, P. Fath, and E. Bucher, "Effects of pn-junctions bordering on surfaces investigated by means of 2D-modeling," in *Conference Record of the Twenty-Eighth IEEE Photovoltaic Specialists Conference - 2000 (Cat. No.00CH37036)*, Sep. 2000, pp. 116–119, doi: 10.1109/PVSC.2000.915768.

[143] O. Breitenstein, M. Langenkamp, O. Lang, and A. Schirrmacher, "Shunts due to laser scribing of solar cells evaluated by highly sensitive lock-in thermography," *Solar Energy Materials and Solar Cells*, vol. 65, no. 1, pp. 55–62, Jan. 2001, doi: 10.1016/S0927-0248(00)00077-5.

[144] K. McIntosh, "Lumps, Humps and Bumps: Three Detrimental Effects in the Current–Voltage Curve of Silicon Solar Cells," 2001.

[145] K. R. McIntosh and C. B. Honsberg, "The Influence Of Edge Recombination On A Solar Cell's IV Curve," p. 5.

[146] S. W. Glunz *et al.*, "High-efficiency silicon solar cells for low-illumination applications," in *Conference Record of the Twenty-Ninth IEEE Photovoltaic Specialists Conference, 2002.*, May 2002, pp. 450–453, doi: 10.1109/PVSC.2002.1190556.

[147] M. Hermle, J. Dicker, W. Warta, S. W. Glunz, and G. Willeke, "Analysis of edge recombination for high-efficiency solar cells at low illumination densities," in *Proceedings of 3rd World Conference onPhotovoltaic Energy Conversion, 2003*, May 2003, vol. 2, pp. 1009-1012 Vol.2.

[148] D. Kray, "Modeling, geometric optimization and isolation of the edge region in silicon solar cells," *Solar Energy Materials and Solar Cells*, vol. 94, no. 5, pp. 830–835, May 2010, doi: 10.1016/j.solmat.2009.12.033.

[149] S. Eiternick, K. Kaufmann, J. Schneider, and M. Turek, "Loss Analysis for Laser Separated Solar Cells," *Energy Procedia*, vol. 55, pp. 326–330, Jan. 2014, doi: 10.1016/j.egypro.2014.08.094.

[150] C. Chan *et al.*, "Edge isolation of solar cells using laser doping," *Solar Energy Materials and Solar Cells*, vol. 132, pp. 535–543, Jan. 2015, doi: 10.1016/j.solmat.2014.10.002.

[151] K. Rühle, M. K. Juhl, M. D. Abbott, L. M. Reindl, and M. Kasemann, “Impact of Edge Recombination in Small-Area Solar Cells with Emitter Windows,” *IEEE Journal of Photovoltaics*, vol. 5, no. 4, pp. 1067–1073, Jul. 2015, doi: 10.1109/JPHOTOV.2015.2434597.

[152] S. Eiternick *et al.*, “High Quality Half-cell Processing Using Thermal Laser Separation,” *Energy Procedia*, vol. 77, pp. 340–345, Aug. 2015, doi: 10.1016/j.egypro.2015.07.048.

[153] J. Wong, R. Sridharan, and V. Shanmugam, “Quantifying edge and peripheral recombination losses in industrial silicon solar cells,” *IEEE Transactions on Electron Devices*, vol. 62, no. 11, pp. 3750–3755, Nov. 2015, doi: 10.1109/TED.2015.2480089.

[154] D. Bertrand, S. Manuel, M. Pirot, A. Kaminski-Cachopo, and Y. Veschetti, “Modeling of Edge Losses in Al-BSF Silicon Solar Cells,” *IEEE Journal of Photovoltaics*, vol. 7, no. 1, pp. 78–84, Jan. 2017, doi: 10.1109/JPHOTOV.2016.2618603.

[155] A. Fell, J. Schön, M. Müller, N. Wöhrle, M. C. Schubert, and S. W. Glunz, “Modeling Edge Recombination in Silicon Solar Cells,” *IEEE Journal of Photovoltaics*, vol. 8, no. 2, pp. 428–434, Mar. 2018, doi: 10.1109/JPHOTOV.2017.2787020.

[156] X. Li, L. Yang, W. Zhang, and Q. Wang, “Study the JSC loss of full area SHJ solar cells caused by edge recombination,” *Journal of Renewable and Sustainable Energy*, vol. 11, no. 2, p. 023503, Mar. 2019, doi: 10.1063/1.5085045.

[157] H. Stolzenburg *et al.*, “Edge recombination analysis of silicon solar cells using photoluminescence measurements,” *AIP Conference Proceedings*, vol. 2147, no. 1, p. 020017, Aug. 2019, doi: 10.1063/1.5123822.

[158] J. Merten, J. M. Asensi, C. Voz, A. V. Shah, R. Platz, and J. Andreu, “Improved equivalent circuit and analytical model for amorphous silicon solar cells and modules,” *IEEE Transactions on Electron Devices*, vol. 45, no. 2, pp. 423–429, Feb. 1998, doi: 10.1109/16.658676.

[159] G. L. Araujo, A. Cuevas, and J. M. Ruiz, “The effect of distributed series resistance on the dark and illuminated current #8212;Voltage characteristics of solar cells,” *IEEE Transactions on Electron Devices*, vol. 33, no. 3, pp. 391–401, Mar. 1986, doi: 10.1109/T-ED.1986.22500.

[160] O. Breitenstein and S. Rißland, “A two-diode model regarding the distributed series resistance,” *Solar Energy Materials and Solar Cells*, vol. 110, pp. 77–86, Mar. 2013, doi: 10.1016/j.solmat.2012.11.021.

[161] L. D. Nielsen, “Distributed series resistance effects in solar cells,” *IEEE Transactions on Electron Devices*, vol. 29, no. 5, pp. 821–827, May 1982, doi: 10.1109/T-ED.1982.20784.

[162] M. Turek, “Current and illumination dependent series resistance of solar cells,” *Journal of Applied Physics*, vol. 115, no. 14, p. 144503, Apr. 2014, doi: 10.1063/1.4871017.

[163] M. Stuckelberger, R. Biron, N. Wyrsch, F.-J. Haug, and C. Ballif, “Review: Progress in solar cells from hydrogenated amorphous silicon,” *Renewable and Sustainable Energy Reviews*, vol. 76, pp. 1497–1523, Sep. 2017, doi: 10.1016/j.rser.2016.11.190.

[164] Imprint, A. us, T. and Conditions, and P. and C. Policy, “24.63% Solar Cell Efficiency For Heterojunction Technology | TaiyangNews.” http://taiyangnews.info/technology/24-63-solar-cell-efficiency-for-heterojunction-technology/ (accessed Dec. 23, 2020).

[165] D. Dirnberger and U. Kraling, “Uncertainty in PV Module Measurement—Part I: Calibration of Crystalline and Thin-Film Modules,” *IEEE Journal of Photovoltaics*, vol. 3, no. 3, pp. 1016–1026, Jul. 2013, doi: 10.1109/JPHOTOV.2013.2260595.

[166] D. Dirnberger, “Uncertainty in PV Module Measurement---Part II: Verification of Rated Power and Stability Problems,” *IEEE Journal of Photovoltaics*, vol. 4, no. 3, pp. 991–1007, May 2014, doi: 10.1109/JPHOTOV.2014.2307158.

[167] D. Dirnberger *et al.*, “Progress in photovoltaic module calibration: results of a worldwide intercomparison between four reference laboratories,” *Measurement Science and Technology*, vol. 25, no. 10, p. 105005, Oct. 2014, doi: 10.1088/0957-0233/25/10/105005.

[168] U. Blieske and G. Stollwerck, “Glass and Other Encapsulation Materials,” in *Semiconductors and Semimetals*, vol. 89, Elsevier, 2013, pp. 199–258.

[169] K. R. McIntosh, N. E. Powell, A. W. Norris, J. N. Cotsell, and B. M. Ketola, “The effect of damp-heat and UV aging tests on the optical properties of silicone and EVA encapsulants,” *Progress in Photovoltaics: Research and Applications*, vol. 19, no. 3, pp. 294–300, May 2011, doi: 10.1002/pip.1025.

[170] L. Dunn, M. Gostein, and B. Stueve, “Literature review of the effects of UV exposure on PV modules,” in *NREL PV Module Reliability Workshop*, 2013, pp. 551–569.

[171] PVLightHouse, *SunSolve*. .

[172] M. Kempe, “Encapsulant Materials for PV Modules,” in *Photovoltaic Solar Energy*, A. Reinders, P. Verlinden, W. van Sark, and A. Freundlich, Eds. Chichester, UK: John Wiley & Sons, Ltd, 2017, pp. 478–490.

[173] M. C. C. de Oliveira, A. S. A. Diniz Cardoso, M. M. Viana, and V. de F. C. Lins, “The causes and effects of degradation of encapsulant ethylene vinyl acetate copolymer (EVA) in crystalline silicon photovoltaic modules: A review,” *Renewable and Sustainable Energy Reviews*, vol. 81, pp. 2299–2317, Jan. 2018, doi: 10.1016/j.rser.2017.06.039.

[174] G. Cattaneo *et al.*, “Lamination process and encapsulation materials for glass–glass PV module design,” *PV-tech*, p. 8, Mar. 2015.

[175] ASTM International, “ASTM D542-14, Standard Test Method for Index of Refraction of Transparent Organic Plastics.” 2014, [Online]. Available: https://www.astm.org/Standards/D542.htm.

[176] ASTM International, “ASTM D1003-13, Standard Test Method for Haze and Luminous Transmittance of Transparent Plastics.” 2013, [Online]. Available: https://www.astm.org/Standards/D1003.htm.

[177] ASTM International, “ASTM D1044-19, Standard Test Method for Resistance of Transparent Plastics to Surface Abrasion by the Taber Abraser.” 2019, [Online]. Available: https://www.astm.org/Standards/D1044.htm.

[178] ASTM International, “ASTM E424-71(2015), Standard Test Methods for Solar Energy Transmittance and Reflectance (Terrestrial) of Sheet Materials.” 2015, [Online]. Available: https://www.astm.org/Standards/E424.htm.

[179] I.-I. E. Commission and others, “IEC 62788-1-4: Measurement procedures for materials used in photovoltaic modules - Part 1-4: Encapsulants - Measurement of optical transmittance and calculation of the solar-weighted photon transmittance, yellowness index, and UV cut-off wavelength,” 2016.

[180] G. Ross and A. W. Birley, “Optical properties of polymeric materials and their measurement,” *Journal of Physics D: Applied Physics*, vol. 6, no. 7, pp. 795–808, May 1973, doi: 10.1088/0022-3727/6/7/203.

[181] R.-J. Zhou and T. Burkhart, “Optical properties of particle-filled polycarbonate, polystyrene, and poly(methyl methacrylate) composites,” *Journal of Applied Polymer Science*, vol. 115, no. 3, pp. 1866–1872, Feb. 2010, doi: 10.1002/app.31331.

[182] N. E. Powell, B. K. Hwang, A. W. Norris, B. M. Ketola, G. Beaucarne, and K. R. McIntosh, "Improved spectral response of silicone encapsulanted photovoltaic modules," in *2010 35th IEEE Photovoltaic Specialists Conference*, Honolulu, HI, USA, Jun. 2010, pp. 002791–002794, doi: 10.1109/PVSC.2010.5616745.

[183] Y. S. Khoo, T. M. Walsh, F. Lu, and A. G. Aberle, "Method for quantifying optical parasitic absorptance loss of glass and encapsulant materials of silicon wafer based photovoltaic modules," *Solar Energy Materials and Solar Cells*, vol. 102, no. Supplement C, pp. 153–158, Jul. 2012, doi: 10.1016/j.solmat.2012.03.008.

[184] G. M. Wallner, R. W. Lang, W. Platzer, and C. Teichert, "Optical properties of polymer films for transparent insulation," *Macromolecular Symposia*, vol. 181, no. 1, pp. 399–410, May 2002, doi: 10.1002/1521-3900(200205)181:1<399::AID-MASY399>3.0.CO;2-O.

[185] G. M. Wallner, W. Platzer, and R. W. Lang, "Structure–property correlations of polymeric films for transparent insulation wall applications. Part 1: Solar optical properties," *Solar Energy*, vol. 79, no. 6, pp. 583–592, Dec. 2005, doi: 10.1016/j.solener.2005.05.006.

[186] G. Oreski, D. Tscharnuter, and G. M. Wallner, "Determination of solar optical properties of transparent polymer films using UV/vis spectroscopy," *Solar Energy Materials and Solar Cells*, vol. 94, no. 5, pp. 884–891, May 2010, doi: 10.1016/j.solmat.2010.01.012.

[187] M. D. Kempe, "Ultraviolet light test and evaluation methods for encapsulants of photovoltaic modules," *Solar Energy Materials and Solar Cells*, vol. 94, no. 2, pp. 246–253, Feb. 2010, doi: 10.1016/j.solmat.2009.09.009.

[188] C. Pitois, A. Hult, and D. Wiesmann, "Absorption and scattering in low-loss polymer optical waveguides," *Journal of the Optical Society of America B*, vol. 18, no. 7, p. 908, Jul. 2001, doi: 10.1364/JOSAB.18.000908.

[189] R. H. French, J. M. Rodríguez-Parada, M. K. Yang, R. A. Derryberry, and N. T. Pfeiffenberger, "Optical properties of polymeric materials for concentrator photovoltaic systems," *Solar Energy Materials and Solar Cells*, vol. 95, no. 8, pp. 2077–2086, Aug. 2011, doi: 10.1016/j.solmat.2011.02.025.

[190] P. A. van Nijnatten, J. M. C. De Wolf, and I. J. E. Schoofs, "Spectrophotometer accessories for thin film characterisation," 2008, p. 6.

[191] H. C. Hulst and H. C. van de Hulst, *Light Scattering by Small Particles*. Courier Corporation, 1981.

[192] S. Chandrasekhar, *Radiative transfer*. Courier Corporation, 2013.

[193] A. Ishimaru, *Wave propagation and scattering in random media*, vol. 2. Academic press New York, 1978.

[194] B. Maheu, J. N. Letoulouzan, and G. Gouesbet, "Four-flux models to solve the scattering transfer equation in terms of Lorenz-Mie parameters," *Applied Optics*, vol. 23, no. 19, p. 3353, Oct. 1984, doi: 10.1364/AO.23.003353.

[195] B. Maheu and G. Gouesbet, "Four-flux models to solve the scattering transfer equation: special cases," *Applied Optics*, vol. 25, no. 7, p. 1122, Apr. 1986, doi: 10.1364/AO.25.001122.

[196] W. E. Vargas, "Generalized four-flux radiative transfer model," *Appl. Opt., AO*, vol. 37, no. 13, pp. 2615–2623, May 1998, doi: 10.1364/AO.37.002615.

[197] C. Roz, "Average crossing parameter and forward scattering ratio values in four-¯ux model for multiple scattering media," *Optics Communications*, p. 13, 2001.

[198] J. Nocedal and S. Wright, *Numerical optimization*. Springer Science & Business Media, 2006.
[199] L. G. Henyey and J. L. Greenstein, “Diffuse radiation in the galaxy,” *The Astrophysical Journal*, vol. 93, pp. 70–83, 1941.
[200] T. J. Bethell and E. A. Bergin, “The Propagation Of Lyα In Evolving Protoplanetary Disks,” *The Astrophysical Journal*, vol. 739, no. 2, p. 78, Oct. 2011, doi: 10.1088/0004-637X/739/2/78.
[201] S. Q. Duntley, “The optical properties of diffusing materials,” *JOSA*, vol. 32, no. 2, pp. 61–70, 1942.
[202] Shott AG, “Schott Optical Glass Data Sheets,” Jan. 2017. [Online]. Available: https://refractiveindex.info/download/data/2017/schott_2017-01-20.pdf.
[203] I. Rosas-Román, M. A. Meneses-Nava, O. Barbosa-García, and J. L. Maldonado, “Simultaneous Height Adjust fitting: An alternative automated fitting procedure for laser-induced plasma spectra composed by multiple Lorentzian profiles,” *Spectrochimica Acta Part B: Atomic Spectroscopy*, vol. 134, pp. 1–5, Aug. 2017, doi: 10.1016/j.sab.2017.05.004.
[204] N. Tanio and Y. Koike, “What Is the Most Transparent Polymer?,” *Polymer Journal*, vol. 32, no. 1, pp. 43–50, Jan. 2000, doi: 10.1295/polymj.32.43.

List of main abbreviations

HJT	Heterojunction technology
CTMod	Cell-To-Module Modelling Tool developed in this work
INES	Institut National de l'Energie Solaire
CTM	Cell-To-Module ratio of perfomance
EROI (ERoEI)	Energy Return On Energy Invested
UV	Ultraviolet
SC	Semi-Conductor
LCOE	Levelized Cost Of Energy
BIPV	Building Integrated Photovoltaic
VIPV	Vehicle Integrated Photovoltaic
PV	Photovoltaic
IQE, EQE	Internal, External quantum Efficiency
SRH	Shockley-Read-Hall recombinations
STC	Standard Test Conditions: AM1.5g spectrum with 1000W/m² integrated power and device temperature of 25°C
MPP	Maximum Power Point
AM1.5g	Standardized solar spectral irradiance corresponding to an air mass of 1.5 at the ground
CEA	Commissariat à l'Energie Atomique et aux Energies Alternatives
BIFI X	Bifacial irradiance: correspond to the ratio X of rear incident power to the front incident power
TCO	Transparent Conductive Oxide
ITO	Indium Tin Oxide, kind of TCO
a-Si:H	Hydrogenated Amorphous Silicon
c-Si	Crystalline Silicon
NIR	Near InfraRed
EVA	Copolymer of Ethylene Vinyl Acetate
ECA	Electro Conductive Adhesive
ARC	Anti-Reflective Coating
LBIC	Light-Induced
GDP	Gross Domestic Product
Wp	Watt peak
ITRPV	International Roadmap for Photovoltaic
TPO	Thermoplastic PolyOlefin polymer

List of figures

List of tables

List of scientific publications

Patents

Julien EYMARD, Felix GERENTON, Samuel HARRISON, Maria-Delfina MUNOZ, "*Procédé de caractérisation électrique d'une cellule photovoltaïque découpée"*, reference CEA: DD19462 SD, demande de brevet français n°1906688 le 20/06/2019

Eric GERRITSEN, Adrien DANEL, Julien EYMARD, *"Module photovoltaïque à bandes conductrices et procédé de fabrication associé",* reference CEA: DD19756 SD, demande de brevet français n°1909632 le 02/09/2019

Julien EYMARD, Vincent BARTH, Eric GERRITSEN, "Module photovoltaïque avec reduction du déséquilibre électrique", reference CEA: DD20013 SD, demande de brevet français n°1915336 le 20/12/2019

Vincent BARTH, Aude DERRIER, Julien EYMARD, *"Encapsulation pour module solaire à éléments de connexion intégrés"*, reference CEA: DD20748 SD, demande de brevet français n° 2009955

Scientific paper

F. Gerenton, J. Eymard, S. Harrison, R. Clerc, D. Munoz, *"Analysis of edge losses on silicon heterojunction half solar cells"*, *Solar Energy Materials and Solar Cells*, vol. 204, p. 110213, Jan. 2020, doi: 10.1016/j.solmat.2019.110213 (published)

A. Danel, J. Eymard, V. Barth, M, Tomassini, E. Gerritsen, A. Bettinelli, C. Roux, *"Both sides now: Optimal bifaciality with silicon heterojunction solar cells"*, Photovoltaics international, vol. 45, p. 29, Nov. 2020, https://store.pv-tech.org/store/photovoltaics-international-volume-45/ (published)

Conferences publications

J. Eymard, B. Commault, F. Gerenton, T. Guérin, R. Clerc, and M. Hebert, *"Performance Simulations Of A 72-Cell, A-Si Het Module With Different Tab-Interconnection Geometries,"* 35th European Photovoltaic Solar Energy Conference and Exhibition, Sep. 2018, doi: 10.4229/35thEUPVSEC20182018-5CV.1.31 (published)

J. Eymard, A. Danel, V. Barth, L. Basset, E. Gerristen, B. Commault, M. Hebert, R. Clerc, *"Optimizing SHJ Solar Cell bifaciality towards a monolithic module architecture",* 36th European Photovoltaic Solar Energy Conference and Exhibition*,* Sep. 2019, isbn: 3-936338-60-4 (online)

A. Danel, J. Eymard, F. Pernoud, J. Diaz, M. Debourdeau, M. Quemin, A. Bettinelli, L. Basset, L. Sicot, S. Harrison, R. Varache, E. Gerristen, P.J. Ribeyron, C. Roux, "Bifacial optimization of Silicon Heterojunction Solar Cells," 36th European Photovoltaic Solar Energy Conference and Exhibition, Sep. 2019, doi: 10.4229/EUPVSEC20192019-2CO.10.6 (published)

J. Eymard, V. Barth, L. Sicot, B. Commault, A. Bettinelli, L. Basset, W. Favre, R. Clerc, A. Derrier, "*CTMOD: A cell-to-module modelling tool applied to optimization of metallization and interconnection of high-efficiency bifacial silicon heterojunction solar module"*, Metallization & Interconnection Workshop for Crystalline Silicon Solar Cells, Jan. 2021, (accepted for publication)